Studies on Third Order Optical Nonlinearity, Photoluminescence and Random Lasing in Pulsed Laser Deposited $Zn_{1-x}Al_xO$ ($0 \leq x \leq 0.10$) and $Zn_{1-x}Ti_xO$ ($0 \leq x \leq 0.05$) Thin Films

by

GYAN PRAKASH BHARTI

DEPARTMENT OF PHYSICS
INDIAN INSTITUTE OF TECHNOLOGY GUWAHATI
GUWAHATI-781039, India
August 2018

Studies on Third Order Optical Nonlinearity, Photoluminescence and Random Lasing in Pulsed Laser Deposited $Zn_{1-x}Al_xO$ ($0 \leq x \leq 0.10$) and $Zn_{1-x}Ti_xO$ ($0 \leq x \leq 0.05$) Thin Films

A Thesis submitted in partial fulfillment of the requirements for the award of the degree of

DOCTOR OF PHILOSOPHY

by

GYAN PRAKASH BHARTI

DEPARTMENT OF PHYSICS
INDIAN INSTITUTE OF TECHNOLOGY GUWAHATI
GUWAHATI-781039, India
August 2018

Dedicated to My Parents

Gyan Prakash Bharti
Registration No. 11612117
Department of Physics
Indian Institute of Technology Guwahati
Guwahati-781039, Assam, India

STATEMENT

I hereby declare that the matter embodied in this thesis is the result of investigations carried out by me at the Department of Physics, Indian Institute of Technology Guwahati, Guwahati, India, under the supervision of **Prof. Alika Khare**. This thesis has not been submitted to any university, institute or elsewhere for the award of the any degree, diploma or associate-ship.

Date: **Gyan Prakash Bharti**

भारतीय प्रौद्योगिकी संस्थान गुवाहाटी
Indian Institute of Technology Guwahati
Department of Physics
Guwahati-781039, Assam State, INDIA
Phone: +91 361 2582705, 2582701, 2690321 to 328 (extn. 2705),
Fax: +91 361 2582749
Dr. Alika Khare
Professor
E-mail: alika@iitg.ac.in, k_alika@yahoo.com

Date: Aug 2018

Certificate

This is to certify that work contained in the thesis entitled '**Studies on Third Order Optical Nonlinearity, Photoluminescence and Random Lasing in Pulsed Laser Deposited $Zn_{1-x}Al_xO$ ($0 \le x \le 0.10$) and $Zn_{1-x}Ti_xO$ ($0 \le x \le 0.05$) Thin Films'** by **Mr Gyan Prakash Bharti** (Roll no 11612117), a student of Department of Physics, Indian Institute of Technology Guwahati, for the award of degree of Doctor of Philosophy, has been carried out under my supervision and the same has not been submitted elsewhere for the award of any other degree.

(Alika Khare)

Acknowledgement

First of all, I would like to offer my sincere gratitude to my thesis supervisor, Prof. Alika Khare, for her invaluable contribution in this thesis. I feel lucky to get an opportunity to work under her guidance. Her dedication and enthusiasm towards research is highly appreciable. Apart from academic, her valuable suggestions and motivation to complete a challenging task, is admirable. Even, during the tough period of the journey, she was kind enough and understood the situation and helped in to overcome the mental tension.

I would like to offer my sincere thanks to the doctoral committee; the chairman, Dr. Ashwini Kumar Sharma, the committee member, Prof. Amarendra Kumar Sarma and external member, Dr. Shrikrishna N. Joshi sir, for timely reviewing my work and providing the necessary feedback/suggestions to improve my work. Their valuable suggestions were critical in shaping the present form of the thesis.

I sincerely thank IIT Guwahati for providing the institute fellowship to carry out my research work. I specially would like to acknowledge the Equal Opportunity Cum Special Reservation Cell, IIT Guwahati, for providing the financial support.

I sincerely thank Department of Physics, IIT Guwahati for providing the necessary experimental facilities to carry out my research work. I would like to extend my thanks to all the technical and non-technical staffs of the department for their help.

I thank the Central Instrument Facility (CIF), IIT Guwahati, for providing the experimental facilities to complete my work. I specially thank Mr. Chandan Borgohain (Techical Officer) for his kind behavior and help.

I would like to acknowledge Prof. B. P. Singh, Department of Physics, IIT Bombay and Dushyant Kushvah, Center for nano research, IIT Bombay, for low temperature photoluminescence measurement.

I acknowledge my seniors; Dr. Abu, Dr. Satchi, Dr. Poulami, Dr. Indrajeet and Dr. Partha. Learning the basic research tools with fundamental approach and working under such a nice and disciplined environment was remarkable. I extend my acknowledgement to my labmates: Dr. Shantakumar, Rahul, Prahlad, Eshita, Gobinda, Sasmita, Sumit and Nagendra for their unconditional help.

I thank my friends; Rahul, Biplob, Sandeep, Samit, Mahesh, Charan, Dhruv, Roshan etc. for making a pleasant stay at hostel. Special thank goes to Rahul for all his contribution and helping hand in academic as well as at personal level.

I would like to remember my Lt. Grandparents (Hardev Ram and Kumari Devi) on this occasion. The golden days spent with them made my childhood, a memorable one despite of harsh circumstances. I would like to acknowledge my maternal uncle & aunty and their family (Pramod

Kumar, Dept. Commdt., BSF and Vinod Kumar, Asst. Commdt., CRPF, Anu bhabhi and Priyanka bhabhi) for their love and blessings which always motivated and inspired me.

Lastly, I acknowledge my parents, my brothers and sisters for their unbounded love & blessings and bearing patience throughout the journey. The smiling faces with sweet talks of all the young members (Aditi, Pari, Shweta, Ritu, Nitu, Ayush, Aditya & Mitu) of my family were always a stress relief for me.

August, 2018 **Gyan Prakash Bharti**

Abstract

The present thesis was aimed to look into the optimum impurity content of Al and Ti in the host ZnO thin film for improved nonlinear optical properties and random lasing.

Both types of thin films of $Zn_{1-x}Al_xO$ (AZO) and $Zn_{1-x}Ti_xO$ (TZO) were fabricated onto fused silica as well as Si substrates via pulsed laser deposition technique. The best crystalline feature, c-axis orientation (dominating 002 plane) was observed at x=0.05 and 0.02 for AZO and TZO thin films respectively. The surface nanostructures for the higher Al content ($x \geq 0.05$) were of the combination of randomly aligned nanorods as well nanowires while that of for Ti, the nanoparticles were of flower like shape.

The band gap energies from 3.26 eV to 3.64 eV and 3.26 eV to 3.40 eV were obtained for AZO and TZO thin films respectively. The room temperature photoluminescence spectra indicated the dominance of near band edge emission in UV and blue spectral range in which free excitonic lines were not well resolved. The defect level emission was observed to be suppressed at optimum concentration of Al and Ti. The low temperature photoluminescence spectra revealed the strong coupling of neutral donor with free exciton, (D^0X) line. The thin films were subjected to modified z-scan measurement illuminated by continuous wave He:Ne laser to measure the third order nonlinear optical coefficients. The two photon absorption induced photoluminescence in the films under illumination of cw He:Ne laser, was also performed and the maximum efficiency was observed for x=0.05 for Al and 0.02 for that of Ti contained in ZnO film.

Finally, the AZO thin films were subjected to Random lasing experiment by using 3rd harmonic of a Q-switched Nd:YAG laser as a pump beam. The effect of Al content (and hence surface morphology) on the photon confinement mechanism and consequently the formation of possible mirror-less optical cavity, were detailed. The lasing threshold for

pure ZnO film was observed to be ~3.2×10^2 MW/cm^2. The maximum quality factors of the most intense resonance mode was 1004 for x=0.05 where the surface structure was dominated by the formation of nano rods with nearly hexagonal facet resulting into the combination of Fabry-Perot (FP) as well as Whispering Gallery Mode (WGM) cavity.

CONTENTS

List of Figures

List of Tables

Abbreviations

arb. unit	Arbitrary Unit
gm	Gram
mbar	Milli bar
meV	Milli electron volt
mL	Milli liter
mW	Milli watt
AFM	Atomic force microscope
AZO	Aluminum doped Zinc Oxide
ATCC	Automated Target Control Carrousel
BM	Burstein Moss
BGN	Band gap normalization
CA	Closed aperture
CCD	Charged coupled device
CW	Continuous wave
DAP	Donor acceptor pair
DLE	Defect level emission
EDX	Energy dispersive X-rays spectrometer
ESA	Excited state absorption
FCA	Free carrier absorption
FESEM	Field emission scanning electron microscope
FP	Fabry-Perot
FRET	Fluorescence resonance energy transfer
FWHM	Full width at half maximum
FX	Free Exciton
He:Ne	Helium Neon
K. E.	Kinetic energy
LIP	Laser induced plasma
LO	Longitudinal optical
LTPL	Low temperature photoluminescence
MPA	Multi-photon absorption

MW	Mega Watt
NBE	Near band edge
NDF	Neutral density filter
NIR	Near Infra-Red
NLA	Nonlinear absorption
NLO	Nonlinear optical
NLR	Nonlinear refraction
NTP	Normal temperature and pressure
OA	Open aperture
OD	Optical density
PL	Photoluminescence
PLD	Pulsed laser deposition
PMT	Photo multiplier tube
PVA	Poly vinyl alcohol
PVD	Physical vapor deposition
RSA	Reverse saturation absorption
RL	Random lasing
RT	Room temperature
SA	Saturation absorption
TCE	Transparent conducting electrode
TES	Two electron satellite
TPA	Two photon absorption
TS-2PA	Two step two photon absorption
TZO	Titanium doped Zinc Oxide
UV	Ultraviolet
VIS	Visible
WGM	Whispering gallery mode

List of Symbols

~	Approximately
°	Degree
$°C$	Degree celsius
α	Linear Absorption coefficient, inter-axial angle
β	Nonlinear absorption coefficient, inter-axial angle
β_x	Full width at half maxima of XRD peak
Δ	Correction factor due to band isotropy
σ	Root mean square size
μ_H	Hall mobility
μs	Micro second
θ	Angle of diffraction, Debye temperature
λ	Wavelength
ν	Frequency
λ_0	Wavelength of resonant mode
$\Delta\lambda$	Mode separation
$\delta\lambda$	fwhm of mode
$\chi^{(3)'}$	Real part of third order nonlinear optical susceptibility
$\chi^{(3)''}$	Imaginary part of third order nonlinear optical susceptibility
a	Hexagonal lattice constant, Varshni's thermal coefficient
a_B^*	Effective Bohr radius
b	Varshni's thermal coefficient
c	Hexagonal lattice constant
f	Focal length
k	Wave vector
k_B	Boltzmann constant
h	Plank's constant
l	Mean free path
l_{gen}	Generation length
l_{pat}	Mean path length
m	Number of photons, Transition coefficient in Tauc's plot
n, n_0'	Linear refractive index

m^*	Reduced effective mass
m_c^*	Conduction band effective mass
m_{min}^*	Minority carrier effective mass
m_{maj}^*	Majority carrier effective mass
m_v^*	Valence band effective mass
n_0	Liner refractive index
n_e	Carrier density
n_0''	Extinction coefficient
n_2'	Real part of Nonlinear refractive index coefficient
n_2''	Imaginary part of nonlinear refractive index coefficient
n_2^{th}	Thermally induced nonlinear refractive index
wt%	Weight percentage
x	Content (Al or Ti)
z_0	Rayleigh length
A	Absorbance
B	Probability parameter, Correlation length
C_v	Specific heat
D	Crystallite size
E_a	Thermal activation energy
E_g	Band gap energy
Hz	Hertz
K	Kelvin
L	Thickness of thin film
L_{eff}	Effective sample thickness
L_C	Cavity length
N_b	No. of equivalent band extrema
N_{crit}	Critical carrier concentration
O_i	Oxygen interstitial
O_{Zn}	Oxygen antisite
Q	Quality factor
R	Reflectivity
S	Refractive index of substrate
T_{open}	Open aperture transmittance
T_{closed}	Closed aperture transmittance

T	Temperature
T_M	Transmission maxima
T_m	Transmission minima
V_O	Oxygen vacancy
V_{Zn}	Zinc vacancy
X_C	Peak position
Zn_i	Zinc interstitial

Chapter 1
Introduction

Zinc oxide (ZnO), a semiconducting material, possesses some excellent properties and has evolved as a candidate for wide range of applications **[1-4]**. Presently, the commercial use of this material is in protective skin creams layer against skin irritation and mild abrasions. Other than this, ZnO nanoparticles are being used in drug delivery system, enhancing bioactivity, cancer cell tissue eradication etc. **[5-8]**. ZnO is also being viewed as a promising candidate for gas sensing application owing to its chemical response towards various gasses like NO_2, H_2, O_3, CO, CH_4, LPG etc. **[9-14]**. There have also been reports regarding ZnO based piezoelectric sensors **[9, 15-18]**.

In the context of optoelectronic devices, certain properties of ZnO allows it to be considered as a superior alternative compared to those of well-established semiconducting materials such as GaN, GaAs etc. **[19]**. The most of the optoelectronics devices operating towards short wavelength regime relies on the direct and wide band gap semiconducting materials, a property equally possessed by ZnO besides having efficient photo luminescent material in UV spectral range at room temperature due to its large excitonic binding energy. The semiconducting materials having large excitonic binding energy prevent the dissociation of excitons under thermal agitation and ensure an efficient excitonic emission and lasing at room temperature (RT) and above **[20]**. Table 1 lists the nature of optical transitions, band gap energies and exciton binding energies of some of the currently used semiconducting materials and provides their comparison with ZnO [**21-25]**. Its thin film can be fabricated on variety of substrates unlike GaN which is limited to some specific substrate (SiC, Sapphire, Si etc) **[26]**. Further, the highly crystalline structure in ZnO can be easily grown at relatively low substrate temperature, (500 ^{0}C) as

Table 1.1: Comparison of semiconducting materials

Serial No.	Semiconductor type	Nature of optical transition	Band gap energy (eV)	Exciton binding energy (meV)
1.	GaN	Direct	3.4	21-23
2.	GaP	Direct	2.25	11
3.	Si	Indirect	1.1	14.7
4.	ZnSe	Direct	2.7	20
5.	TiO_2	Indirect	3.2 (Anatase) 3.0 (Rutile)	------- -------
6.	**ZnO**	**Direct**	**3.37**	**60**

compared to that of GaN which require high substrate temperature ~1000 ^{0}C thereby providing ease in fabrication **[26]**.

ZnO is an *n*-type direct and wide band gap (E_g=3.37 eV) semiconductor. The nature and magnitude of electrical conductivity as well as band gap energy of ZnO can be modulated by infusing it with impurities (*n*-type or *p*-type). The *n*-type doping e.g. Al, Ba, Mg, Cu etc., in ZnO involves substitutional replacement of external donor atoms into the cationic (Zn^{2+}) sites and results into the change in *n*-type electrical conductivity of the system. The *p*-type dopants e.g. N, P, As etc., are substituted at anionic (O^{2-}) sites and consequently modify *p*-type conductivity. However, achieving *p*-type conductivity by incorporating external oxygen rich elements is not as simple because of the strong residual *n*-type conductivity in ZnO. The intrinsic native point defects in ZnO trap the

substitutional external impurity and form deep levels within the band gap and thus, making *p*-type doping, less effective **[27].**

The band gap energy of ZnO can be easily tuned by alloying it with suitable impurities e.g. Mg, Al, Cd, Cu, Ti etc. **[28-32]**. The alloyed material exhibits the blue shifted as well as red shifted absorption edge depending upon the nature of the impurities. The basic mechanism for the band gap renovation in alloyed semiconductor is governed by Burstein Moss (BM) effect and quantum size effect (Quantum Confinement). Generally, the *n*-type impurity leads to a blue shift and *p*-type leads to a red shift in the band gap energy **[33]**. ZnO exhibits strong nonlinear optical characteristics owing to the non-centrosymmetric nature of its wurtzite crystal structure. The third order nonlinear optical coefficients are modulated in presence of impurity elements because of the change in exciton oscillator strength of the system. It is also a good candidate for a possible application in the field of UV Random laser **[34]**. The random lasing characteristics is generally defined as a source of lasing emission due to the strong scattering with the nano-sized randomly distributed grains in bulk as well as in low dimensional nanostructures **[35]**. The optical cavity in the alloyed ZnO can also be easily modulated by controlling the shape of the nanostructures.

1.1 Crystal structure of ZnO

Zinc oxide belongs to the II-VI type semiconductor family which is formed by a binary compound (XY) in which X belongs to II B group and Y belongs to VI A group of the periodic table. In ZnO, zinc ion possesses partially positive cationic character while oxygen ion has partially anionic character. Overall ZnO exhibits partially electronegative characteristics and is therefore termed as intrinsic *n*-type semiconductor.

ZnO in nature, is found in three forms; Zinc blende, rocksalt and hexagonal wurtzite crystal structures **[36]**. The zinc blende structure is in cubic form, although the formation of single crystal is tedious. The rocksalt structure can be grown only at relatively very high pressure. The most thermodynamically stable structure at normal temperature and pressure (NTP) for ZnO is the hexagonal wurtzite structure, where Zn and O atom reside at the corner of a regular tetrahedral structure in which one kind of atoms is surrounded by the other kind of atoms and vice-versa. There are four atoms per unit cell connected by the opposite atoms. Because of tetrahedral connection, the bond distance of the entire nearest neighbor is nearly the same. Figure 1 shows the hexagonal wurtzite crystal structure of ZnO **[4, 36]**. In this crystal structure, there are two polar surfaces which are formed due to Zn and O atoms. These polar surfaces are Zn-terminated (0001) and O-terminated ($000\bar{1}$) surfaces and constitute the two opposite basal planes along c-axis **[36]**. The polar nature of the crystal structure affects the chemical properties as well as the growth mechanism such as defect formation, growth rate, and preferred orientation etc. **[36]**. Further because of the tetrahedral connection between O^{2-} and Zn^{2+} ions, ZnO is non-Centro symmetric which is responsible for exhibiting the nonlinear optical and piezoelectric behavior.

The wurtzite hexagonal crystal structure has three lattice parameters (a=b and c) and the three inter-axial angles (α=β=90^0 and Υ=120^0). The lattice parameters in a unit cell of ideal wurtzite crystal structure are in the ratio of $c/a=\sqrt{8/3}$ =1.633 **[36]**. In Schoenflies notation, the wurtzite crystal structure belongs to C_{6v}^4 space group and in the Hermann-Mauguin notation, it is known to be in P63mc space group **[36]**. The lattice parameters of ZnO for hexagonal wurtzite crystal structure have been reported over the

range of a=3.2475-3.2507Å and c=5.2042-5.207 Å and consequently the c/a ratio also varies within the range of 1.593-1.6035 **[36]**.

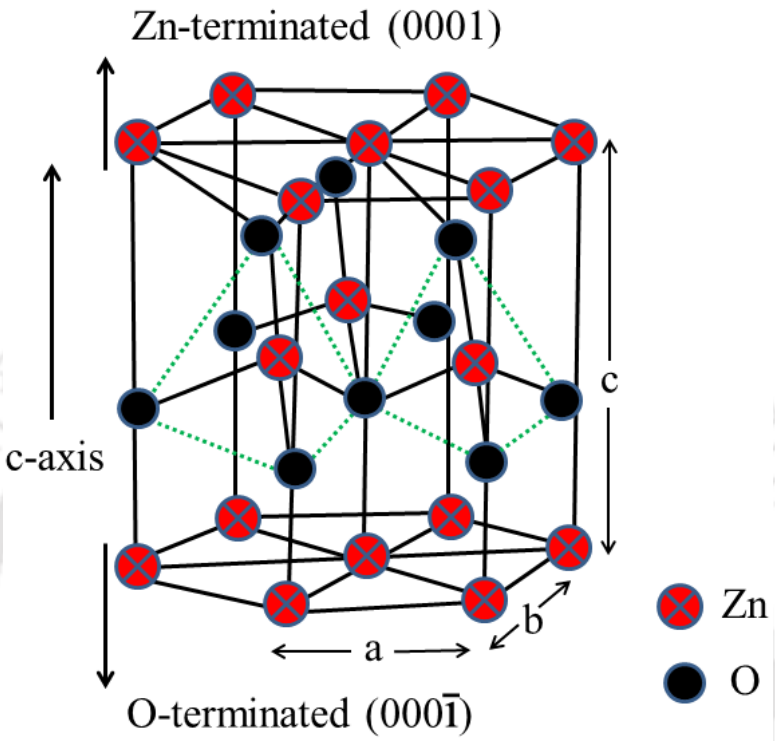

Fig. 1.1 Hexagonal Wurtzite crystal structure of ZnO

1.2 Band structure of ZnO

The band structure of a semiconducting material plays a vital role in framing its optical and electronic properties. The band structure of ZnO is formed from *p*-type valence band and s-type conduction band near the Γ point of the Brillouin zone. Because of the axial symmetry of the wurtzite crystal structure, the valance band near the Γ point splits under the influence of crystal field and spin orbit interaction, into three sub-bands having Γ_9, Γ_7, and Γ_7 symmetries which are assigned as A, B and C respectively, in the order of increasing energies, though there are discrepancies in the correct ordering of the symmetries of A, B and C sub-bands **[37-39]**. The energy separation between these bands

(A, B, C) was estimated to be E_{AB}=10 meV and E_{BC}=34 meV **[39]**. The band gap energies of these sub-bands recorded at 6K are observed at 3.4410 eV, 3.4434 eV and 3.4817 eV respectively **[40]**.

1.2.1 Band gap engineering

Zinc Oxide can be easily alloyed with various other oxides viz; MgO, CdO, CuO, TiO_2 etc for the band gap engineering in order to alter the band gap energy, manipulate the electrical conductivity and to provide optical emission over a wide range in the ultraviolet spectral range. The tailoring of band gap energy towards higher energy in ZnO by Mg, Al, B and Ga doping has been reported in the literature **[28, 41-52]**. In general, the widening of the band gap energies have been explained on the basis of shift of Fermi level into the conduction band due to large free carrier concentration in presence of impurity, also known as Burstein moss (BM) effect and is discussed in the next sub-section. A reduction in the band gap energy (red shift) in ZnO by alloying it with Cd, Mn and Co has also been demonstrated by many research groups **[31, 53-60]**. The decrease in the band gap energy on incorporation of these impurities are mainly caused by the shift in the valence and conduction band as a result of electron-impurity and electron-electron interaction via scattering **[58, 61]**. The *n*-type electrical conductivity of ZnO is easily manipulated by an order of magnitude upon doping of trivalent impurity **[62-64]** providing extra free electrons in the process. The *p*-type conductivity in ZnO is still a challenging task. However, ZnO has been reported to possess p-type conductivity with doping of V^{th} group elements (N, P, As, Sb etc.) **[65-68]**.

The band gap engineering of a semiconductor is addressed on the basis of Burstein Moss (BM) effect and quantum size effect (Quantum Confinement). Apart from these,

the surrounding temperature also plays a crucial role on band gap energy of the semiconductor. All these factors are detailed in the following sub-sections.

1.2.2 Burstein Moss (BM) effect

The large impurity concentration in a semiconductor leads to the alternation in the position of fundamental absorption edge as well as density of states near the brillouin zone center. The basic theory governing the behavior of the optical band gap as a function of carrier concentration is given by Mott **[61, 69].** This theory is a direct consequence of the measure of the critical concentration (N_{crit}), at which insulator-metal transition occurs and is governed by the following relation [61].

$$a_B^* N_{crit}^{1/3} = \frac{1}{4}\left(\frac{\pi}{3}\right)^{1/3} \approx 0.25 \qquad (1.1)$$

where, a_B^* is the effective Bohr radius and N_{crit} is the critical carrier concentration at which insulator-metal transition occurs.

The blue shift of absorption edge in ZnO as a result of *n*-type doping is governed by band filling effect, also known as Burstein Moss (BM) effect **[70]**. According to the BM effect, the conduction band of the degenerate (heavily doped) semiconductor is significantly filled with appropriate high carrier concentration followed by the blocking of lower energy states of valence band. This results in the shift of Fermi level in the conduction band and thus the apparent band gap energy is increased. According to the BM model, the blue shift in the band gap of the degenerate semiconductor is given by the following expression **[71, 72]**.

$$\Delta E_g^{BM} = \frac{\hbar^2 (3\pi^2 n_e)^{2/3}}{2m^*} \qquad (1.2)$$

where n_e is the electron carrier concentration and m^* is the reduced effective mass of electron, defined by the relation $\frac{1}{m^*} = \frac{1}{m_v^*} + \frac{1}{m_c^*}$, where m_v^* and m_c^* are the valence band and conduction band effective masses respectively.

The Equation 2 suggests the inverse relationship between BM shift and carrier effective masses. Thus the semiconductors having light carrier masses exhibit more effective BM shift. As the carrier concentration is increased beyond the Mott critical density the band gap energy of semiconductor decreases because of the reduction of the activation energy of electron transport and reduction of the impurity ionization energy **[61]**. This effect is referred as band gap narrowing, band gap shrinkage or band gap re-normalization effect. The effect of band gap narrowing in heavily doped semiconductor occurs due to the many body interaction effect. The many body interaction involves the interactions among free carriers (electron-electron interaction, hole-hole interaction) and between free carriers and ionized impurities (electron-donor interaction, electron-hole interaction, hole-acceptor interaction etc.). These interaction causes screening effect which results in the lowering of the total energy of the system **[61]**.

The band gap narrowing due to many body interactions at higher carrier density is expressed by the relation **[73, 74]**.

$$\Delta E_g^{BGN} = \frac{1.83\Delta}{r_s N b^{1/3}} R + \frac{0.95}{r_s^{3/4}} R + \frac{\pi}{2} \frac{1}{r_s^{3/4} N_b} \left(1 + \frac{m^*_{\min}}{m^*_{maj}}\right) R \qquad (1.3)$$

where Δ is the correction factor due to the bands anisotropy, R is the Rydberg energy, N_b is the number of the equivalent band extrema and m^*_{min}/m^*_{maj} is the ratio of minority carrier effective mass to majority carrier effective mass and r_s is defined as.

$$r_s = \left(\frac{3}{4\pi n a_B^{*3}}\right)^{1/3} \qquad (1.4)$$

where, a_B* is the effective Bohr radius.

Hence, at very large doping concentration, the effective shift in band gap can be expressed as;

$$\Delta E_g = \Delta E_g^{BM} - \Delta E_g^{BGN} \tag{1.5}$$

1.2.3 Quantum confinement effect

The semiconducting materials exhibit quantum confinement effect in low dimensional structure when the size of the particles become comparable to excitonic bohr radius **[75]**. This results in the blue shift in the absorption as well as the photoluminescence spectra with the decrease in the size of nanoparticles **[76]**.

1.2.4 Temperature effect

The band gap energy of semiconductor is also sensitive to the temperature. The extent of band gap shrinkage or widening depends on the thermal coefficients by the well-known Varshni's equation given by **[77]**.

$$E_g(T) = E_g(T=0) - \frac{aT^2}{T+b} \tag{1.6}$$

where, $E_g(T=0)$ is the band gap energy at 0K, a and b are the Varshni's thermal coefficients. The coefficient, a, gives the limiting value of $-dE_g(T)/dT$ as $T \rightarrow 0$ K and b is related to the Debye temperature **[78]**.

The varshini equation is an empirical equation for the shift in relative position of conduction and valence band based on (1) The temperature dependent lattice expansion and (2) The temperature dependent electron-lattice interaction. In low temperature region,

the thermal expansion coefficient varies in nonlinear fashion with temperature and hence E_g varies non-linearly with T. At high temperature, the effect of temperature on the lattice expansion is linear so, the variation in band gap energy is also linear **[77]**. These two assumptions can be summarized in the following equations **[77]**.

$$\text{For } T<<\theta,\ \Delta E_g \propto T^2 \tag{1.7}$$

$$\text{For } T>>\theta,\ \Delta E_g \propto T \tag{1.8}$$

where, θ is the Debye temperature.

1.3 Photoluminescence in ZnO

The photoluminescence spectra of any semiconducting material provide in-depth information about the band structure, the nature of optical transitions and about the impurity or defect centers etc. The photoluminescence from a semiconducting material is the outcome of radiative recombination of the free electrons in the conduction band and the free holes in the valence band, created under an optical excitation. The photoluminescence from a 2-Dimensional semiconducting material depends on the crystalline quality, the stoichiometry and the grain size of the nanostructures formed.

Owing to the direct and high band gap energy (~3.37 eV) and a large excitonic binding energy (~60 meV), ZnO displays a strong photoluminescence signal in UV range termed as near band edge (NBE) emission **[36]**. Apart from the narrow UV emission, a broad visible band is also exhibited by ZnO which is due to the various defect states present in it, designated as defect level emission (DLE) band **[36]**. The NBE as well as DLE emissions are detailed in Chapter 5.

Under the influence of impurities, it is possible to bring the variation in the PL spectra of ZnO significantly which can lead to tunable light emitting diodes (LEDs) and laser diodes **[43, 79]**. Metal (Cu, Ag, Au etc.) coated ZnO nano structures/thin films exhibit an enhancement in NBE along with suppression of DLE emission as a result of local field enhancement due to strong resonant coupling between the local surface plasmons (LSPs) of metal nano particles and excitons of ZnO **[31, 80, 81]**. In the case of transition metals (Al. Mn, Mg etc.), the reduction in DLE emission band in ZnO is linked to the reduction of the defect states **[43, 82, 83]**. The enhancement in the NBE emission and quenching of DLE emission in ZnO can also be possible via fluorescence resonance energy transfer (FRET) effect when the absorption and emission edges of the two species (donor and acceptor) are in close proximity e.g. ZnO-TiO_2 nano-composite thin film **[84]**. Therefore, an appropriate amount of these external agents can be infused to make a narrower as well as more efficient UV radiation source.

The low temperature PL spectra of ZnO, exhibits several fine structure lines of the excitons (free excitons and bound excitons). The origin of these spectral lines is the temperature dependent nature of the excitons. In general, there are three types of excitons; A-exction, B-exciton and C-exciton which have been assigned according to the splitting of valence band under the influence of crystal field splitting and spin orbit interaction **[85]**. In high quality ZnO crystal, at 10K temperature, A-exciton line, $FX_A^{n=1}$, along with its excited state emission, $FX_A^{n=2}$, have been reported at 3.3771 eV and 3.4220 eV respectively **[86]**. Reynold et. al **[85]** has measured the peak positions of the ground, $FX_B^{n=1}$ and the first excited state, $FX_B^{n=2}$ of B-exciton at 3.3895 eV and 3.4325 eV respectively. The peak positions of ground state, $FX_C^{n=1}$, and first excited state, $FX_C^{n=2}$, of C-exciton are reported to be at 3.4245 eV and 3.4667 eV respectively **[36]**. The bound

excitons lines are observed at slightly lower energy position than that of free exciton lines. These lines are located in the range of 3.348-3.374 eV and are of a total of 12 in numbers which are labeled as I_0-I_{11} **[36]**. There are two types of bound excitons; donor bound excitons (DX) and acceptor bound excitons (AX). These bound excitons are further classified into neutral, singly ionized or doubly ionized donor/acceptor bound excitons **[36]**. At the lower energy side of these bound exciton lines, the two electron satellites (TES) lines are observed within the spectral range of 3.320-3.340 eV. These lines are due to the radiative recombination of a bound exciton to a neutral donor, leaving donor in excited state **[36, 86]**. The donor-acceptor pair (DAP) lines in ZnO are observed in the spectral range of 3.235-3.26 eV in presence of acceptor type impurities, e.g. Nitrogen **[36, 87]**.

Apart from dominating spectral lines as stated above, the longitudinal optical (LO) phonon replicas of these lines are also observed in low temperature PL measurement. These lines are generally of equally spaced with an average separation of ~70-73 meV **[86]**. Depending upon the coupling, the LO phonon lines are termed as FX-*m*LO, DX-mLO and AX-*m*LO, DAP-*m*LO etc. where, *m*=1, 2, 3 signifies the first LO phonon replica, second LO phonon replica, third LO phonon replica respectively **[36]**.

1.4 Non Linear optical properties of ZnO thin film

The optical nonlinearity is another very important feature exhibited by semiconducting materials. The nonlinear optics (NLO) plays a vital role in various fields; optical harmonic generation, optical parametric amplification, N-wave mixing etc **[88-90]**. The nonlinear optical phenomenon can be implemented for various applications including optical phase conjugation, optical parametric oscillator, optical data storage,

optical limiting, optical computing, optical switching, etc **[90-92]**. The NLO phenomenon is the inherent property of any material. The first ever direct application of the nonlinear optics was demonstrated after the invention of laser, via optical harmonics generation **[93]**.

ZnO, being a hexagonal crystal structure possesses both, second and third order optical nonlinearity **[94-96]**. The values of nonlinear optical constants (n_2 and β) can be enhanced in the presence of external impurities. The suitable external impurities in ZnO are transition metals, metal nanoparticles, polymers, dyes etc. Valdez *et. al*. **[97]** has reported a large value of third order nonlinear optical constants in Au and Pt coated ZnO thin film. Sandeep *et. al.* **[98]** has found Mg, as an excellent dopant material for ZnO towards NLO application along with a blue shift in the absorption edge. Irimpan *et. al*. **[99]** observed surface plasmon induced enhanced (~10 times) nonlinear absorption as well as nonlinear refraction in ZnO-Cu nanocomposites. There have been numerous reports on Sn, Er, Ni, Li, Co, Gd, Al etc. doped ZnO exhibiting excellent third order nonlinear optical behavior under pulsed laser **[100-107]**. Under continuous wave (cw) laser irradiation, the dominant mechanism for the optical nonlinearity is different than that of the pulsed laser illumination. The estimated values of the third order nonlinear optical constants are observed to be quite large under cw excitation because of the dominance of thermally induced nonlinear optical effect over electronic nonlinearity **[90]**. Pure ZnO as well as doped ZnO thin films have shown third order nonlinear optical coefficients (β, n_2, $\chi^{(3)}$) as large as ~10 cm/W, ~10^{-4} cm^2/W, ~10^{-3} esu respectively **[105, 108-111]**.

Being a direct and wide band gap semiconductor, ZnO is an active material for up conversion via multiphoton absorption process. The multiphoton absorption depends

upon the excitation wavelength **[112, 113]**. If the photon energy of the pump beam is less than the half of the band gap energy, the emission corresponds to the bound excitons or shallow donor defect states while if the pump energy is more than half of the band gap value, the emission is due to the free excitons **[114]**. There have been numerous reports on multi photon absorption; (two photon absorption (2PA), three photon absorption (3PA) etc.) induced photoluminescence in ZnO thin films and nanostructures pumped via femtosecond lasers **[113, 115, 116]**. The efficiency of two photon absorption (2PA) is significantly enhanced if the up conversion process is mediated via intermediate real states e.g. defects states, instead of virtual states. In this case, the 2PA process is termed as two-step two photon absorption (TS-2PA) process **[117]**. There have been reports on TS-2PA process in ZnO under cw laser pumping. Recently Ghosh *et. al*. **[118]** has reported TPA process in nanostructured ZnO under cw He:Ne laser as a pump operating at 633 nm. The efficiency of TPA process can be improved by introducing defect states via doping in ZnO. Additionally, there have been reports on the generation of 2^{nd} and 3^{rd} harmonic via femtosecond lasers **[115, 119]**.

1.5 Random lasing in ZnO

In a conventional laser, the optical cavity is formed by two mirrors; M_1 and M_2 placed parallel to each other across the longitudinal ends of the active medium as shown in Fig. 1.2 a **[120]**. The light generated from the active medium (AM) undergoes the repeated passes through the active medium via multiple reflections from the mirrors and amplifies in each passage through AM. Once the gain exceeds the losses inside the cavity, the lasing action commences and a laser beam emerges out through the output mirror. On the other hand, a random laser is free from any real cavity formed by the mirrors. In this, the

amplification of photons is carried out by the multiple scattering from the gain media via confinement of optical photons as depicted in Fig. 1.2 b. The strong scattering among the nanoparticles increases the dwell time of the photons inside the gain medium and hence, photons during multiple scattering are amplified **[35]**.

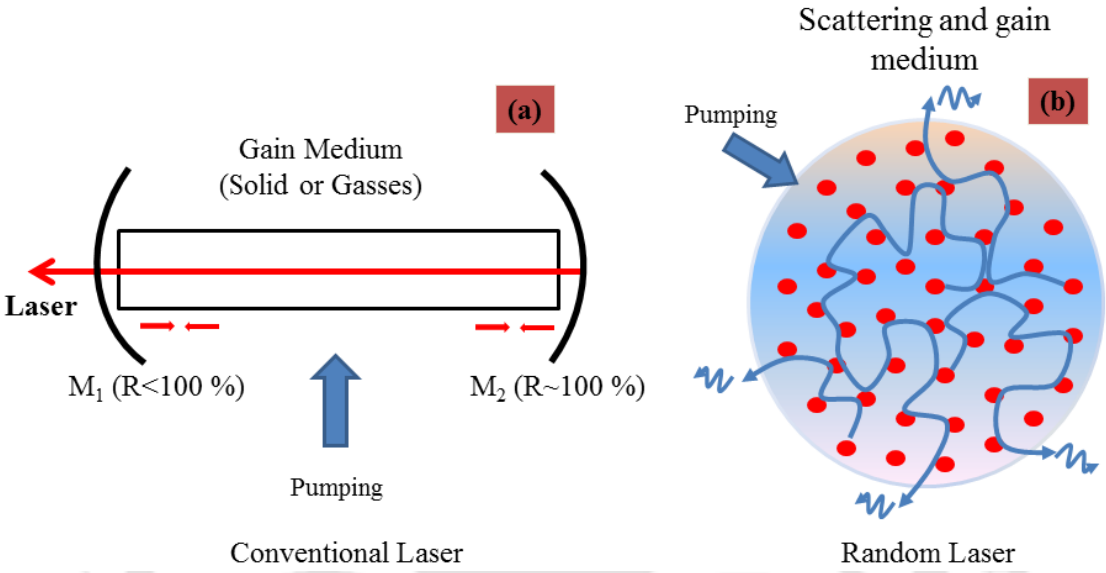

Fig. 1.2 Schematic illustration of (a) conventional laser and (b) random laser

In Random laser, the sample is illuminated by a suitable pump laser. At very low pumping intensity, the sample exhibits a broad photoluminescence band which is the characteristic photoluminescence spectrum of the sample. When the pump intensity crosses the certain threshold, due to onset of stimulated emissions, the emitted band becomes narrow as compared to that of PL emission **[35]**.

Random lasing occurs normally in disordered media. In this, there are two characteristic lengths; the generation length (l_{gen}) and mean path length (l_{path}) which are defined as the average distance traveled by a photon inside the medium before generating a second photon and the average distance travelled by the photon inside the medium before leaving the medium respectively **[121]**. In the case of strong scattering, the l_{path} is

large since the dwell time of photon is increased. All the incoming photons are able to generate at least one additional photon if the condition $l_{path}>l_{gen}$ is satisfied **[121]**.

Random lasing is exhibited by the materials possessing a wide range of physical and chemical compositions such as biological **[122, 123]**, chemical **[124]**, polymers and dyes **[125, 126]**, glasses **[127]**, semiconductors **[128]** etc. The Random lasing has been reported as a useful tool for the sensing applications. Recently, Abegao *et. al*. **[124]** has reported the measurement of milk fat content via measuring the random lasing threshold. A highly sensitive active optical sensor based on the spectral properties of random lasing phenomenon, has been demonstrated by Ignesti *et. al*. **[129]**. The random lasing in semiconducting materials is particularly of great importance for its potential application in solid state laser **[130]**. The major contributory semiconducting materials in the field of random lasing are GaN, GaAsN, ZnS, ZnSe, SnO_2, TiO_2, ZnO etc. **[131-137]**. There have been reports on the reduction in lasing threshold in the metal Nano particles embedded host medium. The presence of nanoparticles act as additional scattering centers and as a result, the random lasing signals are improved **[138-140]**.

Thin films of ZnO can be viewed as an active medium for the generation of mirrorless laser in UV spectral range. The ZnO thin films are normally accompanied by nanostructured surface or nanowires or nanorods or the combination of all these. Therefore, along with PL there is also a possibility of excitation of the ultraviolet lasing in thin film nanostructures via formation of different kinds of optical resonator; Random Laser (RL), Febri-Perot (FP) cavity and Whispering Gallery Mode (WGM) cavity **[112, 141-143]**. In FP cavity, the two opposite facets of the nanostructure (Nano rods or Nano wires) form a pair of parallel mirror like structure as in the conventional FP optical resonator which provides the sufficient feedback for the amplification of optical signal. In

WGM cavity, the generated photon undergoes total multiple internal reflection from the boundary of a single nanostructure (rod or NP) and thus forms a closed loop cavity. In ZnO, having a hexagonal crystal structure, the stimulated lasing emission could be due to the combination of all the three types of mirror-less optical cavities; RL, FP and WGM depending upon the surface structures. Among all three types of cavity, the WGM cavity possess narrower spectral width and hence the quality factor ($Q=\delta\lambda/\lambda$) is often observed to be very high ~3000 **[144]**. There are quite limited numbers of reports especially devoted in the field of ultraviolet lasing in doped ZnO. Recent report on electrically driven ultraviolet random lasing via electroluminescence in Mg doped ZnO (MgZnO) has opened the new scope for tunable laser in the UV spectral range **[145]**.

1.6 Fabrication of pure and doped ZnO thin films

Nanostructured thin film of ZnO is a promising candidate due to its potential applications in the variety of fields such as transparent conducting oxides (TCO), electronics, Opto-electronics, spintronics, solar cells etc. **[1, 146-148]**. Therefore, a great deal of attention is devoted for fabrication of ZnO thin films and its nanostructures via various routes, e.g. sol-gel method **[149-151]**, RF magnetron sputtering **[25, 152]** , spray pyrolysis **[52, 153]**, molecular beam epitaxy **[53, 87]**, atomic layer deposition **[62, 154]**, chemical vapor deposition **[63, 155]** and pulsed laser deposition **[71]**. A high quality film of pure and doped ZnO can be fabricated with ease via pulsed laser deposition (PLD) technique. Highly crystalline ZnO thin film oriented along (002) direction has been reported at low substrate temperature (400-500 ^{0}C) via PLD **[156]**. Novatny *et. al*. **[157]** has reported ZnO thin film via PLD onto various transparent substrates (Sapphire, MgO and fused silica) and observed an epitaxial growth on lattice matched sapphire and MgO

substrates. Perk *et. al*. **[71]** has reported pulsed laser deposited highly crystalline, ZnO as well as doped (Al, Ga) thin film for TCO application. Gas sensing (NO_2) application has also been demonstrated in ZnO thin film deposited via PLD technique **[158]**. Excellent nonlinear optical behavior (second harmonic generation and third harmonic generation) has been observed in pulsed laser deposited ZnO thin films **[159, 160]** by using femtosecond laser.

Pulsed laser deposition (PLD) belongs to the family of physical vapor deposition (PVD) technique. This technique is well known for fabrication of high quality thin films having excellent crystalline structure, stoichiometry, and fabrication at relatively low substrate temperature **[161]**. In this technique, the material to be deposited is ablated in the form of plasma plume under the irradiation of focused high power pulsed laser beam. The generated plasma expands in the ambient environment (Vacuum, O_2, N_2 etc.) and gets deposited onto the substrate placed at an appropriate distance of 3-5 cm from the target surface and parallel to it. To get the optimized quality of the thin film, the various deposition parameters (laser fluence, ambient gas pressure, substrate temperature, target substrate distance, deposition time etc.) are required to be tuned carefully.

In the present thesis, thin films of pure ZnO and Al and Ti infused ZnO are reported via PLD. The working principle of the PLD technique is detailed in chapter 2 on 'Experimental details'.

1.7 Organization of present thesis

The aim of the present dissertation is to carry out systematic studies on the effect of variation of impurities (doping) concentration of two different elements; Al and Ti on the physical, linear and nonlinear optical properties of ZnO thin film. The pulsed laser

deposition technique is adapted to fabricate the thin films of Al doped ZnO (AZO) and Ti doped ZnO (TZO). The optimum deposition parameters for ZnO via PLD were obtained from the literature [162]. The deposited thin films were subjected to X-Ray diffraction (XRD), Laser micro Raman, atomic force microscope (AFM), field emission scanning electron microscope (FE-SEM), UV-visible-NIR spectroscopy and photoluminescence (PL) spectroscopy for characterization. The thin films were also subjected to modified z-scan technique to access the non-linear refraction and absorption coefficients. The multiphoton absorption induced photoluminescence and Random lasing emission in the films are recorded by the experimental setups assembled in house. The low temperature photoluminescence spectra are recorded in order to get in-depth information about the various emission mechanisms in these systems. Finally AZO films were tested for the random laser action.

The content of the present thesis is divided into eight chapters. The overall chapter wise organization is summarized below.

Chapter 1 'Introduction' presents an overview of the material characteristics of ZnO selected for the present study as well as detailed literature survey. It also describes the various band gap engineering mechanisms possible in ZnO facilitating it as a tunable optical source towards UV spectral range. The nonlinear optical properties and random lasing action occurring in ZnO is also highlighted.

Chapter 2 'Experimental details' briefly discusses the major experiments carried out in the present thesis work. This includes pulsed laser deposition (PLD) experimental setup, modified z-scan experimental setup for nonlinear optical characterization, the multiphoton absorption induced photoluminescence (MPA-PL) experimental setup using

cw He:Ne laser and the experimental setup for Random lasing experiment using ns pulsed laser at 355 nm wavelength. The experimental detail of the low temperature photoluminescence in the thin film is also discussed. This chapter also includes the details of all the experimental techniques adopted for the structural characterization; surface morphology study, elemental composition estimation, optical characterization and photoluminescence via X-Ray diffractometer and Micro Raman spectrometer, field emission scanning electron microscope (FESEM), Energy dispersive spectrometer (EDS), UV-vis-NIR and fluorescence spectrometer.

Chapter 3 'Fabrication and characterization of pulsed laser deposited $Zn_{1-x}Al_xO$ ($0 \leq x \leq 0.10$) thin films' discusses the $Zn_{1-x}Al_xO$ ($0 \leq x \leq 0.10$) thin films fabricated by pulsed laser deposition technique. The effect of Al concentration on the structural, surface morphology, linear optical properties (transmission, absorption, band gap energy, refractive index) and photoluminescence emissions are discussed in details.

Chapter 4 'Fabrication and characterization of pulsed laser deposited $Zn_{1-x}Ti_xO$ ($0 \leq x \leq 0.050$) thin films' is devoted on the studies on PLD $Zn_{1-x}Ti_xO$ ($0 \leq x \leq 0.050$) thin films. The effect of Ti concentration on the structural, surface morphology and linear optical properties (transmission, absorption, band gap energy, refractive index, photoluminescence) is detailed in this chapter.

Chapter 5 'Low temperature photoluminescence in pulsed laser deposited $Zn_{1-x}Al_xO$ ($x=0.00$ and $x=0.05$) and $Zn_{1-x}Ti_xO$ ($0 \leq x \leq 0.050$) thin films' as the title suggests is on low temperature photoluminescence studies of $Zn_{1-x}Al_xO$ ($x=0.00$ and $x=0.05$) and $Zn_{1-x}Ti_xO$ ($0 \leq x \leq 0.050$) thin films. In low temperature photoluminescence experiments, the sample temperature is varied from room temperature (300K) to 10K.

Chapter 6 'Nonlinear absorption and refractive index coefficients and multiphoton absorption induced photoluminescence in $Zn_{1-x}Al_xO$ ($0 \leq x \leq 0.10$) and $Zn_{1-x}Ti_xO$ ($0 \leq x \leq 0.050$) thin films', briefly discusses the nonlinear optical characterization and multiphoton absorption induced photoluminescence in $Zn_{1-x}Al_xO$($0 \leq x \leq 0.10$) and $Zn_{1-x}Ti_xO$($0 \leq x \leq 0.050$) thin films. The third order nonlinear optical characterization of the films is carried out by using the modified z-scan experimental setup and the multiphoton absorption induced photoluminescence in the films are studied by using in house developed experimental setups discussed in chapter 2.

Chapter 7 'Random lasing action in pulsed laser deposited $Zn_{1-x}Al_xO$ ($0 \leq x \leq 0.10$) thin films' discusses the Random lasing action in $Zn_{1-x}Al_xO$($0 \leq x \leq 0.10$) thin films. The effect of Al concentration onto the quality factor is detailed.

Chapter 8 'Conclusions' covers the concluding remark on the work detailed in the present thesis and the future possibilities for uncovering the unseen facts.

Bibliography

[**1**] Aleksandra B. Djurisic and Yu Hang Leung, "*Optical Properties of ZnO Nanostructures",* Small, **2** (2006) 944-961.

[**2**] Anderson Janotti and Chris G Van de Walle, "*Fundamentals of zinc oxide as a semiconductor",* Reports on Progress in Physics, **72** (2009) 126501.

[**3**] M Willander et al., "*Zinc oxide nanorod based photonic devices: recent progress in growth, light emitting diodes and lasers",* Nanotechnology, **20** (2009) 332001.

[**4**] Umit Ozgur, et al., "*A comprehensive review of ZnO materials and devices",* Journal of Applied Physics, **98** (2005) 041301.

[**5**] Hua Wang et al., "*Fluorescent dye encapsulated ZnO particles with cell-specific toxicity for potential use in biomedical applications",* Journal of Materials Science: Materials in Medicine, **20** (2008) 11-22.

[**6**] P. K. Mishra et al., "*Zinc oxide nanoparticles: a promising nanomaterial for biomedical applications",* Drug Discovery Today, **22** (2017) 1825-1834.

[**7**] Hamed Mirzaei and Majid Darroudi Mirzaei, "*Zinc oxide nanoparticles: Biological synthesis and biomedical applications",* Ceramics International, **43** (2017) 907-914.

[**8**] Nagarajan Padmavathy and Rajagopalan Vijayaraghavan, "*Enhanced bioactivity of ZnO nanoparticles—an antimicrobial study",* Science and Technology of Advanced Materials, **9** (2016) 035004.

[9] Lokesh Rana et al., "*ZnO/ST-Quartz SAW resonator: An efficient NO_2 gas sensor",* Sensors and Actuators B: Chemical, **252 (**2017**)** 840-845.

[10] Husam S. Al-Salman et al, "*ZnO thin film nanostructures for hydrogen gas sensing applications",* Ceramics International, **39** (2013) S447-S450.

[11] R. Martins et. al, "*Zinc oxide as an ozone sensor",* Journal of Applied Physics, **96** (2004) 1398-1408.

[12] H. Gong et al., "*Nano-crystalline Cu-doped ZnO thin film gas sensor for CO",* Sensors and Actuators B: Chemical, **115** (2006) 247-251.

[13] P. Bhattacharyya et al., "*A low power MEMS gas sensor based on nanocrystalline ZnO thin films for sensing methane",* Microelectronics Reliability, **48** (2008) 1772-1779.

[14] V. M. Latyshev et al., "*Nanostructured ZnO films for potential use in LPG gas sensors",* Solid State Sciences, **67** (2017) 109-113.

[15] E. S. Nour et al., "*Zinc oxide piezoelectric nano-generators for low frequency applications",* Semiconductor Science and Technology, **32** (2017) 064005.

[16] Weiwei Qin et al., "*A high power ZnO thin film piezoelectric generator",* Applied Surface Science, **364** (2016) 670-675.

[17] H. J. Xiang et al., "*Piezoelectricity in ZnO nanowires: A first-principles study",* Applied Physics Letters, **89** (2006) 223111.

[18] A. W. Nowek et al., "*ZnO Thin Films for Applications in Surface Acoustic Wave Actuators",* IEEE, (2016), **DOI:** 10.1109/ICSENS.2016.7808656.

[19] S. Faure et al., "*Comparison of strong coupling regimes in bulk GaAs, GaN, and ZnO semiconductor microcavities",* Physical Review B, **78** (2008) 235323

[20] Michael .H. Huang et al., "*Room-temperature ultraviolet nanowire nanolasers",* Science, **292** (2001) 1897-1899.

[21] S. Strite and H. Morkoc, "*GaN, AlN, and InN: A review",* Journal of Vacuum Science and Technology B, **10** (1932) 1237-1266.

[22] Charles Kittel, *"Introduction to Solid State Physics", Wiley (2005).*

[23] Noriko Saito and Hajime Haneda, "*Hierarchical structures of ZnO sphericalparticles synthesized solvothermally",* Science and Technology of Advamced Materials, **12** (2011) 064707.

[24] W. Shan et al., "*Binding energy for the intrinsic excitons in wurtzite GaN*", Physical Review B, **54** (1996) 16369-16372.

[25] Peng Xing Ping et al., "*Structural and photoluminescent properties of ZnO films deposited by radio frequency reactive sputtering",* Science in China Series G: Physics, Mechanics and Astronomy, **50** (2007) 281-286.

[26] J. C. Fan et al., "*p-Type ZnO materials: Theory, growth, properties and devices",* Progress in Materials Science, **58** (2013) 874-985.

[27] D. P. Norton et al., "*ZnO: growth, doping & processing",* Materials Today, **7** (2004) 34-40.

[28] A. Ohtomo et al., "*$Mg_xZn_{1-x}O$ as a II–VI widegap semiconductor alloy",* Applied Physics Letters, **72** (1998) 2466-2468.

[29] Z. Ben Ayadi et al., "*The properties of aluminum-doped zinc oxide thin films prepared by rf-magnetron sputtering from nanopowder targets",* Materials Science and Engineering: C, **28** (2008) 613-617.

[30] S. Vijayalakshmi et al., "*Characterization of cadmium doped zinc oxide (Cd : ZnO) thin films prepared by spray pyrolysis method",* Journal of Physics D: Applied Physics, **41** (2008) 245403.

[31] Qasem A. Drmosh et al., "*Crystalline nanostructured Cu doped ZnO thin films grown at room temperature by pulsed laser deposition technique and their characterization",* Applied Surface Science, **270** (2013) 104-108.

[32] Haixia Chen et al., "*Ti-incorporated ZnO films synthesized via magnetron sputtering and its optical properties",* Superlattices and Microstructures, **51** (2012) 544-551.

[33] Ali Hassan et al., "*Acceptor-modulated optical enhancements and band-gap narrowing in ZnO thin films",* AIP Advances, **8** (2018) 035212.

[34] V. V. Ursaki et al., "*A comparative study of guided modes and random lasing in ZnO nanorod structures",* Journal of Physics D: Applied Physics, **42** (2009) 095106.

[35] DIEDERIK S. WIERSMA,, "*The physics and applications of random lasers",* Nature Physics, **4** (2008) 359-367.

[36] Hadis Morkoc and Umit Ozgur, "*Zinc Oxide: Fundamentals, Materials and Device Technology",* Wiley-VCH, 2009.

[37] D. G. THOMAS, "*THE EXCITON SPECTRUM OF ZINC OXIDE",* Journal of Physics and Chemistry of Solids, **15** (1960) 86-96.

[38] J. J. HOPFIELD, "*FINE STRUCTURE IN THE OPTICAL ABSORPTION EDGE OF ANISOTROPIC CRYSTALS",* Journal of Physics and Chemistry of Solids, **15** (1960) 97-107.

[39] D. C. Reynolds et al., "*Valence-band ordering in ZnO",* Physical Review B, **60** (1999) 2340-2344.

[40] A. Mang et al., "*BAND GAPS, CRYSTAL-FIELD SPLITTING, SPIN-ORBIT COUPLING, AND EXCITON BINDING ENERGIES IN ZnO UNDER HYDROSTATIC PRESSURE",* Solid State Communications, **94** (1995) 251-254.

[41] A. K. Sharma et al., "*Optical and structural properties of epitaxial MgxZn1−xO alloys",* Applied Physics Letters, **75** (1999) 3327-3329.

[42] Xia Zhang et al., "*Structural and optical properties of Zn1-xMgxO thin films deposited by ultrasonic spray pyrolysis",* Thin Solid Films, **492** (2005) 248-252.

[43] Gaurav Shukla and Alika Khare, "*Effect of Mg doping and substrate temperature on the properties of pulsed laser deposited epitaxial* $Zn_{1-x}Mg_xO$ *thin films",* Applied Physics A, **96** (2009) 713-719.

[44] Henry Hung-Chun Lai et al., "*Dopant-induced bandgap shift in Al-doped ZnO thin films prepared by spray pyrolysis",* Journal of Applied Physics, **112** (2012) 083708.

[45] A. N. Mallika et al., "*Synthesis and optical characterization of aluminum doped ZnO nanoparticles",* Ceramics International, **40** (2014) 12171-12177.

[46] Gyan Prakash Bharti and Alika Khare, "*Structural and linear and nonlinear optical properties of $Zn_{1-x}Al_xO$ (0≤x≤010) thin films fabricated via pulsed laser deposition technique",* Optical Materials Express, **6** (2016) 2063-2080.

[47] Li Gao et al., "*Boron doped ZnO thin films fabricated by RF-magnetron sputtering",* Applied Surface Science, **257** (2011) 2498-2502.

[48] Soaram Kim et al., "*Optical properties and electrical resistivity of boron-doped ZnO thin films grown by sol–gel dip-coating method",* Optical Materials, **35** (2013) 2418-2424.

[49] Caiying Mao et al., "*Effect of B doping on optical, electrical properties and defects of ZnO films",* Journal of Alloys and Compounds, **676** (2016) 135-141.

[50] Charles Muchuweni et al, "*Highly conductive and transparent Ga-doped ZnO thin films deposited by chemical spray pyrolysis",* Optik - International Journal for Light and Electron Optics, 2016. **127** (20): p. 8317-8325.

[51] E. Muchuweni et al., "*Effect of gallium doping on the structural, optical and electrical properties of zinc oxide thin films prepared by spray pyrolysis",* Ceramics International, **42** (2016) 10066-10070.

[52] T. Prasada Rao and M. C. Santhosh Kumar, "*Physical properties of Ga-doped ZnO thin films by spray pyrolysis",* Journal of Alloys and Compounds, **506** (2010) 788-793.

[53] J. W. MARES et al., "*Complex Refractive Indices of $Cd_xZn_{1-x}O$ Thin Films Grown by Molecular Beam Epitaxy",* Journal of ELECTRONIC MATERIALS, **37** (2008) 1665-1673.

[54] Sumanth Joishy and B. V. Rajendra, "*Optical and electrical properties of $Zn_{1-x}Cd_xO$ thin films",* Applied Physics A, **123** (2017) 711(1-9).

[55] S. de Castro et al., "*Defects-related optical properties of $Zn_{1-x}Cd_xO$ thin films",* Materials Science and Engineering: B, **212** (2016) 96-100.

[56] Zaheer Ahmed Khan and Subhasis Ghosh, "*Robust room temperature ferromagnetism in Cu doped ZnO thin films",* Applied Physics Letters, **99** (2011) 042504.

[57] K. Omri et al., "*Magnetic and optical properties of manganese doped ZnO nanoparticles synthesized by sol–gel technique",* Superlattices and Microstructures, **60** (2013) 139-147.

[58] David E. Motaung et al., "*Correlating the magnetism and gas sensing properties of Mn-doped ZnOfilms enhanced by UV irradiation",* RSC Advance, **6** (2016) 26227-26238.

[59] Wei Li et al., "*Enhanced Visible Light Photocatalytic Activity of ZnO Nanowires Doped with Mn^{2+} and Co^{2+} Ions",* Nanomaterials, **7** (2017) 20.

[60] Arockia Jayalatha Kulandaisamy et al., "*Tuning selectivity through cobalt doping in spray pyrolysis deposited ZnO thin films",* Ceramics International, **42** (2016) 1408-1415.

[61] E. F. Schubert, "*Physical Foundations of Solid State Devices",* 2015.

[62] Su Cheol Gong et al., "*Aluminum-doped zinc oxide formed by atomic layer deposition for use as anodes in organic light emitting diodes",* Journal of Vacuum Science & Technology A: Vacuum, Surfaces, and Films, **31** (2013) 01A101.

[63] Chang-Soo Lee and B. T. Ahn, "*IMPROVED OPTICAL TRANSMITTANCE OF BORON DOPED ZNO THIN FILMS BY LOW PRESSURE CHEMICAL VAPOR DEPOSITION WITH PULSE BORON DOPING",* IEEE Explore, Digital Library, (2011) 001294-001297. **DOI:** *10.1109/PVSC.2011.6186195*.

[64] E. Fortunato et al., "*Highly stable transparent and conducting gallium-doped zinc oxide thin films for photovoltaic applications",* Solar Energy Materials and Solar Cells, **92** (2008) 1605-1610.

[65] Z. Y. Xiao et al., "*Stability of p-type conductivity in nitrogen-doped ZnO thin film",* Applied Physics Letters, **92** (2008) 052106.

[66] B Yao et al., "*Mechanism of p-type conductivity for phosphorus-doped ZnO thin film",* Journal of Physics D: Applied Physics, **42** (2009) 015407.

[67] G. Braunstein et al., "*p type doping of zinc oxide by arsenic ion implantation",* Applied Physics Letters, **87** (2005) 192103.

[68] Tzu-Hsuan Kao et al., "*Opto-electrical properties of Sb-doped p-type ZnO nanowires",* Applied Physics Letters, **104** (2014) 111909.

[69] Aron Walsh et al., "*Origin of band gap renormalization in degenerate doped semiconductors",* Physical Review B, **78** (2008) 075211.

[70] ELIAS BURSTEIN, "*Anomalous Optical Absorption Limit in InSb",* Physical Review, **93** (1954) 632-633.

[71] Sang-Moo Park et al., "*Structure and properties of transparent conductive doped ZnO films by pulsed laser deposition",* Applied Surface Science, **253** (2006) 1522-1527.

[72] A. P. Roth et al., "*ABSORPTION EDGE SHIFT IN ZnO THIN FILM AT HIGH CARRIER DENSITIES",* Solid State Communications, **39** (1981) 1269-1271.

[73] S. C. Jain et al., "*Band-gap narrowing in novel III-V semiconductors",* Journal of Applied Physics, **68** (1990) 3747-3749.

[74] A. Abdolahzadeh Ziabari and S. M. Rozati, "*Carrier transport and bandgap shift in n-type degenerate ZnO thin films: The effect of band edge nonparabolicity",* Physica B: Condensed Matter, **407** (2012) 4512-4517.

[75] A. D. Yoffe, "*Low-dimensional systems: Quantum size effects and electronic properties of semiconductor microcrystallites (zero-dimensional systems) and some quasi-two-dimensional systems",* Advances in Physics, **51** (2010) 799-890.

[76] Z. D. Fu, et al., "*Study on the quantum confinement effect on ultraviolet photoluminescence of crystalline ZnO nanoparticles with nearly uniform size",* Applied Physics Letters, **90** (2007) 263113.

[77] Y. P. VARSHNI, "*TEMPERATURE DEPENDENCE OF THE ENERGY GAP IN SEMICONDUCTORS"*, Physica, **34** (1967) 149-154.

[78] Dushyant Kushavah et al., "*Photoluminescence characteristics of CdSe quantum dots: role of exciton–phonon coupling and defect/trap states",* Materials Research Express, **4** (2017) 075007.

[79] H. Kim et al., "*Effect of aluminum doping on zinc oxide thin films grown by pulsed laser deposition for organic light-emitting devices",* Thin Solid Films, **377** (2000) 798-802.

[80] X. D. Zhou et al., "*Mechanism of the enhancement and quenching of ZnO photoluminescence by ZnO-Ag coupling",* EPL (Europhysics Letters), **93** (2011) 57009.

[81] Xuehong Li et al., "*Effects of localized surface plasmons on the photoluminescence properties of Au-coated ZnO films",* Optics Express, **17** (2009) 8735-8740.

[82] Bhupendra K Sharma and Neeraj Khare, "*Stress-dependent band gap shift and quenching of defects in Al-doped ZnO films",* Journal of Physics D: Applied Physics, **43** (2010) 465402.

[83] Jin Li et al., "*Structural and photoluminescence of Mn-doped ZnO single-crystalline nanorods grown via solvothermal method",* Colloids and Surfaces A: Physicochemical and Engineering Aspects, **349** (2009) 202-206.

[84] H. Y. Lin et al., "*Giant enhancement of band edge emission based on ZnO/TiO_2 nanocomposites",* Optics Express, **15** (2007) 13832-13837.

[85] D. C. Reynolds et al., "*Neutral-donor–bound-exciton complexes in ZnO crystals",* Physical Review B, **57** (1998) 12151-12155.

[86] A. Teke et al., "*Excitonic fine structure and recombination dynamics in single-crystallineZnO",* Physical Review B, **70** (2004) 195207.

[87] S. J. Jiao et al., "*Donor–acceptor pair luminescence of nitrogen doping p-type ZnO by plasma-assisted molecular beam epitaxy",* Journal of Luminescence, **122-123** (2007) 368-370.

[88] J. J. H. Gielis et al., "*Optical second-harmonic generation in thin film systems",* Journal of Vacuum Science & Technology A: Vacuum, Surfaces, and Films, **26** (2008) 1519.

[89] Y. R. Shen, "*Principles Of Nonlinear Optics". Wiley-Interscience, 2003.*

[90] Robert W. Boyd, "*Nonlinear optics",* Academic Press, 2008.

[91] S. J. Mathews et al., "*Large third-order optical nonlinearity and optical limiting in symmetric and unsymmetrical phthalocyanines studied using Z-scan",* Optics Communications, **280** (2007) 206-212.

[92] Fryad Z. Henari et al., "*Third-order optical nonlinearity and all-optical switching in porous silicon",* Applied Physics Letters, **67** (1995) 323.

[93] P. A. Franken et al., "*Generation of Optical Harmonics",* Physical Review Letters, **7** (1961) 118-119.

[94] M. C. Larciprete et al., "*Second order nonlinear optical properties of zinc oxide films deposited by low temperature dual ion beam sputtering",* Journal of Applied Physics, **97** (2005) 023501.

[95] M. C. Larciprete et al., "*Characterization of second and third order optical nonlinearities of ZnO sputtered films",* Applied Physics B, **82** (2005) 431-437.

[96] Ja-Hon Lin et al., "*Two-photon resonance assisted huge nonlinear refraction and absorption in ZnO thin films",* Journal of Applied Physics, **97** (2005) 033526.

[97] Martin Trejo-Valdez et al., "*Study of the electrical and nanosecond third order nonlinear optical properties of ZnO films doped with Au and Pt nanoparticles",* Thin Solid Films, **605** (2016) 84-88.

[98] C. S. Suchand Sandeep et al., "*Sol-gel synthesis and nonlinear optical transmission in* $Zn_{1-x}Mg_xO(x\leq0.2)$ *thin films".* Applied Physics Letters, **89** (2006). 063102.

[99] Litty Irimpan et al., "*Enhanced luminescence and nonlinear optical properties of nanocomposites of ZnO-Cu",* Journal of Material Research, **23** (2008) 2836-2845.

[100] A Rherari et al., "*Effect of lithium on linear and nonlinear optical properties of Sn-doped zinc oxide prepared by spray pyrolysis",* IOP Conf. Series: Materials Science and Engineering, **186** (2017) 012002.

[101] Vinay Kumari et al., "*Nonlinear optical properties of erbium doped zinc oxide (EZO) thin films",* Optics Communications, **285** (2012) 2182-2188.

[102] C. Torres-Torres et al., "*Optical Kerr phase shift in a nanostructured nickel-doped zinc oxide thin solid film",* Optics Express, **21** (2013) 21357.

[103] C. Torres-Torres et al., "*Stimulated Emission and Optical Third-Order Nonlinearity in Li-Doped ZnO Nanorods",* Journal of Physical Chemistry C, **113** (2009) 13515–13521.

[104] YAN Teng-Fei et al., "*The Third-Order Nonlinear Optical Properties in Cobalt-Doped ZnO Films",* Chinese Physics Letters, **32** (2015) 077801.

[105] K. Spoorthi et al., "*Investigations on nonlinear optical properties of electron beam treated Gd:ZnO thin films for photonic device applications",* Laser Physics, **27** (2017) 065403.

[106] K. Bahedi et al., "*Influence of strain/stress on the nonlinear-optical properties of sprayed deposited ZnO:Al thin films",* Applied Surface Science, **257** (2011) 8003-8005.

[107] Zim Maung Htwe et al., "*Ultrafast carrier dynamics and third order nonlinear optical properties of aluminum doped zinc oxide (AZO) thin films",* Optical Materials, **66** (2017) 580-588.

[108] Albin Antony et al., "*Influence of electron beam irradiation on nonlinear optical properties of Al doped ZnO thin films for optoelectronic device applications in the cw laser regime",* Optical Materials, **62** (2016) 64-71.

[109] M. Abd-Lefdil et al., "*Third harmonic generation process in Al doped ZnO thin films",* Journal of Alloys and Compounds, **584** (2014) 7-12.

[110] M. Abd-Lefdil et al., "*Structural, photoinduced optical effects and third-order nonlinear optical studies on Mn doped and Mn–Al codoped ZnO thin films under continuous wave laser irradiation",* Laser Physics, **24** (2014) 035404.

[111] K. K. Nagaraja et al., "*Third-order nonlinear optical properties of Mn doped ZnO thin films under cw laser illumination",* Optical Materials, **35** (2013) 431-439.

[112] C. F. Zhang et al., "*Multiphoton absorption pumped ultraviolet stimulated emission from ZnO microtubes",* Applied Physics Letters, **91** (2007) 142109.

[113] D. C. Dai et. al., "*Efficient multiphoton-absorption-induced luminescence in singlecrystalline ZnO at room temperature",* Optics Letters, **30** (2005) 3377-3379.

[114] Pingxin Xiong et al., "*Ultraviolet luminescence enhancement of ZnO two-dimensional periodic nanostructures fabricated by the interference of three femtosecond laser beams",* New Journal of Physics, **13** (2011) 023044.

[115] C. F. Zhang et al., "*Femtosecond pulse excited two-photon photoluminescence and second harmonic generation in ZnO nanowires",* Applied Physics Letters, **89** (2006) 042117.

[116] Susanta Kumar Das et al., "*Multiphoton-absorption induced ultraviolet luminescence of ZnO nanorods using low-energy femtosecond pulses",* Journal of Applied Physics, **108** (2010) 043107.

[117] S. L. Chen et al., "*Efficient upconversion of photoluminescence via two-photon absorption in bulk and nanorod ZnO",* Applied Physics B, **108** (2012) 919-924.

[118] Poulami Ghosh and Ashwini K. Sharma, "*Two-photon induced photoluminescence and lasing in pulsed-laser deposited ZnO nanostructures pumped by continuous wave He-Ne laser",* Optical Materials, **66** (2017) 651-658.

[119] Zouhair Sofiani al., "*Third harmonic generation in undoped and X doped ZnO films (X: Ce, F, Er, Al, Sn) deposited by spray pyrolysis",* Journal of Applied Physics, **101** (2007) 063104.

[120] K. Thyagarajan and Ajoy Ghatak, "*Lasers: Fundamentals and Applications",* Springer, 2010. **Second Edition**.

[121 Hui Cao, "*Random lasers: development feature and applications",* Optics and Photonics News, (2005) 24-29.

[122] Dengfeng Huang et al., "*Low threshold random lasing actions in natural biological membranes",* Laser Physics Letters, **13** (2016) 065603.

[123] Randal C. Polson and Z. Valy Vardeny, "*Random lasing in human tissues",* Applied Physics Letters, **85** (2004) 1289-1291.

[124] Luic M. G. Abegao et al., "*Measuring milk fat content by random laser emission",* Scientific Reports, **6** (2016) 35119.

[125] J. Kitur et al., "*Dependence of the random laser behavior on the concentrations of dye and scatterers",* Journal of Optics, **12** (2010) 024009.

[126] Liling Yang et al., "*Effective random laser action in Rhodamine 6G solution with Al nanoparticles",* Applied Optics, **50** (2011) 1816-1821.

[127] Michele Gaio et al., "*Tuning random lasing in photonic glasses",* Optics Letters, **40** (2015) 1611.

[128] H. Cao et al., "*Random Laser Action in Semiconductor Powder",* Physical Review Letters, **82** (1999) 2278-2281.

[129] Emilio Ignesti et al., "*A new class of optical sensors: a random laser based device",* Scientific Reports, **6** (2016).

[130] Mikhail A. Noginov, "*Solid-State Random Lasers",* Springer Series in Optical Sciences 2005. **ISBN: 10: 0-387-23913-8**.

[131] Masaru Sakai et al., "*Random laser action in GaN nanocolumns",* Applied Physics Letters, **97** (2010) 151109.

[132] B. Q. Sun et al., "*Epitaxially grown GaAsN random laser",* Journal of Applied Physics, **93** (2003) 5855-5858.

[133] Yue Wang et al., "*Coherent Random lasing from CdSe/CdS/ZnS quantum dots",* JSAP, **18p-D5-9** (2013).

[134] Toru Takahashi et al., "*Blue-light-emitting ZnSe random laser",* Optics Letters, **34** (2009) 3923-3925.

[135] H. Y. Yang et al., "*Ultraviolet coherent random lasing in randomly assembled SnO_2 nanowires",* Applied Physics Letters, **94** (2009) 241121.

[136] SHU ZHU, et al., "*Random lasing at the edge of a TiO_2 nanotube thin film",* Applied Optics, **55** (2016) 5091-5094.

[137] Peiliang Chen et al., "*Electrically pumped ultraviolet random lasing in ZnO",* Optics Express, **17** (2009) 4712-4717.

[138] Cih-Su Wang et al., "*Surface-Plasmon-Enhanced Ultraviolet Random Lasing from ZnO Nanowires Assisted by Pt Nanoparticles",* Applied Physics Express, **5** (2012) 062003.

[139] Lihua Ye et al., "*Enhancement of random lasing assisted by Ag nanoparticle doped dye medium in solidified fiber",* Laser Physics, **26** (2016) 045001.

[140] Jiajia Yin et al., "*The shape effect of Au particles on random laser action in disordered media of Rh6G dye doped with PMMA polymer",* Journal of Modern Optics, **63** (2016) 1998-2002.

[141] C. Cachoncinlle et al., "*Random lasing of ZnO thin films grown by pulsed-laser deposition",* Applied Surface Science, **336** (2015) 103-107.

[142] H. Cao et al., "*Ultraviolet lasing in resonators formed by scattering in semiconductor polycrystalline film",* Applied Physics Letters, **73** (1998) 3656-3658.

[143] J. Dai et al., "*Combined whispering gallery mode laser from hexagonal ZnO microcavities",* Applied Physics Letters, **95** (2009) 191117.

[144] Gangyi Zhu et al., "*Lasing Behavior Modulation for ZnO Whispering-Gallery Microcavities",* ACS Applied Materials & Interfaces, **4** (2012) 6195-6201.

[145] Mohammad Suja et al., "*Electrically driven deep ultraviolet MgZnO lasers at room temperature",* Scientific Reports, **7** (2017) 2677.

[146] S. J. PEARTON et al., "*ZnO Spintronics and Nanowire Devices",* Journal of Electronic Materials, **35** (2006) 862-868.

[147] Jia Huang et al., "*Applications of ZnO in organic and hybrid solar cells",* Energy & Environmental Science, **4** (2011) 3861-3877.

[148] Gyu-Chul Yi et al., "*ZnO nanorods for electronic and photonic device applications",* Proceeding of SPIE, **6003** (2005) 600301.

[149] V. Musat et al., "*Al-doped ZnO thin films by sol–gel method",* Surface and Coatings Technology, **180-181** (2004) 659-662.

[150] D Aryanto et al., "*Preparation and structural characterization of ZnO thin films by sol-gel method",* Journal of Physics: Conferernce Series, **817** (2017) 012025.

[151] S. Ben Yahia et al., "*Raman study of oriented ZnO thin films deposited by sol-gel method",* Spectrochim Acta A Mol Biomol Spectrosc, **71** (2008) 1234-8.

[152] Q. P. Wang et al., "*Violet luminescence emitted from ZnO films deposited on Si substrate by rf magnetron sputtering",* Applied Surface Science, **201** (2002) 123–128.

[153] A. Ashour et al., "*Physical properties of ZnO thin films deposited by spray pyrolysis technique",* Applied Surface Science, **252** (2006) 7844-7848.

[154] Hsing-Chao Chen et al., "*Low-Threshold Stimulated Emission in ZnO Thin Films Grown by Atomic Layer Deposition",* IEEE JOURNAL OF SELECTED TOPICS IN QUANTUM ELECTRONICS, **14** (2008) 1053-1057.

[155] Doyoung Kim et al., "*Fabrication of rough Al doped ZnO films deposited by low pressure chemical vapor deposition for high efficiency thin film solar cells",* Current Applied Physics, **10** (2010) S459-S462.

[156] F. K. SHAN et al., "*Studies of ZnO Thin Films On Sapphire (0001) Substrates Deposited by pulsed laser deposition",* Journal of Electroceramics, **13** (2004) 189–194.

[157] M. Novotny et al., "*Structural characterization of ZnO thin films grown on various substrates by pulsed laser deposition",* Journal of Physics D: Applied Physics, **45** (2012) 225101.

[158] D. Padilla-Rueda et al., "*Room temperature pulsed laser deposited ZnO thin films as photoluminiscence gas sensors",* Applied Surface Science, **259** (2012) 806-810.

[159] H. Cao et al., "*Second harmonic generation in laser ablated zinc oxide thin films",* Applied Physics Letters, **73** (1998) 572-574.

[160] G. I. Petrov et al., "*Efficient third-harmonic generation in a thin nanocrystalline film of ZnO",* Applied Physics Letters, **83** (2003) 3993-3995.

[161] Douglas B Chrisey and Graham K. Hubler, "*Pulsed Laser Depostiion OF THIN FILMS",* John Willey and Sons, Inc. : p. ISBN: 0-471-59218-8.

[162] Gaurav Shukla, "*Pulsed laser deposition and characterization of AlN, TIO_2, and $Zn_{1-x}Mg_xO$ ($0<x<0.7$) semiconductor thin films",* PHD Thesis, (2011).

Chapter 2
Experimental details

Pulsed laser deposition (PLD) technique now a days is being viewed as an excellent fabrication tool for depositing the thin films over a wide range of materials including pure metals and nonmetals, semiconductors, complex ceramics, etc. **[1, 2]**. This technique offers a controlled growth rate and desired stoichiometry of thin films by carefully selecting the appropriate deposition parameters. In the present thesis, the PLD technique is being employed for the fabrication of $Zn_{1-x}Al_xO$ ($0 \leq x \leq 0.10$) and $Zn_{1-x}Ti_xO$ ($0 \leq x \leq 0.050$) thin films onto fused silica and Si substrates. The deposited thin films were characterized by using various analytical tools such as X-ray Diffraction (XRD), Laser Micro Raman Spectrometer, Energy Dispersive X-rays Spectrometer (EDX), Field Emission Scanning Electron Microscope (FESEM), Stylus Profilometer, UV-VIS-NIR Spectrophotometer and Fluorescence Spectrometer. The third order nonlinear optical characteristics, multiphoton absorption induced photoluminescence (MPA-PL) and random lasing (RL) in the thin films were studied using in-house assembled experimental setups. The low temperature photoluminescence measurement in these thin films was also carried out by assembling an indigenous experimental setup.

2.1 Preparation of PLD targets for $Zn_{1-x}Al_xO$ ($0 \leq x \leq 0.10$) and $Zn_{1-x}Ti_xO$ ($0 \leq x \leq 0.050$) thin films

Pure ZnO, $Zn_{1-x}Al_xO$ ($0 \leq x \leq 0.10$) and $Zn_{1-x}Ti_xO$ ($0 \leq x \leq 0.050$) targets for PLD were prepared from their respective powder via solid state reaction method. The proportions of ZnO (s. d. fine-chem Ltd., 99%) and Al_2O_3 (MERCK, 99.9%,) and TiO_2 (Ranboxy, 98%) powders for preparation of $Zn_{1-x}Al_xO$($0 \leq x \leq 0.10$) and $Zn_{1-x}Ti_xO$ ($0 \leq x \leq 0.050$) pellet are listed in the table 2.1 and 2.2, respectively.

Table 2.1 Composition of ZnO and Al_2O_3 in $Zn_{1-x}Al_xO$ ($0 \leq x \leq 0.10$) for target preparation

Sr. No.	**$Zn_{1-x}Ti_xO$ Samples (x)**	**Amount of ZnO (gm)**	**Amount of Al_2O_3 (gm)**
1.	Pure ZnO (x=0)	5.000	0.000
2.	$Zn_{0.99}Al_{0.01}O$ (x=0.01)	4.968	0.031
3.	$Zn_{0.98}Al_{0.02}O$ (x=0.02)	4.937	0.063
4.	$Zn_{0.97}Al_{0.03}O$ (x=0.03)	4.904	0.095
5.	$Zn_{0.95}Al_{0.05}O$ (x=0.05)	4.840	0.159
6.	$Zn_{0.93}Al_{0.07}O$ (x=0.07)	4.775	0.225
7.	$Zn_{0.90}Al_{0.10}O$ (x=0.10)	4.674	0.325

Table 2.2 Composition of ZnO and TiO_2 in $Zn_{1-x}Ti_xO$ ($0 \leq x \leq 0.050$) for target preparation

Sr. No.	**$Zn_{1-x}Ti_xO$ Samples (x)**	**Amount of ZnO (gm)**	**Amount of TiO_2 (gm)**
1.	Pure ZnO (x=0)	5.000	0.000
2.	$Zn_{0.995}Ti_{0.005}O$ (x=0.005)	4.975	0.025
3.	$Zn_{0.990}Ti_{0.010}O$ (x=0.010)	4.951	0.049
4.	$Zn_{0.980}Ti_{0.020}O$ (x=0.020)	4.902	0.098
5.	$Zn_{0.970}Ti_{0.030}O$ (x=0.030)	4.853	0.147
6.	$Zn_{0.950}Ti_{0.050}O$ (x=0.050)	4.754	0.246

For the preparation of pure ZnO target, its powder was initially grinded gently by hand in Mortar and pestle for 2 hrs. The powder was constantly stirred by a spatula during the grinding process to obtain homogeneous and nearly uniform particle size distribution. A solution of an organic binder, Polyvinyl Alcohol (PVA), having 5% concentration was used as a binder. The PVA solution is volatile in nature and evaporates out after sintering. For the preparation of 5% PVA solution, 5 gm powder of PVA was mixed in 100 mL of distilled water and thoroughly mixed using magnetic hot plate to obtain a homogeneous solution. The solution is then allowed to cool down for 24 hrs in order to form a gel like texture. The small quantity of this gel is added in the grinded powder (~5 gm) and mixed thoroughly and further grinded for nearly 2 hrs. Finally, the prepared powder is pressurized up-to 3 tons using KBr pressure machine to form a dense circular pellets of ~13 mm diameter.

Similar process was adopted for the preparation of $Zn_{1-x}Al_xO$ ($0 \leq x \leq 0.10$) and $Zn_{1-x}Ti_xO$ ($0 \leq x \leq 0.050$) targets for the PLD of thin film by taking the appropriate amount of ZnO and Al_2O_3 or TiO_2 powders as listed in table 2.1 and 2.2, respectively.

2.1.1 Sintering of pellets

Sintering is the process of diffusion of different sized grains to form a compact material. The prepared pellets were sintered at 1150 ^{0}C for 6 hrs. in an electric furnace. The photograph of pure ZnO pellet before and after the sintering is shown in the Fig. 2.1. The size of the sintered target is ~11 mm. The AZO and TZO pellets were also sintered in the similar manner. The reduction in size of the pellets after sintering was due to the formation of dense compact structure after sintering.

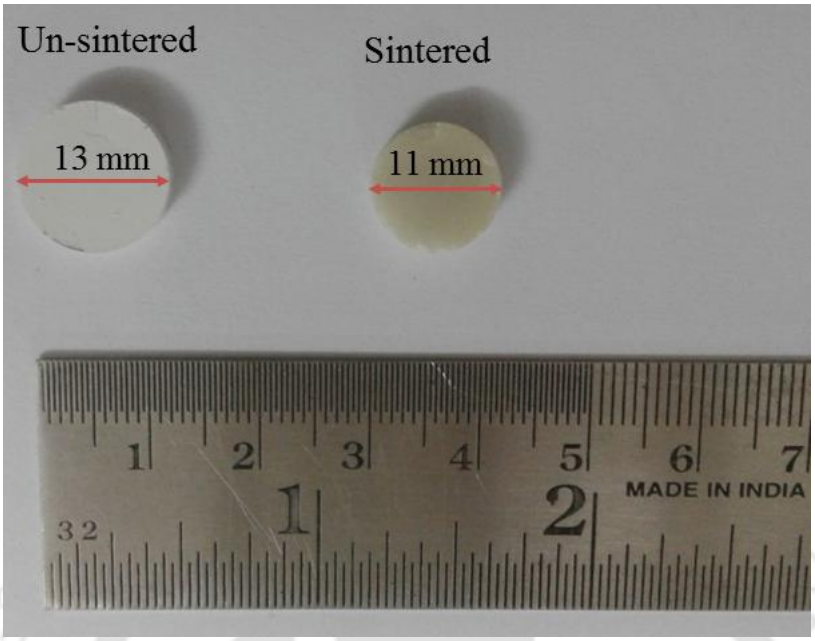

Fig. 2.1 PLD targets of pure ZnO; un-sintered (left) and sintered at 1150 ^{0}C (right).

2.2 Preparation of substrate

The thin films of pure ZnO, $Zn_{1-x}Al_xO$ ($0 \leq x \leq 0.10$) and $Zn_{1-x}Ti_xO$ ($0 \leq x \leq 0.05$) were deposited onto fused silica and silicon substrates. Both these types of substrates were thoroughly cleaned by Acetone and dried prior to the deposition of the films.

2.3 Pulsed laser deposition (PLD) set-up

Pulsed laser deposition technique is simple yet versatile which can be used for deposition of thin films of complex materials with high quality. The pulsed laser deposition (PLD) belongs to the family of physical vapor deposition (PVD). In this technique, a high power pulsed laser is focused on to a sintered target furnishing the target plasma plume which expands in the background ambient and deposited on to the substrate placed few cm apart from the target. The basic mechanisms involved in the PLD process, are classified into three steps (a) laser-matter interaction resulting into ablation

and vaporization of target material and formation of laser induced plasma (LIP), (b) interaction of LIP with the incident laser beam via inverse-bremsstrahlung as well as expansion and cooling of plasma and (c) growth of the film onto the substrate.

Laser ablation involves absorption of laser radiation by the target material leading to electronic excitation, breakdown and plasma formation, etc. For creation of LIP, a minimum focal intensity of the order of ~10^8 W/cm^2 is required. Generally, nano-second lasers: Q switched Nd: YAG and excimer lasers, are capable of delivering such a high intensity **[1]**. The ablation from the target material depends on the properties of the material such as absorption coefficient (α), reflectivity (R), specific heat (C_v) and thermal conductivity (K) etc. It also depends on the laser parameters (laser energy, wavelength, pulse width). In nanosecond laser ablation, the laser pulse width is larger as compared to that of the time interval of entire interactions taking place inside the material. In the initial stage of the laser pulse, the absorption of laser energy by the material leads to the ablation and breakdown of the material. The LIP consists of neutral atoms, ions and electrons etc. In the second stage, the plasma expansion takes place under ambient gas. During the expansion of laser plasma, it absorbs the laser energy via inverse bremsstrahlung process causing further ionization and increases the surrounding temperature. The pressure of the initially formed plasma plume near the target is very high at the initiation of plasma which commences with the nearly solid density (of the target) along with very high kinetic energy (K.E.) of the emitted particles. This generates a pressure gradient between the plasma plume near the target and the ambient environment (~10^{-6}-10^{-1} mbar) which results in the expansion of plasma plume with an expansion velocity of ~10^3-10^5 m/sec. During the plasma expansion, it gets cool down and simultaneously the interaction with the ambient gas leads to the formation of molecular species if applicable (e.g. formation

of oxide/nitrides etc.). In the final stage, as a result of condensation and nucleation of the molecular species, the formation of thin film onto the substrate takes place. The nucleation and growth of the film is dependent on the dynamics of the LIP, the surface energy of the substrate, etc.

Conventionally PLD is viewed to be limited to deposition over small area (~1-2 cm^2) only. But this limitation is overcome by incorporating multiple laser beams **[3]** as well as by translating the substrate and laser beam suitably **[4]**. Another problem with this technique is the ejection of large particulates (in the form of liquid droplets or clusters) from the target and being deposited directly on the substrate thus rendering the poor surface quality. But, this problem can be overcome by carefully optimizing the deposition parameters in particular the laser fluence, background pressure and target to substrate distance **[2, 5, 6]**.

There are some major advantages of PLD over other fabrication techniques. One of the salient features of PLD is the easy control over deposition parameters depending on the properties of the target and the required thin films. Another major advantage of PLD is its ability to transfer the stoichiometry from the target to the deposited thin film. The fabrication of highly crystalline thin film of even very complex material can easily be achieved at relatively low substrate temperature by this technique as compared to those of other thin film deposition techniques.

The schematic diagram of the pulsed laser deposition (PLD) setup used for deposition of $Zn_{1-x}Al_xO$ ($0 \leq x \leq 0.10$) and $Zn_{1-x}Ti_xO$ ($0 \leq x \leq 0.05$) thin films in the present work is shown in Fig. 2.2. A beam from the second harmonic of a high power Q-switched Nd:YAG laser (Quanta System, HYL-101, ~10 ns, 10 Hz) was focused from outside, after steering it suitably, with high damage threshold right angled prism (not shown in

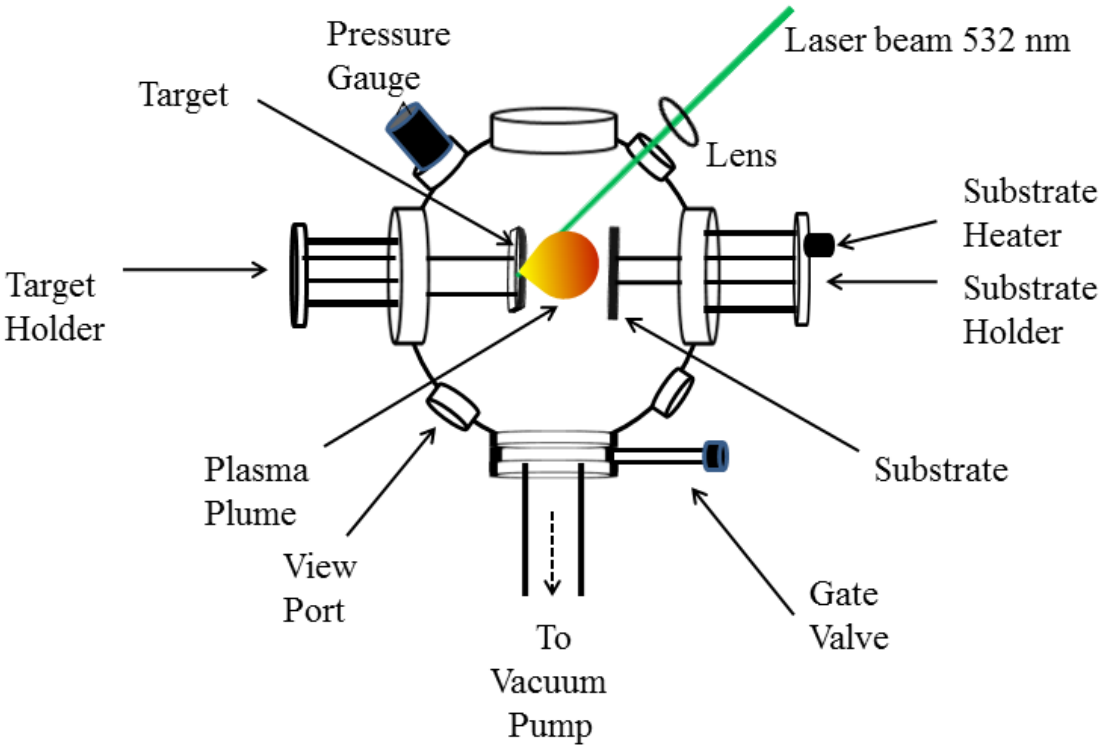

Fig. 2.2 Schematic diagram of pulsed laser deposition (PLD) chamber.

Fig. 2.2), onto the target placed inside the PLD chamber by a plano-convex lens of 35 cm focal length. Prior to the deposition, the PLD chamber was evacuated to a base pressure of 2.5×10^{-5} mbar by a turbo molecular pump (Pfeiffer, Hi Pace 300 C) backed by rotary pump (Pfeiffer, DUO 10MC). The turbo pump was connected to the bottom of the PLD chamber through a 100 CF port. The PLD target (sintered pellets) was mounted onto motorized target carrousel which was installed inside the PLD chamber through one of the 150 CF port. The substrate (fused silica and Si) was mounted on the substrate holder through another 150 CF port opposite to the target port of the PLD chamber. The substrate holder was equipped with resistive heating to maintain the desired temperature during deposition. All the thin films were deposited at a substrate temperature of ~500 ^{0}C. The substrate to target distance during fabrication for all the thin films was at kept at ~3 cm. The deposition of the films was carried out under an oxygen environment, at a

pressure of 10^{-1} mbar. The pressure inside the chamber was monitored by a compact cold cathode gauge (Pfeiffer, IKR 251) and pirani gauge (Pfeiffer, PCR 280 and Hind HiVac, HPS-2) working in the low pressure regime (10^{-2}-10^{-7} mbar) and high pressure regime (10^{3}-10^{-3} mbar) respectively. The thin films were deposited at a laser fluence of ~10 J/cm^2. All the thin films were deposited for 30 minutes duration.

All these parameters for depositing the $Zn_{1-x}Al_xO$ ($0 \leq x \leq 0.10$) and $Zn_{1-x}Ti_xO$ ($0 \leq x \leq 0.05$) thin films are listed in table 2.3.These are the optimized parameters for fabrication of pure ZnO thin film via PLD **[7]**.

Table 2.3 Deposition parameters for $Zn_{1-x}Al_xO$ ($0 \leq x \leq 0.10$) and $Zn_{1-x}Ti_xO$ ($0 \leq x \leq 0.05$) thin films via PLD.

Serial No.	**Parameters**	**Numerical Value**
1.	Ambient Pressure	2.5×10^{-5} mbar
2.	Oxygen Pressure	10^{-1} mbar
3.	Substrate Temperature	500 ˚C
4.	Laser Fluence	10 J/cm^2
5.	Substrate to Target Distance	3 cm
6.	Deposition Time	30 minutes
7.	Substrate	Fused Silica, Silicon

2.4 Characterization of PLD thin films

2.4.1 Energy dispersive X-ray spectroscope (EDX)

The stoichiometry of PLD AZO and TZO thin film was investigated by energy dispersive x-ray spectroscope (EDX) (M/s Sigma Zeiss, Germany).

2.4.2 Field emission scanning electron microscope (FESEM)

The surface morphology and the shape of nanostructures formed in thin films were studied by field emission scanning electron microscope (FESEM) (M/s Sigma Zeiss, Germany). A thin layer of gold coating was applied on the samples before loading these inside the instrument.

2.4.3 X-Ray diffraction

The X-ray diffraction (XRD) technique is a non-contact and non-destructive measurement tool to study the crystalline phases present in the sample (bulk or thin film) and to measure the crystallite size, unit cell dimensions, strain, stress, defect structures etc. of these phases **[8]**. In the present thesis work, the XRD spectra of the thin film samples were recorded by X-Ray diffractometer (Model No. Rigaku, TTRAX III 18 kW) operating at 1.5406 Å of Cu-$K_{\alpha 1}$ line.

2.4.4 Raman spectroscopy

Raman spectroscopy is another non-destructive sensitive analytical tool to record the optical phonon spectra of the sample in bulk, thin film as well as in liquid phase. In the present work, Laser Micro Raman spectrometer (LabRam HR-800, Jobin Vyon)

equipped with Ar-ion laser operating at a wavelength of 488 nm was used for thin films of AZO and TZO in backscattering geometry.

2.4.5 Stylus profilometer

The thickness of the pulsed laser deposited $Zn_{1-x}Al_xO$ ($0 \leq x \leq 0.10$) and $Zn_{1-x}Ti_xO$ ($0 \leq x \leq 0.05$) thin films was measured using Stylus Profilometer (Veeco DekTak 150).

2.4.6 UV-VIS-NIR spectrophotometer

The linear optical characterization of the deposited thin films was carried out by UV-VIS-NIR spectrophotometer (Model No. SHIMADZU UV-3101 PC). The absorption as well as transmission spectra were recorded in the spectral range of 200-2000 nm. The absorption coefficients and band gap energy of the films were estimated from the Beer-Lambert's law and Tauc's plot respectively absorption spectra. The linear refractive index and thickness of the films were measured from the transmission spectra using Swanepoel envelope method **[9]**.

2.4.7 Fluorescence spectrometer

The steady state photoluminescence spectra of the deposited thin films of $Zn_{1-x}Al_xO$ ($0 \leq x \leq 0.10$) and $Zn_{1-x}Ti_xO$ ($0 \leq x \leq 0.05$) were recorded by using Flouromax spectrometer (Edinburg Instruments, Model No. FS920) equipped with Xenon lamp by exciting the samples at a wavelength of 320 nm.

2.5 Modified Z-Scan set-up

The basic idea of Single beam Z-scan technique for the determination of nonlinear optical constants in thin films as well as in bulk crystal was developed for the first time by M. Sheik Bahae et. al **[10]**. This technique is based on the measurement of the nonlinear optical loss and phase distortion imposed on the Gaussian beam under the presence of nonlinear optical medium. In this technique, the intensity of transmitted signal from the sample is measured as a function of sample position translated along the beam direction around the focal region (-z to +z) of a Gaussian beam.

In the conventional Z-scan experimental setup, as was originally proposed, the use of photodiode as a detector requiring the scanning for open aperture (OA) z-scan (for Nonlinear absorption coefficient) and closed aperture (CA) z-scan (for nonlinear refractive index) separately, both of which require precise alignment of the detector. In the modified Z-scan setup, the photodiode is replaced by CCD and the OA as well as CA data can be extracted from the single scan only **[11]**. Figure 2.3 shows the schematic of the modified z-scan experimental setup used for the third order nonlinear optical characterization of the $Zn_{1-x}Al_xO$ ($0 \leq x \leq 0.10$) and $Zn_{1-x}Ti_xO$ ($0 \leq x \leq 0.05$) thin films in the present work.

In this, a continuous wave (cw) He:Ne laser (Melles Griot, 05-LHP-927), having 632.8 nm wavelength, was focused onto the sample by a biconvex lens of focal length (L) of 5 cm. The sample was mounted on a micro positioner stage to enable its translation along longitudinal (z-axis) direction. A CCD was placed to capture the transmitted beam from the sample. A neutral density filter (NDF) of 3.0 Optical Density (OD) was placed in front of CCD to avoid its saturation. An aperture of ~ 6mm diameter was placed after

the sample in order to prevent the scattered light entering into CCD. The thin film sample was translated from -12 mm to 12 mm around both sides of the focal plane (z=0) in a step of 1 mm and the transmitted beam was captured onto the CCD for each and every location.

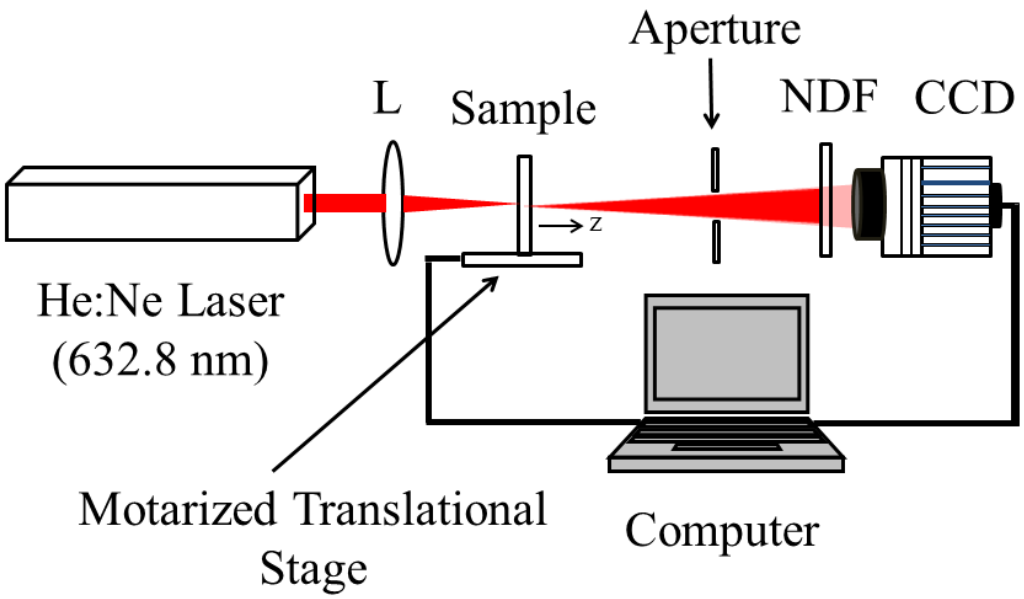

Fig. 2.3 Modified z-scan experimental set-up.

The diameter (d) of the direct beam was measured by imaging it on the CCD directly before the lens and was found to be ~1.5 mm. From this, the beam waist, $\omega_0 = f\lambda/d$, was found to be ~21 microns. The Rayleigh length ($z_0 = \pi\omega_0^2/\lambda$) was estimated to be ~2.2 mm which is much larger than the thickness of the thin film thus satisfying the thin sample approximation required for z-scan **[10]**. The peak intensity (I_0) at the focal plane was estimated to be 1.12 kW/cm^2. The information about the open as well as closed aperture z-scan signal was deduced from these single scanned images only. The integrated intensity over the entire image (open z-scan, OA) as a function of distance w.r.t. focal point gives the information about the absorptive nonlinearity present in the sample. The closed aperture z-scan data was extracted by placing a suitable synthetic

aperture from a MATLAB program in the central region of the images of open z-scan and the integrated intensity of these partially masked images (closed z-scan, CA) revealed the nonlinear refractive index. The linear aperture transmittance, the ratio of closed aperture signal and open aperture signal (S = CA/OA) was kept at 0.4 which was the optimum value in order to exclude the contribution of the absorptive nonlinearity for determination of refractive nonlinearity **[11]**.

The nonlinear absorption coefficients (β) of the PLD thin films of $Zn_{1-x}Al_xO$ ($0 \leq x \leq 0.10$) and $Zn_{1-x}Ti_xO$ ($0 \leq x \leq 0.050$) were estimated by using the normalized OA data fitted to the equation 2.1 **[10]**:

$$T_{open}(z) = 1 - \frac{\beta I_0 L_{eff}}{2^{3/2}\left[1+(z/z_0)^2\right]} \tag{2.1}$$

where, β, I_0, z_0 and L_{eff} being the nonlinear absorption coefficient, peak intensity at the focal plane (z = 0), Rayleigh length and effective sample thickness, respectively. Effective sample thickness (L_{eff}) is defined as $L_{eff} = (1-e^{-\alpha L})/\alpha$ where 'α' is the linear absorption coefficient and 'L' is the actual thin film thickness.

The nonlinear refractive index (n_2) was extracted by fitting the normalized CA data to the equation 2.2 **[10]**:

$$T_{closed}(z) = 1 - \frac{4n_2 I_0 L_{eff}(z/z_0)k}{\left[1+(z/z_0)^2\right]\left[9+(z/z_0)^2\right]} \tag{2.2}$$

where k is the magnitude of the wave vector.

The third order nonlinear susceptibility can be determined from n_2 and β. The relation between complex nonlinear refractive index ($n_{2,complex}$) and third order complex

susceptibility ($\chi^{(3)}_{complex}$) is expressed by equation 2.3 **[12, 13]**:

$$n_{2,complex} = \frac{12\pi^2 \chi^{(3)}_{complex}}{n_0 n_0 ' c} \tag{2.3}$$

$$n_{2,complex} = n_2 ' + i n_2 '' \tag{2.4}$$

$$n_o = n_o ' + i n_o '' \tag{2.5}$$

where, n_o' n_o'' are the real and imaginary part of the linear refractive index and n_2' and n_2'' are that of nonlinear refractive index.

The complex susceptibility $\chi^{(3)}_{complex}$ is defined by the equation 2.6:

$$\chi^{(3)}_{complex} = \chi^{(3)} ' + i\chi^{(3)} '' \tag{2.6}$$

where, $\chi^{(3)}'$ and $\chi^{(3)}''$ are the real and imaginary part of the third order optical susceptibility.

From equations 2.3-2.6, real and imaginary parts of the $\chi^{(3)}_{complex}$, can be separated and are given by.

$$\chi^{(3)} ' = 10^{-7} \frac{n_0 ' c}{12\pi^2} (n_0 ' n_2 ' - n_0 '' n_2 '') \tag{2.7}$$

$$\chi^{(3)} '' = 10^{-7} \frac{n_0 ' c}{12\pi_2} (n_0 ' n_2 '' + n_0 '' n_2 ') \tag{2.8}$$

In the present case, the real part of the linear refractive index, $n_0' = n$, the linear extinction coefficient, $n_0'' = (\alpha\lambda/4\pi)$, the real part of the nonlinear refractive index $n_2' = n_2$ and imaginary part of the nonlinear refractive index $n_2'' = (\beta\lambda/4\pi)$. From the measurement of n, n_2 and β, the real and imaginary parts of the $\chi^{(3)}$ was determined for AZO as well as TZO PLD thin films.

2.6 Multiphoton absorption induced photoluminescence (MPA-PL) experimental set-up

The multiphoton absorption induced photoluminescence (MPA-PL) in the AZO and TZO thin films are studied using in-house assembled experimental setup as shown in Fig. 2.4.

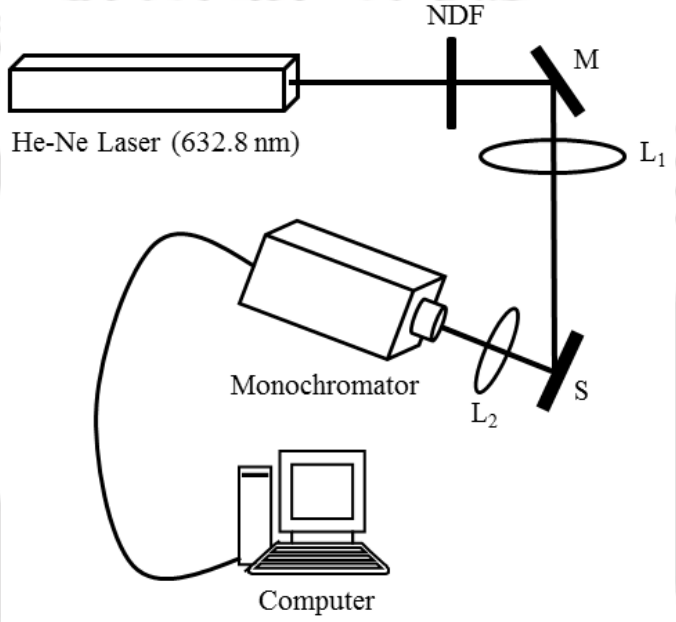

Fig. 2.4 MPA-PL experimental set-up.

A 32 mW cw He:Ne laser operating at 632.8 nm wavelength was steered by using a mirror (M) towards the thin film sample as a pump beam. A cylindrical lens (L_1) of 25 cm focal length was used to focus the beam on the sample (S) as shown in Fig. 2.4. The focal region on the surface of the sample was observed to be of the form of a rectangular strip of dimensions 2000 × 600 μm^2. The sample was oriented at ~ 45° to the incident beam and the fluorescence signal was imaged by a convex lens (L_2) of 5 cm focal length on the entrance slit of monochromator (SPEX 750M) and detected by a photomultiplier tube (PMT). The output of PMT signal was interfaced to the computer. The cylindrical lens

was oriented in the manner so that the larger side of the focal rectangular spot on the sample was parallel to the entrance slit of the monochromator. The monochromator was scanned in the spectral range of 330–390 nm to record the multiphoton induced PL spectra. A neutral density filter (NDF) of various optical densities (OD) was introduced in the path of incident beam in order to study the dependence of PL signal on the pump intensity.

2.7 Low temperature photoluminescence experimental set-up

The experimental set-up assembled for recording the low temperature photoluminescence (LTPL) spectra of the $Zn_{1-x}Al_xO$ (x=0.00 and x=0.05) and $Zn_{1-x}Ti_xO$ ($0 \leq x \leq 0.05$) thin films is shown in Fig. 2.5. The PL spectra were recorded from room temperature (300K) to 10K in an interval of 10K.

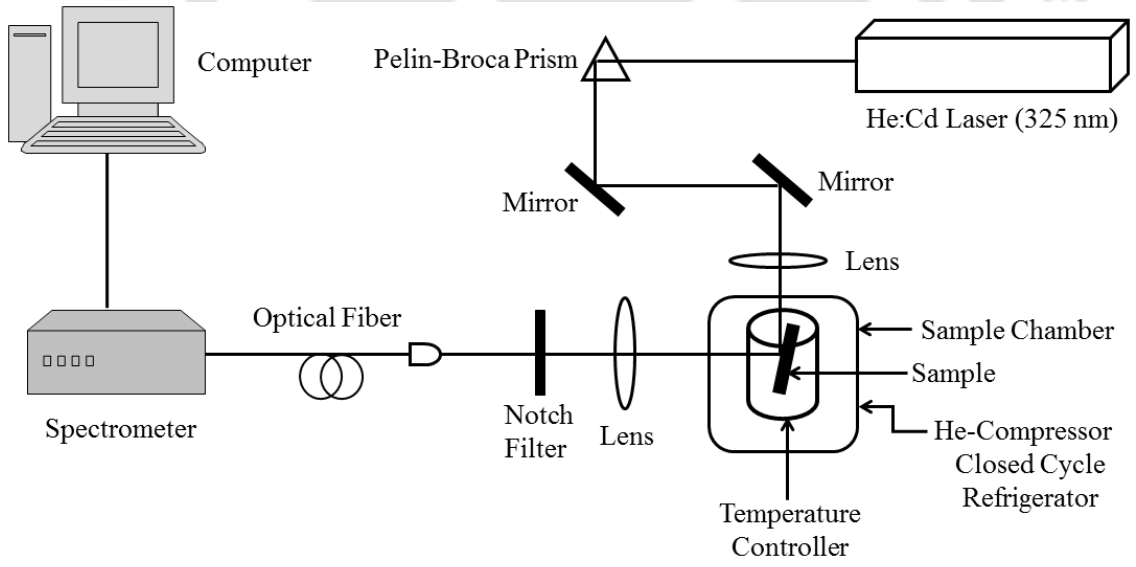

Fig. 2.5 Schematic diagram of LTPL set-up.

The thin film under investigation was mounted on the copper sample holder attached to the cold finger of a He closed cycle refrigerator (CTI Cryogenics 8200 Compressor).

Cold finger was equipped with a heater and temperature sensor for regulating and monitoring the temperature. A temperature controller (Cryo-con 32B) was attached to the sample holder to monitor the temperature of the sample. The sample chamber was sealed with a shroud with optical windows to monitor the sample position as well as to irradiate it and collect the PL signal. A cw He:Cd laser (λ=325 nm) having output power of 25 mW was used as an excitation source. The laser beam was steered by a Pellin-Broca Prism and a pair of mirrors as shown in fig 2.5. The laser beam was focused onto the sample by a 15 cm focal length at grazing incidence so as to illuminate the large area of the sample. The PL signal was collected by another lens (f=25 cm) and was fed on to the optical fiber connected to the entrance port of the spectrometer (SpectraPro 2500i, Act. Res. Corp.). A notch filter at 325nm was placed just before the fiber to obstruct the pump radiation from entering into the spectrometer. The signal was detected by CCD and was interfaced to computer. The PL spectrum was recorded in the spectral range of 330 nm to 730 nm for all the samples.

2.8 Random lasing experimental set-up

The experimental set-up used for the observation of random lasing (RL) in the pulsed laser deposited $Zn_{1-x}Al_xO$ ($0 \leq x \leq 0.10$) thin films, is shown in Fig. 2.6. The 3rd harmonic of a Q-switched Nd:YAG laser (Spectra Physics-Model No. INDI-HG) having 10 ns pulse duration and repetition rate of 10 Hz, was used as pump beam. As the Nd: YAG laser was delivering very high laser energy therefore in order to avoid the ablation/damage of the film, a clean glass plate was inserted in the path of the laser beam to reflect ~10% of the energy to be used as the pump beam for RL. The beam transmitted through the glass plate was suitably dumped as shown in Fig 2.6 for safety. The pump beam was loosely focused

on the sample using a convex lens of 25 cm focal length at an angle of incidence of ~45°. The beam spot on the target was estimated by

$$\omega(z) = \omega_0 \left[1 + \left(\frac{z}{z_0} \right)^2 \right]^{1/2} \tag{2.9}$$

where $\omega(z)$ is the beam spot at a distance of z from the focal plane, and $\omega_0 = f\Delta\theta$ is the beam waist (spot size at the focus) where, f being the focal length of the lens and $\Delta\theta$ is the divergence angle of the laser beam.

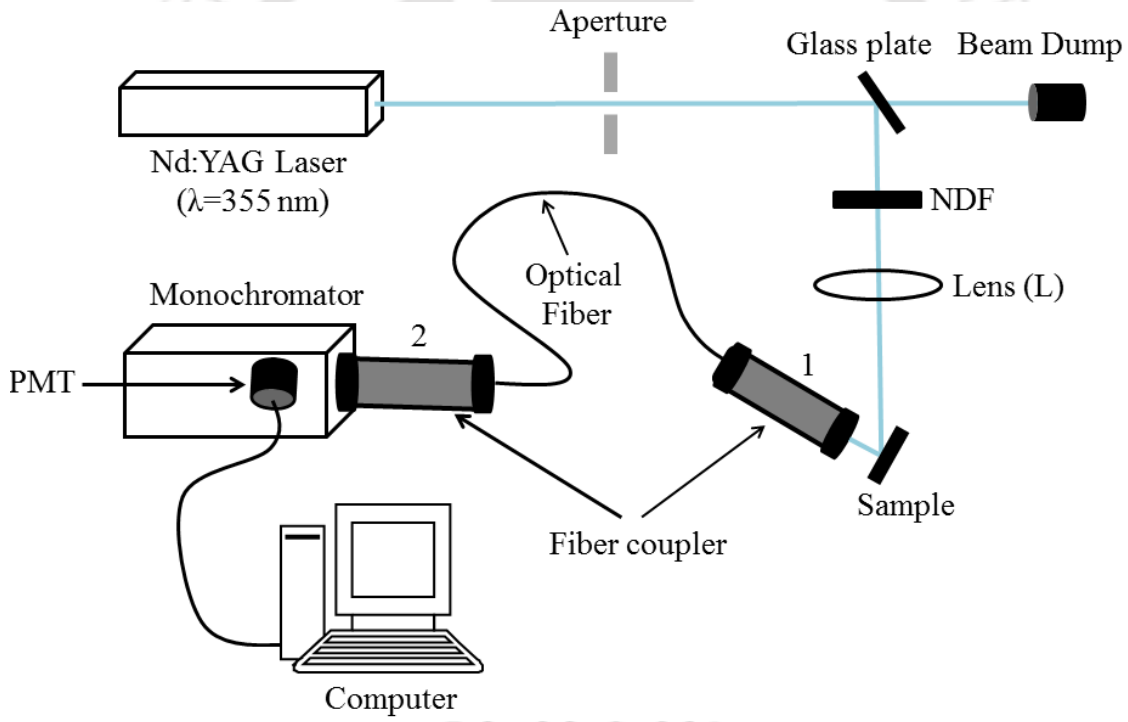

Fig. 2.6 Schematic diagram of Random lasing experiment.

The RL signal from the films was collected via two optical fiber couplers. The plane of the optical coupler 1 and that of the film were made parallel to each other in order to collect the maximum possible signal. The both the optical couplers (1 or 2) comprised of combination of two lenses each. For the coupler 1, first lens makes the input

radiation collimated (The distance between the sample and the first lens was same as that of the focal length of this lens). The role of the second lens was to focus the collimated radiation coming out of the first lens, on the optical fiber. The other end of the optical fiber was connected to the optical coupler 2, mounted directly on the entrance slit of the monochromator (SPEX 750M). The dispersed spectrum from the monochromator was detected by photomultiplier tube (PMT) attached to it and interfaced to the computer. The monochromator was scanned in the range of 360 nm to 420 nm to record the random lasing signal. An aperture of diameter ~10 mm was placed in front of the laser beam to curtail the peripheral 2nd harmonic signal. A set of neutral density filters (NDFs) were used in the path of the pump beam (after the glass plate) to vary the incident pump intensity. The lasing threshold (I_{th}), in pure ZnO film was assessed by varying the pump energy in the range of 1.0-5.4 mJ using NDF. The maximum pump intensity was limited to 10.94×10^2 MW/cm^2 corresponding to 5.4 mJ (which was below the damage threshold of the film).

Bibliography

[**1**] Douglas B. Chrisey and Graham K. Hubler, "*PULSED LASER DEPOSITION OF THIN FILMS",* John Wiley & Sons. Inc., 1994.

[**2**] A. T. T. Mostako et al., "*Mirrorlike pulsed laser deposited tungsten thin film",* Review of Scientific Instruments, **82** (2011) 013101.

[**3**] R.W Eason et al., "*Multi-beam pulsed laser deposition for advanced thin-film optical waveguides",* Journal of Physics D: Applied Physics, **47** (2014) 034007.

[**4**] A. T. T. Mostako et al., "*Note: Large area deposition of Rh single and Rh/W/Cu multilayer thin films on stainless steel substrate by pulsed laser deposition technique",* Review of Scientific Instruments, **85** (2014) 046101

[**5**] A. T. T. Mostako, "*Studies on pulsed laser deposited Mo, W and Rh thin films for First Mirror Applilcation",* PHD Thesis, 2013.

[**6**] A. T. T. Mostako et al., "*Pulsed laser deposition of thin film of molybdenum",* Journal of Physics: Conference Series, **208** (2010) 012114.

[7] Gaurave Shukla, "*Pulsed laser deposition and characterization of AlN, T_iO_2, and $Zn_{1-x}Mg_xO$ (0<x<0.7) semiconductor thin films",* PHD Thesis, 2011.

[**8**] C. Richard Brundle et al., "*Encyclopedia of Materials Characterization-Surfaces, Interfaces, Thin Films",* Manning Publications Co., 1992.

[**9**] R Swanepoel, "*Determination of the thickness and optical constants of amorphous silicon",* J. Phys. E: Sci. Instrum., **16** (1983) 1214-1222.

[**10**] MANSOOR SHEIK-BAHAE et al., "*Sensitive Measurement of Optical Nonlinearities Using a Single Beam",* IEEE J. Quantum Electronics, **26** (1990) 760-769.

[**11**] Indrajeet Kumar and A. Khare, "*Modified Z-scan set-up using CCD for measurement of optical nonlinearity in PLD carbon thin film",* Optics & Laser Technology, **77** (2016) 51-54.

[**12**] David D. Smith et al., "*z-scan measurement of the nonlinear absorption of a thin gold film",* Journal of Applied Physics, **86** (1999) 6200-6205.

[**13**] Boyd, R.W., "*Nonlinear optics",* Academic Press, 2008.

Chapter 3

Fabrication and characterization of pulsed laser deposited $Zn_{1-x}Al_xO$ ($0 \leq x \leq 0.10$) thin films

Zinc oxide (ZnO) has emerged as an important material towards various applications **[1]**. It possesses direct and large band gap energy (3.37 eV) with high excitonic binding energy (60 meV), a desirable feature for fabrication of the optoelectronic devices working towards short wavelength regime **[2]**. ZnO is transparent in visible region (400-700 nm) and conducting (*n*-type) semiconductor thus is suitable for transparent conducting electrode (TCE) for solar panel display, thin film transistors, light emitting diodes etc. **[3-5]**. The optical and electronic behavior of ZnO can be further tailored over a wide range by alloying it with suitable impurity. The impurity content has to be limited to certain extent in order to avoid the impurity defects as well as secondary phase formation **[6]**.

In this chapter, the fabrication of thin films of $Zn_{1-x}Al_xO$ ($0 \leq x \leq 0.10$) via pulsed laser deposition (PLD) technique and their characterization is presented. The effect of Al percentage on the film crystallinity was studied by using the X-Rays diffraction (XRD) and Raman spectroscopic measurement. Variations in the absorption coefficients, linear refractive indices and band gap energies in the films as a function of Al content via UV-VIS-NIR spectrometer are detailed. The effect of Al concentration on the room temperature photoluminescence in the film is also presented.

3.1 Experimental details

The details about the preparation of the PLD targets of pure ZnO and Al doped ZnO (AZO) have been already discussed in Sec. 2.1, Chap. 2. The $Zn_{1-x}Al_xO$ ($0 \leq x \leq 0.10$) thin films were deposited onto fused silica and Silicon substrates via PLD technique. All

the thin films were fabricated at a laser fluence of ~10J/cm^2, oxygen pressure of ~0.1 mbar, substrate temperature of ~500 ^{0}C and at a substrate to target distance of ~3 cm. The thin films were deposited for 30 minutes duration. The thickness of the films was estimated using Swanepoel envelope method. All the AZO films were subjected to energy dispersive X-rays spectrometer (EDX), XRD, Raman spectrometer, UV-VIS-NIR spectrometer and Fluorescence spectrometer in order to study the influence of x (Al concentration) on the properties of these films.

3.2. Energy dispersive X-rays spectra of $Zn_{1-x}Al_xO$ ($0 \leq x \leq 0.10$) thin films

The PLD technique is famous for the fruitful transfer of stoichiometry from target to the thin film under some optimum deposition parameters. To test this, all the PLD films of AZO were subjected to the EDX measurement. The EDX spectra of $Zn_{1-x}Al_xO$ ($0 \leq x \leq 0.10$), averaged over three distinct locations of each films, are shown in Fig. 3.1.

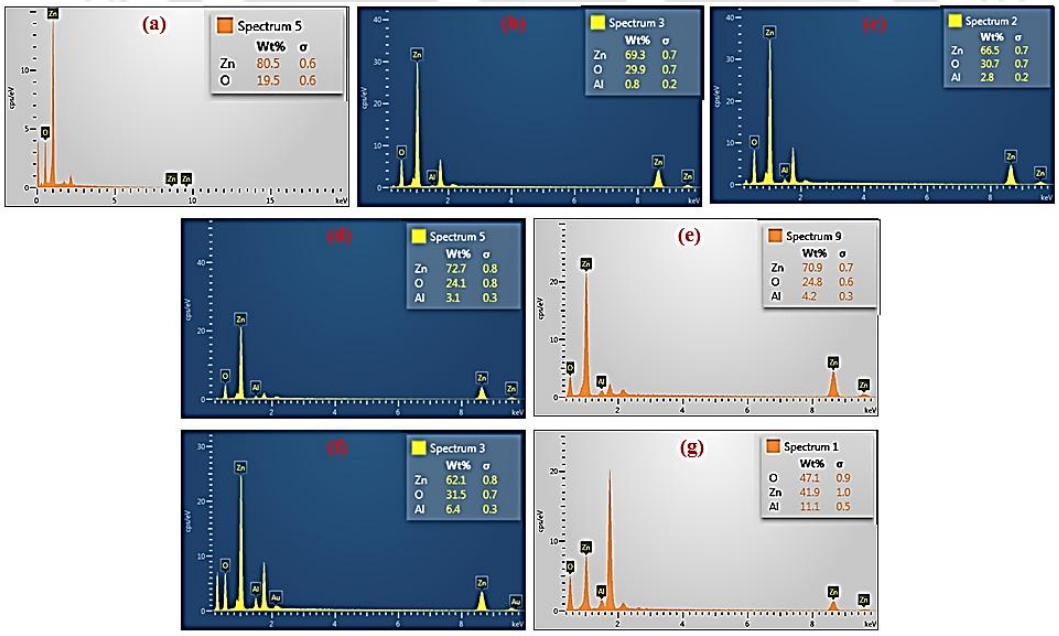

Fig. 3.1 EDX spectra of PLD $Zn_{1-x}Al_xO$ ($0 \leq x \leq 0.10$) thin films (a) x=0.00, (b) x=0.01, (c) x=0.02, (d) x=0.03, (e) x=0.05, (f) x=0.07 and (g) x=0.10.

The plot of the Al content (wt%) in thin film samples estimated using EDX spectra vs Al content (wt%) in respective powder (bulk) samples is shown in Fig. 3.2.

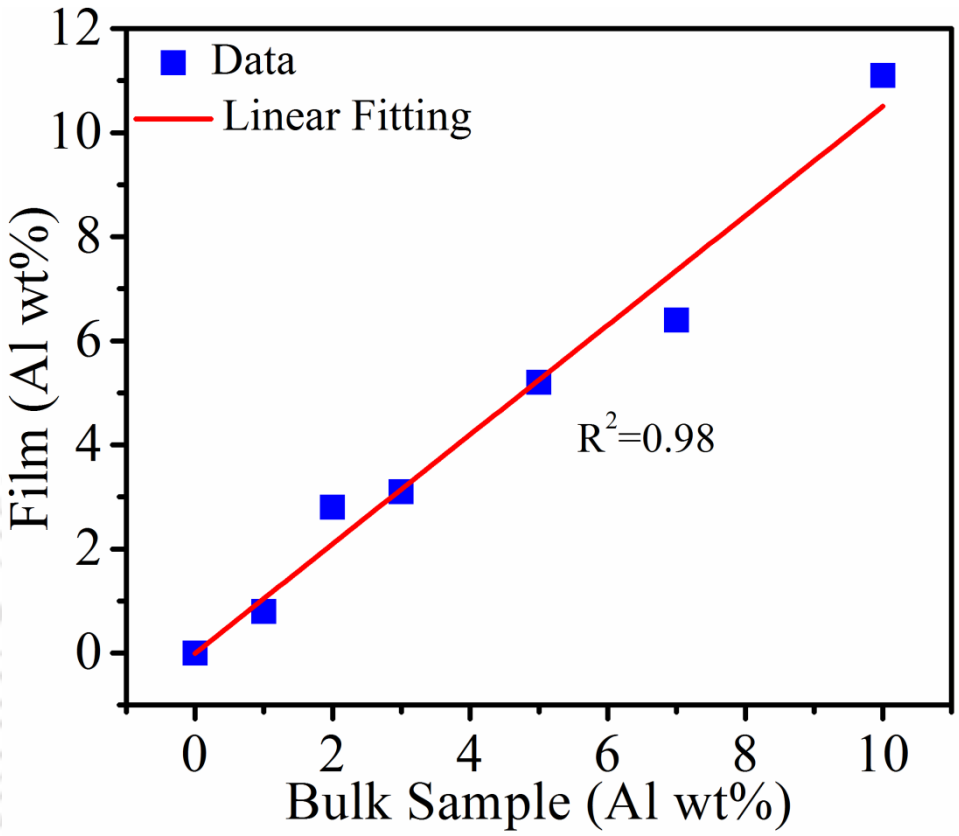

Fig. 3.2 Plot of Al content in thin films vs. bulk sample.

The wt% of Al content in the film is nearly same as that of the respective target, Fig. 3.2, confirming the stoichiometric transfer from the target to the PLD films of AZO.

3.3 XRD spectra of $Zn_{1-x}Al_xO$ ($0 \leq x \leq 0.10$) thin films

Figure 3.3 shows the XRD pattern of $Zn_{1-x}Al_xO$ ($0 \leq x \leq 0.10$) thin films deposited onto fused silica substrate via pulsed laser deposition technique. The XRD spectra were recorded in the 2θ range of 20-60 degree. All the films exhibited diffraction peaks of (100), (002), (101), (102) and (110). The dominance of the (002) diffraction peak in all

the samples indicates the preferred orientation of the films along c-axis of hexagonal wurtzite crystal structure. From the Fig. 3.3, it is clearly observed that the intensity of the (002) diffraction peak is increased with Al concentration up to x=0.05 and then falls down slightly for x=0.10.

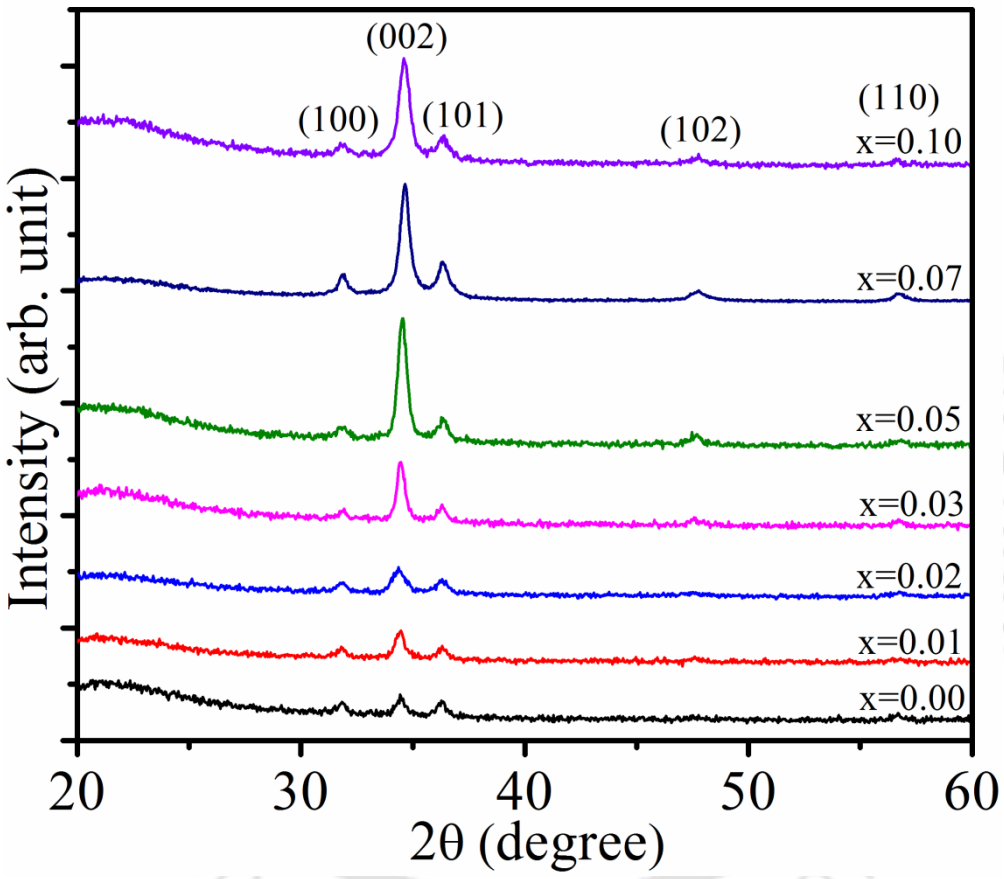

Fig. 3.3 XRD pattern of $Zn_{1-x}Al_xO$ ($0 \leq x \leq 0.10$) thin films.

The average crystallite size (D) and lattice constants (a and c) was estimated by using the following equations **[7, 8]**;

$$D = \frac{0.9\lambda}{\beta_x Cos(\theta_{002})} \tag{3.1}$$

where, λ is the wavelength of the Cu-Kα line (~1.5407 Å), β_x represents the full width at half maxima (FWHM) of (002) peak and θ is the diffraction angle.

The lattice constants, *a* and *c* are given by equations 3.2 and 3.3 respectively **[8]**.

$$a = \frac{\lambda}{3^{1/2} \sin\theta_{100}} \tag{3.2}$$

$$c = \frac{\lambda}{\sin\theta_{002}} \tag{3.3}$$

Figure 3.4 shows the crystallite size, from eqn. 3.1, as a function of x. For pure ZnO, the crystallite size is 17 nm and that of 19 nm for x=0.05 and thereafter it decreases further with the increase in x and reduces to 15 nm for x=0.10.

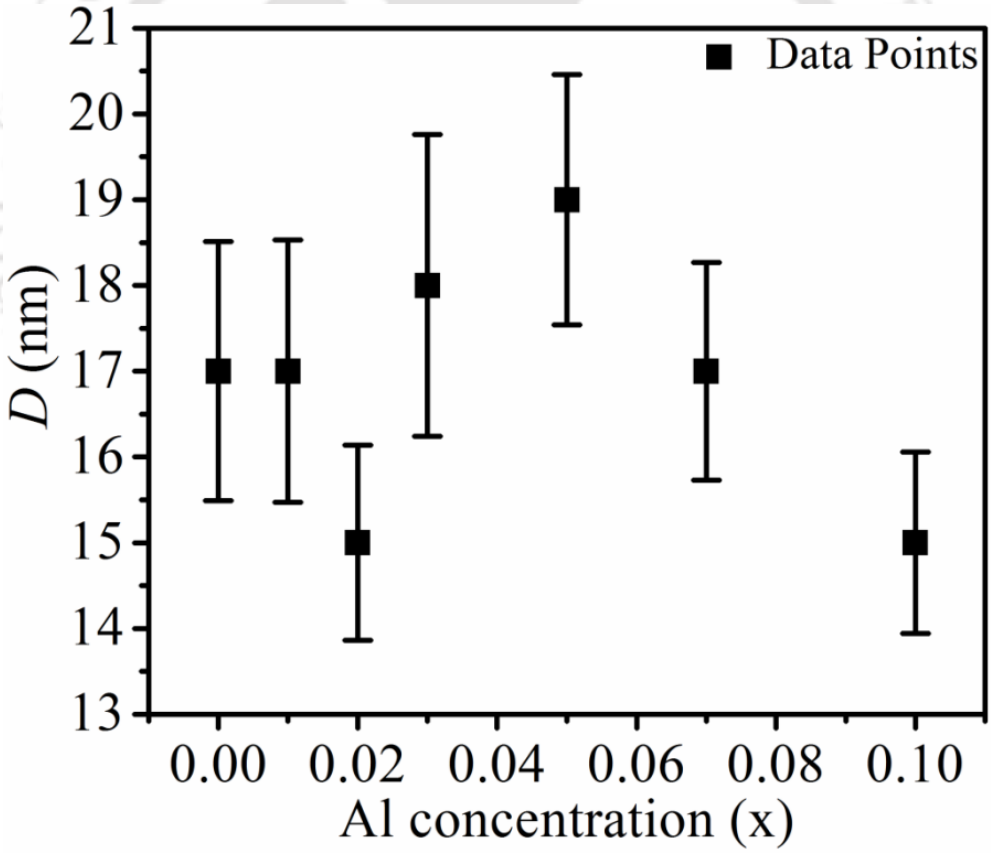

Fig. 3.4 Average crystallite size with Al concentration.

The estimated average crystallite size (*D*), lattice parameters (*a* and *c*) and axial ratio (*c*/*a*) of the hexagonal lattice structure of AZO thin films are listed in Table 3.1.

Table 3.1 Lattice constants (*a* and *c*), crystallite size (*D*) in $Zn_{1-x}Al_xO$ thin films for (002) plane.

x (wt %)	*D* (nm)	*a* (Å)	*c* (Å)	*c/a*
0.00	17±1.5	3.240	5.204	1.606
0.01	17±1.5	3.238	5.211	1.609
0.02	15±1.2	3.238	5.210	1.609
0.03	18±1.7	3.237	5.196	1.605
0.05	19±1.5	3.236	5.188	1.603
0.07	17±1.3	3.234	5.189	1.605
0.10	15±1.1	3.236	5.191	1.604

Since the radius of Zn^{2+} ions (0.60 Å) is greater than that of Al^{3+} (0.53 Å), therefore film under goes additional stress and strain with Al-doping hence resulting into small modifications in the crystallite size and the lattice parameters **[9, 10]**. The marginal changes in the lattice parameters of (002) peak suggest the partial replacement of Zn^{2+} ions with the Al^{3+} ions in the crystal lattice. From table 3.1, the film having x=0.05 has the maximum value of the crystallite size indicating the best crystallinity in it. The minimum value of lattice constants (*a* and *c*) for this particular sample confirms that film is under compressive stress. The decrease in the crystallinity at 10 wt% of Al concentration may be due to the excessive stress and defects present in this film. In fact, during formation of the Al-doped films, the replacement of Zn^{2+} ions by Al^{3+} ions takes place. The mismatch in ionic radii of the Zn^{2+} ions and Al^{3+} results in decreasing the

crystallite size for higher level of Al-doping, x=0.10. The ratio of lattice parameters (*c*/*a*) for all the films is estimated to be ~1.6 which is close to the hexagonal crystal structure.

3.4. Raman spectra of $Zn_{1-x}Al_xO$ ($0 \leq x \leq 0.10$) thin films

ZnO belongs to C_{6v} point group symmetry and there are 4 atoms per unit cell leading to 12 phonon branches. Out of these there are 9 optical and 3 acoustical phonon branches. There is an A_1 branch, a doubly degenerate E_1 branch, two doubly degenerate E_2 branches and two B branches **[11]**. The A_1 and E_1 branches are Raman and IR active, E_2 branches are Raman active only and B branches are Raman inactive **[12]**. Figure 3.5 shows the Raman spectra of $Zn_{1-x}Al_xO$ ($0 \leq x \leq 0.10$) thin films deposited on fused silica recorded in the range of 200-800 cm^{-1} by exciting it with 488 nm line of Argon ion laser. .

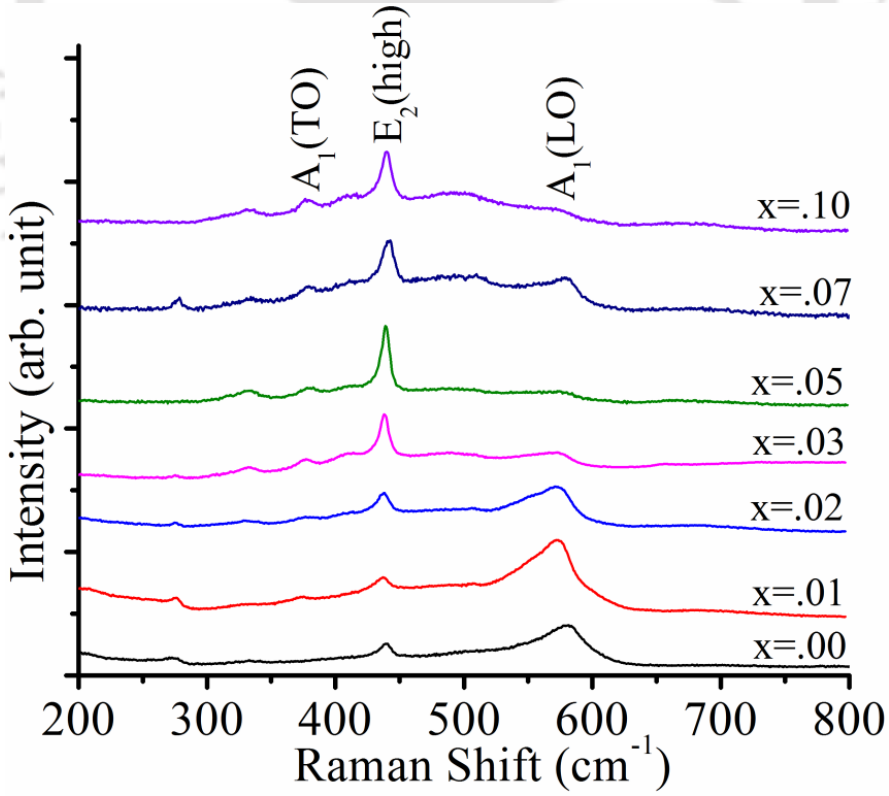

Fig. 3.5 Raman spectra of $Zn_{1-x}Al_xO$ ($0 \leq x \leq 0.10$) thin films.

The observed dominating Raman modes in the present studies are optical phonon modes E_2 (high) and A_1 (LO) at 438 cm^{-1} and 578 cm^{-1} respectively. Apart from these, A_1 (TO) mode at 378 cm^{-1} is also present in the Al doped films. A weak peak at 279.2 cm^{-1} is also observed in the pure as well as Al doped ZnO thin films which is due to the silent B_1 Raman mode **[13]**. The enlarged view of dominating E_2 (high) mode at 438 cm^{-1} is shown separately in Fig. 3.6 and the peak intensity for all values of x is listed in table 3.2. It indicates the increase in intensity up-to 5 wt% of Al content and thereafter, a slight decrease in intensity for 10 wt% doping. This confirms that at 5wt % the film possesses highly c-axis oriented wurtzite phase which is in confirmation with the XRD observation.

The dominating E_2(high) Raman mode in $Zn_{1-x}Al_xO$ films exhibits slight shift in the peak position which could be due to the defects and stress present in these films **[10, 14]** .

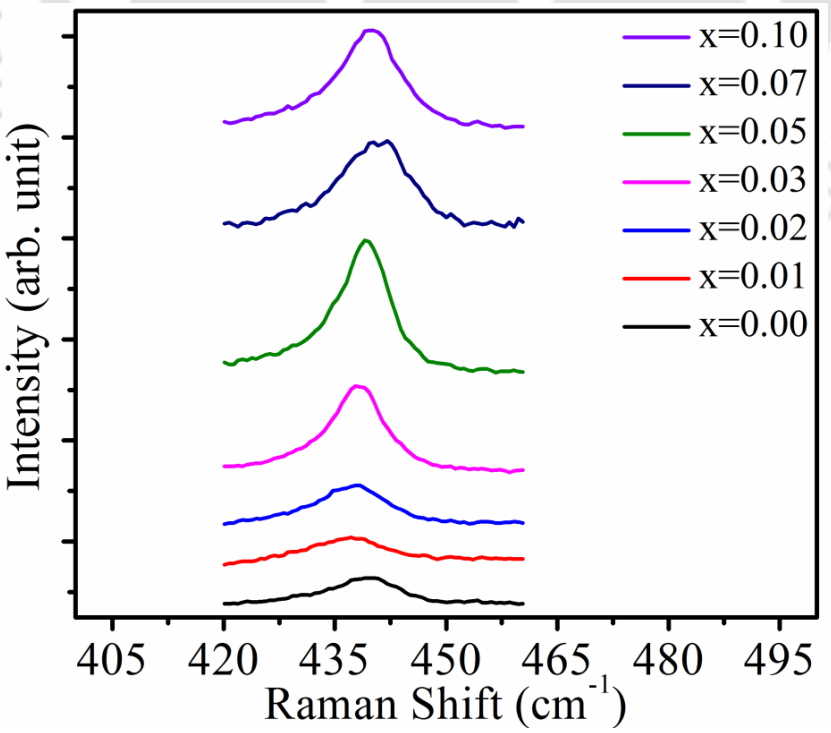

Fig. 3.6 Expanded view of the E_2(high) mode of $Zn_{1-x}Al_xO$ thin films.

Table 3.2 Peak intensity for E_2 (high) peak in $Zn_{1-x}Al_xO$ ($0 \leq x \leq 0.10$) thin films.

Serial No.	**Sample (x)**	**Intensity (arb. unit)**
1.	0.00	504.4
2.	0.01	427.3
3.	0.02	724.4
4.	0.03	1672.6
5.	0.05	2561.9
7.	0.07	1853.2
6.	0.10	1890.9

For the film at 5wt% concentration of Al, the Raman shift exactly matches with that of pure ZnO film. This shows the optimum Al doping at which the mutual replacement of Zn^{2+} by the Al^{3+} takes place and similar result is also supported by the XRD data as shown in Fig. 3.3.

3.5 UV-VIS-NIR spectra of $Zn_{1-x}Al_xO$ ($0 \leq x \leq 0.10$) thin films

Figure 3.7 depicts the absorption spectra of the PLD $Zn_{1-x}Al_xO$ ($0 \leq x \leq 0.10$) thin films deposited on fused silica substrate. The linear absorption coefficients (α) of the films are estimated by using the Beer-Lambert law expressed by the following equation **[15]**:

$$\alpha(v) = 2.303\left(\frac{A}{L}\right) \tag{3.4}$$

where, *A* is the absorbance and *L* is the thickness of the film measured by Swanepoel envelope method and is briefed towards the end of this section.

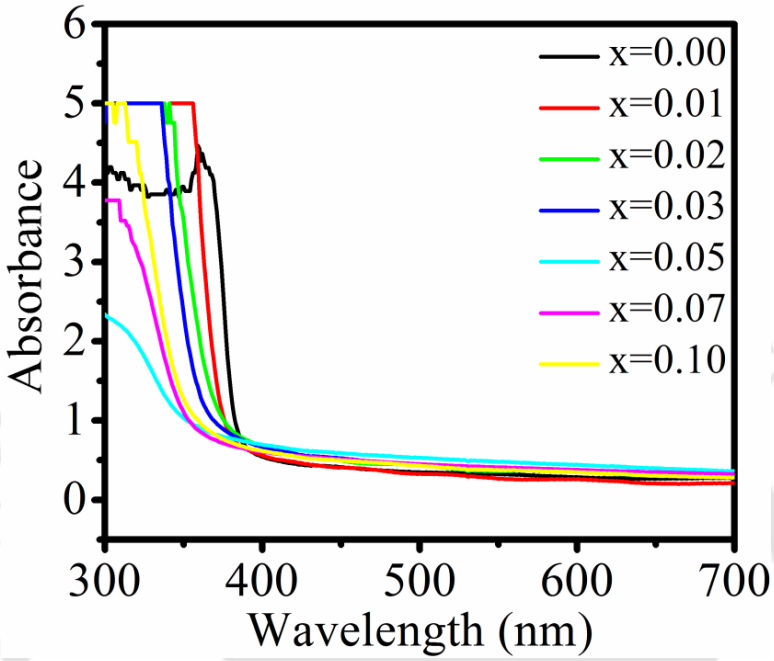

Fig. 3.7 Absorbance spectra of $Zn_{1-x}Al_xO$ ($0 \leq x \leq 0.10$) thin films.

The band gap energy (E_g) of $Zn_{1-x}Al_xO$ ($0 \leq x \leq 0.10$) thin films is determined from the absorption spectra from following equation in Tauc' plot **[15, 16]**:

$$\alpha h\nu = B(h\nu - E_g)^m \tag{3.5}$$

where, $h\nu$ is the incident photon energy, m is the transition coefficient and B is the measure of the disorder of the material and is known as the probability parameter for transition. For direct and allowed transition m=1/2 **[16].**

In Tauc's plot method, the intercept on the axis of extrapolation of the linear portion of the graph between $(\alpha h\nu)^2$ vs. $h\nu$, gives the estimation of E_g values. The Tauc's plot for all the thin film samples is shown in Fig. 3.8. The extrapolated linear portion upto the $(\alpha h\nu)^2$=0 for x=0.05 thin film sample is shown in inset, Fig. 3.8.

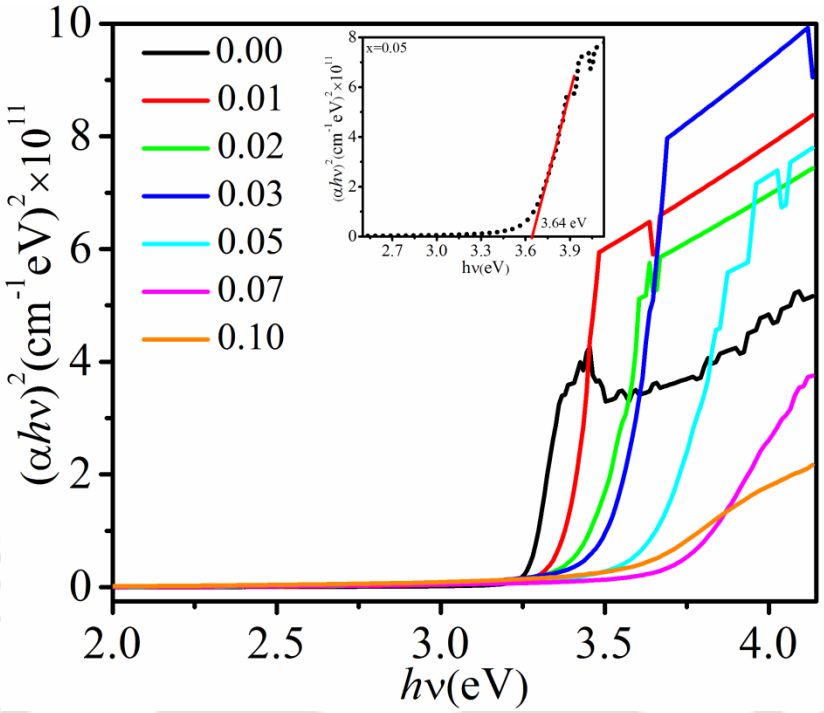

Fig. 3.8 Tauc's plot of $Zn_{1-x}Al_xO$ ($0 \leq x \leq 0.10$) thin films and linear fitted graph for x=0.05 sample (inset).

The band gap energies (E_g) and absorption coefficients (α) (at λ=633 nm) of the thin films are plotted as a function of Al concentration and is shown in Fig. 3.9.

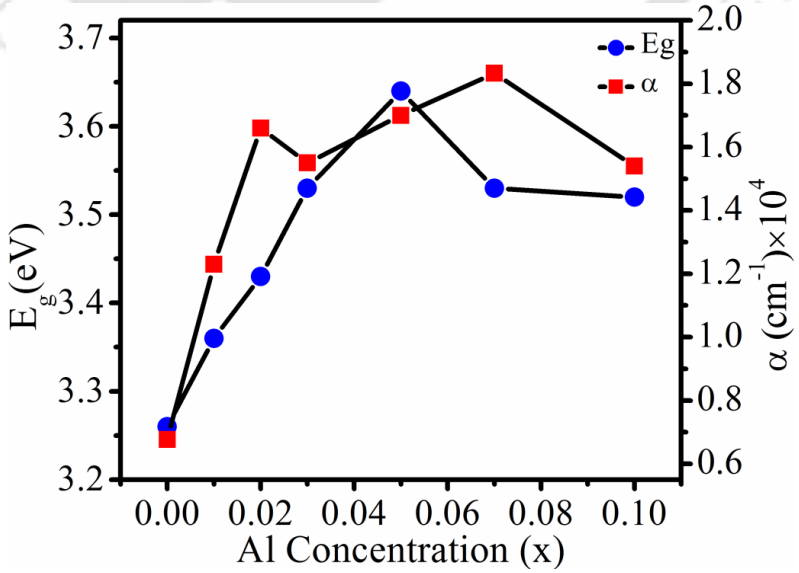

Fig. 3.9 Variation of E_g and α with Al content (x) in $Zn_{1-x}Al_xO$ ($0 \leq x \leq 0.10$) thin films.

The estimated E_g and α for $Zn_{1-x}Al_xO$ ($0 \le x \le 0.10$) thin film are listed in table 3.3.

Table 3.3 Absorption coefficient (α) and band gap energy (E_g) of $Zn_{1-x}Al_xO$ thin films.

Serial No.	Al Content (x)	Abs. Coeff. α (cm^{-1}) (at λ=633nm)	E_g (eV)
1.	0.00	6.77×10^{3}	3.26±0.11
2.	0.01	1.23×10^{4}	3.36±0.15
3.	0.02	1.66×10^{4}	3.43±0.17
4.	0.03	1.55×10^{4}	3.53±0.24
5.	0.05	1.70×10^{4}	3.64±0.21
6.	0.07	1.50×10^{4}	3.53±0.15
7.	0.10	1.54×10^{4}	3.52±0.07

The band gap energy of the $Zn_{1-x}Al_xO$ thin films is enhanced from 3.26 eV to 3.64 eV with the increase in Al concentration up-to 5wt %. The blue shift in the band gap of AZO thin films can be explained via Burstein Moss (BM) effect **[17]**. According to the BM effect, the conduction band of the heavily doped (degenerate) semiconductor is significantly filled with large carrier concentration and the lowest valence energy states are blocked, consequently the Fermi level gets shifted in the conduction band and hence the apparent band gap energy is increased. ZnO doped with Al element can be treated as degenerate semiconductor. The expression for the shift in band gap, ΔE_g^{BM}, of the degenerate semiconductor is given by the following expression **[17, 18]**:

$$\Delta E_g^{BM} = \frac{\hbar^2 (3\pi^2 n_e)^{2/3}}{2m^*} \qquad (3.6)$$

where, n_e is the free electron concentration and m^* is the reduced effective mass. The reduced effective mass, m^* is defined by the relation; $\frac{1}{m^*} = \frac{1}{m_v^*} + \frac{1}{m_c^*}$, where m_v^* and m_c^* are the valence band and conduction band effective masses respectively and their values are taken from literature **[19, 20]**.

Equation 3.6 suggests the inverse relationship between BM shift and carrier effective masses. Therefore heavily doped semiconductors having light carrier masses (*n* type) exhibit the large BM shift. Hence the band gap is blue shifted with the increase in x in the AZO film. When the carrier concentration is increased beyond the Mott critical density in heavily doped n-type semiconductor, the carrier-carrier and carrier-impurity interactions start dominating and result into the band narrowing **[21]**.

The interaction among the free charge carriers at high Al concentration results in neutralizing the charge carriers and form a non-conducting layer of Aluminum Oxide (Al_2O_3) just below the conduction band **[22]**. This non-conducting layer prevents the motion of the charge carriers resulting in decreasing the mobility and hence the resistivity is increased. Thus there is a strong competition between the BM effect and many body interaction effect as the carrier concentration is increased. These interactions lead to the band edge shrinking effect and so the band gap energy starts decreasing as the Al content is increased beyond 5 wt%.

Carrier density (n_e) in the AZO thin films was evaluated using the equation (3.6) and its variation with x is displayed in Fig. 3.10. The carrier concentration is found to be in the range of 10^{18}-10^{20} cm^{-3}, enough to show the BM effect **[23]**. It is found to be maximum at an optimum Al doping of 5 wt%. The further increase in the Al doping

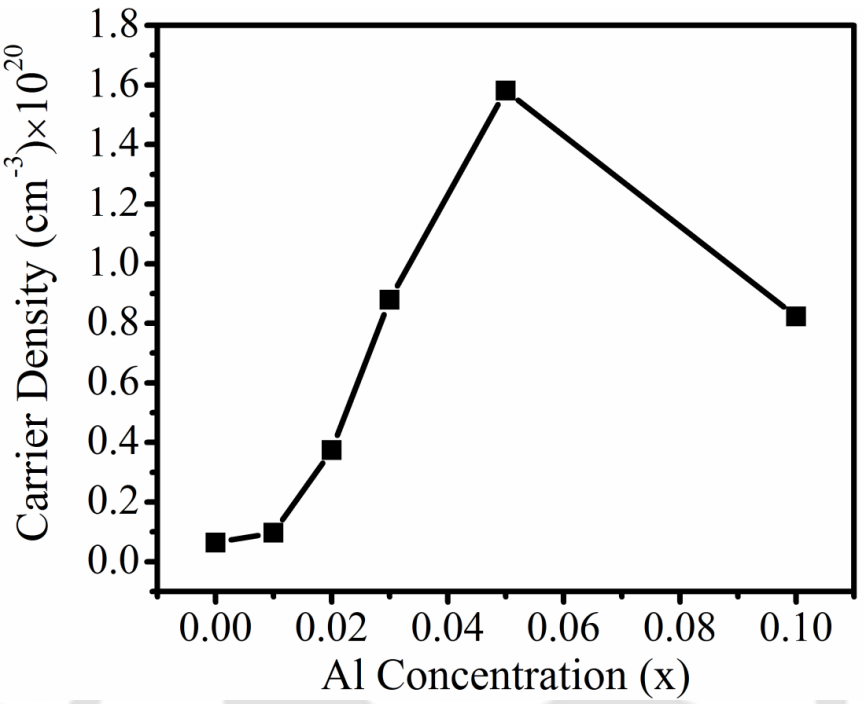

Fig. 3.10 Evolution of carrier density with the Al doping concentration.

causes the lowering in the carrier density. This lowering in the carrier density leads to the decrease in the crystallinity in the film which is in good agreement with the XRD and Raman data.

Figure 3.11 shows the transmission spectra of $Zn_{1-x}Al_xO$ thin films in the spectral range of 300-2000 nm. The optical transmission in the ZnO film decreases with the increase in the Al content. This could be because of the large free carrier absorption. In *n*-type degenerate semiconductor, the absorption coefficient (α) is related to the carrier concentration (n_e) by the equation 3.7 **[24]**:

$$\alpha = \frac{C\lambda^2 n_e}{\mu_H} \tag{3.7}$$

where, C is a constant, λ is the wavelength of the incident radiation and μ_H is the hall mobility.

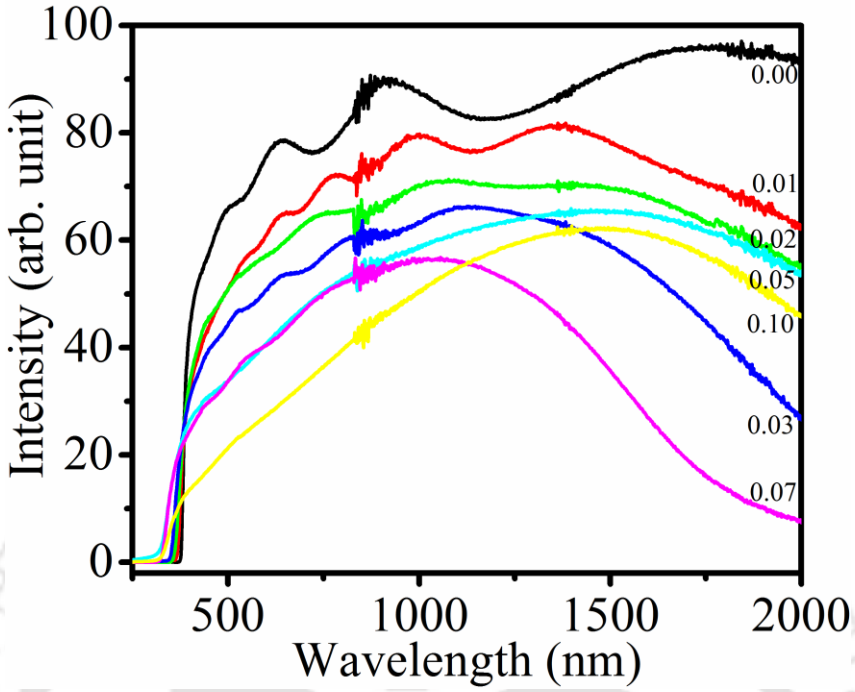

Fig. 3.11 Transmission spectra of $Zn_{1-x}Al_xO$ thin films.

The equation 3.7 indicates that the absorption coefficient is directly proportional to the free electron concentration. Thus, thin films having large Al concentration and consequently the higher free carrier concentration possess high absorption. Therefore, the thin film samples (x>0.00) exhibit low optical transmission as compared to that of pure ZnO thin film.

Linear refractive index of the $Zn_{1-x}Al_xO$ thin films were estimated by analyzing the transmission spectra using swanepoel envelope method **[25]**. The Swanepoel envelope fitted transmission spectra of pure ZnO thin film is shown in Fig. 3.12 as an example. The linear refractive indices of the films were extracted from following equations **[25]**.

$$n = \left[N + (N^2 - S^2)^{1/2} \right]^{1/2} \tag{3.8}$$

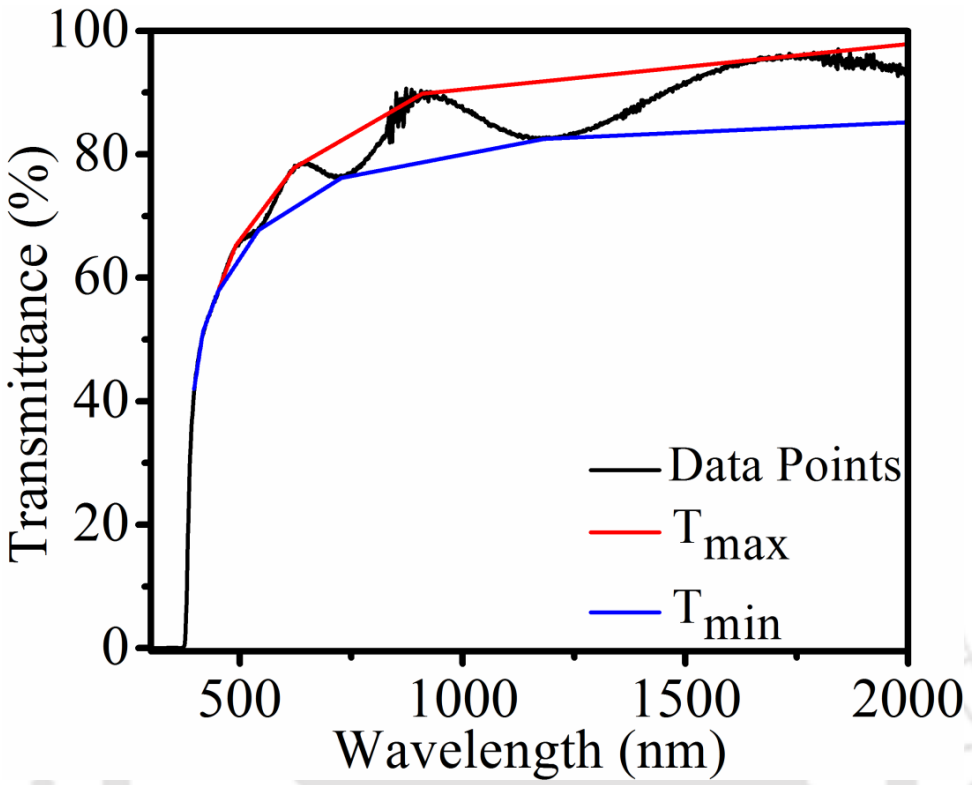

Fig. 3.12 Swanepoel envelope fitted spectra of pure ZnO thin film.

where N is expressed as

$$N = 2S\frac{T_M - T_m}{T_M T_m} + \frac{S^2 + 1}{2} \tag{3.9}$$

and S (=1.458) is the refractive index of the fused silica substrate. T_M and T_m are the consecutive transmission maxima and minima respectively.

The values of n obtained from equation 3.8 are fitted to the Cauchy dispersion relation given by equation 3.10.

$$n(\lambda) = C + \frac{D}{\lambda^2} \tag{3.10}$$

where, C and D are the Cauchy parameters.

The parameter, *C*, is independent of λ and is known as static refractive index, n_s. After obtaining the values of *C* and *D* from the fitted equation 3.10, the variation in the linear refractive indices with wavelength for various Al content is plotted and is shown in Fig. 3.13.

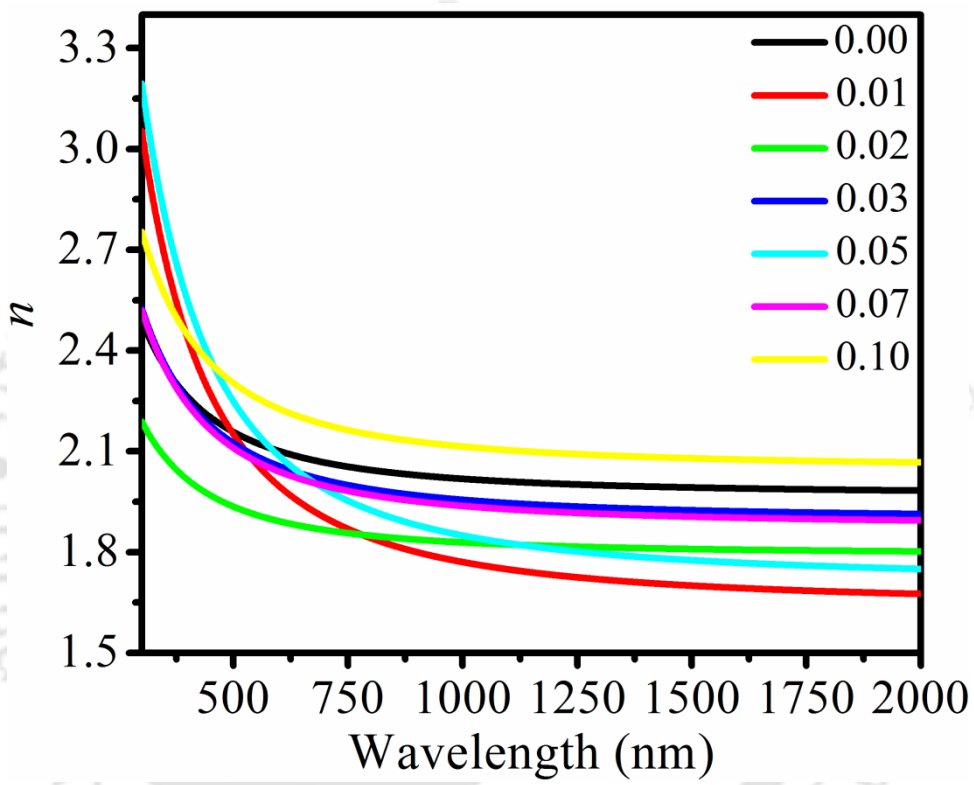

Fig. 3.13 Variation of refractive indices of Al doped ZnO thin films as a function of wavelength.

The decrease in refractive index with wavelength confirms the normal dispersion behavior for all the samples. The thickness of the films was estimated from following expression **[25]**:

$$L = \frac{\lambda_1 \lambda_2}{2(\lambda_1 n_2 - \lambda_2 n_1)} \tag{3.11}$$

where, λ_1 and λ_2 are the wavelengths of two consecutive maxima or two consecutive

minima in the transmission spectra and n_1 and n_2 are the respective refractive indices.

The evaluated results, thickness of the film and linear refractive index, n (at a wavelength of 633 nm) with x are listed in Table 3.4.

Table 3.4 Variation of refractive index (n) with the Al doping in the $Zn_{1-x}Al_xO$ films.

Sr. No.	Al Content (x)	Thickness (L)	Refractive index (n) (at λ=633nm)
1.	0.00	520	2.087
2.	0.01	490	1.984
3.	0.02	550	1.887
4.	0.03	476	2.042
5.	0.05	512	2.040
6.	0.07	547	2.020
7.	0.10	480	2.214

It can be observed from Table 3.4 that there is a slight decrease in the refractive index of AZO film with the increase in Al concentration till 2 % thereafter it increases. This could be due to the lower refractive index of Al_2O_3 as compared to that of ZnO upto 2wt%. The increase in the refractive index for higher content of Al ($x>0.02$) in the films could be attributed to the increased carrier concentration. This behavior is nearly in agreement with that of reported in literatures **[26-28]**.

3.6. Photoluminescence spectra of $Zn_{1-x}Al_xO$ ($0 \leq x \leq 0.10$) thin films

Figure 3.14 shows the room temperature photoluminescence (RTPL) spectra of $Zn_{1-x}Al_xO$ ($0 \leq x \leq 0.10$) thin films recorded using the fluorescence spectrophotometer by exciting with 320 nm line of a Xenon lamp. Pure ZnO exhibits a strong and narrow peak in ultraviolet region and a broad peak extending throughout the visible region. These two peaks are assigned as near band edge (NBE) peak and defect level emission (DLE) peak respectively. The narrow NBE band in the ultraviolet region originated from the radiative transition within the band edge of ZnO. The NBE band in ultraviolet region (365-400 nm) in the samples is attributed to the free exciton emission and emission due to excitons bound with the donors and acceptors impurities **[29]**.

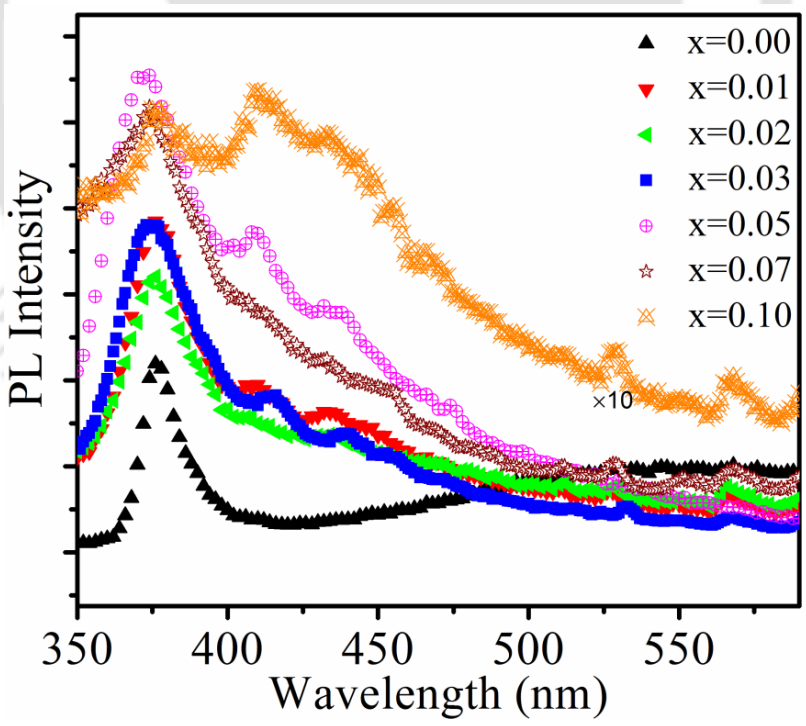

Fig. 3.14 PL spectra of $Zn_{1-x}Al_xO$ ($0 \leq x \leq 0.10$) thin films.

In order to understand the origin of the luminescence in the $Zn_{1-x}Al_xO$ ($0 \leq x \leq 0.10$) thin films, the PL spectra are de-convoluted and shown in Fig. 3.15.

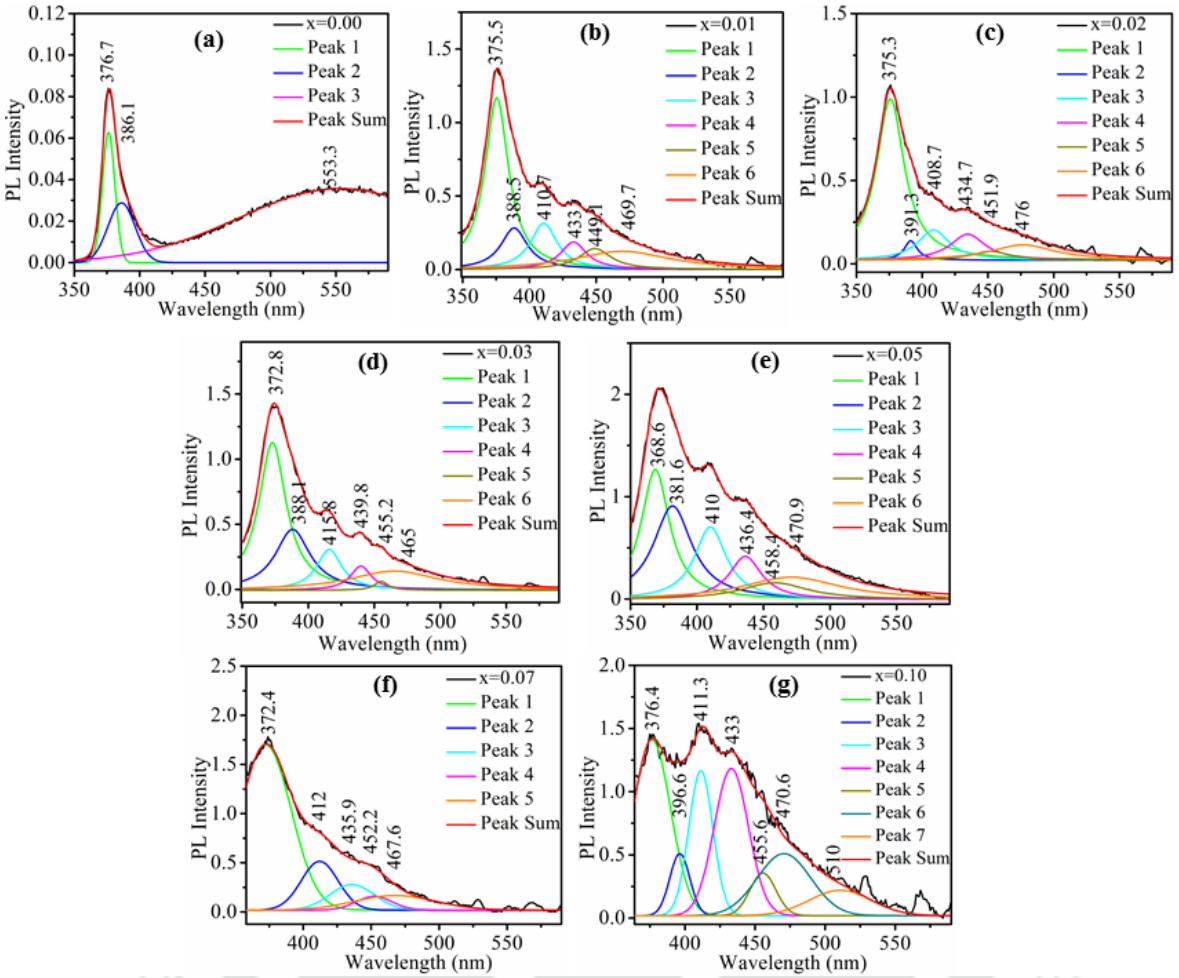

Fig. 3.15 De-convoluted PL spectra of $Zn_{1-x}Al_xO$ ($0 \leq x \leq 0.10$) thin films.

Nature of the profile of the photoluminescence spectra depends on the crystalline quality of the films. In the pure ZnO and highly Al doped ZnO ($x>0.05$) films, the PL spectra are well fitted with the Gaussian profile while those for $0.01 \leq x \leq 0.05$, the spectra are fitted with Lorentzian profile. In fact, the film with improved crystalline quality possesses uniform or small variation over the crystallite size and thus PL broadening follows the homogeneous nature and hence the broadening is dominated by the Lorentzian function whereas the poor crystalline film shows large variation in the crystallite sizes, the broadening becomes inhomogeneous and follows Gaussian profile.

These observations are in agreement with XRD and Raman measurement, Fig. 3.3 and 3.5 respectively.

Pure ZnO film, Fig. 3.15 (a) exhibits two significant peaks centered at 376.7 (~3.29 eV) nm and 386.1 (~3.21 eV) nm in the UV range and a broad peak centered at 553.3 (~2.24 eV) nm in the visible region. These two peaks are associated with exciton and exciton complexes. The first peak centered at 376.7 nm (3.29 eV) is due to the free excition recombination and the second peak at 386.1 (3.21 eV) is due to the donor-acceptor pair which is more favorable at room temperature. The peak centered at 553.3 nm could be due to the combined effect of the radiative recombination of the free electrons excited to the conduction band and the photo generated free holes trapped at various oxygen vacancies associated point defects (V_O^+ and V_O^{++}) because of the lower formation energy of the V_O among all the intrinsic defects in Zn rich environment **[30, 31]**.

The PL spectra of samples (x>0.00) are comprized of 4 main emission range, UV region (350-385 nm), the violet region (385-455 nm), the blue region (455-490 nm) and the green-yellow region (495-590 nm). The PL intensity in the $Zn_{1-x}Al_xO$ film is highly influenced due to the presence of Al and consequently the defect related peaks (green and yellow bands) are observed to be eliminated gradually as the Al content is increased in the $Zn_{1-x}Al_xO$ films. The quenching of broad defect band in Al doped ZnO thin film is also reported by some other research groups **[32-34]**. The reduction in the green band of PL spectra with increasing Al concentration in $Zn_{1-x}Al_xO$ samples signifies the reduction in the intrinsic defects in the films **[34, 35]**.

The enhancements of the UV signal in Al doped ZnO thin film is attributed to the increased absorption with the increase in Al concentration, Table 3.3. The higher absorption enables more population in the excited state which undergoes a radiative transition and consequently, the NBE emission is enhanced. However, the excess amount of Al in ZnO causes deterioration in the UV band which could be due to the involvement of more deep level defects (interstitial as well as vacancy defects) in the film.

The de-convoluted PL spectra, Fig. 3.15 (b-g), reveals additional significant peaks in the violet-blue region positioned at 410 nm (~3.024 eV), 435 nm (~2.850 eV), 450 nm (~2.755 eV) and 470 nm (~2.63) in all the AZO films. The integrated intensity of these three major peaks, coming due to the various defects at 410 nm, 435 nm and 450 nm is plotted as a function of Al concentration and is shown in Fig. 3.16. The various probable shallow and deep level defects associated with these peaks, arising under the presence of Al, are also labeled along with the peak position in Fig. 3.16.

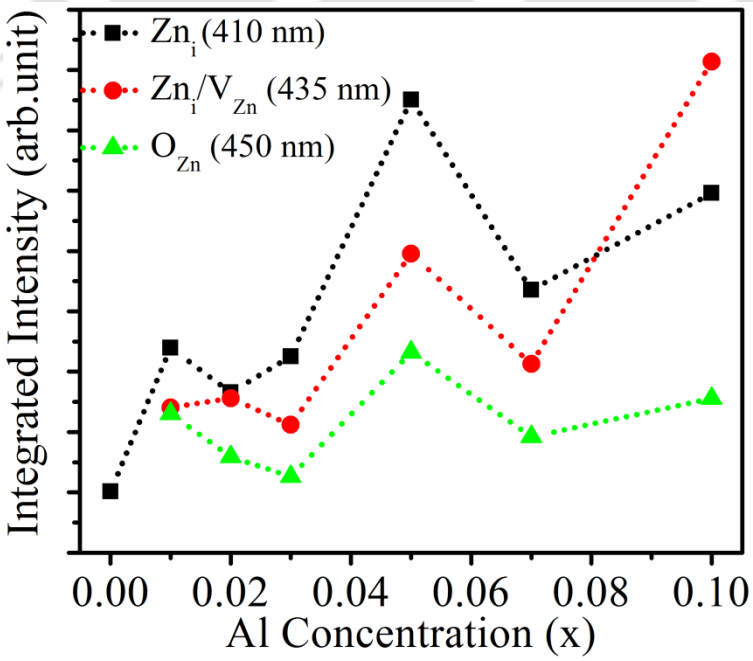

Fig. 3.16 Variation of defect concentration with Al concentration.

The emission line near to 410 nm (~3.024 eV) is observed in all the Al doped ZnO films which is believed to be originating from the radiative transition from zinc interstitial (Zn_i) to the valence band (VB) **[36]**. The integrated intensity of this emission peak is enhanced in the higher Al doped ZnO films ($x \geq 0.05$) which could be due to the excessive substitution of Al^{3+} ions confining the Zn^{2+} ions within the interstitial positions resulting the increase in the density of the Zn_i defect. As shown in Fig. 3.16, the Zn_i defect density increases with increasing Al content up-to x=0.05 only and for higher x values (x>0.05) it reduces slightly. This could be due to the fact that with the increase in Al concentration, the density of mutually substituted Al^{3+} ions by Zn^{2+} ions increases which accumulates Zn_i defects in the system. For higher Al concentration, there might be emergence of other kinds of defect centers such as V_{Zn} and O_{Zn} which leads to reduction of the Zn_i associated emission. The emission peak around 435 nm (~2.85 eV) also appearing in all the films (x>0.00) is due to the recombination between the Zn_i energy level to zinc vacancy (V_{Zn}) **[37]**. It is commonly believed that the Zn_i level exists at ~0.22 eV below the conduction band and the V_{Zn} level is at ~3.06 eV below the conduction band minima. Hence, a radiative recombination of photo excited electrons trapped at Zn_i level to the holes at V_{Zn} level, may lead to the photoluminescence at ~435 nm **[37]**. The integrated intensity of this emission peak is slightly lower as compared to that of the peak centered at ~410 nm. This suggests the low concentration of Zn_i/V_{Zn} defect in Al doped films which actually contribute towards the emission of former band. However, in higher Al content, the film behaves as oxygen efficient system which can result in the increment in the density of V_{Zn} defect and consequently the emission peak at 435 nm is enhanced for x>0.05 samples. This has also been represented in Fig. 3.16. The photoluminescence component centered at ~450 nm is thought to be originated from the recombination of electrons trapped at the

various extended Zn_i states to the holes in the valence band **[37]**. At higher wavelength side, in the range of 460-470 nm, a peak is visible which is associated with the oxygen antisite (O_{Zn}) defect **[36]**. This peak arises at the trailing edge of the PL band and is of relatively low intensity, suggesting the low concentration of O_{Zn}. This defect shows a non-monotonic behavior in the Al doped ZnO thin films, Fig. 3.16. Initially, it slightly decreases up-to x=0.03, shows maximum at x=0.05 and then reduces for further values of x. This mixed characteristic of O_{Zn} defect in the case of impurity, Al, could be mainly due to its high formation energy and unstable nature. This defect is more favored in oxygen rich condition under irradiation or ion implantation. For higher Al concentration, the probably formation of non-conducting layer of Al_2O_3 reduces the Oxygen concentration hence, O_{Zn} defect is also reduced.

There is a clear indication of the shift of the DLE band towards blue region from the green region and is the evidence of the reduction of the oxygen associated vacancies in the samples for x>0.00. This is more likely to be originated from the Zinc associated defects or oxygen antisite defects. The Al doped ZnO system can act as an oxygen rich system and therefore, the green-yellow band, 495-590 nm, which is predominantly associated with V_O related defects, is suppressed significantly. The samples x=0.07 and x=0.10 exhibit a broad emission in violet-blue emission range along with reduction in the green band. This is more likely to be due to the excessive disordering in the samples due to relatively large concentration of Al.

3.7 Conclusion

The $Zn_{1-x}Al_xO$ ($0 \leq x \leq 0.10$) thin films were deposited onto fused silica substrate via PLD technique. The XRD and Raman measurement revealed the c-axis oriented

hexagonal wurtzite phase for all the films. The best crystallinity was observed for x=0.05. The optical band gap was observed to be tunable with the aluminum content (x) from 3.26 eV to 3.64 eV. The largest band gap was observed in the thin film having Al content of 5wt%. For the higher value of x, the estimated band gap energy was observed to be decreased slightly. The blue shift in the optical band gap with Al content (x) from x=0.00 to x=0.05 was mainly due to the Burstein moss effect arising due to the high *n*-type doping effect while a slight red shift for higher x value was due to the band gap renormalization effect associated with many body interaction effect. The variation in the linear refractive index with x was marginal in these films. The films exhibited UV and blue emission dominated photoluminescence signal in RTPL spectra. Also, the green emission in the Al doped film was observed to be reduced with the Al concentration in the film due to the reduction in the oxygen defects.

Bibliography

[**1**] U. Ozgur et al., "*A comprehensive review of ZnO materials and devices"*. Journal of Applied Physics, **98 (**2005) 041301.

[**2**] A. B. Djurisic et al., "*ZnO nanostructures for optoelectronics: Material properties and device applications",* Progress in Quantum Electronics, **34 (**2010) 191-259.

[**3**] Jia Huang et al., "*Applications of ZnO in organic and hybrid solar cells"*. Energy & Environmental Science, **4** (2011) 3861-3877.

[**4**] Yong Seob Park and Han-Ki Kim, "*Characteristics of sputtered Al-doped ZnO films for transparent electrodes of organic thin-film transistor",* Thin Solid Films, **519** (2011) 8018-8022.

[**5**] H. Kim et al., "*Doped ZnO thin films as anode materials for organic light-emitting",* Thin Solid Films, **420-421** (2002) 539–543.

[**6**] Klaus Ellmer and Nndre Bikowski, "*Intrinsic and extrinsic doping of ZnO and ZnO alloys",* Journal of Physics D: Applied Physics, **49** (2016) 413002.

[**7**] Nese Kavasoglu and A. Sertap Kavasoglu, "*Metal–semiconductor transition in undoped ZnO films deposited by spray pyrolysis",* Physica B: Condensed Matter, **403** (2008) 2807-2810.

[**8**] C. Suryanarayana and M. Grant Norton, "*X-Ray diffraction: A practical approach",* Springer Science Business Media, LLC, 1998.

[9] R. D. SHANNON, "*Revised Effective Ionic Radii and Systematic Studies of Interatomie Distances in Halides and Chaleogenides",* Acta Crystallographica, **A32** (1976) 751-767.

[10] Gyan Prakash Bharti and Alika Alika Khare, "*Structural and linear and nonlinear optical properties of $Zn_{1-x}Al_xO$ ($0 \leq x \leq 010$) thin films fabricated via pulsed laser deposition technique",* Optical Materials Express, **6** (2016) 2063-2080.

[11] Hadis Morkoc and Umit Ozgur, "*Zinc Oxide: Fundamentals, Materials and Device Technology",* Wiley-VCH, 2009.

[12] T. C. Damen et al., "*Raman Effect in Zinc Oxide",* Physical Review, **142** (1966) 570-574.

[13] F. J. Manjon et al., "*Silent Raman modes in zinc oxide and related nitrides",* Journal of Applied Physics, **97** (2005) 053516.

[14] R. Vinodkumar et al., "*Highly conductive and transparent laser ablated nanostructured Al: ZnO thin films",* Applied Surface Science, **257** (2010) 708-716.

[15] S. T. Tan et al., "*Blueshift of optical band gap in ZnO thin films grown by metal-organic chemical-vapor deposition",* Journal of Applied Physics, **98** (2005) 013505.

[16] A. El-Denglawey el al., "*Physical aging effects on the structural and optical properties of nano As-Se-Tl films",* Journal of Non-Crystalline Solids, **449** (2016) 34-40.

[17] ELIAS BURSTEIN, "*Anomalous Optical Absorption Limit in InSb",* Physical Review, **93** (1954) 632-633.

[18] A. Abdolahzadeh Ziabari and S. M. Rozati, "*Carrier transport and bandgap shift in n-type degenerate ZnO thin films: The effect of band edge nonparabolicity",* Physica B: Condensed Matter, **407** (2012) 4512-4517.

[19] Tadatsugu MINAMI et al., "*Optical Properties of Aluminum Doped Zinc Oxide Thin Films Prepared by RF Magnetron Sputtering",* Japaness Journal of Applied Physics, **24** (1985) L605-L607.

[20] R. E. DIETZ et al., "*Excitons and the Absorption Edge of ZnO",* Journal of Applied Physics, **32** (1961) 2282-2286.

[21] S. C. Jain et al., "*Band-gap narrowing in novel III-V semiconductors",* Journal of Applied Physics, **68** (1990) 3747-3749.

[22] Jianhua Hu and Roy G. Gordon, "*Textured aluminum-doped zinc oxide thin films from atmospheric pressure chemical-vapor deposition",* Journal of Applied Physics, **71** (1992) 880-890.

[23] A. P. Roth et al., "*ABSORPTION EDGE SHIFT IN ZnO THIN FILM AT HIGH CARRIER DENSITIES",* Solid State Communications, **39** (1981) 1269-1271.

[24] A. V. Singh et al., "*Doping mechanism in aluminum doped zinc oxide films",* Journal of Applied Physics, **95** (2004) 3640-3643.

[25] R Swanepoel, "*Determination of the thickness and optical constants of amorphous silicon",* Journal of Physics E: Scientific Instruments, **16** (1983) 1214-1222.

[26] Mujdat Caglar et al., "*The effects of Al doping on the optical constants of ZnO thin films prepared by spray pyrolysis method",* Journal of Materials Science: Materials in Electronics, **19** (2007) 704-708.

[27] H. Kim et al., "*Effect of aluminum doping on zinc oxide thin films grown by pulsed laser deposition for organic light-emitting devices",* Thin Solid Films, **377** (2000) 798-802.

[28] Zhaohui Qiao et al., "*Dielectirc modeling of transmittance spectra of thin ZnO-Al films",* Thin Solid Films, **496** (2006) 520–525.

[29] Bingqiang Cao et al., "*Different ZnO Nanostructures Fabricated by a Seed-Layer Assisted Electrochemical Route and Their Photoluminescence and Field Emission Properties",* Journal of Physical Chemestry C, **111** (2007) 2470-2476.

[30] Anderson Janotti and Chris G Van de Walle, "*Fundamentals of zinc oxide as a semiconductor",* Reports on Progress in Physics, **72** (2009) 126501.

[31] J. D. Ye et al., "*Correlation between green luminescence and morphology evolution of ZnO films",* Applied Physics A, **81** (2005) 759-762.

[32] Yaodong Liu and Jianshe Lian, "*Optical and electrical properties of aluminum-doped ZnO thin films grown by pulsed laser deposition",* Applied Surface Science, **253** (2007) 3727-3730.

[33] Haixia Chen et al., "*Enhanced mechanism investigation on violet-blue emission of ZnO films by incorporating Al and Zn to form ZnO-Al-ZnO films",* Optical Materials, **62** (2016) 505-511.

[34] Bhupendra K Sharma and Neeraj Khare, "*Stress-dependent band gap shift and quenching of defects in Al-doped ZnO films",* Journal of Physics D: Applied Physics, **43** (2010) 465402.

[35] Debajyoti Das and Praloy Mondal, "*Photoluminescence phenomena prevailing in c-axis oriented intrinsic ZnO thin films prepared by RF magnetron sputtering",* RSC Advance, **4** (2014) 35735-35743.

[36] Cheol Hyoun Ahn et al., "*A comparative analysis of deep level emission in ZnO layers deposited by various methods",* Journal of Applied Physics, **105** (2009) 013502.

[37] Haibo Zeng et al., "Blue Luminescence of ZnO Nanoparticles Based on Non-Equilibrium Process: Defects Origins and Emission Controls", Advanced Functional Materials, 20 (2010) 561-572.

Chapter 4

Fabrication and characterization of pulsed laser deposited $Zn_{1-x}Ti_xO$ ($0 \leq x \leq 0.050$) thin films

Titanium as an impurity in host ZnO possesses more than one charge valence state thereby enhances the *n*-type conductivity more than group III dopants **[1-3]**. Therefore, ZnO-TiO_2 composite offers good optical transparency along with high free carrier density and is being viewed as an excellent choice towards transparent conducting oxide (TCO) applications **[4]**. The overlapping of the positions of absorption and emission spectra of TiO_2 and ZnO respectively can control the defect level emission and consequently the near band edge emission can be significantly enhanced **[5]**. TiO_2 has relatively higher refractive index as compared to that of ZnO thus making it feasible to tailor the refractive index of host ZnO infused with Ti and is useful for optical communication, data storage devices and optical switching etc. **[6]**. The large difference in the ionization states of Zn and Ti in the ZnO and TiO_2 respectively, causes excessive free electrons in the ZnO-TiO_2 system which controls the band gap energy, conductivity etc. **[1, 7]**. Besides these aforementioned applications, the Ti doped ZnO has also been reported in optoelectronics, thin film transistors, photo detector etc. **[4, 8-10]**. However, due to the difference in the crystal structures of these two species, the excess amount of TiO_2 into host ZnO can cause serious structural disorder and limits its application. Therefore, it is essential to study the systematic variation of the Ti content to get an optimum concentration useful for diverse applications.

The $Zn_{1-x}Ti_xO$ ($0 \leq x \leq 0.050$) thin films fabricated via pulsed laser deposition technique onto fused silica substrate, is reported in this chapter. The deposition parameters for TZO film are same as that of the AZO films and are listed in Table 2.3,

Chap. 2. Similar to AZO thin films as described in the previous chapter, Chap. 3, PLD TZO films were also subjected to structural, optical and photoluminescence characterization. In addition, these were also subjected to field emission scanning electron microscope (FESEM) for surface morphology and particle size distribution.

4.1 Energy dispersive X-rays spectra of $Zn_{1-x}Ti_xO$ ($0 \leq x \leq 0.050$) thin films

Figure 4.1 shows the energy dispersive X-rays (EDX) spectra of pulsed laser deposited $Zn_{1-x}Ti_xO$ ($0 \leq x \leq 0.050$) thin films.

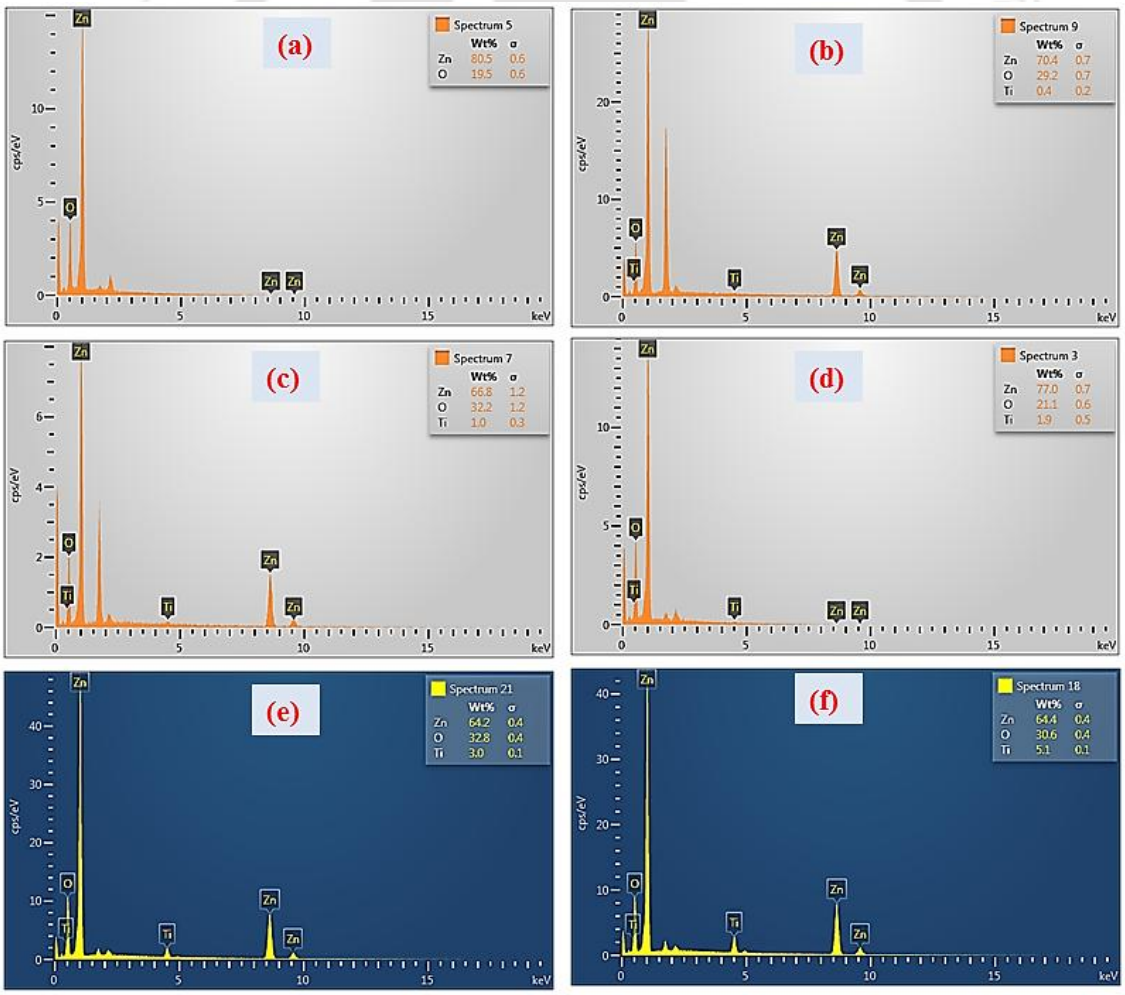

Fig. 4.1 EDX spectra of $Zn_{1-x}Ti_xO$ ($0 \leq x \leq 0.050$) thin films (a) x=0.000, (b) x=0.005, (c) x=0.010, (d) x=0.020, (e) x=0.030 and (f) x=0.050.

The estimated amount of Ti (wt%) from EDX measurement in the $Zn_{1-x}Ti_xO$ ($0 \leq x \leq 0.050$) thin films is plotted against the amount of Ti (wt%) in corresponding TZO powder (bulk) form and is shown in Fig. 4.2. All the data points are the average over 3 distinct places of respective thin film samples.

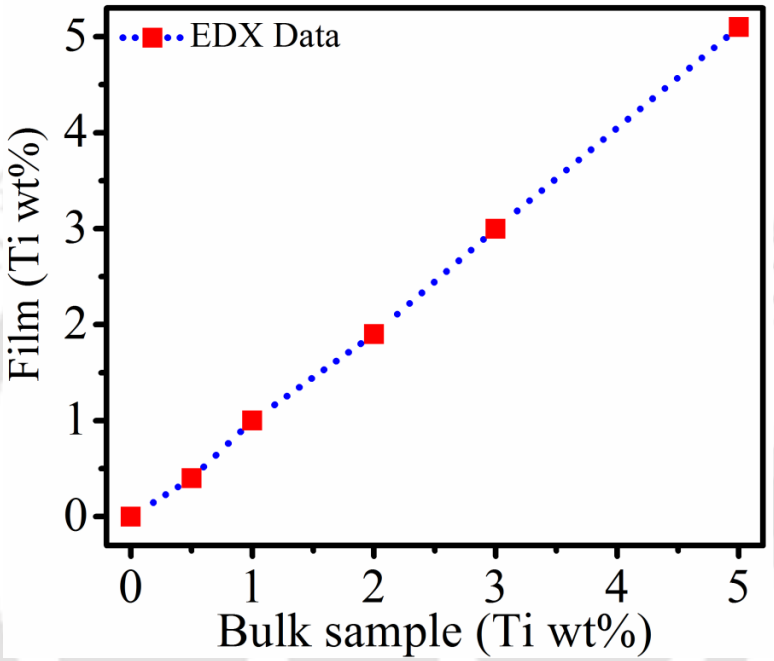

Fig. 4.2 Plot of Ti content in thin film vs. bulk sample.

The reasonable matching of the Ti content indicates the nearly stoichiometric transfer from the target to the PLD films of TZO.

4.2 XRD spectra of $Zn_{1-x}Ti_xO$ ($0 \leq x \leq 0.050$) thin films

Figure 4.3 shows the XRD spectra of the $Zn_{1-x}Ti_xO$ ($0 \leq x \leq 0.050$) thin film deposited onto fused silica substrate. Similar to the XRD spectra of AZO thin films, Fig. 3.3, Chap. 3, the TZO films also exhibit various diffraction peaks (*hkl*) indexed as (100), (002), (101), (102) and (110). All the samples exhibit polycrystalline nature in general but for x=0.020 it shows the preferential c-axis orientation along (002) plane. It is also

observed that the preferred orientation along (002) plane is improved in the $Zn_{1-x}Ti_xO$ (TZO) thin films with the addition of Ti content till x=0.020. At higher values of x, (>0.020), the (002) peak is distorted and the other phases; (100) and (101) are appearing to be more prominent.

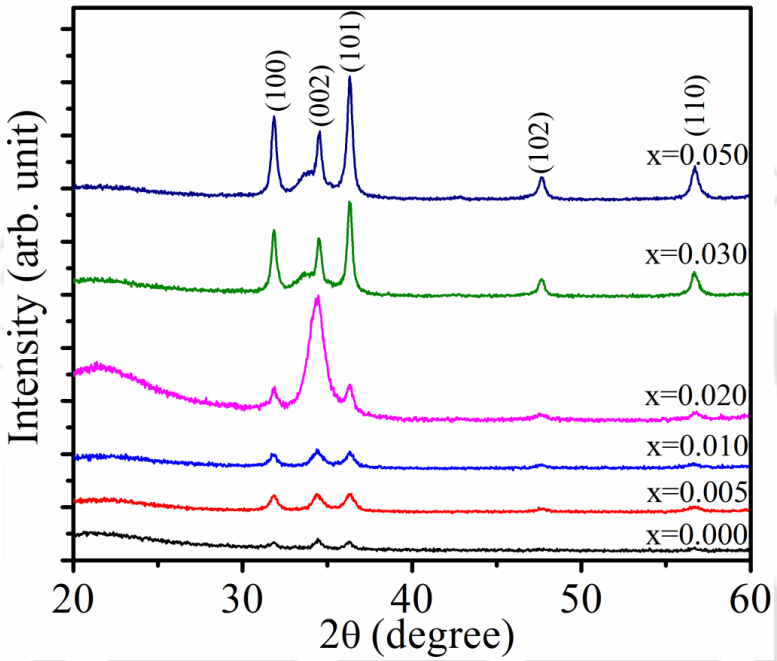

Fig. 4.3 XRD spectra of $Zn_{1-x}Ti_xO$ ($0 \le x \le 0.050$) thin films.

The distortion in the (002) peak could be due to the excess free electrons which occupy the vacant space between the lattice positions and void formation due to the addition of relatively large amount of Ti. Since the substitution of Ti for Zn atom employs a mutual replacement of Zn^{2+} ions by Ti^{4+} ions, hence additional 2 free electrons contribute towards the free carrier density. These free carriers can accommodate within the interstitial positions and thus can cause the deterioration in the c-axis oriented 002 peak. Jeng-Lin Chung et. al. **[11]** has reported that the excess of TiO_2 in ZnO makes the ZnO-TiO_2 composite, more amorphous in nature due to the segregation of excess Ti atoms at the grain boundaries. For 002 plane, crystallite size (*D*), and the lattice

parameters (*a* and c) were estimated by using eqn. 3.1-3.3, Chap. 3 and are listed in table 4.1.

Table 4.1 Variation of crystallite size and lattice parameter of $Zn_{1-x}Ti_xO$ ($0 \leq x \leq 0.050$) thin films.

Sample (x)	**002 peak position (degree)**	***D* (nm)**	***a* (Å)**	***c* (Å)**	**c/a**
0.000	34.46	17.0±1.5	3.240	5.204	1.603
0.005	34.42	11.9±0.6	3.241	5.207	1.607
0.010	34.42	11.4±0.7	3.243	5.209	1.606
0.020	34.37	7.8±0.2	3.244	5.214	1.607
0.030	34.53	26.0±0.6	3.239	5.192	1.603
0.050	34.52	25.9±0.7	3.239	5.192	1.602

The average crystallite size (*D*) in the (002) plane in TZO thin films shows a large variation in the range of 7.8-26 nm. From table 4.1, initially there was a decrease in the average crystallite size with the increase in x value till x=0.020 where it attains the minimum value of 7.8 nm. The decrease in the grain size in Ti doped ZnO thin film is mainly due to the minor mismatch in the ionic radii of the Ti^{4+} and Zn^{2+} ions. Since the estimated lattice constants (*a*, *c*) are observed to be less than that of the stress free lattice constants of pure ZnO hence, films undergo a compressive stress which results in the decrease in the grain size. A decrease in average crystalline size in Ti doped ZnO nanoparticles is also reported by Milton et. al **[12]**. A further increment in x leads to an increase in *D* values. This could be due to the abnormally large thickness of the samples

for x>0.020 as depicted in Table 4.2. With the increase in the film thickness, the carrier concentration increases **[13]**. Therefore, the surface energy or grain boundary energy will be lowered due to its interaction with dopants. This will favor the adsorption of the impinging atoms and results in the larger crystallite size. It is observed that x=0.020 is a transition point where the substitution of Ti^{4+} ion at Zn^{2+} ion is most appropriate for the crystalline quality of the film. A small deviation of the lattice parameters in the $Zn_{1-x}Ti_xO$ film from the pure ZnO could be due to the difference in ionic radii of the participating species ($r(Zn^{2+})$=60 pm, $r(Ti^{4+})$=60.5 pm) **[14]**. Tsay et. al. have also reported quite similar variation in the lattice parameter (*c*) in sol-gel derived $Zn_{1-x}Ti_xO$ thin films **[15]**. The ratio of lattice parameters (*c*/*a*) is estimated to be ~1.60 which is closed to the hexagonal crystal structure. However, this ratio shows a deviation from the ideal c/*a* ratio ($\sqrt{8/3} = 1.63$) of the wurtzite hexagonal ZnO structure **[16]**. The estimated lattice constants in the present case are smaller than that of the lattice constants of stress free bulk ZnO crystal (a_0=3.253Å and c_0=5.209Å) [JCPDS data files] indicating the compressive stress in the films.

4.3 Raman spectra of $Zn_{1-x}Ti_xO$ ($0 \le x \le 0.050$) thin films

Figure 4.4 shows the Raman spectra of $Zn_{1-x}Ti_xO$ ($0 \le x \le 0.050$) thin films deposited onto fused silica substrate. The absence of any signature of Raman peaks related to TiO_2 in the $Zn_{1-x}Ti_xO$ ($0 \le x \le 0.050$) thin films is in consistence with the XRD result, Fig. 4.3. This also implies the uniform substitution and mutual replacement of Ti^{4+} ions with the Zn^{2+} ions in the thin film samples. The differences in the ionic radii of the two constituents (Ti^{4+} and Zn^{2+}) are quiet small therefore; the substitution of Ti^{4+} ions with Zn^{2+} ions doesn't affect the wurtzite crystal structure. The observed Raman modes in

the films positioned at 99 cm^{-1}, 438 cm^{-1} and 577 cm^{-1} correspond to E_2 (low), E_2 (high) and A_1 (LO) respectively. The suppression of A_1(LO) peak in TZO films suggests the reduction of defect density in the system.

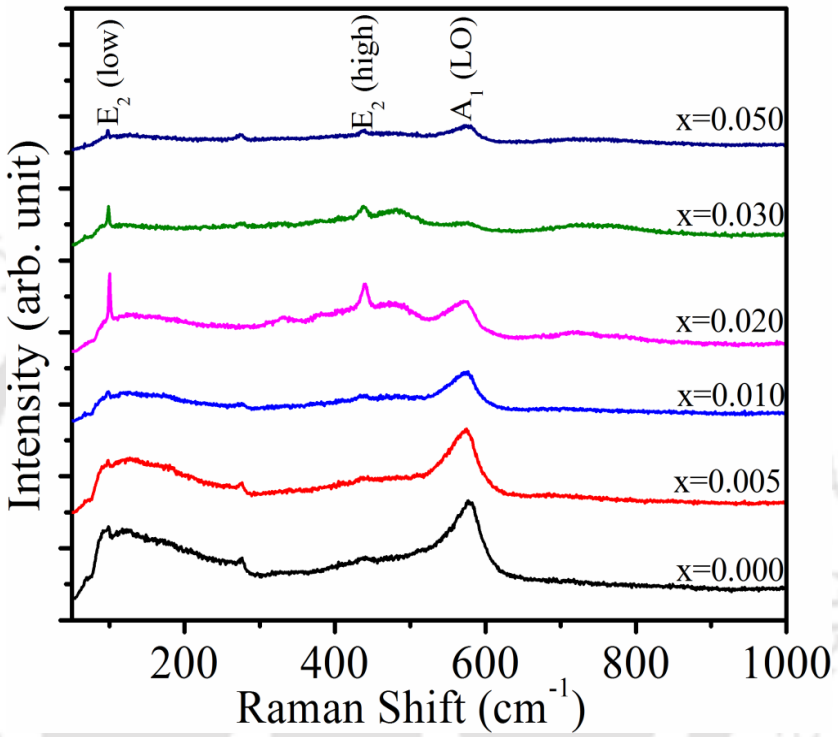

Fig. 4.4 Raman spectra of $Zn_{1-x}Ti_xO$ ($0 \leq x \leq 0.050$) thin films.

The clear emergence of E_2(low) and E_2(high) peak in presence of Ti ions indicates the wurtzite crystal structure. These peaks are very narrow and its intensity is maximum for x=0.020 which is in consensus with XRD observation. Similar to the observation of $Zn_{1-x}Al_xO$ thin films, Fig. 3.5, Chap. 3, the $Zn_{1-x}Ti_xO$ thin films also exhibit a weak signature of silent B_1 Raman mode.

4.4 UV-VIS-NIR spectra of $Zn_{1-x}Ti_xO$ ($0 \leq x \leq 0.050$) thin films

Figure 4.5 depicts the absorption spectra of $Zn_{1-x}Ti_xO$ ($0 \leq x \leq 0.050$) thin films recorded in the spectral range of 200-1000 nm. From this, absorption coefficient, α, is

calculated by using the equations 3.4-3.5, Chap. 3. The thickness of the thin film required for the calculation of α was measured via stylus profilometer and is listed in table 4.2. It is observed that with increasing Ti content, the thin film thickness increases despite of keeping all the other experimental conditions same. This increase in thickness is more pronounced for x>0.020. The inclusion of Ti into ZnO induces the free carrier concentration which results in increasing the absorption of the incident laser energy. Higher laser absorption lowers the ablation threshold resulting in increased ablation rate from the material **[17]** thereby increasing the deposition rate and hence higher thickness. Apart from this, the composite ZnO-TiO_2 has lower melting point as compared to that of pure ZnO (ZnO_{mp}=1975 ^{0}C, TiO_{2mp}=1843 ^{0}C) which also favors relatively higher ablation rate as compared to that of pure ZnO **[16-18]**.

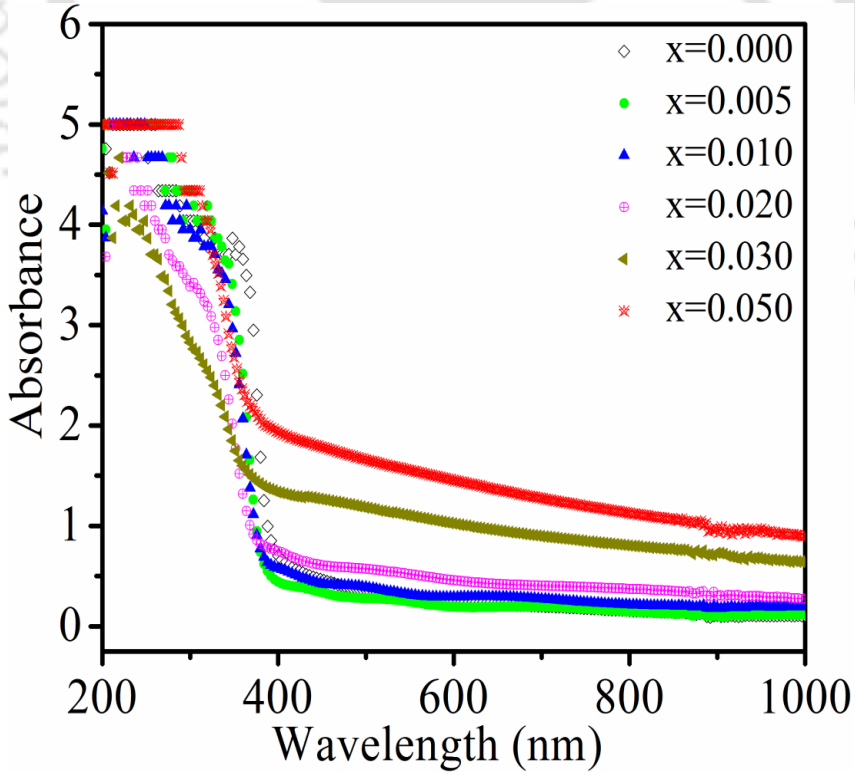

Fig. 4.5 Absorption spectra of $Zn_{1-x}Ti_xO$ ($0 \leq x \leq 0.050$) thin films.

The absorption edge is observed to be slightly shifted towards the lower wavelength with the addition of Ti in ZnO. This blue shift of the absorption edge is continued till x=0.020 and retraced to the red shift for higher values of x ($x \geq 0.030$). The band gap energy of the TZO thin films was estimated using Tauc's plot **[19]**.

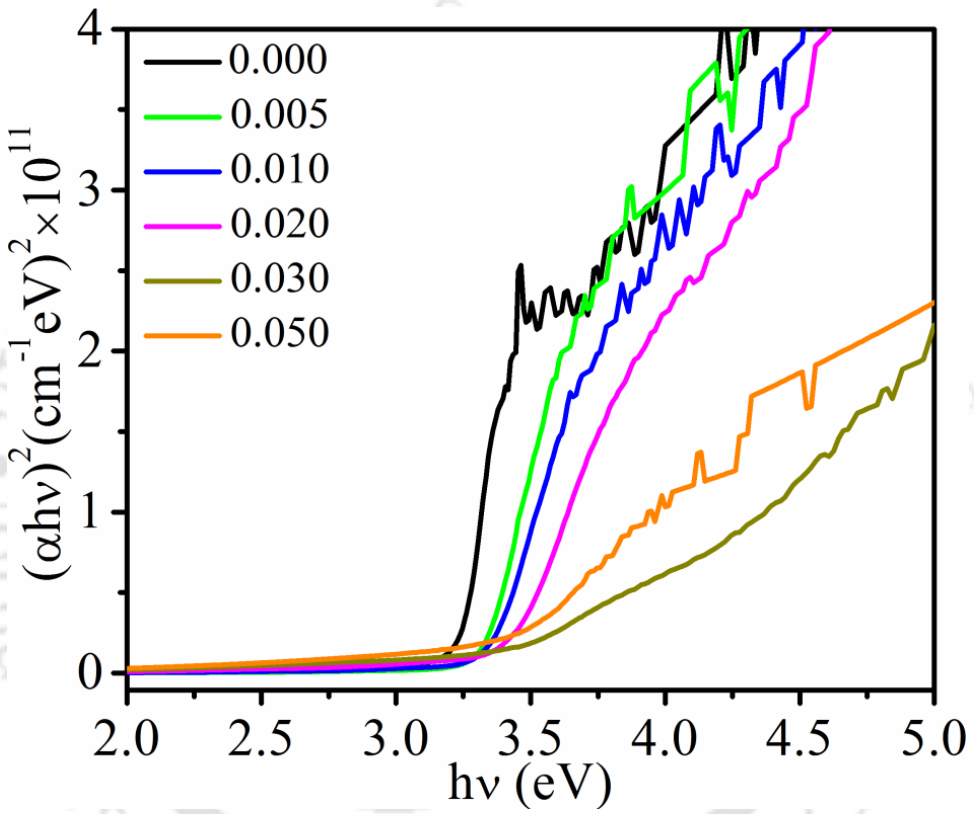

Fig. 4.6 Tauc's plot of $Zn_{1-x}Ti_xO$ ($0 \leq x \leq 0.050$) thin films.

The band gap estimated from the tauc′s plot (equation 3.4-3.5, Chap. 3) is also listed in the table 4.2.

A marginal increase in the band gap energy is observed in the TZO thin films with x till x=0.020 while it reduces slightly for the higher Ti content (x>0.020). The increase in the optical band gap energy for the TZO film is due to the quantum confinement effect

as the crystallite size of the films is decreased as the Ti content is increased in the TZO samples, table 4.3 **[20]**.

Table 4.2 Thin film thickness (L), linear absorption coefficients (α) and band gap energy (E_g) with Ti concentration (x).

Sample (x)	**Thickness (nm)**	**Abs. Coeff. (cm^{-1})$\times 10^4$ at λ=633 nm**	**Band gap energy (eV)**
0.000	520	0.677	3.26±0.11
0.005	680	0.640	3.29±0.06
0.010	690	0.985	3.30±0.06
0.020	650	1.527	3.40±0.05
0.030	1000	2.247	3.25±0.08
0.050	1200	2.669	3.12±0.11

Since the exciton Bohr radius (a_B) of ZnO is 2.34 nm and the estimated crystallite sizes for the lower content of Ti as impurity in ZnO film is in the range of 7.8-11.8 nm, therefore, a weak quantum size effect could be possible **[21]**. At higher Ti concentration ($x>0.02$), the carrier concentration is increased enormously in the conduction and valence band which leads to the shrinkage of band gap as a result of enhanced carrier-carrier and carrier-impurity interaction **[22]**.

The UV-Vis-NIR transmission spectra of the $Zn_{1-x}Ti_xO$ ($0 \leq x \leq 0.050$) thin film fabricated via PLD technique are shown in Fig 4.7 in the spectral range of 200-2000 nm.

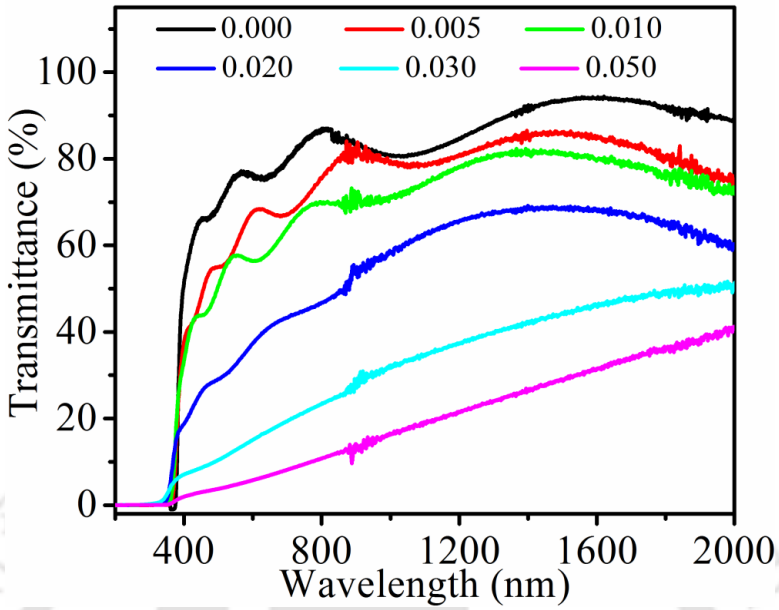

Fig. 4.7 Transmission spectra of $Zn_{1-x}Ti_xO$ ($0 \leq x \leq 0.050$) thin films.

It is very obvious that the transmittance of the TZO thin films decreases with the increase in the Ti concentration. Furthermore, the interference fringes start diminishing at higher Ti concentration and disappear completely beyond x=0.020. The low optical transmittance at higher Ti concentration in ZnO thin film could be due to the strong absorption in thin films including linear absorption and free carrier absorption. At higher Ti concentration ($x>0.020$), the complete absence of interference fringes in the spectrum indicates the deterioration of the film quality which is also indicated by the XRD and Raman measurements, Fig 4.3 & 4.4. Therefore, the linear refractive indices (*n*) could be estimated in the TZO thin films using Swanepoel envelope method, eqn. 3.8-3.10, Chap. 3 only up-to $0 \leq x \leq 0.020$.

Figure 4.8 shows the plot of refractive indices vs. wavelength and the variation in the value of *n* at λ=633 nm with Ti concentration is displayed in the inset.

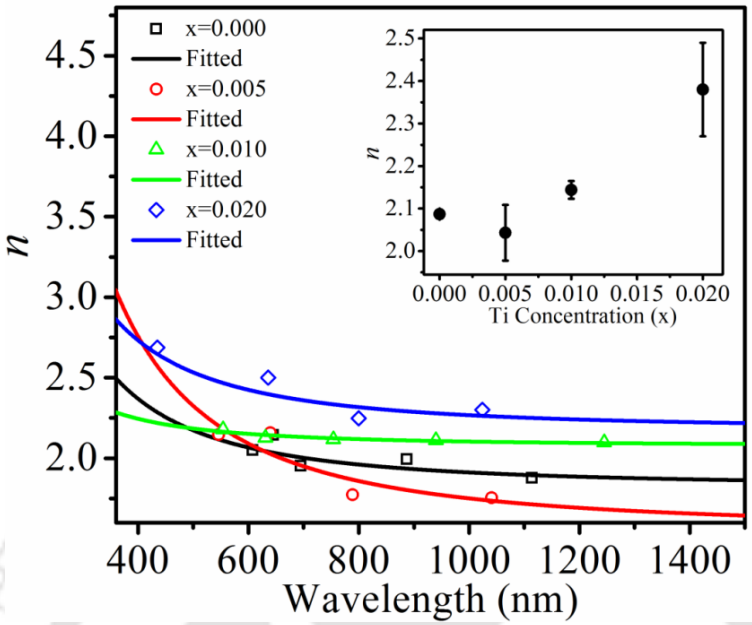

Fig. 4.8 Variation of linear refractive indices in $Zn_{1-x}Ti_xO$ ($0 \leq x \leq 0.050$) thin films and the variation of n (at λ=633 nm) with Ti content along with error bar (inset).

The estimated linear refractive index decreases with the increase in wavelength which signifies the normal dispersion. The linear refractive indices in $Zn_{1-x}Ti_xO$ thin films increase for $0 \leq x \leq 0.02$ as shown by the Fig. 4.8 (inset). The sample x=0.005 shows slightly lower value of n as compared to that of pure ZnO, which is within the error bar. The increase in refractive indices with x may be due to the increased carrier concentration and is in accordance with that of documented in literature **[23]**. The linear refractive index of TiO_2 is higher as compared to ZnO hence the refractive index of ZnO can be tailored with the infusion of low concentration of Ti ions.

4.5 Surface microstructure study of $Zn_{1-x}Ti_xO$ ($0 \leq x \leq 0.050$) thin films

The particle size distribution in the TZO films can be obtained via field emission scanning electron microscope (FESEM). Figure 4.9 shows the FESEM micrographs of $Zn_{1-x}Ti_xO$ ($0 \leq x \leq 0.050$) thin films. The surface of pure ZnO, Fig 4.9 (a), displays mixed

shapes of nano clusters of spherical as well as diamond shaped particles. The average particle size of the structure was estimated to be ~196 nm.

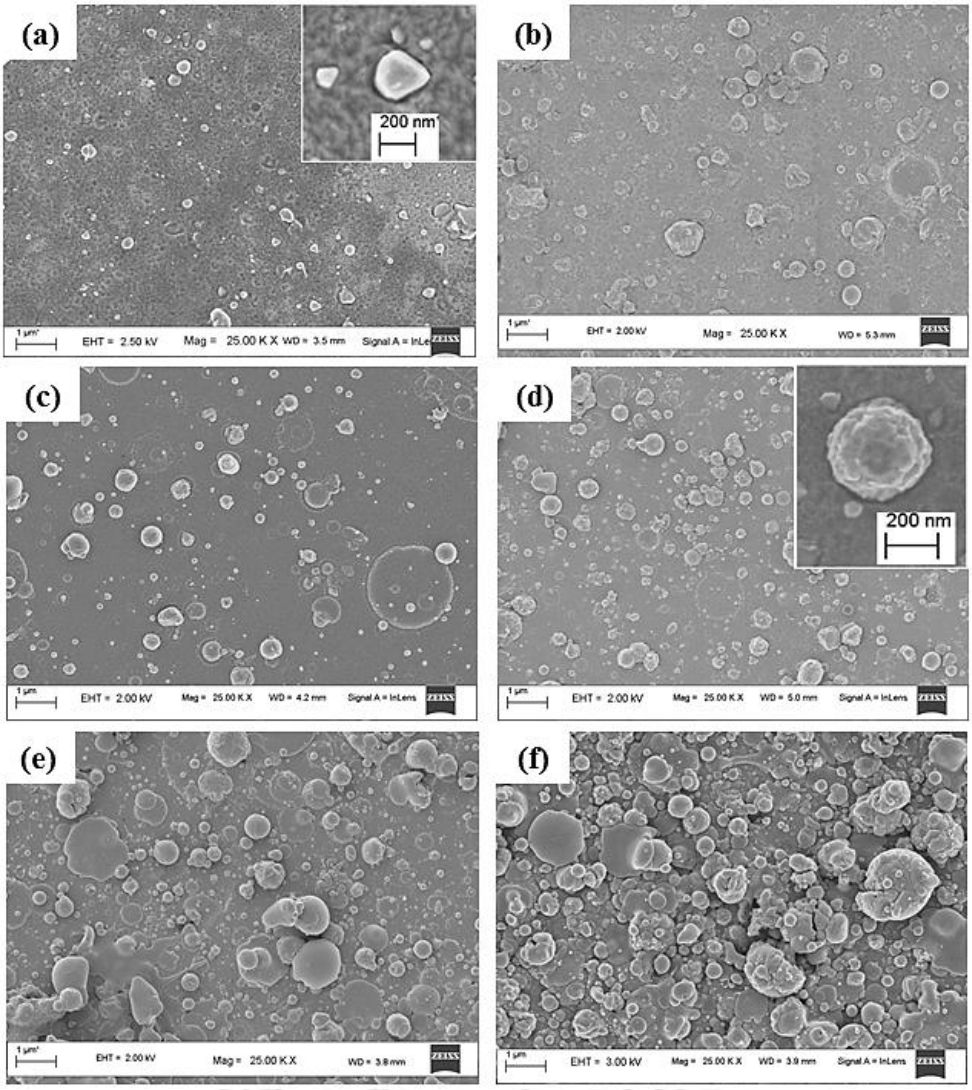

Fig. 4.9 FESEM images of $Zn_{1-x}Ti_xO$ ($0 \leq x \leq 0.050$) thin films (a) x=0.000, (b) x=0.005, (c) x=0.010, (d) x=0.020, (e) x=0.030 and (f) x=0.050.

On incorporation of Ti in the film, the morphology of the ZnO, the shapes of the particles is nearly spherical and finally become marigold flower like structure for x=0.020 film as shown in the inset of Fig 4.9 (d). At the higher concentration of Ti, the clusters are relatively densely packed texture. With the increase in Ti, the ablation threshold reduces

resulting in the enhancement in the particle flux arising at the substrate and hence facilitating the formation of bigger densely packed clusters. This formation of densely packed structure in TZO films at high Ti concentration have also been reported via sputtering technique **[24]**.

The distribution of the grain size in $Zn_{1-x}Ti_xO$ ($0 \leq x \leq 0.050$) thin films is displyaed in Fig. 4.10.

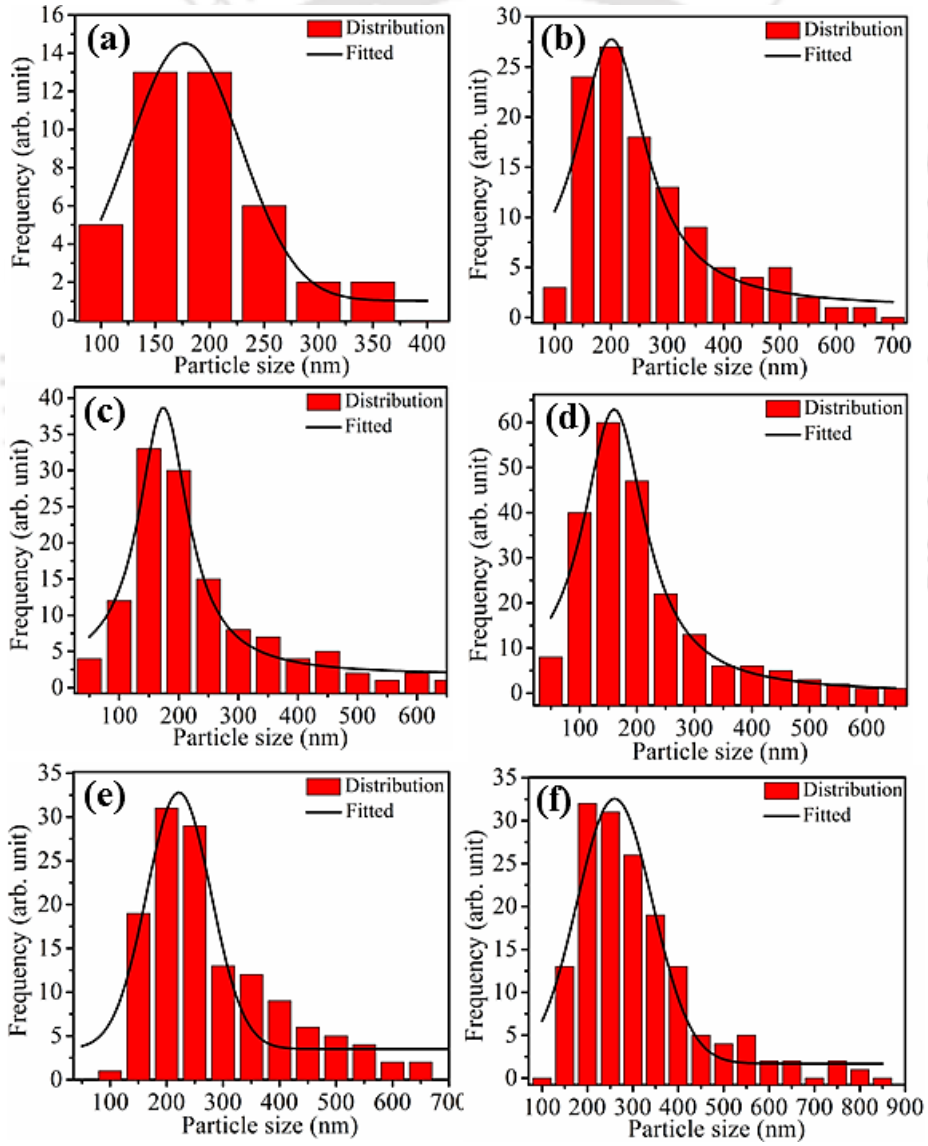

Fig. 4.10 Particle size distribution of $Zn_{1-x}Ti_xO$ ($0 \leq x \leq 0.050$) thin films (a) x=0.000, (b) x=0.005, (c) x=0.010, (d) x=0.020, (e) x=0.030 and (f) x=0.050.

The average particle size estimated by fitting the particle size distribution in the $Zn_{1-x}Ti_xO$ ($0 \leq x \leq 0.050$) films is listed in table 4.3.

Table 4.3 Variation of average particle size in $Zn_{1-x}Ti_xO$ ($0 \leq x \leq 0.050$) thin films.

Sr. No.	Sample (x)	Distribution	Average Particle size (nm)
1.	0.000	Gaussian	196
2.	0.005	Lorentzian	200
3.	0.010	Lorentzian	174
4.	0.020	Lorentzian	160
5.	0.030	Gaussian	221
6.	0.050	Gaussian	260

It is observed that the distribution of the nanostructured particles are of Gaussian nature for pure ZnO (x=0.000) and $Zn_{1-x}Ti_xO$ (x>0.020) films while that of $0.005 \leq x \leq 0.020$, distribution is well fitted with Lorentzian function. This observation is in accordance with the observed XRD result, Fig. 4.3. For the good crystalline films, the particle size follows the homogeneous size distribution and thus Lorentzian but for inhomogeneous and random growth it follows Gaussian distribution **[25]**.

4.6 Photoluminescence spectra of PLD $Zn_{1-x}Ti_xO$ ($0 \leq x \leq 0.050$) thin films

Figure 4.11 shows the room temperature photoluminescence spectra of $Zn_{1-x}Ti_xO$ ($0 \leq x \leq 0.050$) thin films recorded in the range of 350-730 nm. Similar to the PL spectra

shown in $Zn_{1-x}Al_xO$ ($0 \leq x \leq 0.10$) thin film, Fig. 3.14, Chap. 3, the $Zn_{1-x}Ti_xO$ ($0 \leq x \leq 0.050$) thin films also show NBE as well as DLE emission bands.

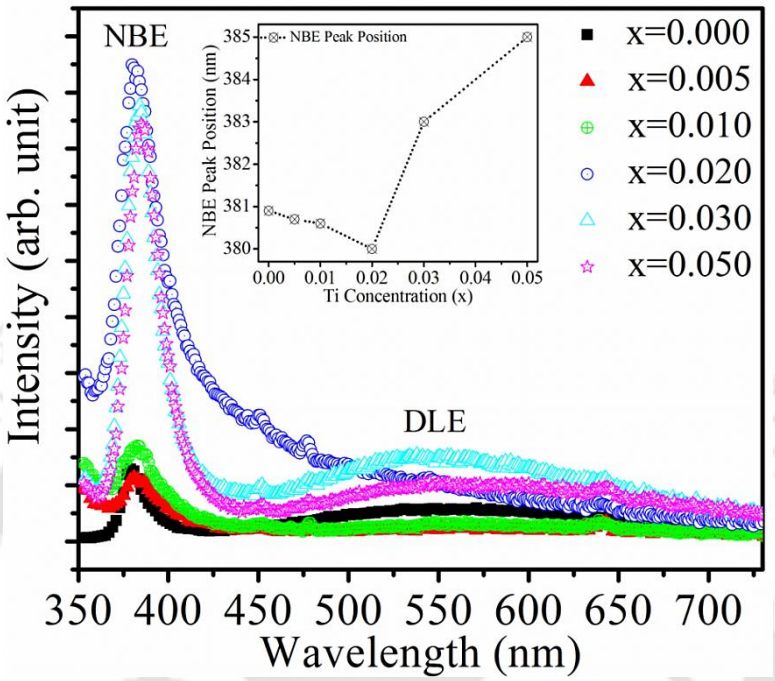

Fig. 4.11 Photoluminescence spectra of $Zn_{1-x}Ti_xO$ ($0 \leq x \leq 0.050$) thin films and variation of NBE peak position with Ti concentration (Inset).

From Fig 4.11, it is observed that the NBE peak intensities of the films containing low concentration of Ti ($x \leq 0.010$) are comparable to that of pure ZnO (x=0.000) film. In the case of higher Ti concentration ($x > 0.010$), there is a rapid enhancement in the NBE emission. The NBE peak intensity is maximum for x=0.020 thin film sample. At higher values of x (>0.020), there is not much variation in the intensity of NBE band and is observed to be comparable to that of x=0.020. Although there is remarkable deterioration in the crystalline quality for x=0.030 and 0.050 yet comparatively strong NBE emissions is attributed to the large thickness of these samples **[26].** However, the defect related emission band is observed to be enhanced along with the NBE band for x>0.020 samples.

This could be probably again due to poor surface quality as well as crystallinity of these films.

The UV emission peak as shown in Fig. 4.11 (Inset), shifts towards the shorter wavelength side with the increase in the x values ($0 \leq x \leq 0.020$) while with further increase in x (>0.020), it leads to a red shift. It is also worthwhile to mention that the UV emission peak follows one to one correspondence with the corresponding band gap energy of $Zn_{1-x}Ti_xO$ films, indicating the band to band recombination during the photoluminescence process.

For the details, NBE band in the range of 360 to 460 nm are de-convoluted and are shown in Fig. 4.12.

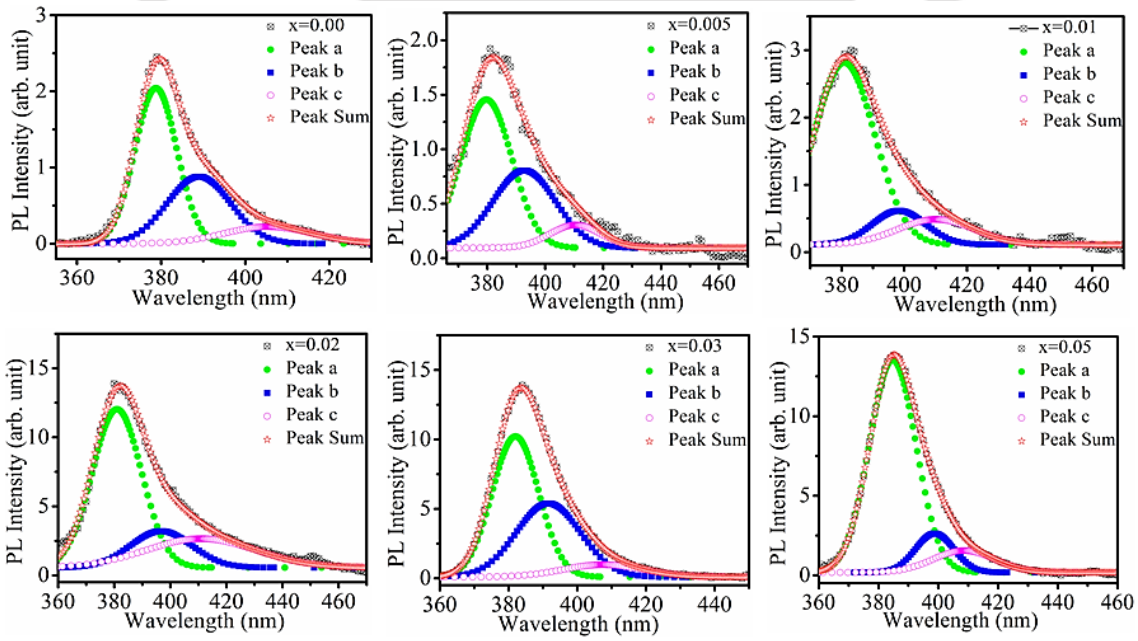

Fig. 4.12 De-convoluted NBE PL spectra of $Zn_{1-x}Ti_xO$ ($0 \leq x \leq 0.05$) thin films.

The de-convoluted spectra depict the three separate peaks, namely a, b and c positioned around 380 nm (3.26 eV), 394 nm (3.14 eV) and 410 nm (3.02 eV)

respectively. The first peak, (a), which lies at 3.26 eV corresponds to the emission of free exciton (FX) **[27, 28]**. The second peak (b) positioned at 3.14 eV is usually considered to be originated from the donor bound excitons **[29, 30]**. The third component, peak c, at 3.02 eV having least intensity, could be due to the radiative recombination of electrons captured at zinc interstitial (Zn_i) to the holes residing at zinc vacancy (V_{Zn}) sites **[31]**.

Figure 4.13 depicts the variation of integrated intensity of individual peak as a function of Ti concentration (x).

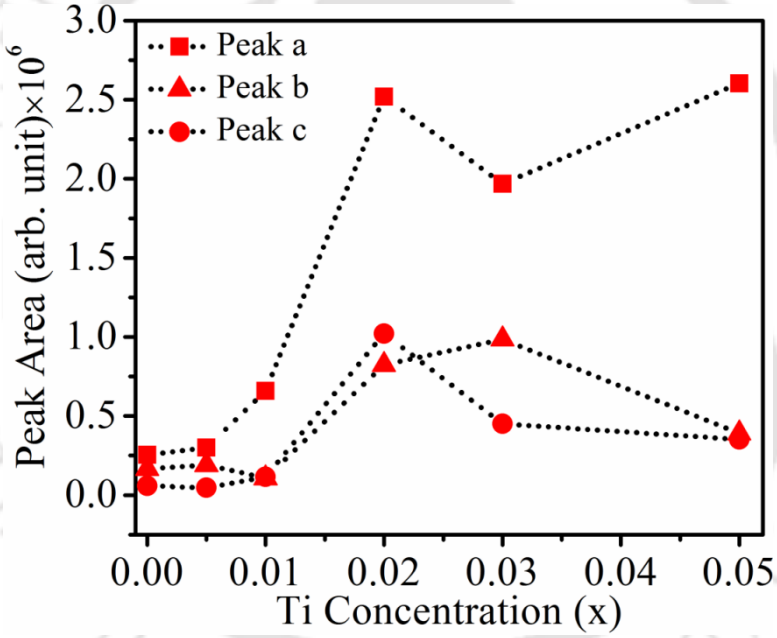

Fig. 4.13 Variation of integrated intensity of $Zn_{1-x}Ti_xO$ ($0 \le x \le 0.05$) thin films for NBE peak.

The most intense peak, peak a, for the thin film sample at x=0.020 exhibits a maximum intensity which is nearly six times as compared to that of x=0.00 sample. The average crystallite size estimated from the XRD measurement is gradually decreased from 17 nm to 7.8 nm for $0 \le x \le 0.020$) and thereafter increased to 26 nm for $x > 0.020$. Therefore, a weak quantum size effect could be possible for the x=0.020 thin film sample

resulting into the enhancement in the NBE emission along with suppression of DLE band **[21]**.

The DLE emission is strongly influenced by the presence of Ti in ZnO. Since, the origin of DLE band is due to the various point and surface defects hence the addition of Ti in ZnO makes a remarkable impact on these defects. The DLE peak is completely extinguished in x=0.020 sample. The nominal reduction in the DLE peak occurs due to the improvement in the crystalline quality while the quenching of the DLE peak might be due to the quantum confinement effect. To get in-depth information about the possible defects associated with the visible emission in the range of 450-730 nm, the DLE bands are fitted with Gaussian function into 4 distinct peaks assigned as p, q, r and s positioned at 510 nm (~2.43 eV), 570 nm (~2.17 eV), 635 nm(~1.95 eV) and 690 nm (~1.79 eV) respectively. Figure 4.14 show these de-convoluted spectra of DLE bands in $Zn_{1-x}Ti_xO$ ($0 \le x \le 0.05$) thin films.

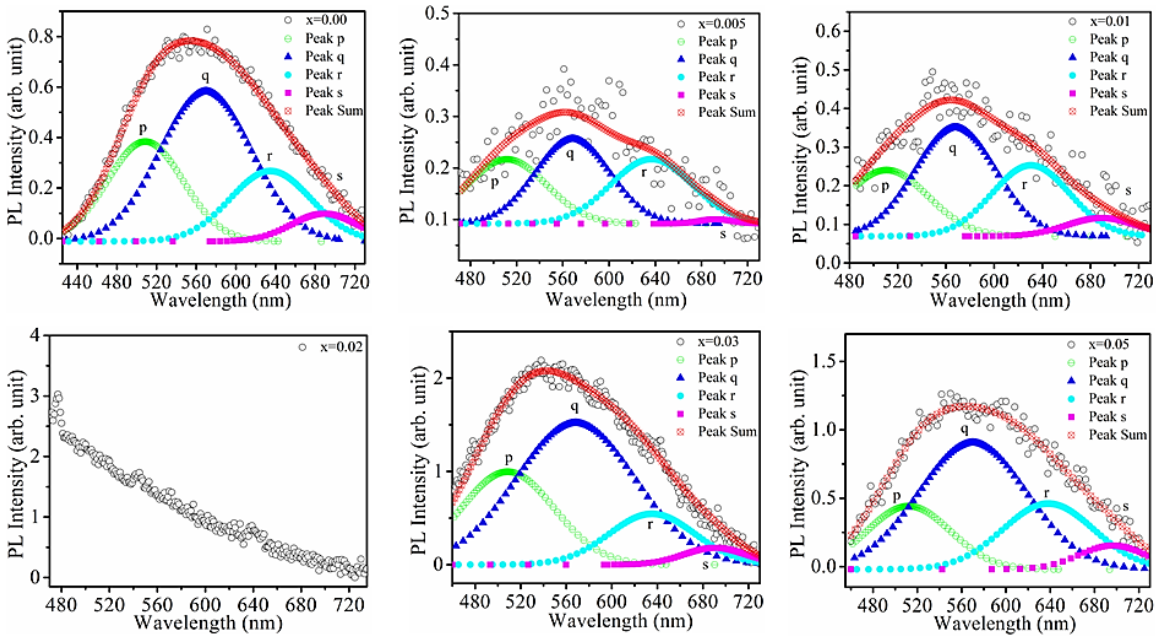

Fig. 4.14 De-convoluted DLE bands in $Zn_{1-x}Ti_xO$ ($0 \le x \le 0.050$) thin films.

Generally, the broad visible emission in ZnO is considered to be from the various intrinsic native defects; V_O, O_i, V_{Zn}, Zn_i, O_{Zn} etc **[32]**. As no direct evidence of the presence of an impurity atom is found in either XRD or Raman measurement so, the possibility of the contribution of the direct impurity element in the visible emission is ruled out.

The energy level diagram depicting the possible recombination mechanism during the photoluminescence in TZO thin films is illustrated in Fig. 4.15.

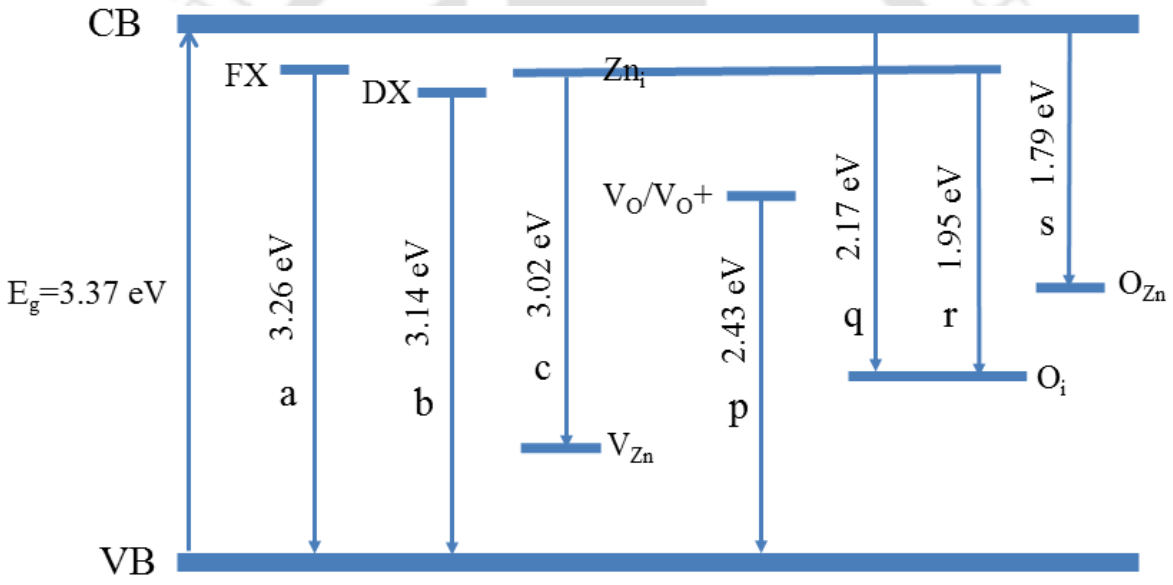

Fig. 4.15 Energy level diagram of $Zn_{1-x}Ti_xO$ ($0 \le x \le 0.050$) thin films.

The peak p, at 510 nm (2.43 eV) falling in green region, is originated from the radiative recombination of intrinsic oxygen vacancy (V_O) or singly ionized oxygen vacancy (V_O^+) defect **[33-35].** However, there are controversies among researchers for the assignment of exact locations of V_O defect within the band gap of ZnO and accordingly the origin of green band as well as its position is reported to be varying in literatures **[35-37]**. The second peak, q positioned at 570 nm (2.17 eV), in the yellow region, is

originated from oxygen interstitial (O_i) defect which are more favorable in oxygen rich environment **[34, 38]**. The red emission at 635 nm (1.95 eV), peak r, involves Zn_i and O_i defects. The energy separation between O_i to CB is ~2.28 eV and Zn_i defect is ~0.22 eV below the conduction band minima, hence, a radiative recombination of these two may result in a red emission **[34, 38, 39]**. The peak, s, in deep red region, is the result of recombination of photo excited electrons with holes at oxygen antisite (O_{Zn}) position **[40]**. A plot of integrated intensities of all these four peaks (p, q, r and s) as a function of Ti concentration (x) is shown in Fig. 4.16.

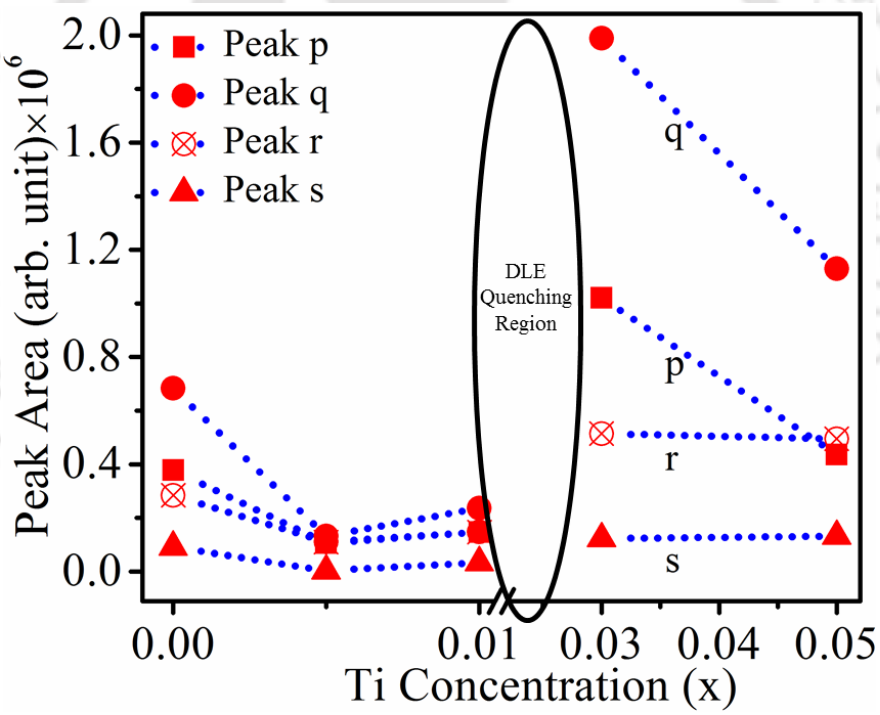

Fig. 4.16 Variation of integrated intensity of de-convoluted DLE peak with Ti concentration.

From Fig. 4.16, it is observed that the intensity of these peaks decreases with increasing Ti concentration up-to x=0.010. At x=0.020, the defect related emission is completely quenched and then for x=0.030, it increases and then at x=0.050, it falls down

for p and q but for peaks r and s, the changes are marginal. In pure ZnO film (x=0.00), the prominent appearance of all the four peaks suggests the Zn-rich stoichiometry of the film. The major defect states (V_O, V_{Zn}, O_i and O_{Zn}) are observed to be influenced in presence of Ti. The mutual replacement of Zn^{2+} by Ti^{4+} ions leads to formation of Zn deficient system hence the oxygen vacancy, V_O, is expected to be reduced with the increase in Ti concentration. In addition, it may also assist in creating the interstitial oxygen defect (O_i), zinc vacancy (V_{Zn}) and oxygen antisite (O_{Zn}) defects in the system. As it is seen that the maximum contribution of the component (peak p and q) in the DLE band is associated with the O_i and V_{Zn} defects therefore, the inclusion of Ti in ZnO helps in the formation of interstitial oxygen and zinc vacancy more as compared to that of the reduction in oxygen vacancy despite of the low formation energy of V_O defect. It has been reported that the addition of Ti in ZnO enhanced the O/Zn ratio in Ti doped ZnO thin films **[41-43]**. Therefore, the densities of optically active defects (V_O, V_{Zn}, O_i, Zn_i and O_{Zn}) are altered with the concentration of Ti in the ZnO thin films.

The ratio of visible peak intensity (I_{DLE}) to the UV peak intensity (I_{NBE}) is a measure of the optical quality of the films. Lower value of the I_{DLE}/I_{NBE} ratio indicates reduction in the defect levels. In the present case, all the samples exhibit I_{DLE}/I_{NBE} value less than unity. The ratio, I_{DLE}/I_{NBE}, as a function of Ti concentration is shown in Fig. 4.17. As shown in Fig. 4.17, the I_{DLE}/I_{NBE} ratio in the pure ZnO thin film is observed to be ~0.45 and it gradually decreases with the Ti concentrations for $0<x\leq0.010$ and for $x>0.020$. For the Ti concentration of x=0.020, the ratio of I_{DLE}/I_{NBE} is not applicable since the DLE band is completely suppressed, Fig. 4.14 as there is no clear appearance of visible DLE peak at this particular Ti concentration. This is the 'PL Quenching Effect' of the visible emission in the film. This effect arises due to various factors such as

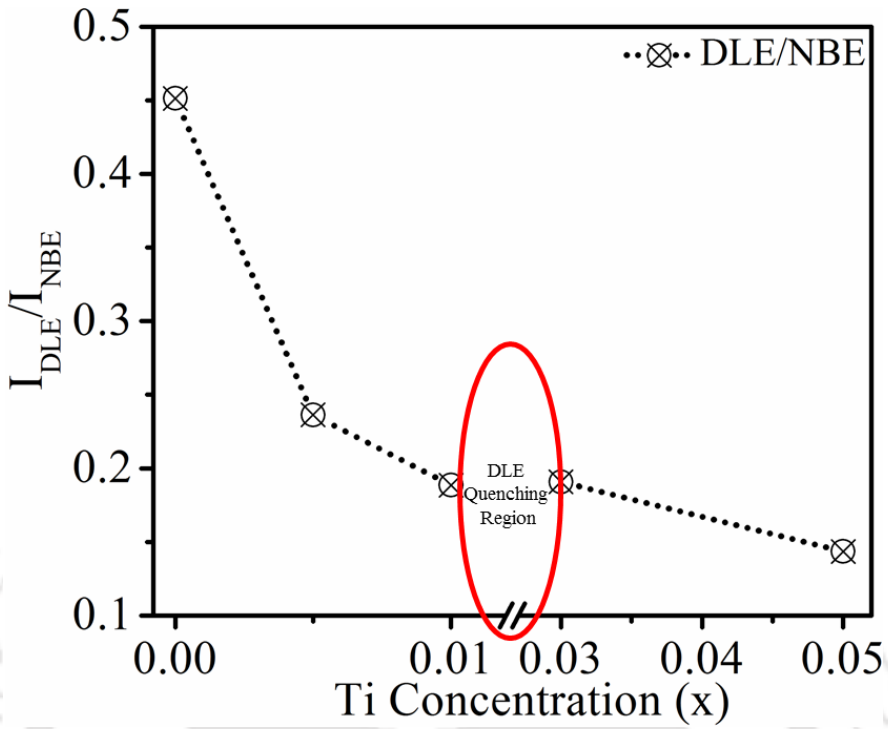

Fig. 4.17 Plot of I_{DLE}/I_{NBE} ratio with Ti concentration.

crystalline quality, quantum size effect and fluorescence resonance energy transfer (FRET) effect **[5]**. The suppression of visible emission and enhancement in UV emission in ZnO-TiO_2 nano composite is explained on the basis of fluorescence resonance energy transfer effect **[5, 44]**. In the present case, no clear signature of TiO_2 phase is observed in XRD spectra, Fig. 4.1. So, the possibility of FRET effect in the present case is quite low. However, the contribution from this effect cannot be completely ruled out since both the species (TiO_2 and ZnO) form a donor-acceptor pair suitable for FRET effect. The other two possibilities (quantum size effect and crystalline quality) can play significant role on the quenching effect. The $Zn_{1-x}Ti_xO$ films shows a weak quantum confinement effect for x=0.020, since the estimated crystallite size (7.8 nm) is found to be in close proximity to the exciton bohr radius (2.34 nm) of ZnO **[21]**. This may lead to the band gap widening effect as well as dominant excitonic recombination and as a result, the DLE emission is

completely quenched. The crystalline quality also influence the PL emission in ZnO [45]. Since, the preferred orientation of the film is confined along (002) direction for x=0.020 sample so, crystal quality of the film is improved which in turn reduces the density of defects and results in the suppression of DLE emission.

4.7 Conclusion

The crystalline and phase identification of the PLD $Zn_{1-x}Ti_xO$ ($0 \leq x \leq 0.050$) films were carried out via XRD and Raman measurement. The estimated axial ratio (c/a) confirmed the wurtzite hexagonal crystal structure in the deposited thin films. The best crystallinity was observed at x=0.02. The optical band gap energy in the thin films was observed to be increased initially from 3.26 eV to 3.40 eV for $0 \leq x \leq 0.020$ and thereafter it was decreased to 3.12 eV for higher Ti content ($x > 0.020$). The refractive index could be tuned in the range of 2.087-2.380 by controlling the Ti as impurity in these films. The films showed photoluminescence signal covering UV-Visible region. An enhancement in the UV photoluminescence and complete quenching of the visible emission in the $Zn_{1-x}Ti_xO$ (x=0.020) film was observed.

Bibliography

[1] Yang-Ming Lu et al., "*Improving the conductance of ZnO thin films by doping with Ti",* Thin Solid Films, **447-448** (2004) 56-60.

[2] Young Ran Park and Kwang Joo Kim, "*Optical and electrical properties of Ti-doped ZnO films observation of semiconductor–metal transition",* Solid State Communications, **123** (2002) 147–150.

[3] Zhixin Wan et al., "*Electrical and optical properties of Ti doped ZnO films grown on glass substrate by atomic layer deposition",* Materials Research Bulletin, **57** (2014) 23-28.

[4] Wenda Zhao et al., "*A study on Ti-doped ZnO transparent conducting thin films fabricated by pulsed laser deposition",* Applied Surface Science, **305** (2014) 481-486.

[**5**] H. Y. Lin et al., "*Giant enhancement of band edge emission based on ZnO/TiO_2 nanocomposites",* Optics Express, **15** (2007) 13832-13837.

[**6**] J. J. Robillard, "*All-optical switching with fast-response variable-index materials",* Optical Engineering, **42** (2003) 3575.

[7] Haixia Chen et al., "*Optical properties of Ti-doped ZnO films synthesized via magnetron sputtering",* Journal of Alloys and Compounds, **534** (2012) 59-63.

[**8**] Li-Wei Chang et al., "*Enhanced optoelectronic performance from the Ti-doped ZnO nanowires",* Journal of Applied Physics, **109** (2011) 074318.

[9] Kwang-Seok Jeong et al., "*An analysis on applicability of Ti-doped ZnO films as the channel layer of TFTs",* IEEE Nanotechnology Materials and Device Conference, **FrP1-1.5** (2010) 321-324.

[10] P. S. Shewale et al., "*Ti doped ZnO thin film based UV photodetector: Fabrication and characterization",* Journal of Alloys and Compounds, **624** (2015) 251-257.

[11] Jeng-Lin Chung et al., "*Electrical and optical properties of TiO_2-doped ZnO films prepared by radio-frequency magnetron sputtering",* Journal of Physics and Chemistry of Solids, **69** (2008) 535-539.

[12] Milton A. Martinez Julca et al., "*Induced structural defects in Ti-doped ZnO and its two-photon-excitation",* Proceeding SPIE **9722** (2016) 97221E.

[13] Kristin Bergum et al., "*Thickness dependent structural, optical and electrical properties of Ti-doped ZnO films prepared by atomic layer deposition",* Applied Surface Science, **332** (2015) 494-499.

[14] R. D. SHANNON, "*Revised Effective Ionic Radii and Systematic Studies of Interatomie Distances in Halides and Chaleogenides",* Acta Crystallographica, **A32** (1976) 751-767.

[15] Chien-Yei Tsay et al., "*The properties of transparent semiconductor $Zn_{1-x}Ti_xO$ thin films prepared by the sol–gel method",* Thin Solid Films, **518** (2009) 1603-1606.

[16] Hadis Morkoc and Umit Ozgur, "*Zinc Oxide: Fundamentals, Materials and Device Technology",* Wiley-VCH, 2009.

[17] Douglas B. Chrisey and Graham K. Hubler, "*PULSED LASER DEPOSITION OF THIN FILMS",* John Wiley and Sons. Inc. , 1994.

[18] Z. Nowotny, "*Oxide Semiconductor for Solar Energy Conversion: Titanium Dioxide",* CRC, Taylor & Francis Group, 2012.

[19] Gyan Prakash Bharti and Alika Khare, "*Structural and linear and nonlinear optical properties of $Zn_{1-x}Al_xO$ ($0 \leq x \leq 0.10$) thin films fabricated via pulsed laser deposition technique",* Optical Materials Express, **6** (2016) 2063-2080.

[20] A. P. Alivisatos, "*Perspectives on the Physical Chemistry of Semiconductor Nanocrystals",* Journal of Physical Chemistry, **100** (1996) 13226-13239.

[21] R. T. Senger and K. K. Bajaj, "*Optical properties of confined polaronic excitons in spherical ionic quantum dots",* Physical Review B, **68** (2003)

[22] Litty Irimpan et al., "*Enhanced luminescence and nonlinear optical properties of nanocomposites of ZnO-Cu",* Journal of Materials Research, **23** (2008) 2836-2845.

[23] R. Sridhar et al., "*Spectroscopic study and optical and electrical properties of Ti-doped ZnO thin films by spray pyrolysis",* Spectrochimica Acta Part A: Molecular and Biomolecular Spectroscopy, **120** (2014) 297-303.

[24] J. Liu et al., "*Effects of Ti-doped concentration on the microstructures and optical properties of ZnO thin films",* Superlattices and Microstructures, **52** (2012) 765-773.

[25] Gyan Prakash Bharti and Alika Khare, "*Single and multiphoton absorption induced photoluminescence in pulsed laser deposited $Zn_{1-x}Al_xO(0 \leq x \leq 0.10)$ thin films",* Journal of Luminescence, **197** (2018) 135-141.

[26] Eun Sub Shim et al., "*Effect of variation of the film thickness on the structural and optical properties of ZnO thin films deposited on sapphire substrate using PLD",* Applied Surface Science, **186** (2002) 474-476.

[27] Y. C. Kong et al., "*Ultraviolet-emitting ZnO nanowires synthesized by a physical vapor deposition approach",* Applied Physics Letters, **78** (2001) 407-409.

[28] Sang Hyo Lee et al., "*Photoluminescence Analysis of Energy Level on Li-Doped ZnO Nanowires Grown by a Hydrothermal Method",* Applied Physics Express, **5** (2012) 095002.

[29] Santa Chawla et al., "*Growth, microstructure, UV and orange pink emission from ZnO nanocones",* Journal of Crystal Growth, **310** (2008) 3517-3521.

[30] Bingqiang Cao et al., "*Temperature-dependent shifts of three emission bands for ZnO nanoneedle arrays",* Applied Physics Letters, **88** (2006) 161101.

[31] Haibo Zeng et al., "*Blue Luminescence of ZnO Nanoparticles Based on Non-Equilibrium Processes: Defect Origins and Emission Controls",* Advanced Functional Materials, **20** (2010) 561-572.

[32] U. Ozgur et al., "*A comprehensive review of ZnO materials and devices",* Journal of Applied Physics, **98** (2005) 041301.

[33] M. D. McCluskey and S. J. Jokela, "*Defects in ZnO",* Journal of Applied Physics, **106** (2009) 071101.

[34] Cheol Hyoun Ahn et al., "*A comparative analysis of deep level emission in ZnO layers deposited by various methods",* Journal of Applied Physics, **105** (2009) 013502.

[35] J. Cizek et al., "*Origin of green luminescence in hydrothermally grown ZnO single crystals",* Applied Physics Letters, **106** (2015) 251902.

[36] Lukas Schmidt-Mende and Judith L. MacManus-Driscoll, "*ZnO – nanostructures, defects, and devices",* Materials Today, **10** (2007) 40-48.

[37] Sesha Vempati et al., "*One-step synthesis of ZnO nanosheets: a blue-white fluorophore",* Nanoscale Research Letters, **7** (2012) 470.

[38] Costas Tsakonas et al., "*Intrinsic photoluminescence from low temperature deposited zinc oxide thin films as a function of laser and thermal annealing",* Journal of Physics D: Applied Physics, **46** (2013) 095305.

[39] Feng Han et al., "*Surface plasmon enhanced photoluminescence of ZnO nanorods by capping reduced graphene oxide sheets",* Optics Express, **22** (2014) 11436.

[40] Anderson Janotti and Chris G Van de Walle, "*Fundamentals of zinc oxide as a semiconductor",* Reports on Progress in Physics, **72** (2009) 126501.

[41] jeng-Lin Chung et al., "*Preparation of TiO_2-doped ZnO films by radio frequency magnetron sputtering in ambient hydrogen–argon gas",* Applied Surface Science, **255** (2008) 2494-2499.

[42] Shaker A. Bidier et al., "*Structural and optical characteristics of Ti-doped ZnO nanorods deposited by simple chemical bath deposition",* Journal of Materials Science: Materials in Electronics, **28** (2017) 11178-11185.

[43] Jing-Chie Lin et al., "*Structure and characterization of the sputtered ZnO, Al-doped ZnO, Ti-doped ZnO and Ti, Al-co-doped ZnO thin films",* Materials Express, **5** (2015) 153-158.

[44] Chun-Yu Lee et al., "*Enhanced ultraviolet electroluminescence from ZnO nanowires in TiO_2/ZnO coaxial nanowires/poly(3,4-ethylenedioxythiophene)-poly(styrene-sulfonate) heterojunction",* Journal of Applied Physics, **107** (2010) 034310.

[45] F. K. Shan et al., "*Substrate effects of ZnO thin films prepared by PLD technique",* Journal of the European Ceramic Society, **24** (2004) 1015-1018.

Chapter 5

Low temperature photoluminescence in pulsed laser deposited $Zn_{1-x}Al_xO$ (x=0.00 and x=0.05) and $Zn_{1-x}Ti_xO$ ($0 \leq x \leq 0.050$) thin films

The excitonic structure in room temperature photoluminescence spectra of AZO and TZO thin films, Chap. 3 and 4, were not well resolved. The near band edge (NBE) in ZnO is dominated by purely free exciton recombination at room temperature but at lower temperature, a coupling between exciton-donors, exciton-acceptor, exciton-phonon dominates since the rate of dissociation of excitons decreases with the decrease in temperature. This results into the evolution of sharp PL lines in the UV range because of the lower bound exciton binding energy **[1, 2].** The visible PL in ZnO, which is mainly associated with various defects states, also exhibits some interesting features in low temperature region. Depending upon the formation energies of the defects, the radiative recombination of the carriers trapped at various defect states, is altered with the temperature **[2]**. The low temperature not only suppresses the DLE emission but also shifts its spectral range. Generally, the band gap energy of the semiconducting materials is increased with the decrease in the sample temperature and is governed by a well-established varshni's equation **[3]**.

In this chapter, the low temperature photoluminescence in $Zn_{1-x}Al_xO$ (x=0.00 and x=0.05) and $Zn_{1-x}Ti_xO$ ($0 \leq x \leq 0.050$) thin films deposited via pulsed laser deposition technique is described. In all the sets of samples, AZO and TZO, the photoluminescence signals were recorded by varying the sample temperature from 10K to 300K in an interval of 10K as described in Chap. 2, Sec. 2.7, Fig. 2.5. The evolution of some of the distinct

excitons lines in UV spectral range as well as defects associated lines in the low temperature is reported.

5.1 Low temperature photoluminescence spectra of $Zn_{1-x}Al_xO$ (x=0.00 and x=0.05) thin films

Figure 5.1 (a-b) shows the photoluminescence spectra of pulsed laser deposited (PLD) pure ZnO and 5wt% Al doped ZnO (AZO) thin films recorded in the temperature range of 10K to 300K. At room temperature (RT) the photoluminescence (PL) spectra of ZnO, as discussed in Sec. 3.6, Chap. 3, comprised of mainly two emission bands; one narrow band near the ultraviolet region which is the result of radiative recombination of carriers within the band edge and is known as near band edge (NBE) emission and another quite broad band covering the whole visible spectral region, is designated as defect level emission (DLE) band **[2]**.

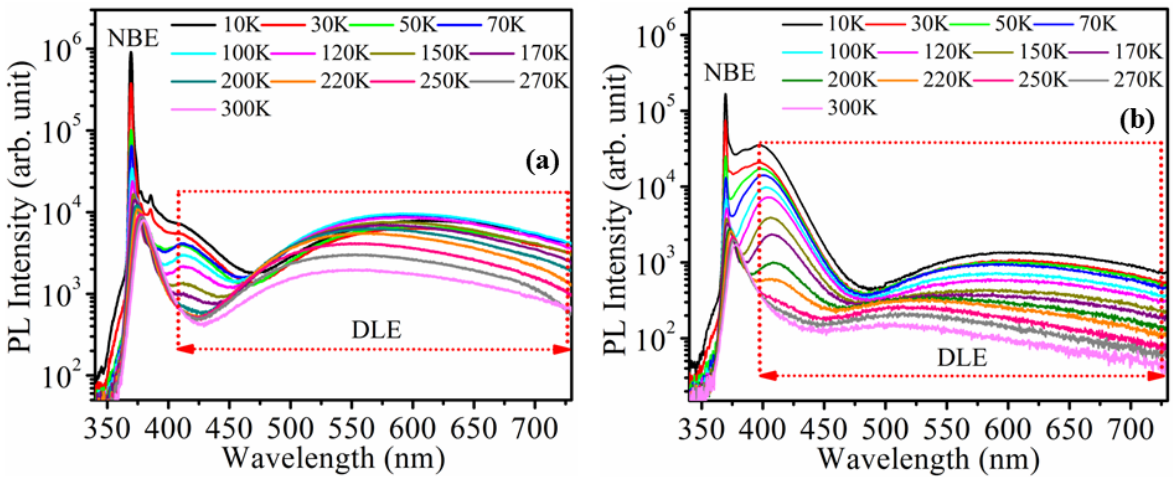

Fig. 5.1 Photoluminescence spectra with temperature (a) x=0.00 and (b) x=0.05 thin films

Unlike room temperature, DLE emission, at low temperature, there is a prominent one additional band, appearing in the blue spectral range which is also related to the defects states.

5.1.1 NBE band in ZnO and AZO films

Figure 5.2 shows the expanded view of NBE band within the range of 340 nm to 400 nm as a function of sample temperature in PLD ZnO thin films. To distinguish the contribution of individual distinct transitions, the spectra were de-convoluted and as an example shown in Fig. 5.2 (b) at a temperature of 10K. The Gaussian fitting of peaks 4 and 5 are displayed separately in inset, Fig. 5.2 (b) for clarity.

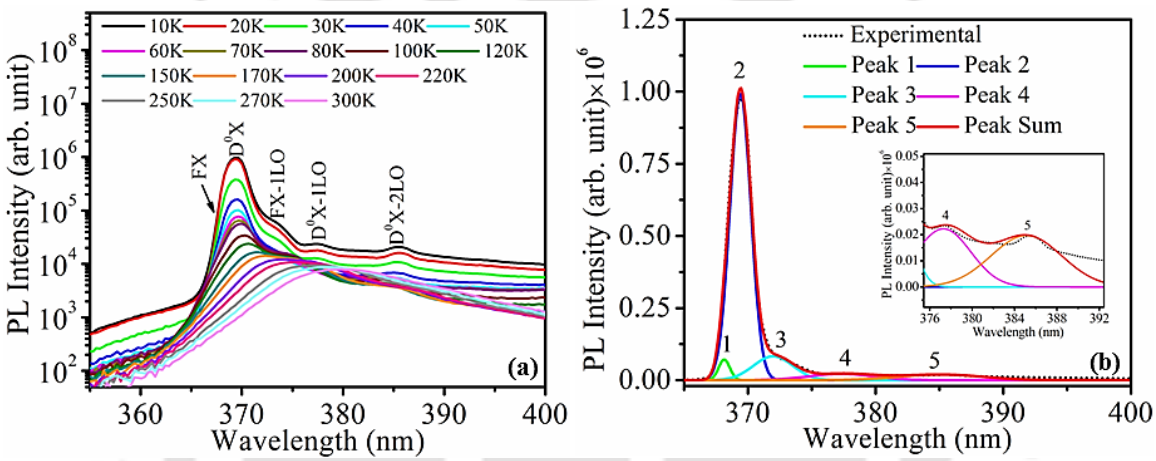

Fig. 5.2 Variation of NBE peak with temperature for (a) pure ZnO film and (b) de-convoluted spectra at 10 K.

At RT, the NBE band in ZnO, Fig. 5.2 (a) is observed to be positioned at 378 nm. This band is the result of the dominating FX transition due to its high exciton binding energy along with overlapping of emission lines due to free exciton (FX), bound excitons (donor bound as well as acceptor bound), exciton complexes etc **[4]**. As the temperature is lowered upto 180K, the emissions for all these excitons start appearing distinctly because of the lower binding energies **[5]**. At 10K, Fig. 5.2 (b), the distinct spectral lines were observed to be positioned at 368 nm (3.370 eV), 369.4 nm (3.356 eV), 373.6 (3.319 eV), 377.3 nm (3.286 eV), and 385.6 nm (3.215 eV) assigned as peak 1, 2, 3, 4 and 5

respectively. The peak 1 having highest energy is the signature peak of free exciton (FX) line of ZnO **[2, 6]**. The most intense peak, peak 2, is the result of the exciton bound to neutral donor and is designated as D^0X line **[2, 6]**. At the shoulder of trailing edge of D^0X line, peak 3, the first longitudinal optical (LO) phonon replica of FX line is observed and assigned as FX-1LO line **[6]**. The other two peaks at lower energy positions, 3.286 eV and 3.215 eV, inset in Fig. 5.2 (b), are due to the longitudinal optical (LO) phonon replicas of D^0X line and are designated as D^0X-1LO and D^0X-2LO respectively having energy separation of 70.7 meV among them **[2]**. Because of the polar nature of ZnO, the coupling between the LO phonons and exciton/bound excitons are very prominent and so, these lines are well resolved at low temperature measurement only **[7]**.

The temperature dependence of all the five peaks of NBE emission lines in ZnO film are shown in Fig. 5.3. The temperature variation of peak positions of FX and D^0X lines clearly shows the decrease in energy with the increase in temperature indicating the

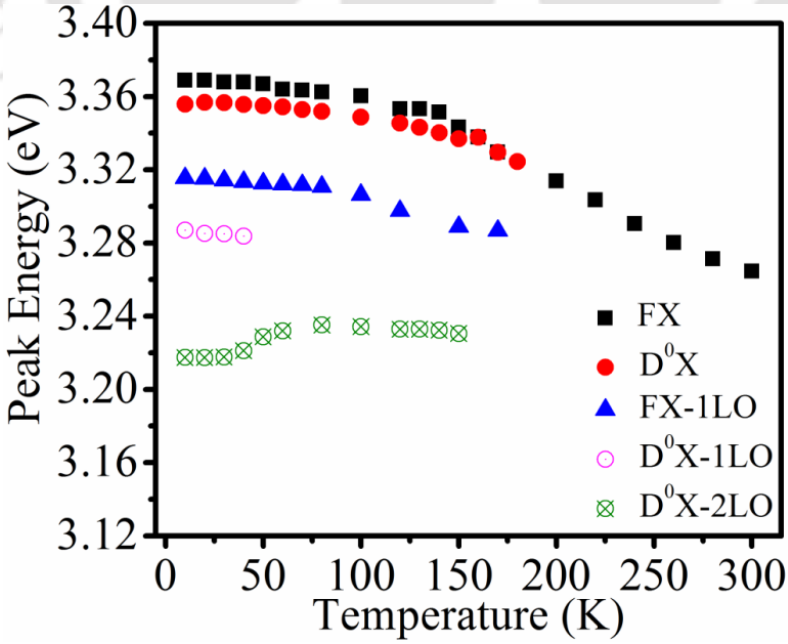

Fig. 5.3 Temperature dependence of NBE lines in ZnO thin film.

excitonic origin of these lines. It is also observed that above 180K, the D^0X line disappears completely. This is due to the dissociation of neutral bound excitons into the free exciton owing to the lower binding energy of later as compared to that of FX **[8, 9]**. The binding energy of D^0X line can be estimated from the difference of the energy positions of FX and D^0X lines **[10]**. In the present case, for ZnO thin film, the binding energy of D^0X line is found to be 15 meV which corresponds to an equivalent temperature of 174.1K. This value is close to the observed value of 180K corresponding to thermal dissociation of D^0X line.

The low temperature photoluminescence (LTPL) spectra of AZO, Fig. 5.1 (b), show a remarkable difference as compared to that of pure ZnO film. The expanded low temperature PL spectra in UV range of 360 to 400 nm for $Zn_{0.95}Al_{0.05}O$ PLD thin film along with a de-convoluted spectrum for 10K temperature (inset) are shown in Fig. 5.4.

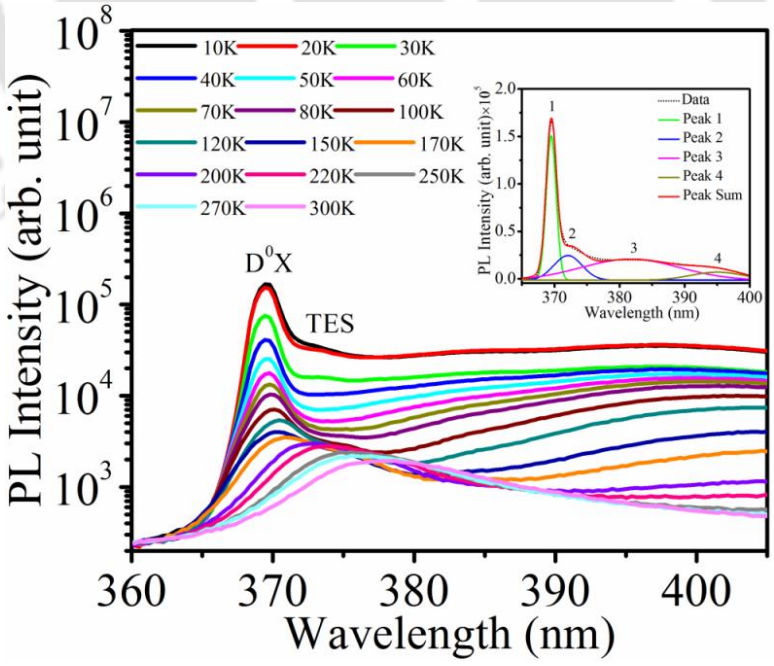

Fig. 5.4 Expanded view of NBE band in $Zn_{0.95}Al_{0.05}O$ thin film.

Unlike bare ZnO thin film, it displays D^0X line as the dominating line. The de-convoluted spectrum, inset Fig. 5.4, depicts three other peaks of very low intensity as compared to that of D^0X line. The peak 2, and 3 positioned at 373.1 nm (3.323 eV) and 381.7 nm (3.248 eV) are due to two electron satellite (TES) and donor acceptor pair (DAP) transitions respectively **[2, 11]**. At the trailing edge of the spectrum, a weak peak at 395 nm (3.139 eV) is due to the radiative recombination of carriers involving Zn_i and valence band (VB) **[12].** These peaks are observed at only very low temperature but at higher temperature this distinct appearance diminishes and as a result broadens the violet-blue band for higher temperature.

The temperature dependent peak position of the excitonic lines is governed by the empirical Varshni's equation given by the equation 5.1 **[3]**:

$$E_g(T) = E_g(0) - \frac{aT^2}{b+T} \tag{5.1}$$

where $E_g(0)$ is the band gap energy at 0K and a and b are the Varshni's thermal coefficients. The coefficient, a, gives the limiting value of $-\frac{dE_g(T)}{dT}$ as $T \rightarrow 0$ K and b is related to the Debye temperature **[13]**.

Figure 5.5 shows the FX line of pure ZnO and D^0X line of AZO, fitted with equation 5.1. The Varshni's thermal coefficients (a and b) and $E_g(0)$ were estimated by fitting the NBE transitions (FX, D^0X, FX-1LO, D^0X-1LO), for ZnO, to Eqn. 5.1 and are listed in table 5.1. The D^0X-2LO line was showing some anomalous behavior and did not follow the equation 5.1 and hence the associated thermal coefficients could not be evaluated.

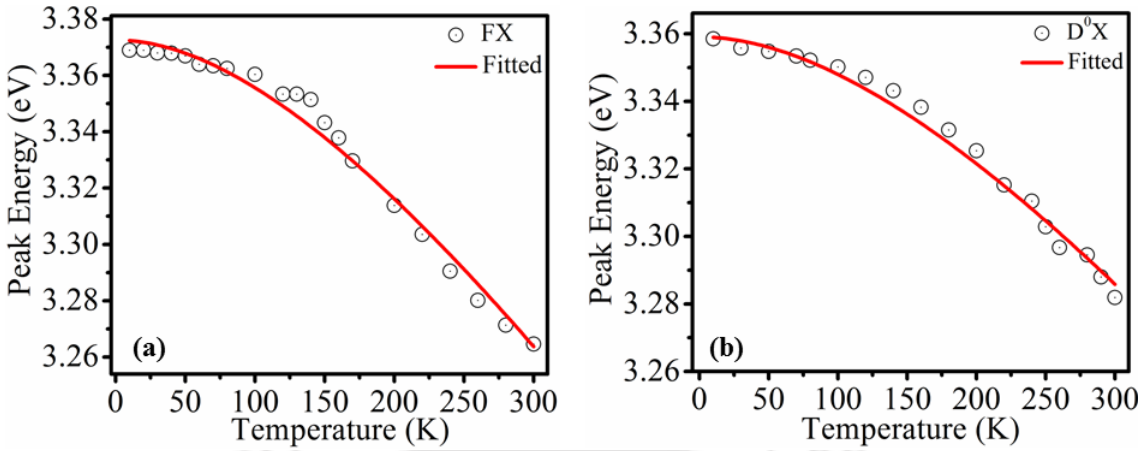

Fig. 5.5 Varshni's equation fitted (a) FX lines in ZnO film and (b) D^0X line in AZO film

Table 5.1 Varshni's thermal coefficients in ZnO thin film.

Sr. No.	Transition	$E_g(0)$ (eV)	a (eV/K)	b (K)
1.	FX	3.372	0.00085	400
2.	D^0X	3.358	0.00053	398
3.	FX-1LO	3.317	0.00060	382
4.	D^0X-1LO	3.287	0.00011	7

The estimated Varshni's thermal coefficients (a and b) for FX, D^0X, FX-1LO and D^0X-1LO are found to be consistent with the earlier reported values **[10, 14]**.

The peak intensities of free FX and D^0X lines follow the Arrhenius equation given below **[15]**:

$$I(T) = \frac{I_0}{A + B\exp(-E_a / k_B T)} \tag{5.2}$$

where, I_0 represents the peak intensity at 0K, A and B are constants, E_a is the activation

energy and k_B is the Boltzman's constant.

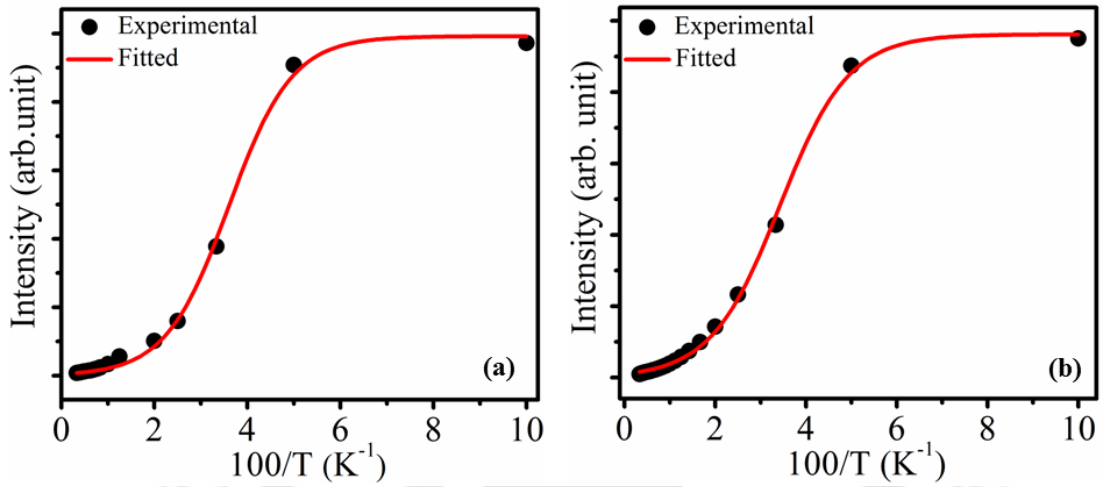

Fig. 5.6 Arrhenius plot of D^0X line in pure ZnO and AZO films.

Figure 5.6 shows the Arrhenius plot for D^0X line for ZnO and AZO (x=0.05) thin film. The estimated Varshni's thermal coefficients and activation energies for dominating D^0X lines in pure ZnO and 5wt% Al doped ZnO are listed in Table 5.2 for comparison.

Table 5.2 Varshni's thermal coefficients and activation energy in ZnO and AZO thin film

Sample (x)	***a* (eV/K)**	***b* (K)**	**E_a (meV)**
ZnO	$0.00053\pm1.8\times10^{-5}$	398	12.69±0.50
AZO (x=0.05)	$0.00060\pm9.8\times10^{-6}$	455	11.34±0.22

The estimated E_a values for D^0X lines in ZnO and AZO thin films are in good agreement with the reported values **[15, 16]**. The value of E_a for AZO thin film is found to be lower as compared to that of pure ZnO. The lower value of E_a for D^0X line in AZO suggests the strong coupling of neutral donor to exciton at low temperature in comparison

to that of ZnO **[16]**. Hence, confirming the complete dominance of D^0X line over all the other lines in AZO.

5.1.2 DLE band in ZnO and AZO films

The low temperature DLE spectra of ZnO as well as AZO films, as shown in Fig.5.1, comprised of two distinct spectral range: blue range (390 to 450 nm) and an extended range of green to red (475 to 720 nm). The enlarge view of PL spectra in the blue spectral range, 380-450 nm, are shown in Fig. 5.7 (a, b).

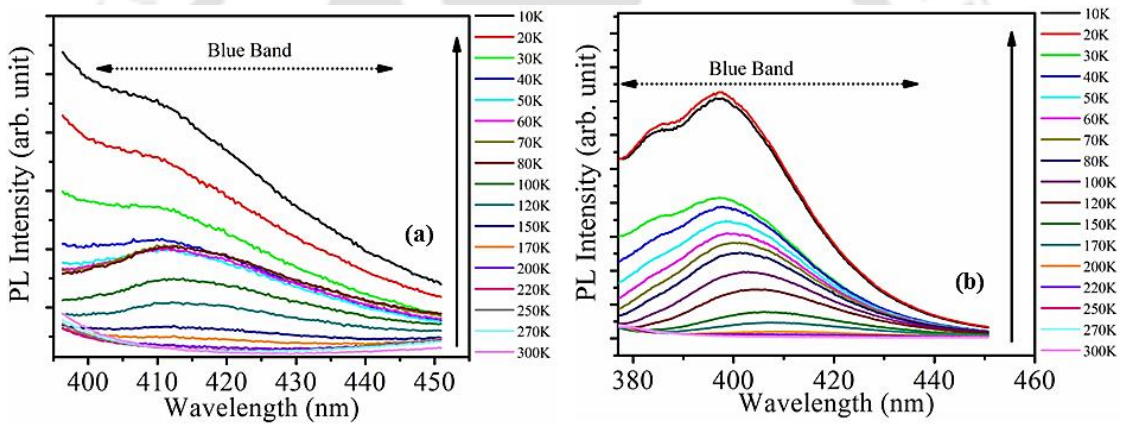

Fig. 5.7 Blue band in (a) ZnO and (b) AZO thin film.

The first defect broad band centered at 411.9 nm (3.010 eV) in ZnO is associated with the radiative recombination involving Zn interstitial (Zn_i) and Zn vacancy (V_{Zn}) within the band gap of ZnO. This band is assigned as 'Blue band'. Intensity of 'Blue band' is comprehensively enhanced in the case of AZO film as compared to that of ZnO film, Fig. 5.7 (b). The position of Zn_i defect is ~0.22 eV below the conduction band and that of V_{Zn} defect is ~3.06 eV **[12]**. The possible transitions for this band could be through two radiative recombination channels comprising Zn_i to VB and CB to V_{Zn} **[12, 17]**. In AZO thin film, the excess Al may force the Zn ions to reside at the interstitial positions

and simultaneously creating the zinc vacancy sites **[17]**. Therefore, the transition involving Zn_i and V_{Zn} defect is increased and results in the enhancement in the Blue band in AZO thin film as compared to that of pure ZnO thin film. It also shows the multiple peaks due to the various closely spaced Zn_i defect levels.

Figure 5.8 (a, b) shows the variation of green-red DLE band and the ratio of peak intensities of DLE to NBE band as a function of sample temperature in pure ZnO thin film respectively. The film shows a gradual red shift with the decrease in the sample temperature.

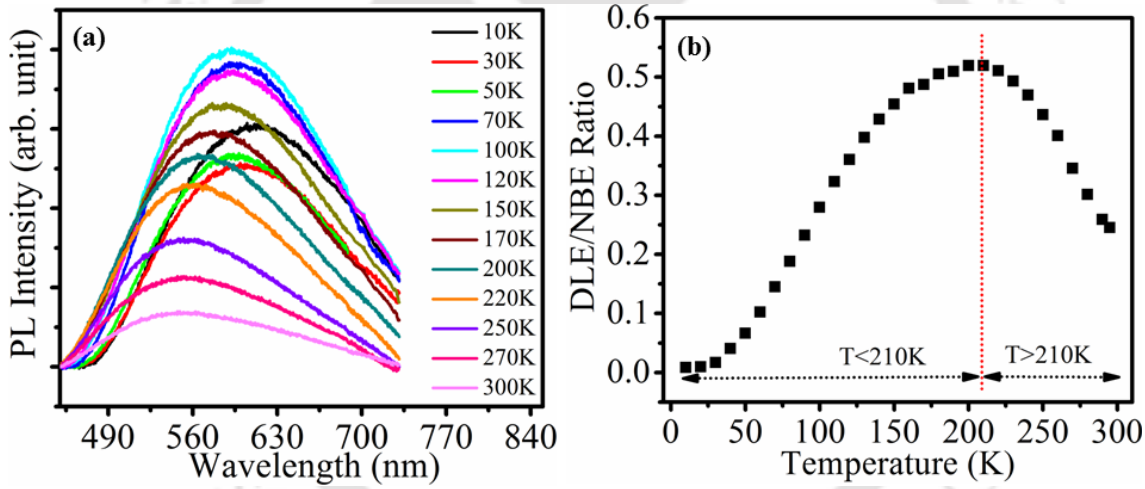

Fig. 5.8 (a) Blue to red and (b) Ratio of intensity of DLE and NBE in pure ZnO thin film.

The variation of the DLE to NBE ratio with temperature in pure ZnO film, Fig. 5.8 (b), exhibits two different regimes. In the temperature range of T<210K, the ratio increases almost linearly with temperature. This normal behavior in the observed variation is due to the thermal quenching of bound excitons and simultaneous involvement of defect states in the film such as V_O, where with increase in temperature, the oxygen vacancies are expected to be increased. In the second region, T>210K, the

anomalous behavior could be due to the negative thermal quenching effect **[18]**.

Figure 5.9 shows the variation of the DLE peak position and Peak intensity in ZnO and AZO thin film with temperature. Both the films showed a gradual red-shift in the DLE peak position with lowering of the sample temperature. Pure ZnO film exhibits a red shift from 545 nm (2.275 eV) to 607 nm (2.043 eV) while AZO thin film shows a red shift from 505 nm (2.455 eV) to 600 nm (2.067 eV) with the reduction in the sample

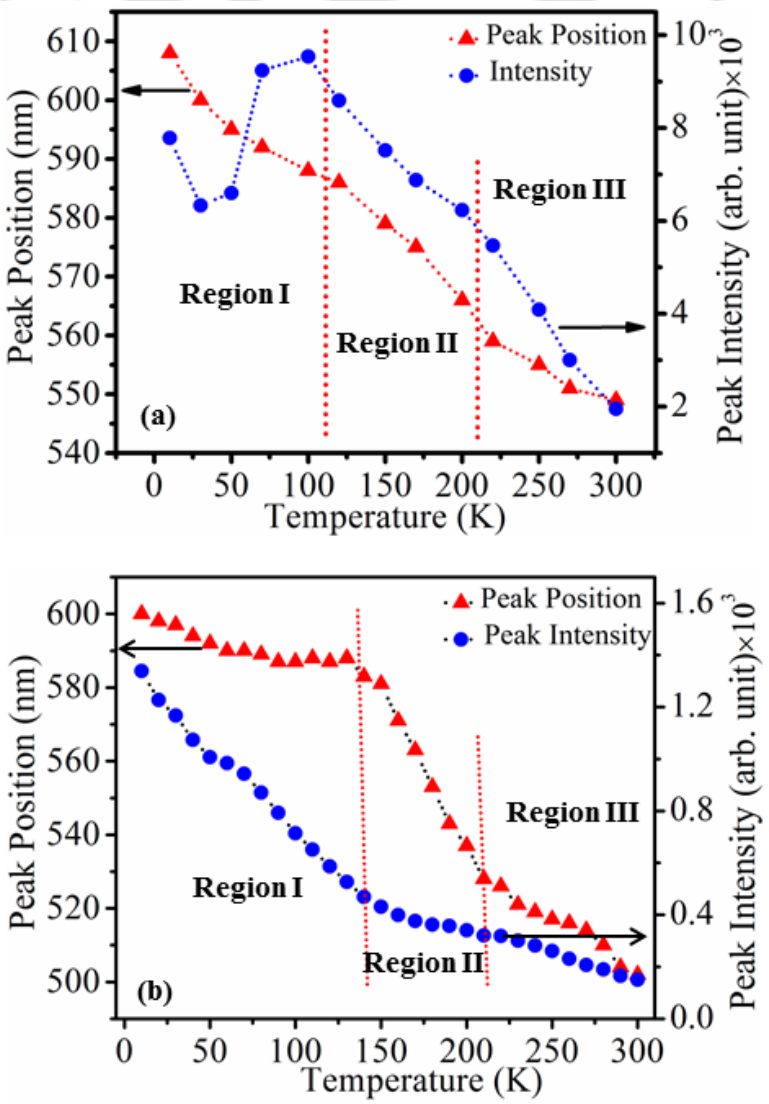

Fig. 5.9 Variation of DLE peak position and intensity in (a) x=0.00 and (b) x=0.05 thin film.

temperature from 300K to 10K. The red shift with the temperature in the visible PL band in the film is linked to confinement of carriers at defect centers **[19]**. The peak intensities are observed to be gradually increased with the decrease in the sample temperature. This could be due to the reduction in the non-radiative recombination with the decrease in the temperature.

The green DLE emission involving V_O states can be divided into three different range of temperature, Fig. 5.9, and can be explained with the help of energy level diagram describing all the transitions associated with the ZnO and AZO thin film displayed in Fig. 5.10. At low temperature, region I, the radiative recombination channel is from the bottom of the extended Zn_i states to V_O. Since at very low temperature (10-130K), all the excited electrons can relax to lowest of Zn_i states so, a radiative recombination of e-h pair results in low energy emission. In the region II, temperature range of 120K-210K, the trapped electrons at the Zn_i site get sufficient thermal energy and occupy the higher extended Zn_i states. Hence, a recombination from these excited states of Zn_i to holes at the V_O state, results in the emission of photons of relatively higher energy. In the higher temperature range of 210K-300K, region III, the electrons trapped in the higher excited states of Zn_i can further move to conduction band minima. Therefore, the radiative recombination of conduction band electrons to the holes at the V_O site, results in higher energy emission (lower wavelength). There is also the possibility of alternative route to the green band emission involving V_O as shown in Fig. 4.15, Chap. 4, and also reported in literatures particularly at room temperature **[20-22]** via radiative recombination involving intrinsic V_O and VB. This will happen if V_O is lying more close to CB rather than VB. The actual position of V_O defect is still under controversy and has a large span within the band gap of ZnO **[23-26]**.

The AZO thin film shows slightly different temperature dependence of the DLE band in all the three regions as compared to that of pure ZnO film, Fig. 5.9 (a, b). In region I and III, the rate of change of DLE peak position with Temperature is more in ZnO as compared to AZO thin film while in region II, the AZO film shows relatively faster change as compared to that of ZnO. These transitions involve V_O defects and as described in Sec. 3.6, Chap. 3, the V_O defect are reduced in AZO compared to ZnO therefore radiative recombination is terminated to VB rather than V_O.

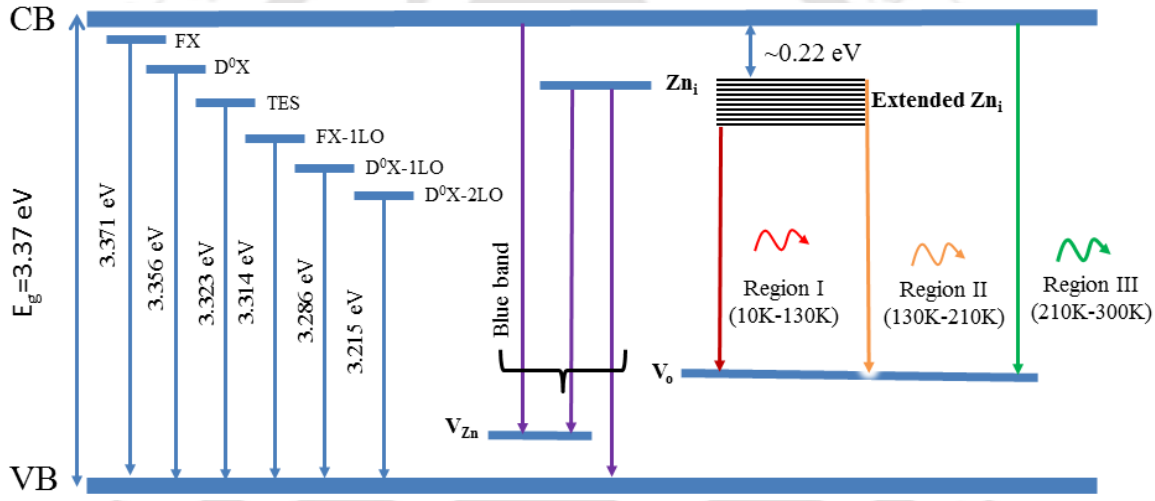

Fig. 5.10 Energy level diagram of NBE and DLE bands in the films.

5.2 Low temperature photoluminescence spectra of $Zn_{1-x}Ti_xO$ (0≤x≤0.050) thin films

The low temperature photoluminescence spectra of $Zn_{1-x}Ti_xO$ (0.010≤x≤0.050) thin films are shown in Fig. 5.11 along with pure ZnO (repeated) for comparison. Similar to the pure ZnO as well as AZO, the $Zn_{1-x}Ti_xO$ (TZO) thin films also exhibit both NBE as well as DLE emission bands at low temperature.

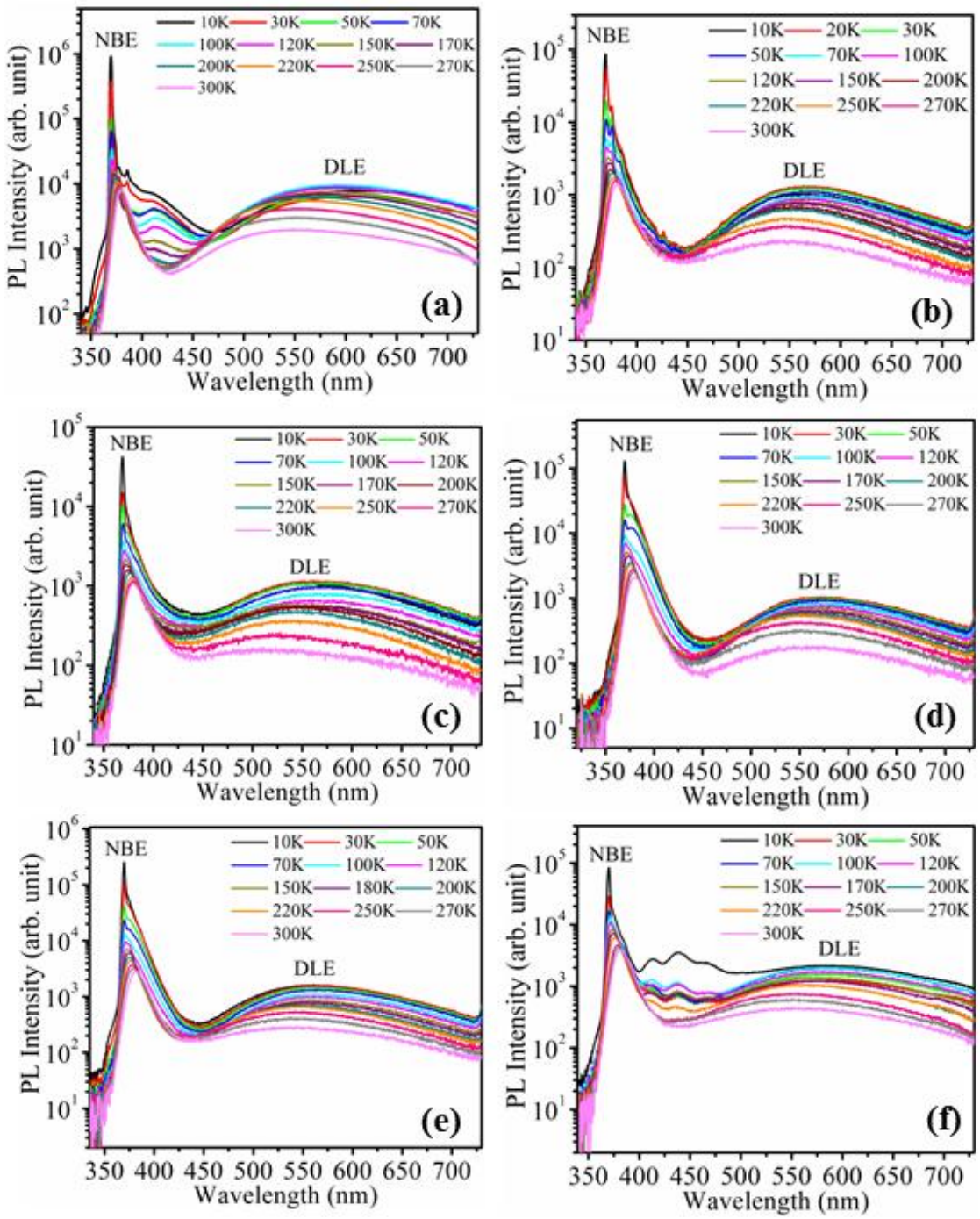

Fig. 5.11 Low temperature PL spectra of $Zn_{1-x}Ti_xO$ (a) x=0.000, (b) x=0.005, (c) x=0.010, (d) x=0.020, (e) x=0.030 and (f) x=0.050 thin films.

5.2.1 NBE band in TZO thin films

The expanded spectra of NBE bands in TZO thin films in the spectral range of 350 to 400 nm, are shown in Fig. 5.12 (a-e).

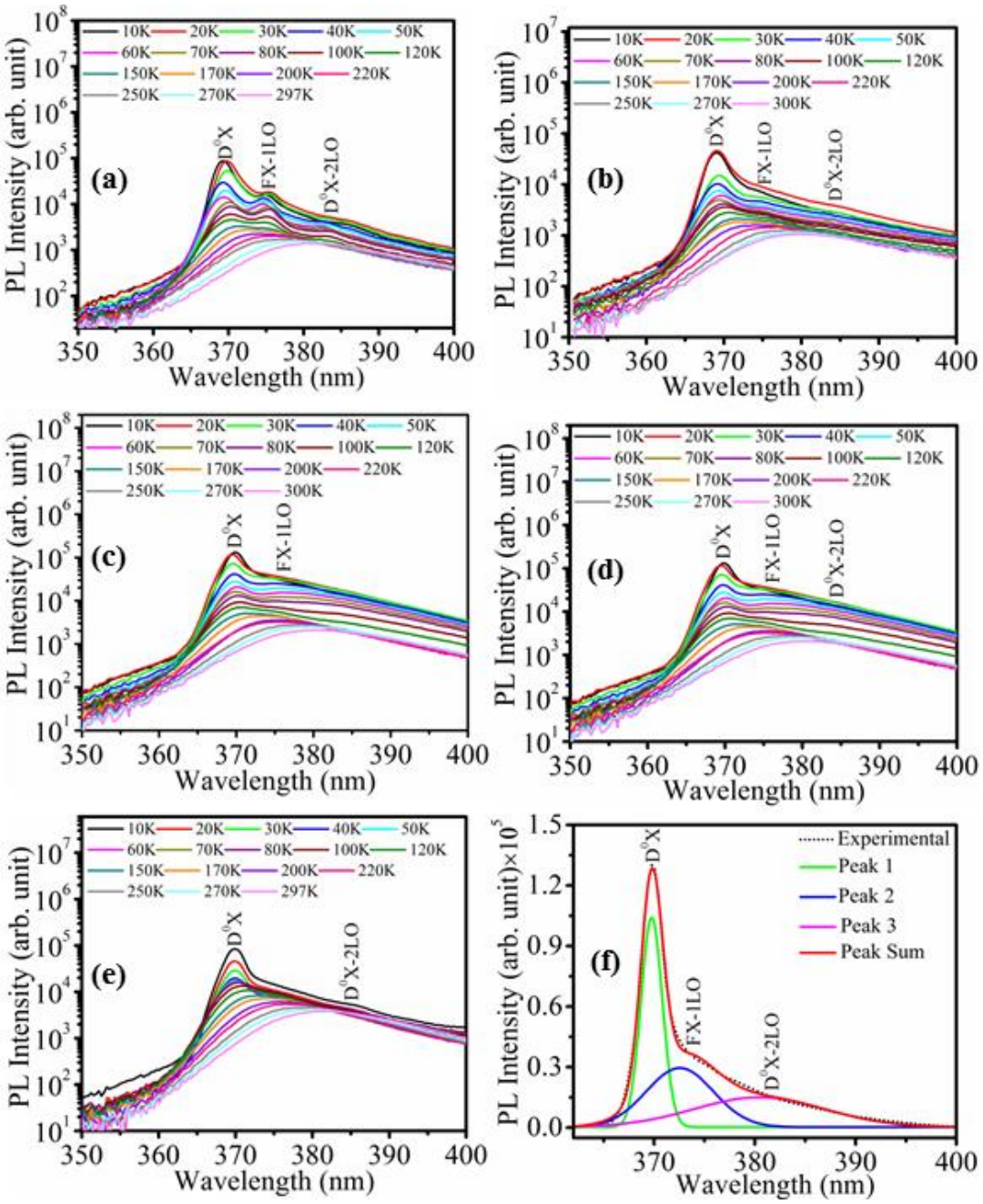

Fig. 5.12 NBE band in $Zn_{1-x}Ti_xO$ (a) x=0.005, (b) x=0.010, (c) x=0.020, (d) x=0.030, (e) x=0.050 and (f) de-convoluted spectra for x=0.020 thin film.

These spectra are comprised of dominating D^0X lines in all the samples. Unlike AZO thin film, the TZO films exhibit additional line at 375.6 nm (3.301 eV) which is at a separation of ~70 meV from the position of FX line and assigned as FX-1LO line **[6]**. Additionally, at an energy separation of ~140 meV from the D^0X line, a very faint line was observed corresponding to D^0X-2LO line. Unlike pure ZnO, the first longitudinal optical phonon replica of D^0X, D^0X-1LO, line was not observed in TZO thin films. As the Ti concentration is increased beyond x=0.010, the D^0X-2LO line was completely disappeared and the NBE spectra were dominated by D^0X and FX-1LO only.

The dominating D^0X line as observed in TZO samples were subjected to the equation 5.1 for estimation of Varshni thermal coefficients (*a*, *b*). The estimated values of *a* and *b* were plotted as a function of Ti concentration and is shown in Fig. 5.13.

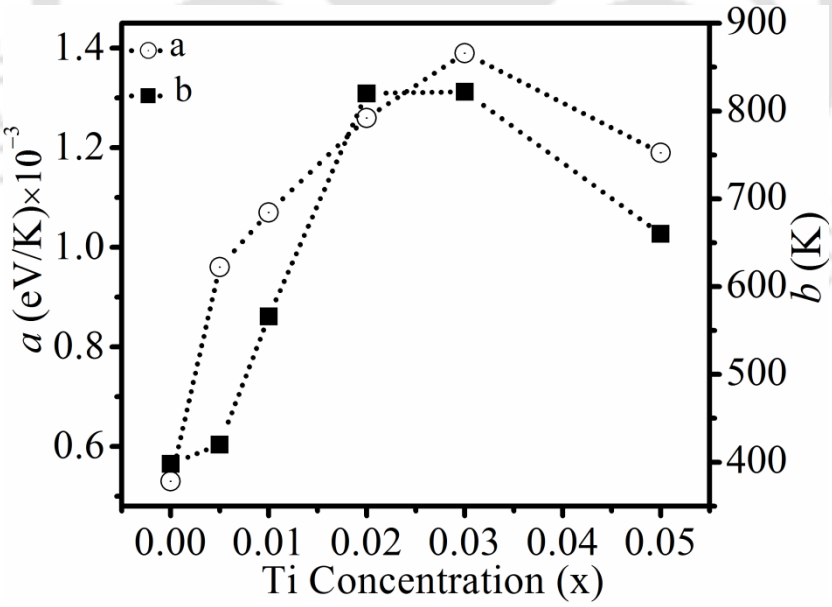

Fig. 5.13 Variation of Varshni's thermal coefficients (*a* and *b*) with Ti concentration.

Both the Varshni's thermal coefficients, *a* and *b*, are observed to be increased with Ti concentration till x=0.020 thereafter there is a slight decrease in these values. The

larger '*a*' value signifies the greater rate of change of peak position with temperature which consequently affects the thermal dissociation structure of D^0X **[16]**.

The activation energy of D^0X line in TZO thin films was obtained by fitting the plot of D^0X intensity vs 100/T using eqn 5.2. Figure 5.14 depicts the variation of the estimated activation energies with Ti concentration. The low activation energy in TZO thin film as compared to pure ZnO signifies the existence of D^0X emission at low temperature in much more pronounced way as compared to that of pure ZnO.

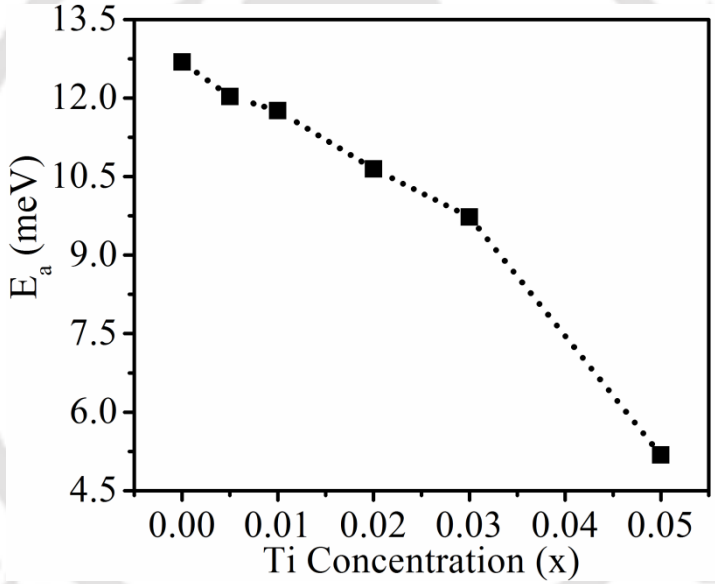

Fig. 5.14 Variation of E_a with Ti concentration.

5.2.2 DLE band in TZO thin films

The blue band in TZO thin films behaves differently as compared to AZO film. At low Ti content, there is hardly any signature of blue emission, Fig. 5.11. In contrast, the NBE emission gets broadened because of the increase in the point defects responsible for blue emission. At the maximum Ti concentration (x=0.050), there is an evolution of three distinct bands in the spectral range of 400-485 nm, Fig. 5.11 (f). These lines in 5wt%

TZO thin film could be due to the structural defects. As seen in the spectrum, Fig 4.1, Chap. 4, the crystalline quality of this particular film was worst (polycrystalline) thus,

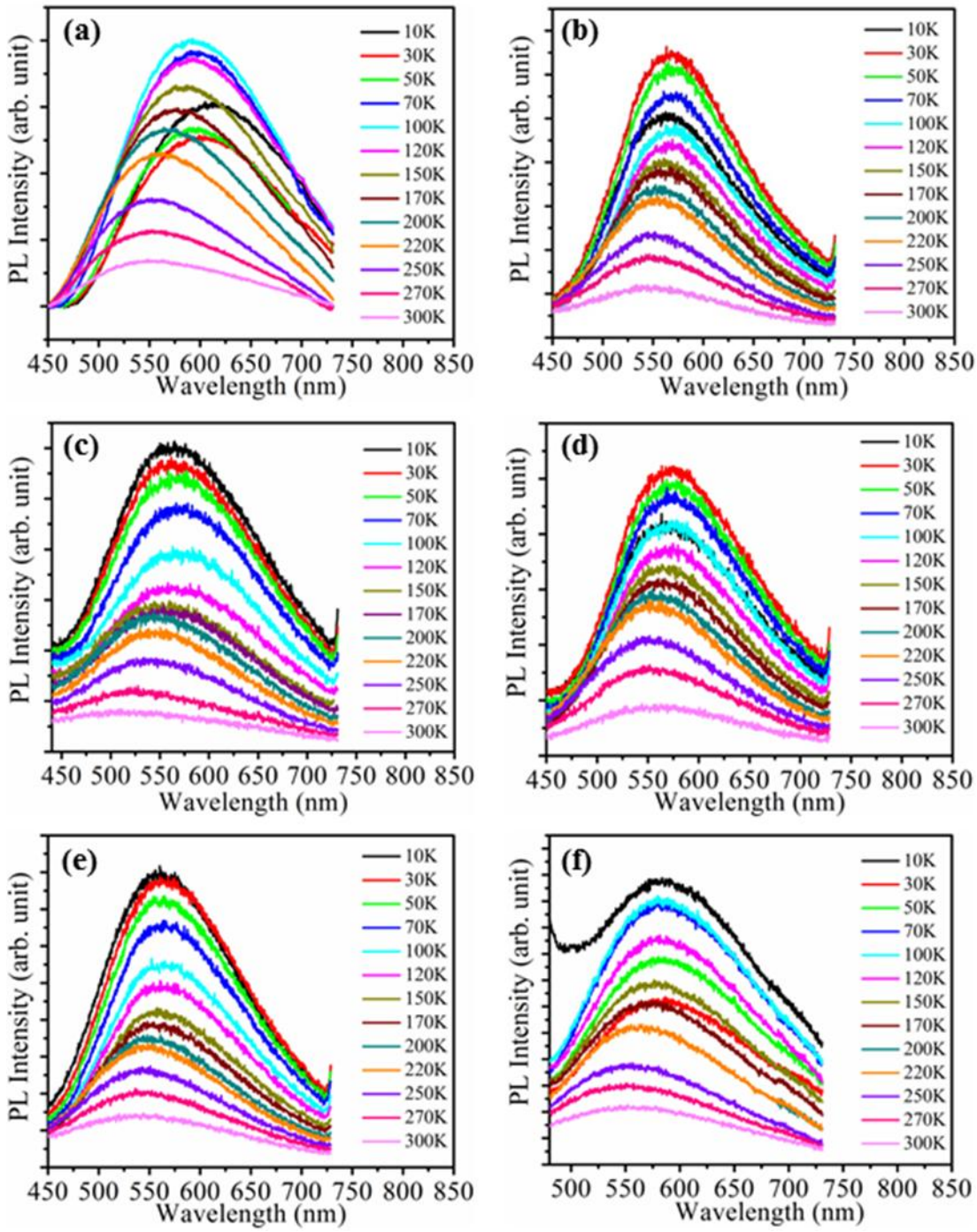

Fig. 5.15 DLE band in $Zn_{1-x}Ti_xO$ (a) x=0.000, (b) x=0.050, (c) x=0.010, (d) x=0.020, (e) x=0.030 and (f) x=0.05 thin films.

possibility of structural defects is quite obvious in the film. The second DLE band in TZO thin film in the spectral range of 450 nm to 720 nm, is shown in Fig. 5.15 along with that of pure ZnO (represented for comparison).

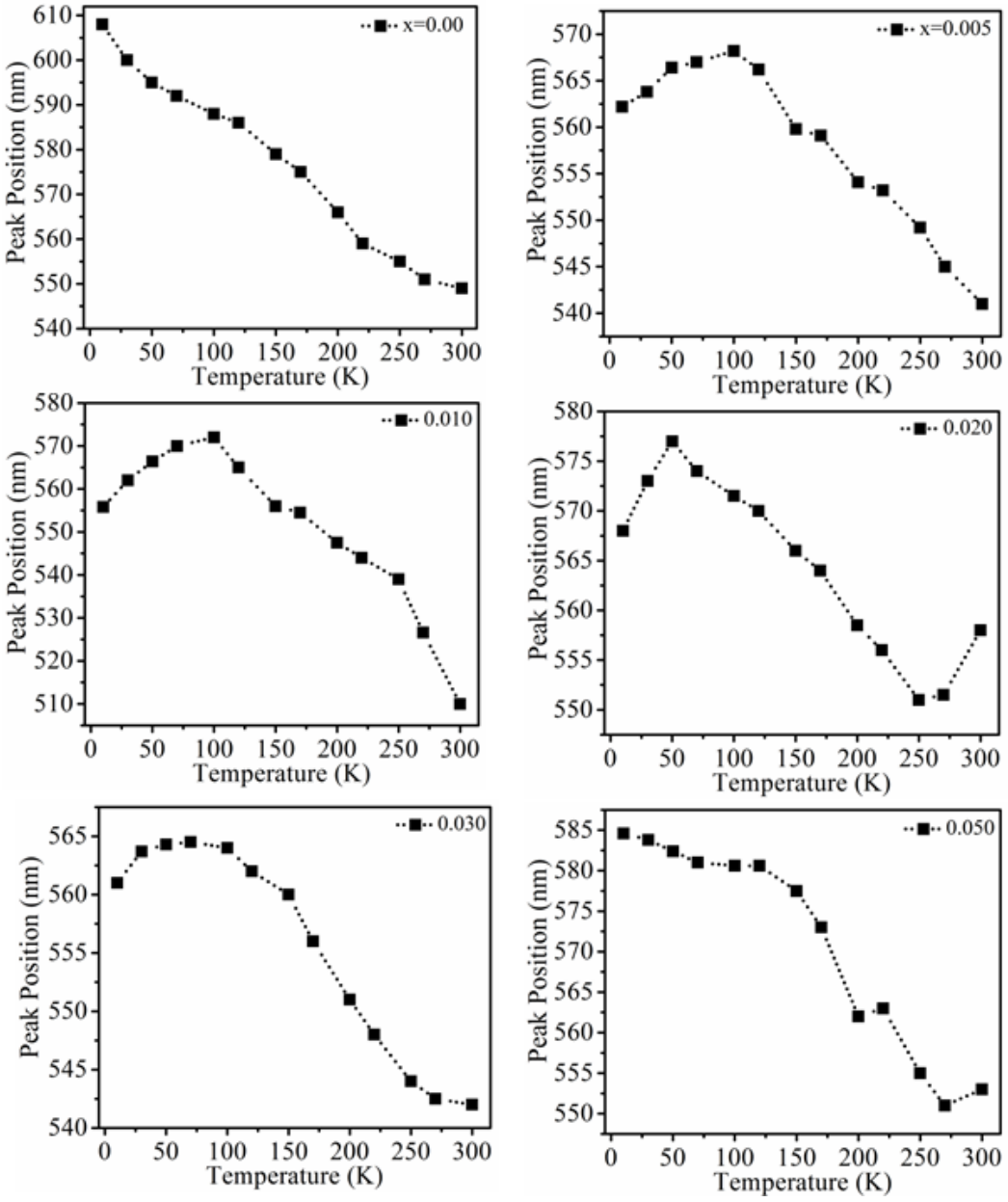

Fig. 5.16 Variation of DLE peak position with temperature in TZO thin films.

Figure 5.16 displays the variation of DLE peak position as a function of sample temperate in TZO thin films. At room temperature and slightly below till ~100K, TZO

samples exhibit the similar trend of red shift with the decrease in temperature as that of ZnO. But at low temperature range (T=10K to 100K), it is primarily due to the incorporation of Ti in the system which may favor additional non-radiative channels, prevents the usual variation and exhibit the blue shift (but for x=0.05) with the decrease in temperature. In TZO thin films, the rate of change of variation of DLE peak with T is observed to be lower as compared to that of pure ZnO film.

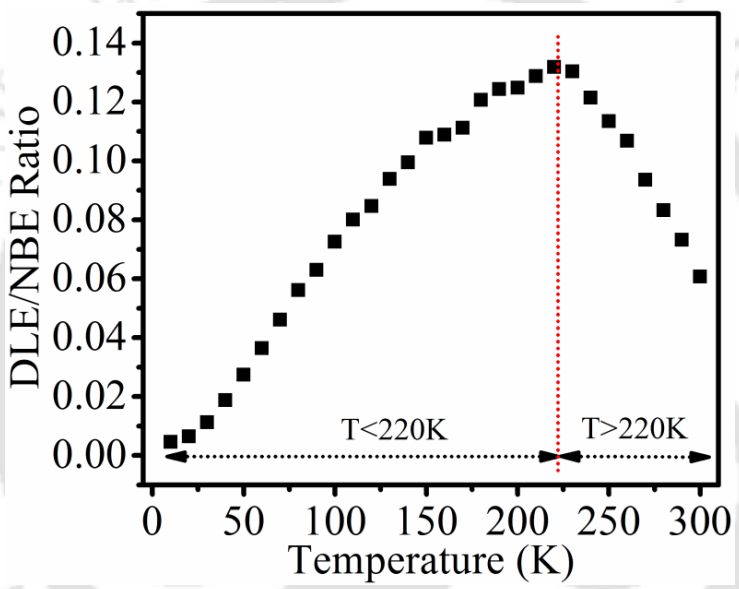

Fig. 5.17 Plot of ratio of DLE to NBE peak intensities in x=0.02 thin film.

The plot of ratio of DLE and NBE peak intensity in the case of x=0.02 sample is shown in Fig. 5.17. There are two temperature windows similar to ZnO, where the variation in the DLE/NBE ratio is different. In the temperature regime, T<220K, the ratio shows nearly a linear increase with the temperature which is due to the increase in the rate of radiative recombination at lower temperatures while beyond T>220K, this trend gests reversed. At a temperature of T=220K, this ratio is maximum signifying the dominance of defect associated emission around this temperature. Hence, temperature has a significant role in transfer of the energy from CB to defects states in the films. In both, the low

temperature (10K) as well as high temperature (300K), the lower values of DLE/NBE suggest the complete dominance of NBE emission over DLE emission. The complete quenching of DLE emission at room temperature in TZO thin film at x=0.02 has also been discussed, Fig. 4.11, Sec. 4.7, Chap. 4 where the sample was excited with 320 nm of Xenon lamp and thus comparison with Fig. 5.8 (b) and 5.17 (with a different excitation wavelength of 325 nm) further confirms this behavior.

5.3 Conclusion

The temperature dependent photoluminescence spectra of pulsed laser deposited $Zn_{1-x}Al_xO$ (x=0.00 and x=0.05) and $Zn_{1-x}Ti_xO$ (0≤x≤0.050) thin films are presented in this chapter. The pure ZnO film showed well separated FX, D^0X, FX-1LO, D^0X-1LO, D^0X-2LO lines in the NBE band (360-400 nm) within low temperature range, 10K-180K. In the temperature range of 180K to 300K all the individual lines were merged together and broadened the NBE emission and finally at RT, the band was observed to be completely dominated by FX recombination. On contrary, the NBE bands of AZO as well as TZO thin films were observed to be dominated by D^0X line. The AZO film showed weak signature of TES as well as DAP transitions while TZO film showed LO phonon replicas of FX and D^0X lines along with dominating D^0X line. No clear signature of FX line in low temperature range was observed in the presence of impurities. The AZO films showed a broad blue emission band which was due to the presence of Zn_i and V_{Zn} defects in the film. Unlike AZO, the blue band was absent in TZO film for low Ti concentration (upto x=0.030). The higher Ti content (x=0.050), this band was observed to be appearing distinctly. The estimated '*a*' and '*b*' values in TZO thin films from Varshni's equation for dominating D^0X line were observed to be increased in presence of TZO as compared to

that of pure ZnO film. The activation energies for thermal dissociation were estimated using single channel Arrhenius equation and were found to be decreased in AZO as well as TZO thin film as compared to that of pure ZnO film.

Bibliography

[1] Magnus Willander et al., "*Progress on one-dimensional zinc oxide nanomaterials based photonic devices",* Nanophotonics, **1** (2012).

[2] Hadis Morkoc and Umit Ozgur, "*Zinc Oxide: Fundamentals, Materials and Device Technology",* Wiley-VCH, 2009.

[3] Y. P. Varshni, "*TEMPERATURE DEPENDENCE OF THE ENERGY GAP IN SEMICONDUCTORS",* Physica, **34** (1967) 149-154.

[4] Bingqiang Cao et al., "*Different ZnO Nanostructures Fabricated by a Seed-Layer Assisted Electrochemical Route and Their Photoluminescence and Field Emission Properties",* Journal of Physical Chemistry C, **111** (2007) 2470-2476.

[5] D. C. Reynolds et al., "*Neutral-donor–bound-exciton complexes in ZnO crystals",* Physical Review B, **57** (1998) 12151-12155.

[6] U. Ozgur et al., "*A comprehensive review of ZnO materials and devices",* Journal of Applied Physics, **98** (2005) 041301.

[7] Sang-heon LEE et al., "*Temperature-dependent photoluminescence of ZnO thin films deposited by using the sol-gel dip-coating method",* Journal of the Korean Physical Society, **61** (2012) 1171-1176.

[8] D. W. Hamby et al., "*Temperature dependent exciton photoluminescence of bulk ZnO",* Journal of Applied Physics, **93** (2003) 3214-3217.

[9] Qingjiang Yu et al., "*Fabrication and Optical Properties of Large-Scale ZnO Nanotube Bundles via a Simple Solution Route*", Journal of Physical Chemistry C, **111** (2007) 17521-17526.

[10] Yueh-Chien Lee et al., "*Temperature-Dependent Excitonic Luminescence in ZnO Thin Film Grown by Metal Organic Chemical Vapor Deposition",* Japanese Journal of Applied Physics, **48** (2009) 112302.

[11] A. Teke et al., "*Excitonic fine structure and recombination dynamics in single-crystalline ZnO",* Physical Review B, **70** (2004) 195207.

[12] Cheol Hyoun Ahn et al., "*A comparative analysis of deep level emission in ZnO layers deposited by various methods",* Journal of Applied Physics, **105** (2009) 013502.

[13] Dushyant. Kushavah et al., "*Photoluminescence characteristics of CdSe quantum dots: role of exciton–phonon coupling and defect/trap states",* Materials Research Express, **4** (2017) 075007.

[14] D. Sentosa et al., "*Temperature dependent photoluminescence studies of ZnO thin film grown on (111) YSZ substrate",* Journal of Crystal Growth, **319** (2011) 8-12.

[15] V. Sh. Yalishev et al., "*Study of the photoluminescence emission line at 3.33 eV in ZnO films",* Journal of Applied Physics, **112** (2012) 013528.

[16] A. B. M. A. Ashrafi, et al., "*Temperature-dependent photoluminescence of ZnO layers grown on 6H-SiC substrates",* Journal of Applied Physics, **95** (2004) 7738-7741.

[17] Gyan Prakash Bharti and Alika Khare, "*Single and multiphoton absorption induced photoluminescence in pulsed laser deposited $Zn_{1-x}Al_xO(0≤x≤0.10)$ thin films",* Journal of Luminescence, **197** (2018) 135-141.

[18] Yukun Wu et al., "*Negative thermal quenching of photoluminescence in annealed ZnO–Al_2O_3 core–shell nanorods",* Physical Chemistry Chemical Physics, **17** (2015) 5360-5365.

[19] Bingqiang Cao et al., "*Temperature-dependent shifts of three emission bands for ZnO nanoneedle arrays",* Applied Physics Letters, **88** (2006) 161101.

[20] Linhua Xu et al., "*Realization of strong violet and blue emissions from ZnO thin films by incorporation of Cu ions",* Materials Research Bulletin, **99** (2018) 144-151.

[21] Sanjaya Brahma et al., "*Self-assembled ZnO nanoparticles on ZNO microsheet: ultrafast synthesis and tunable photoluminescence properties*", Journal of Physics D: Applied Physics, 4**8** (2015) 225305

[22] Qiang Shi et al., "*Enhancing blue luminescence from Ce-doped ZnO nanophosphor by Li doping",* Nanoscale Research Letters, **9** (2014) 480.

[23] Lukas Schmidt-Mende et al., "*ZnO – nanostructures, defects, and devices",* Materials Today, **10** (2007) 40-48.

[24] Sesha Vempati et al., "*One-step synthesis of ZnO nanosheets: a blue-white fluorophore",* Nanoscale Research Letters, **7** (2012) 470.

[25] J. Cizek et al., "*Origin of green luminescence in hydrothermally grown ZnO single crystals",* Applied Physics Letters, **106** (2015) 251902.

[26] Igor Beinik et al., "*Photoresponse from single upright-standing ZnO nanorods explored by photoconductive AFM",* Beilstein Journal of Nanotechnology, **4** (2013) 208-217.

Chapter 6

Nonlinear absorption and refractive index coefficients and multiphoton absorption induced photoluminescence in $Zn_{1-x}Al_xO$ ($0 \le x \le 0.10$) and $Zn_{1-x}Ti_xO$ ($0 \le x \le 0.050$) thin films

Nonlinear optics is the interaction of light with the mater under high intense optical field. It plays a key role in visualizing some of the spectacular optical phenomenon such as optical phase conjugation, optical parametric oscillation, optical harmonic generation, optical switching, optical limiting etc. **[1-3]**. The efficiency of these phenomenon depends on the strength of the nonlinear optical (NLO) coefficients; nonlinear absorption coefficient, nonlinear refractive index and nonlinear optical susceptibility. The NLO coefficients are measured via various measurement techniques such as nonlinear interferometry, ellipse rotation, degenerate waves mixing, harmonic generation, z-scan etc **[4-9]**. Among these, the z-scan technique is relatively simple and sensitive technique for estimation of NLO coefficients. This technique is based on the beam distortion imposed by the optical nonlinearity within the sample.

ZnO, being of hexagonal wurtzite crystal structure, is seen as an excellent candidate towards nonlinear optical (NLO) response. The NLO coefficient in ZnO can be comprehensively enhanced with impurity because of the increase in oscillator strength and de-localized electron cloud in the composite system. The *n*-type doped semiconductors have shown a remarkable improvement in the NLO coefficients of ZnO. The common impurity elements reported in host ZnO enhancing the NLO coefficients are Mn, Mg, Er, Ni etc **[10-13]**. Aluminum (Al) and titanium (Ti) are also suitable dopants in ZnO for improvement in the third order NLO coefficients because of the enhanced

conductivity as a result of increased free carrier concentration **[8]**. In majority of the reports, the NLO coefficients measured in doped ZnO is under pulsed laser illumination. ZnO. However, under continuous wave (cw) illumination, there are very limited numbers of reports in doped ZnO. Therefore, for the measurement of NLO coefficients in pure ZnO as well as Al and Ti doped ZnO thin films were performed by z-scan measurement under cw He:Ne laser illumination.

In this chapter, measurements on third order nonlinear optical coefficients in the pulsed laser deposited (PLD) thin films of $Zn_{1-x}Al_xO$ ($0 \le x \le 0.10$) and $Zn_{1-x}Ti_xO$ ($0 \le x \le 0.050$) by modified Z-scan technique are reported. The modified Z-scan experimental setup has been briefly discussed in Sec. 2.5, Chap. 2. The experimental parameters used for the estimation of NLO coefficients are also detailed in section 2.5, chapter 2. The thin films were also subjected to multiphoton absorption induced photoluminescence characterization under cw He:Ne laser excitation. The experimental setup employed for this has been described in section 2.6, chapter 2.

6.1 Nonlinear absorption and refractive index coefficients for $Zn_{1-x}Al_xO$ ($0 \le x \le 0.10$) PLD thin films

Figure 6.1 shows the normalized open aperture z-scan plot for $Zn_{1-x}Al_xO$ ($0 \le x \le 0.10$) thin films along with the data fitted to Eqn. 2.1, Chap. 2. The error bars in the data points are the standard deviations calculated over 10 images for each location of z. All the films exhibit a transmittance minima at z=0 in the spectra, suggesting the reverse saturation absorption (RSA) behavior. In the present z-scan experiment, under the cw laser illumination (λ=632.8 nm), the dominant process for the nonlinear absorption could

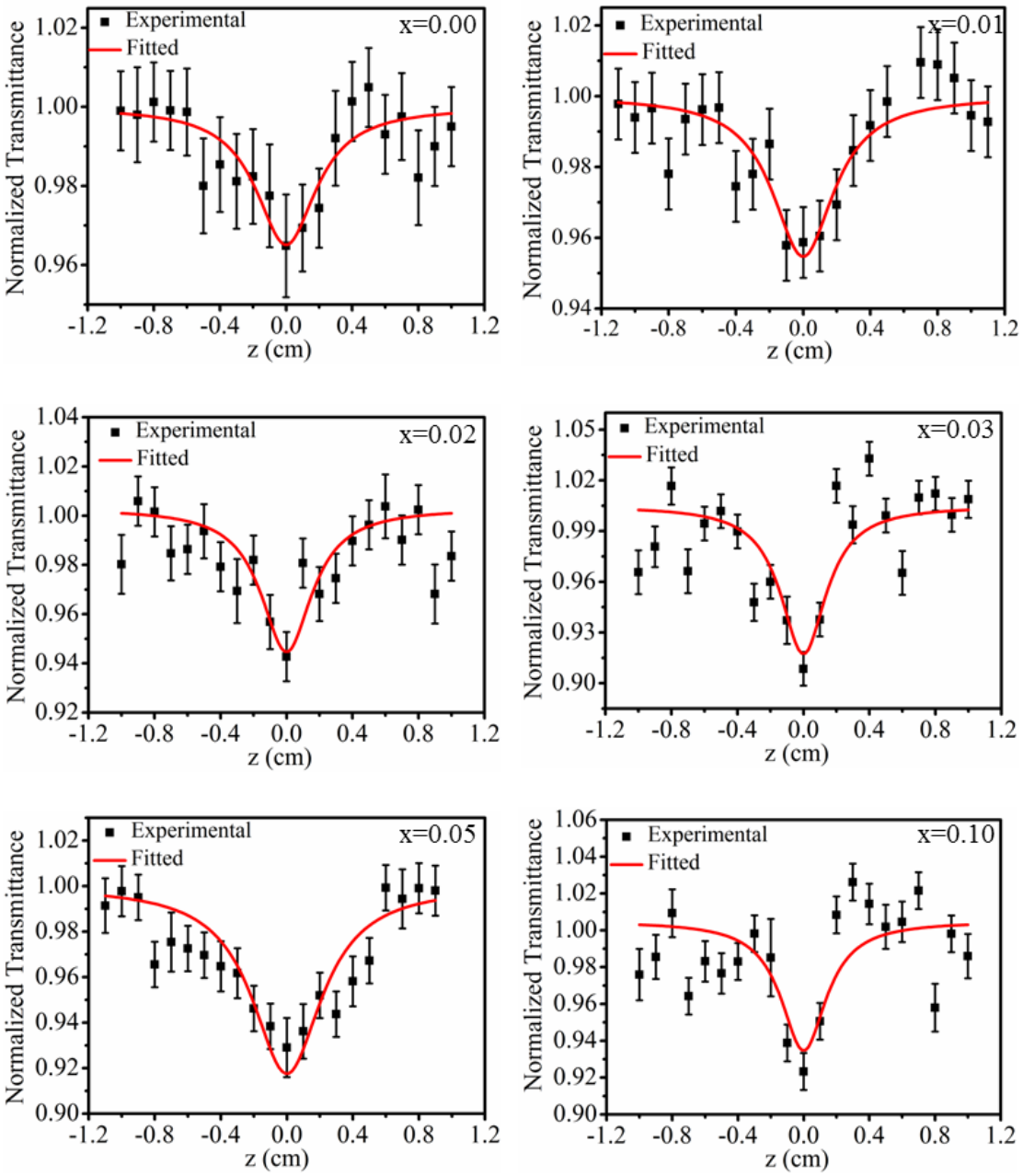

Fig. 6.1 Open aperture z-scan curves for $Zn_{1-x}Al_xO$ ($0 \le x \le 0.10$) thin films.

be due to FCA which depends on wavelength as factor λ^p, where $p>1$. The value of p lies in the range of $1.5 \le p \le 3.5$ **[14]**. However, a contribution from the two photon absorption process (TPA) cannot be neglected as the pump photon energy (hv=1.92 eV) is more than half of the band gap energy of AZO films **[15, 16]**.

Figure 6.2 shows the closed aperture (CA) z-scan graphs of $Zn_{1-x}Al_xO$ ($0 \le x \le 0.10$) thin films along with data fitted to Eqn. 2.2, Chap. 2. A pre-focal transmittance maxima followed by a post focal minima in the CA graphs indicate the negative nonlinear (Δz_{p-v})

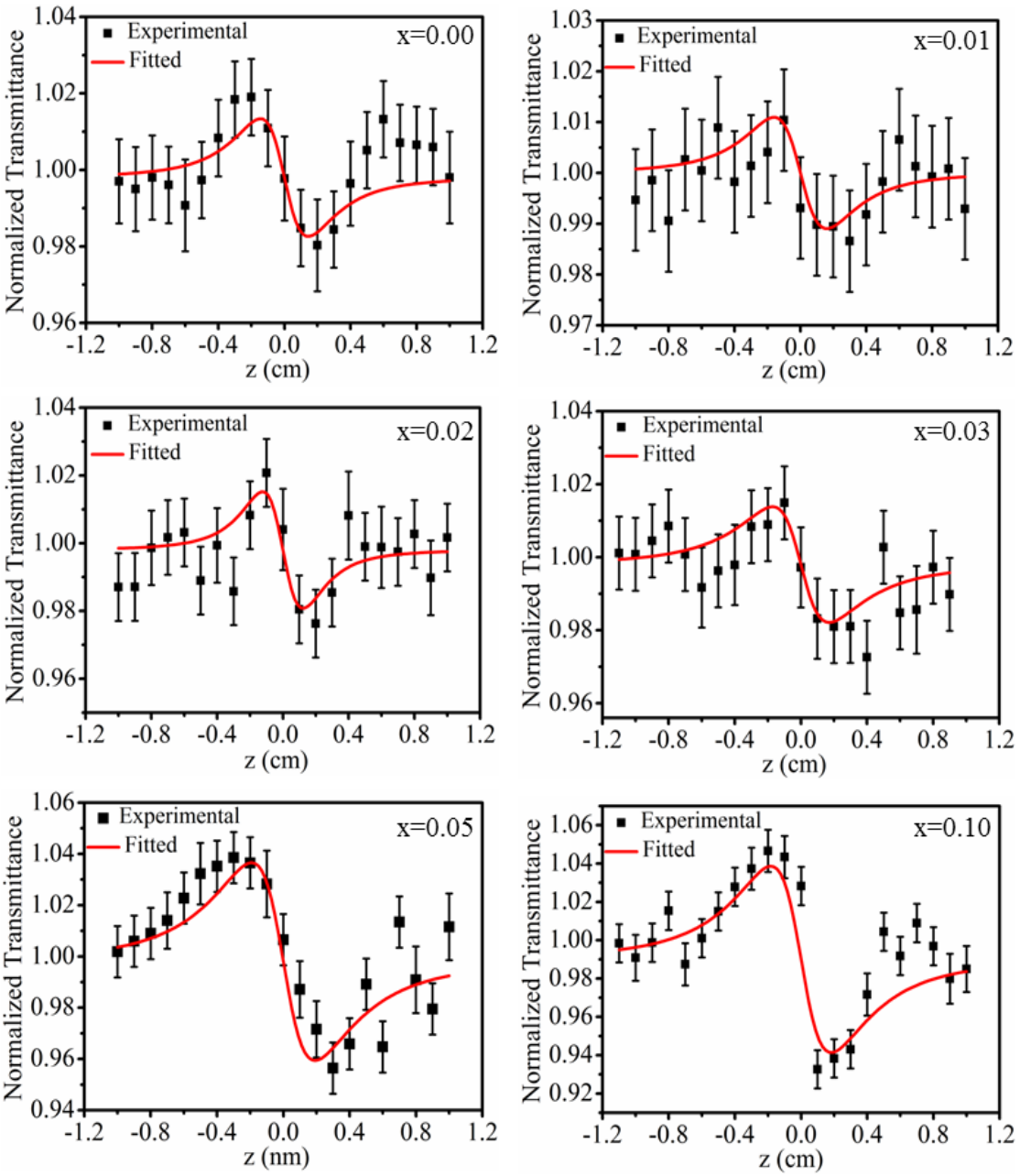

Fig. 6.2 Closed aperture z-scan curves of $Zn_{1-x}Al_xO$ ($0 \le x \le 0.10$) thin films.

refraction (self-defocusing) in all these films. Additionally, the peak and valley separation in these turns out to be in the range of $(1.69\text{-}1.8)\times z_0$ which satisfies the condition for third order NLO process **[9]**.

The nonlinear absorption coefficient (β) and nonlinear refractive index (n_2) of the PLD $Zn_{1-x}Al_xO$ ($0 \le x \le 0.10$) thin films were estimated from their respective open and closed aperture data points from Eqns. 2.1-2.2, Chap. 2. The variation of β and n_2 as a function of Al concentration is shown in Fig. 6.3

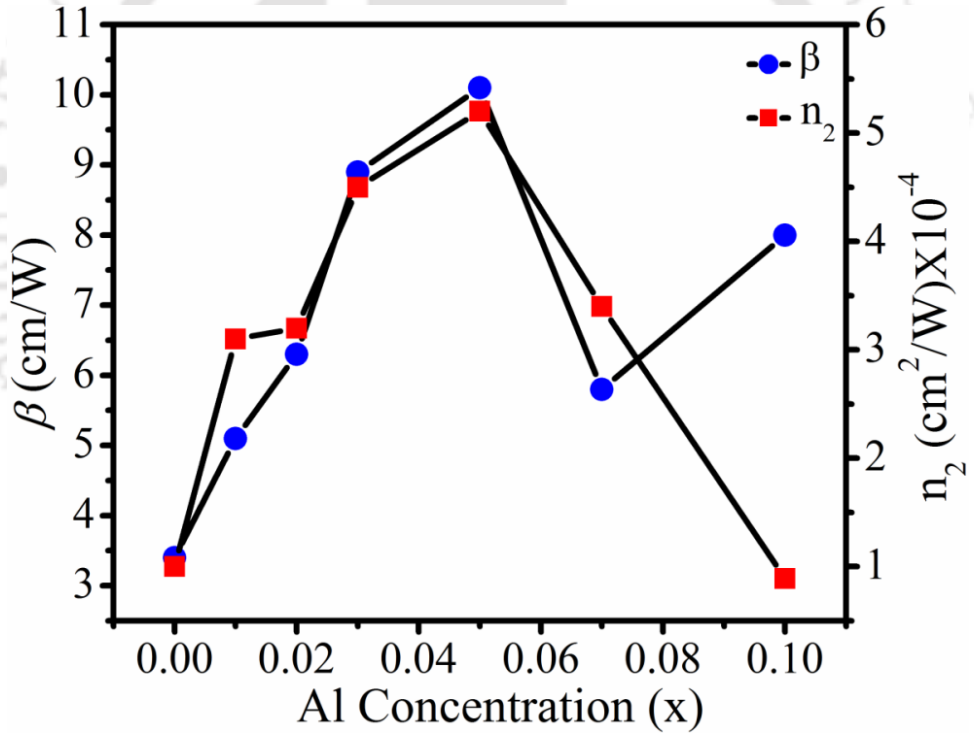

Fig. 6.3 Variation of β and n_2 with Al concentration.

Both NLO coefficients are observed to be increased with the increase in the Al content in the films till x=0.05 and thereafter decreased. The increasing behavior can be explained in terms of the improvement in crystallinity towards preferred c-axis orientation with the Al doping concentration, Fig. 3.3, Chap. 3 along with the increase in

the carrier concentration and hence the nonlinearity is increased **[8]**. The decrease in optical nonlinearity at higher impurity level, x=0.10, is accounted due to the loss of carrier concentration as shown in Fig. 3.10, Chap. 3.

The real as well as imaginary parts of the third order NLO susceptibilities ($\chi^{(3)\prime}$ and $\chi^{(3)\prime\prime}$) were estimated by using the equations 2.7 and 2.8 respectively, Chap. 2. The estimated third order NLO coefficients (β, n_2, $\chi^{(3)\prime}$ and $\chi^{(3)\prime\prime}$) are listed in table. 6.1.

Table 6.1 Nonlinear optical coefficients (β, n_2, $\chi^{(3)\prime}$ and $\chi^{(3)\prime\prime}$) of $Zn_{1-x}Al_xO$ (0≤x≤0.10) thin films.

Sr. No.	Al Content (x)	β (cm/W)	n_2 (cm^2/W) $\times10^{-4}$	$\chi^{(3)\prime}$ (esu) $\times10^{-3}$	$\chi^{(3)\prime\prime}$ (esu) $\times10^{-3}$
1.	0.00	3.4±0.3	1.0±0.1	5.45±1.04	1.02±0.19
2.	0.01	5.1±0.4	3.1±0.4	15.53±3.36	1.78±0.38
3.	0.02	6.3±0.4	3.2±0.4	15.22±2.98	2.19±0.43
4.	0.03	8.9±0.7	4.5±0.5	23.17±5.60	3.21±0.77
5.	0.05	10.1±0.7	5.2±0.5	26.74±5.64	3.75±0.79
6.	0.07	5.8±0.4	3.4±0.3	17.33±3.37	2.14±0.41
7.	0.10	8.0±0.6	0.89±0.09	4.90±0.77	2.43±0.38

From table 6.1, it is shown that the numerical values of NLO coefficients (β and n_2) along with the nonlinear optical susceptibilities ($\chi^{(3)\prime}$ and $\chi^{(3)\prime\prime}$), are fairly large as

compared to that of observed under short pulsed laser illumination **[17, 18]**. This is due to the thermal origin of the nonlinearity in the films illuminated via continuous wave (cw) laser. Under cw laser, the thermally induced optical nonlinearity plays a vital role in the semiconductor due to its large response time (τ) for the thermally induced refractive index change, falling within the range of $1\text{sec} < \tau < 100\ \mu\text{s}$ **[1]**.

The highly absorbing media can induce a change in linear refractive index and the thermally induced nonlinear refractive index (n_2^{th}) related to this change is given by:

$$n_2^{th} = \left(\frac{dn}{dT}\right)\frac{\alpha R^2}{\kappa} \qquad (6.1)$$

where (dn/dT) is the refractive index variation with temperature. An estimation of n_2^{th}, using the various parameters ($dn/dT = 0.13\times10^{-4}$ / ^{0}C and $\kappa = 0.30$ W/cm ^{0}C) from the literature **[19]** for pure ZnO and keeping into account the present geometrical parameters for z-scan experimental setup, comes out to be $\sim10^{-3}$ cm^2/W indicating that the thermal nonlinearity over rules over the other factors in the present case.

6.2 Effect of Ti concentration on nonlinear absorption and refractive index coefficients on $Zn_{1-x}Ti_xO$ ($0 \le x \le 0.050$) thin films

Figure 6.4 shows the OA z-scan spectra for the $Zn_{1-x}Ti_xO$ thin films along with error bars. Similar to the OA spectra of $Zn_{1-x}Al_xO$ thin films, the $Zn_{1-x}Ti_xO$ thin films also exhibit a transmittance minima at focus (z=0), indicating the feature of RSA in all the samples. The closed aperture z-scan graph of the $Zn_{1-x}Ti_xO$ ($0 \le x \le 0.050$) thin films is shown in Fig. 6.5. These are similar to that of AZO films; peak followed by valley

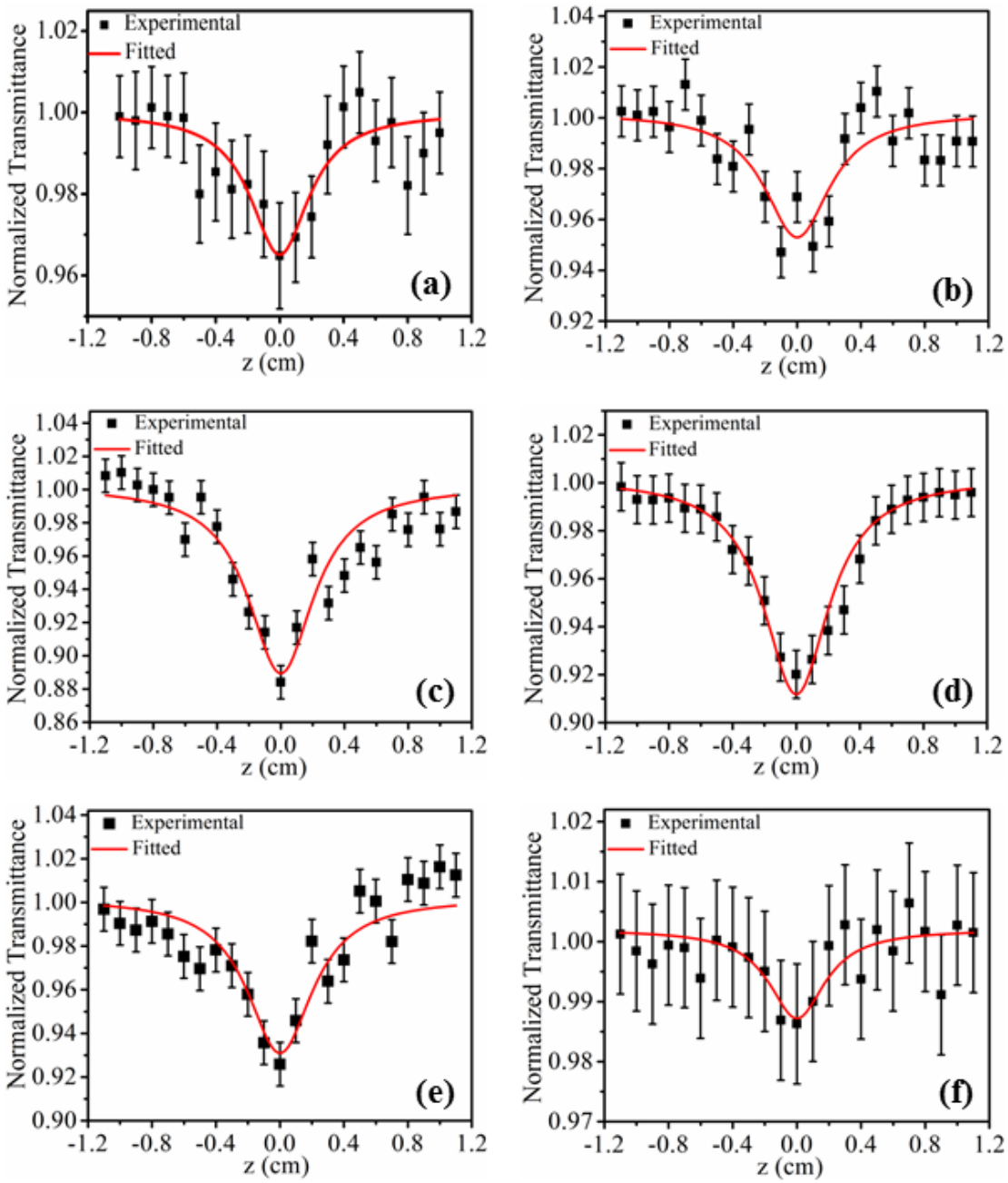

Fig. 6.4 Open aperture z-scan graph of $Zn_{1-x}Ti_xO$ thin films (a) x=0.000, (b) x=0.005, (c) x=0.010, (d) x=0.020, (e) x=0.030 and (f) x=0.050.

configuration in the neighborhood of focal plane indicating self-defocusing in these films too.

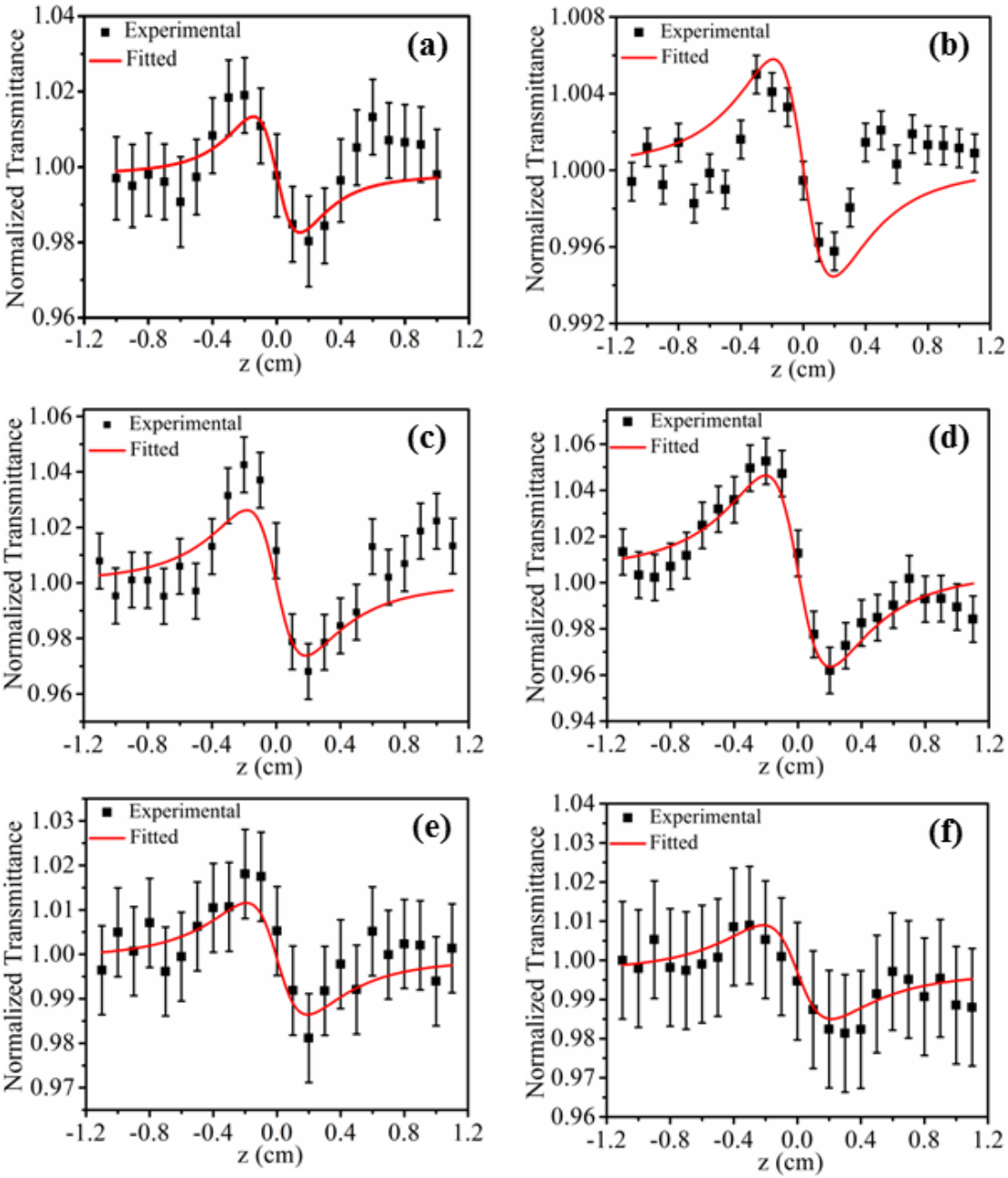

Fig. 6.5 Closed aperture z-scan graph of $Zn_{1-x}Ti_xO$ thin films (a) x=0.000, (b) x=0.005, (c) x=0.010, (d) x=0.020, (e) x=0.030 and (f) x=0.050.

Figure 6.6 shows the variation of absorption coefficient (α), nonlinear absorption coefficient (β) and nonlinear refractive index (n_2) with Ti concentration, x obtained from the z-scan measurement. The value of nonlinear absorption coefficients (β) in the Z_{1-}

$_xTi_xO$ thin film is found to be maximum for x=0.020 and thereafter it drops down with further increase in the value of x. Since the observed nonlinear absorption in the films is dominated by FCA hence the NLA is increased in the TZO thin films as compared to that of pure ZnO film. This is also supported by the fact that the conductivity of TZO thin films is enhanced as a result of large free carrier density as compared to that of pure ZnO which in turn enhances the optical nonlinearity **[8, 20, 21]**.

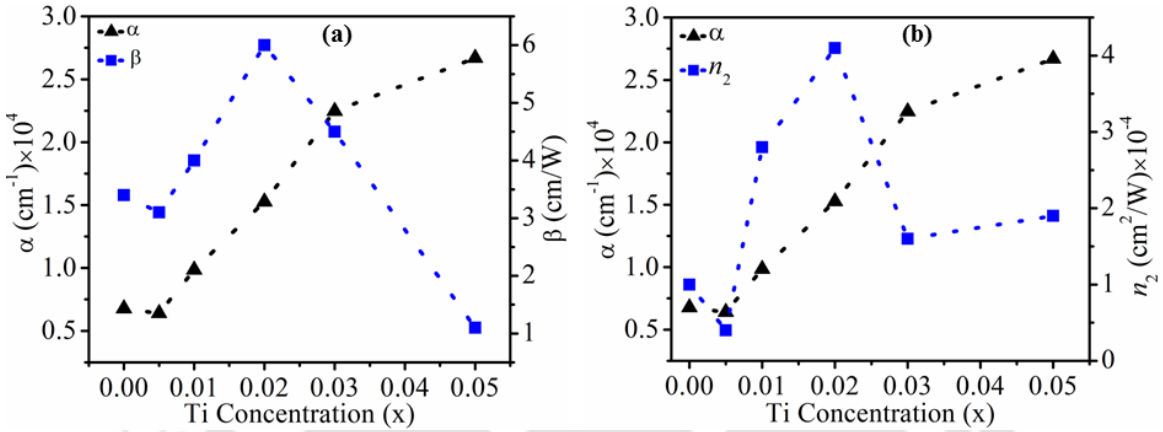

Fig. 6.6 Variation of (a) nonlinear absorption coefficient (β) and (b) nonlinear refractive index (n_2) with linear absorption coefficient in $Zn_{1-x}Ti_xO$ ($0 \le x \le 0.05$) thin films.

The other reason for the enhancement in NLA coefficient in TZO thin films could be due to the enormous photoluminescence signal (Sec. 4.7, Chap. 4) as a result of fluorescence resonance energy transfer (FRET) effect **[22]**. This effect is more prominent in a set of materials whose absorption and emission bands are close enough. In this process the photo generated electron hole pair of the donor atom undergo a non-radiative energy transfer to the acceptor atom resulting into the huge enhancement of band edge emission from the acceptor.

It is remarkable to note that the n_2^{th} is proportional to α (Eqn. 6.2) which supports

the increasing behavior of n_2 with the increasing Ti concentration till x=0.020 since the magnitude of α increases with x as shown in Fig. 6.6. This further justifies the thermally induced optical nonlinearity in the films. Similar values have also been reported earlier for thermally induced nonlinearity in ZnO and other materials **[2, 10, 23, 24]**. The observed values of β and n_2 do not follow the linear relationship with α for x>0.020. This discrepancy arises due to the deterioration of the crystalline quality of the films for x>0.020 as indicated by XRD and Raman observation, Fig. 4.3 and 4.4, Chap. 4.

The values of third order nonlinear optical constants (β, n_2, $\chi^{(3)\prime}$, $\chi^{(3)\prime\prime}$) obtained in the present case are summarized in the table 6.2. Similar to AZO, in TZO also, the NLO coefficients are significantly large compared to that of measured with short pulsed laser.

Table 6.2 Nonlinear optical coefficients (β, n_2, $\chi^{(3)\prime}$ and $\chi^{(3)\prime\prime}$) of $Zn_{1-x}Ti_xO$ ($0 \le x \le 0.050$) thin films.

Sr. No.	**Sample (x)**	**β (cm/W)**	**n_2 (cm^2/W) $\times 10^{-4}$**	**$\chi^{(3)\prime}$ (esu) $\times 10^{-3}$**	**$\chi^{(3)\prime\prime}$ (esu) $\times 10^{-3}$**
1.	0.000	3.4±0.2	1.0±0.1	5.45±1.04	1.02±0.19
2.	0.005	3.1±0.4	0.4±0.1	2.05±0.44	0.84±0.12
3.	0.010	4.0±0.3	2.8±0.6	15.16±3.64	1.44±0.13
4.	0.020	6.0±0.3	4.1±0.5	24.63±3.17	2.62±0.15
5.	0.030	4.5±0.5	1.6±0.3	-------	-------
6.	0.050	1.1±0.2	1.9±0.4	-------	-------

6.3 Two photon absorption induced photoluminescence in $Zn_{1-x}Al_xO$ ($0 \le x \le 0.10$) thin films

Multiphoton absorption is a nonlinear process which is highly sensitive to the crystalline structure of the material and the excitation laser intensity hence it depends on the impurity content in the sample which tailors this property. The addition of an impurity introduces various defects related states and consequently modifies the band edge luminescent centers. Figure 6.7 (a) shows multiphoton absorption induced UV-PL (MPA-PL) emission spectra recorded at room temperature by using the experimental setup, Fig.2.4 detailed in section 2.4, Chap. 2 employing a cw He:Ne laser at 632.8 nm as a pump beam. All the samples exhibit UV emission in the spectral range of 340-370 nm. Figure 6.7 (b) shows the enlarged view of MPA-PL for x=0.00 thin film sample. The position of the UV emission in the multi photon absorption is observed to be slightly blue shifted w. r. t. that of UV emission under single photon excitation, Fig 3.14, Chap 3. This shift may be due to either band to band recombination or recombination due to hot

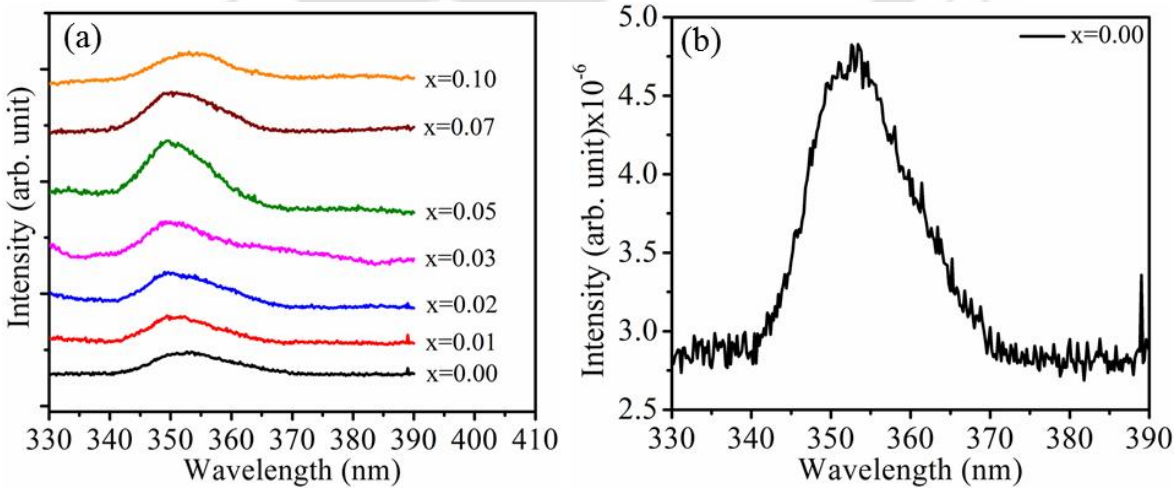

Fig. 6.7 Multiphoton PL spectra of (a) $Zn_{1-x}Al_xO$ ($0 \le x \le 0.10$) and (b) x=0.00 thin film under an optical excitation of 632.8 nm wavelength.

carriers as excess heat is generated in laser irradiation process while using cw laser **[25]**. This can be explained by considering possible recombination processes in direct band gap semiconductor (ZnO) as illustrated in Fig. 6.8 **[25]**. Band structure of ZnO is formed from *p*-type valence band and *s*-type conduction band near the Γ point of the Brillouin zone. Under the influence of crystal field and spin orbit interaction, valence band near the Γ point splits into three sub-bands having Γ_9, Γ_7, and Γ_7 symmetries which are assigned as A, B and C in the order of increasing energies **[26]**. In direct band gap semiconductors,

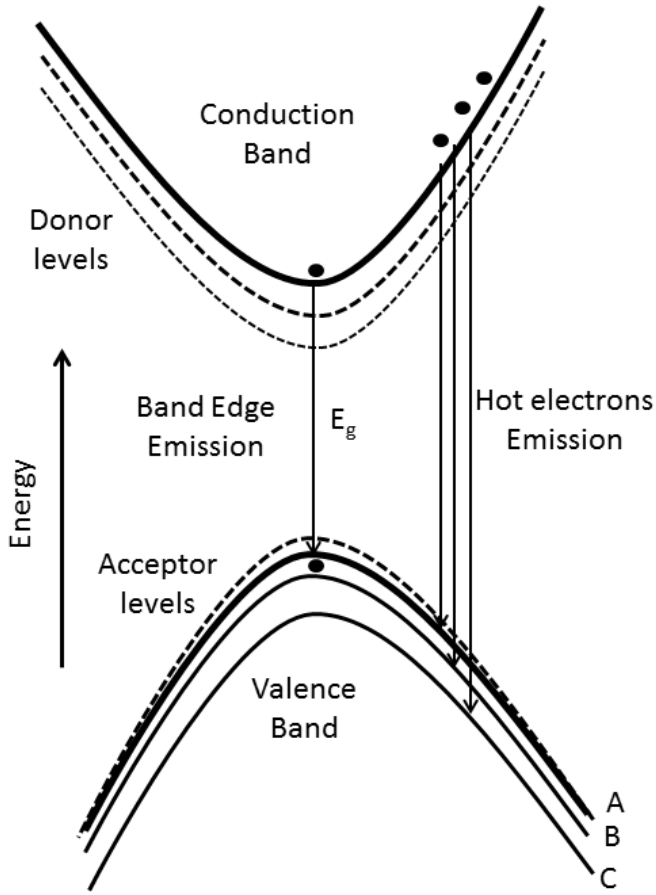

Fig. 6.8 Recombination processes in semiconductors.

various recombination processes occur. The band to band recombination process where recombination takes place between free electrons in the conduction band and holes in the valance band resulting in the emission of photons having energy equal to or slightly lower than the band gap of semiconductor. The other kind of radiative recombination process in which emitted photon energy is greater than the band gap energy, is the recombination due to hot electrons. Hot electrons are the free carriers in the semiconductor which are generated under the influence of thermal agitation. The process which governs the hot electrons is also known as free carrier absorption (FCA). Free carrier absorption is a nonlinear absorption process which depends on the free carrier density as well as the excitation wavelength. The hot electrons which are pushed deeper into the conduction band undergo a radiative transition before thermalizing to the bottom of the conduction band minima. Thus, the emission wavelength under multiphoton absorption induced photoluminescence is blue shifted as compared to that of the single photon absorption induced photoluminescence.

Figure 6.9 shows the variation of peak position (X_c) of MPA-PL and free carrier concentration, *n*, as a function of x (Al concentration) **[27]**. A gradual blue shift in the MPA-PL spectra is observed in the films with the increase in the Al concentration upto x=0.05 but it displays the red shift for x>0.05. This trend is similar to that of the band gap energy, Fig. 3.9, Chap. 3. The FWHM of MPA-PL emission is relatively narrower than that of single photon excitation, Fig. 3.14, Chap. 3. This could be due to the relatively lower decay time of the excited states in multi photon excitation scheme compared to that of the single photon absorption case.

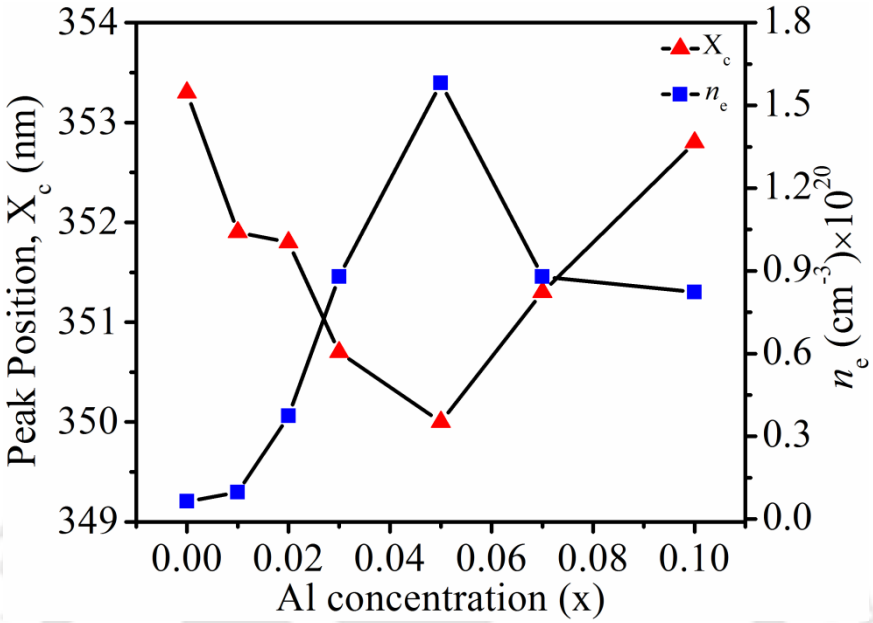

Fig. 6.9 Variation of MPA-PL peak position and free carrier concentration in $Zn_{1-x}Al_xO$ ($0 \le x \le 0.10$) thin films.

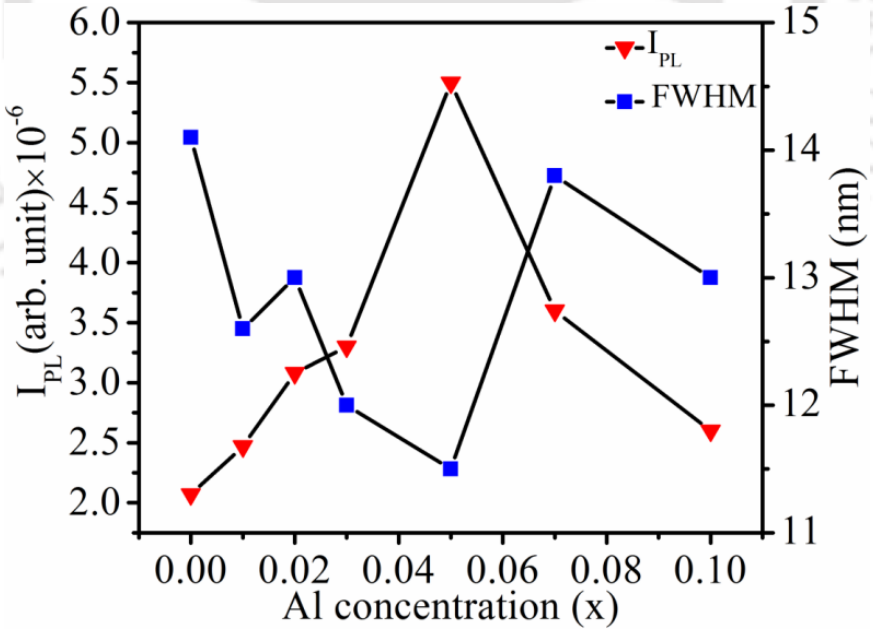

Fig. 6.10 Plot of FWHM and I_{PL} vs. Al content.

The dependence of the FWHM and peak intensity of the MPA-PL on the Al concentration (x) is shown in Fig. 6.10. It displays the increase in MPA-PL intensity and

decrease in the FWHM with x till x=0.05 and thereafter, the trend is reversed. The relative narrowing of FWHM with increasing the Al concentration can be due to the increase in the free carrier concentration in the $Zn_{1-x}Al_xO$ films as shown in Fig. 6.9, which tends to reduce the carrier life time.

The MPA-PL for x=0.05 sample as a function of pump laser intensity in the range of 330-390 nm is shown in Fig. 6.11.

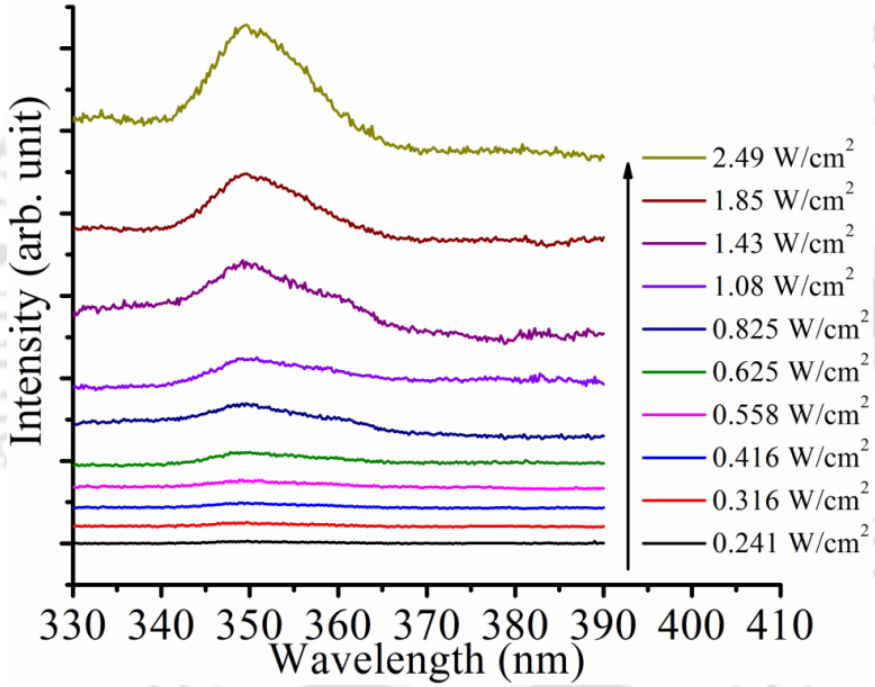

Fig. 6.11 Plot of MPA-PL spectra with the excitation pump intensity.

The relation between pump intensity and the emitted PL intensity for multi-photon absorption process is given by **[28]**.

$$Log(I_{PL}) = C + mLog(I_{EXC}) \tag{6.2}$$

where I_{PL} being the PL intensity, I_{EXC} is the pump (excitation) intensity, C is a constant and m determines the multi-photon absorption process.

The Log(Log) plot of photoluminescence intensity (I_{PL}) vs. excitation intensity (I_{EXC}) for the Al doped ZnO thin films is shown in Fig. 6.12. From Fig. 6.12, the slope, *m*, obtained using the equation 6.3, lies within 1 and 2, suggesting two photon absorption (TPA), being the dominating process for photoluminescence. Since the samples under MPA-PL study is irradiated with cw He:Ne laser having photon energy ($h\nu$=1.96 eV) which is greater than the half of the band gap energy of the sample ($E_g/2$=1.63 eV), the absorption process in the MPA-PL is dominated by the two photon absorption **[15]**.

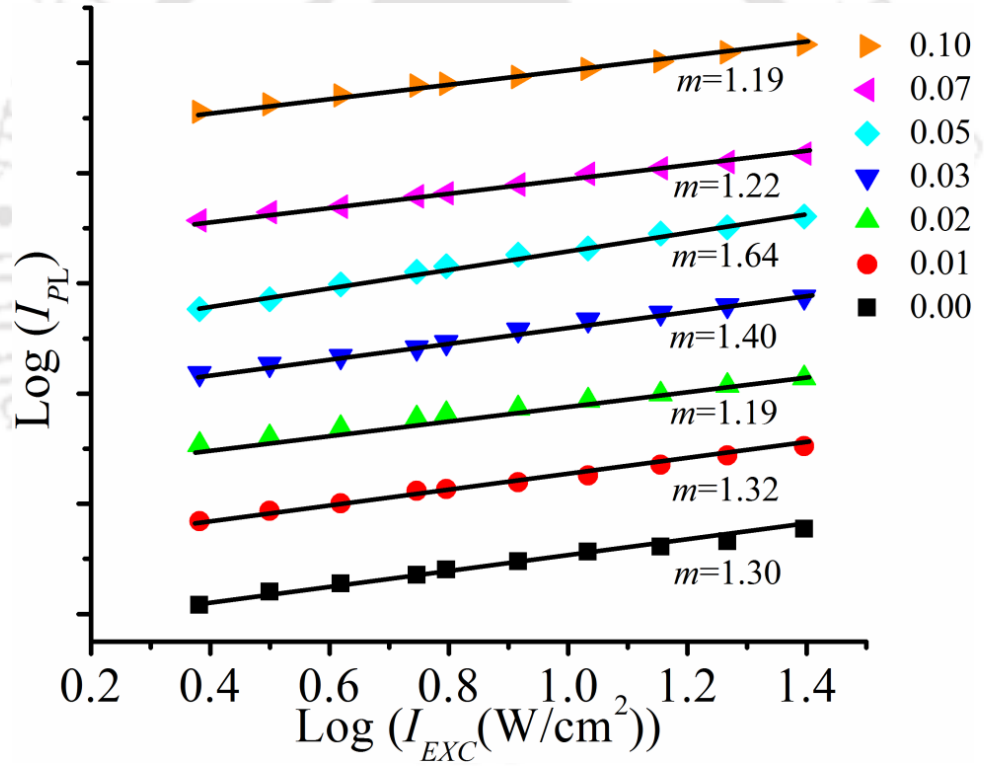

Fig. 6.12 Log(Log) plot of photoluminescence intensity (I_{PL}) vs. excitation intensity (I_{EXC}).

The value of slope, *m*, is maximum (1.64) for x=0.05 indicating the conversion of the two photon process is most efficient in the case of 5wt% Al doping. As the Al concentration is increased, the free carrier concentration is increased resulting in the

electrical conductivity of the $Zn_{1-x}Al_xO$ composite **[29]**. The increased electrical conductivity can cause the significant enhancement in the optical nonlinearity **[8]**. Hence the TPA conversion efficiency is observed to be enhanced with the increase in the Al concentration. At higher Al doping ($x>0.05$), an insulating layer of Al_2O_3 might be formed which prohibits the charge movement resulting in the decrease in the electrical conductivity and hence making multiphoton conversion efficiency poor **[30]**.

6.4 Two photon absorption induced photoluminescence in $Zn_{1-x}Ti_xO$ ($0 \le x \le 0.050$) thin films

Figure 6.13 depicts the multiphoton absorption induced PL (MPA-PL) spectra of $Zn_{1-x}Ti_xO$ ($0 \le x \le 0.050$) thin films under cw He:Ne laser (λ=632.8 nm) excitation.

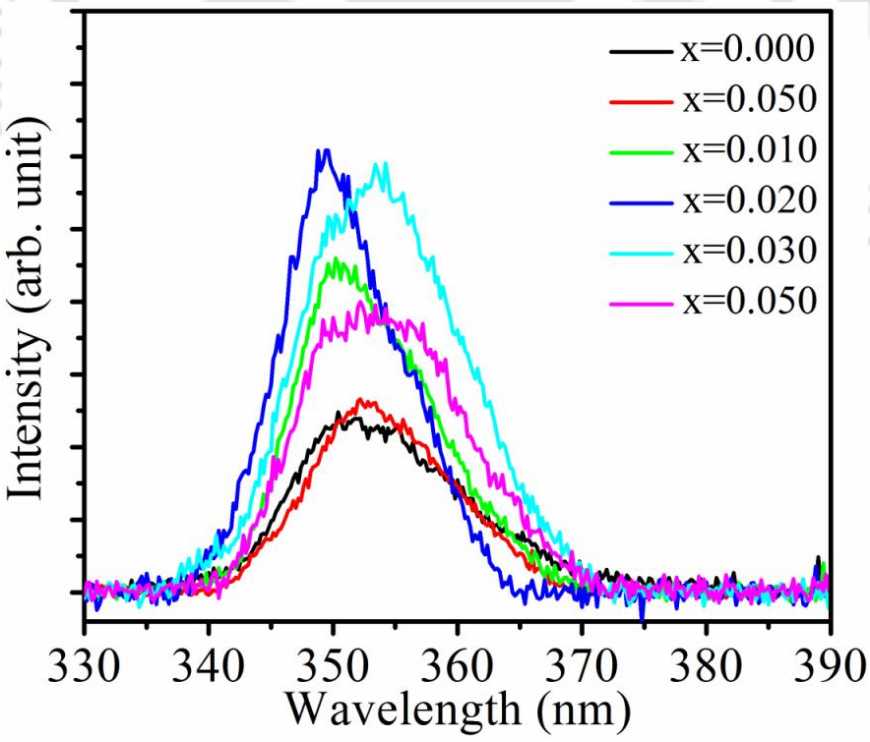

Fig. 6.13 MPA-PL graphs of $Zn_{1-x}Ti_xO$ ($0 \le x \le 0.050$) thin films.

All the samples show a strong photoluminescence signal in the UV range of 349.5-353 nm. There is a clear modification in the peak positions as well as peak intensities as a function of Ti content in the films. Figure 6.14 shows the variation of MPA-PL peak position (X_C) as well as peak intensity as a function of Ti content (x). The MPA-PL position shifts from 352.8 nm to 349.5 nm (3.514 to 3.55) eV for the thin film samples, $0.000 \le x \le 0.020$ while it is slightly red shifted from 349.5 nm to 353 nm (3.55 to 3.51) eV for higher Ti content ($x > 0.020$). The shift in MPA-PL peak position towards the higher energy value is primarily due to the combined effect of optical band gap widening caused by the quantum size effect and higher free carrier concentration in the $Zn_{1-x}Ti_xO$ ($0.000 \le x \le 0.020$) thin films. The dominant MPA-PL emission for x=0.020 sample is the consequence of better crystallinity among all the samples.

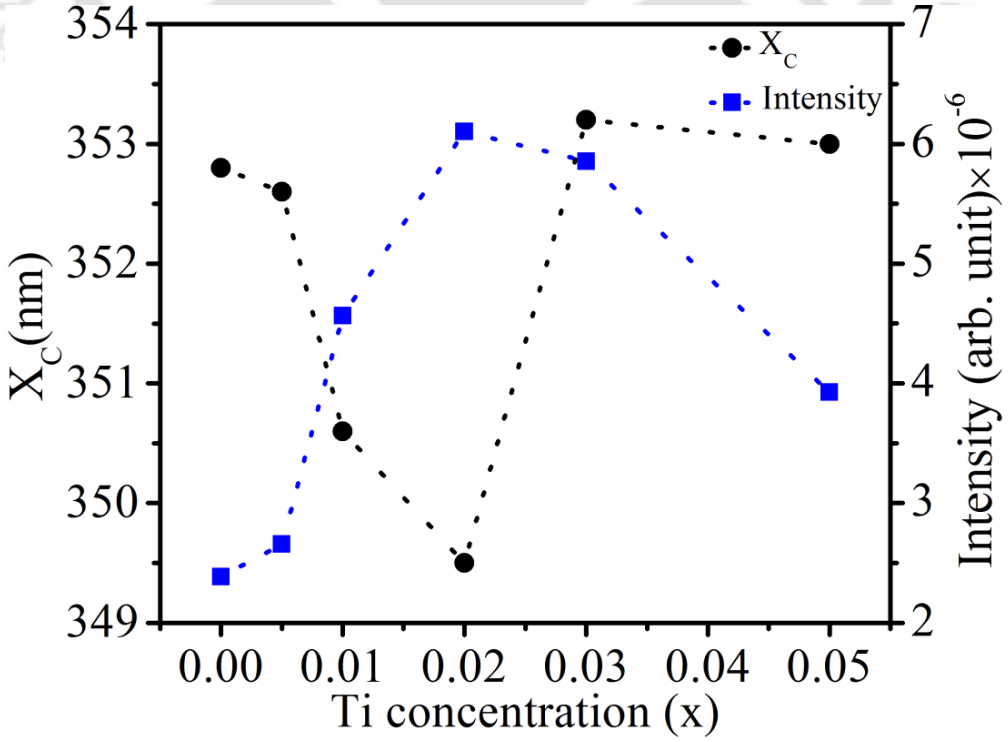

Fig. 6.14 Variation of MPA-PL peak position with Ti concentration.

The integrated intensity of the MPA-PL peak also follows the similar trend as that of the single photon absorption PL with the Ti content despite of the difference in the PL mechanism in both the cases. The similarity in the observation of the two results could be due to the strong influence of the crystalline quality and microstructures in the films.

Similar to the MPA-PL spectra observed in $Zn_{1-x}Al_xO$ thin films, the MPA-PL peak position (X_C) undergoes a blue shift as compared to their respective UV-PL under single photon excitation, Fig. 4.11, Chap. 4. This shift could be again associated with the radiative recombination of hot carriers in the conduction band. The pure electronic MPA-PL process is associated with the intermediate virtual state and has been reported under ultra-short pulsed lasers **[31-33]**. The present case of multiphoton absorption induced photoluminescence in TZO can be thought of the absorption of optical photons initiated via intermediate defects states within the band gap, Fig. 4.5, Chap. 4. Since the optical photon energy from pump He:Ne laser is ~1.96 eV so it is capable of excitation of intermediate states. The lifetime of hot carriers above the conduction band is very short so, before relaxing to the conduction band minima, a radiative recombination of hot electrons and the holes in the valence band results into the optical emission at slightly higher photon energy than that of optical band gap energy of ZnO.

Figure 6.15 shows the plot of MPA-PL spectra as a function of excitation pump intensity for all the TZO thin films. These spectra are recorded by varying the excitation pump intensity in the range of 0.24-2.49 W/cm^2. It is noted that there is hardly any shift in peak position with the variation in excitation pump intensity similar to that of AZO which is again attributed to the stability of the Nano crystallites in the films.

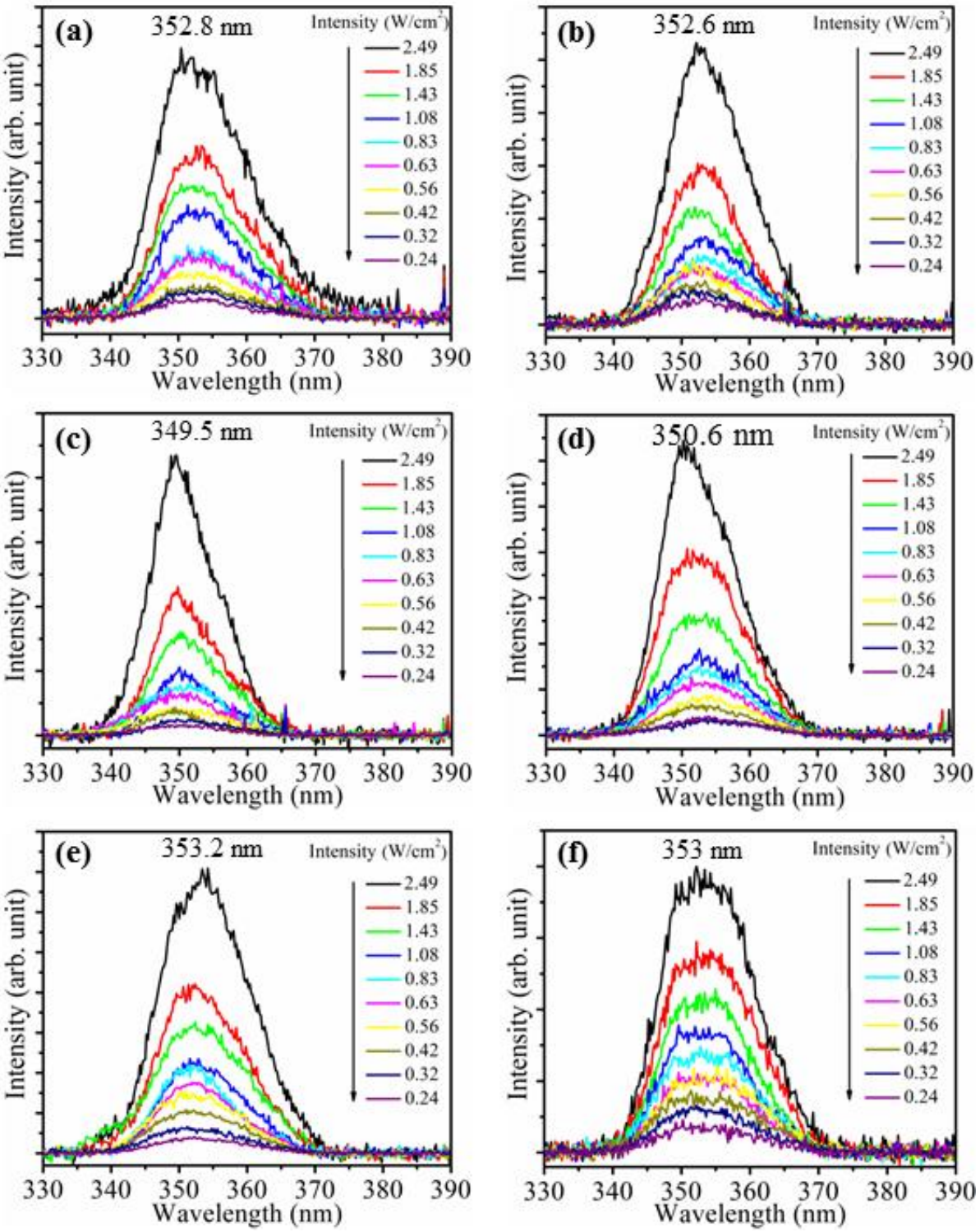

Fig. 6.15 Variation of the MPA-PL graph as a function of excitation pump intensity in $Zn_{1-x}Ti_xO$ ($0 \le x \le 0.05$) thin films.

The log-log plot of excitation intensity and MPA-PL intensity along with linear fit is shown in Fig. 6.16.

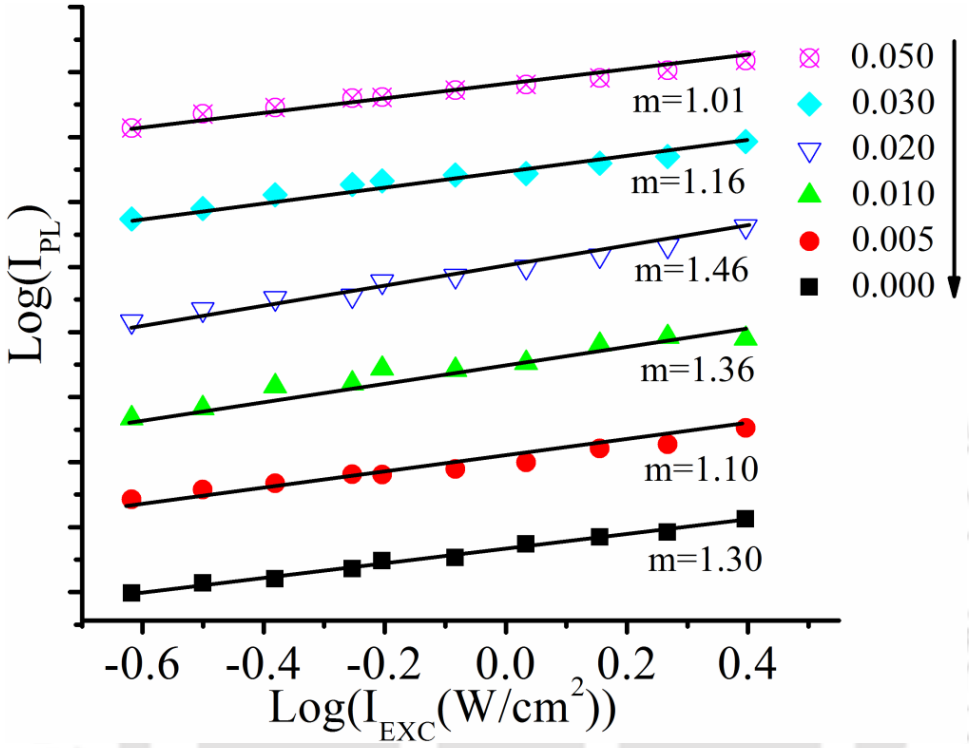

Fig. 6.16 log-log plot of I_{PL} vs I_{EXC} in $Zn_{1-x}Ti_xO$ thin films.

The slope, *m* obtained from the linear fitting of the graph using the equation 1, lies within 1 and 2, suggesting TPA, being the dominating process for photoluminescence.

In ZnO, AZO and TZO thin films, there are various mid gap levels formed due to the supply of donor atoms. The position of these defects states lie either near the bottom of conduction band minima, near the mid band gap or near the valence band maxima. Therefore, these defect states can also contribute in the up-conversion of optical photons via multiphoton absorption process. The incident photon energy creates charge carriers and these charge carriers can be captured by the defect states. Now, before, radiative

decays of these intermediate states via spontaneous emission, the continuous supply of input photons may lead the further excitation of charge carriers to higher into the conduction band which in turn gives rise to the relatively higher energy emission after decay. Chen et al. **[34]** has shown that the involvement of intermediate defect states can significantly improve the efficiency of upconversion process.

6.5 Conclusions

The pulsed laser deposited $Zn_{1-x}Al_xO$ ($0 \le x \le 0.10$) and $Zn_{1-x}Ti_xO$ ($0 \le x \le 0.05$) thin films were characterized for third order optical nonlinearity and tested for multiphoton absorption induced photoluminescence. The thin films in both the cases possessed absorptive as well as refractive nonlinearity as confirmed by z-scan measurement performed by cw laser. The films exhibited reverse saturation absorption. The values of, the third order nonlinear optical coefficients (β, n_2, $\chi_R^{(3)}$, $\chi_I^{(3)}$) in the $Zn_{1-x}Al_xO$ ($0 \le x \le 0.10$) thin films were found to be 3.4-10.1 cm/W, (1.0-5.2)$\times 10^{-4}$ cm^2/W, (5.45-26.74)$\times 10^{-3}$ esu and (1.02-3.75)$\times 10^{-3}$ esu respectively while that of for $Zn_{1-x}Ti_xO$ ($0 \le x \le 0.050$) were obtained to be 1.1-6.0 cm/W, (0.4-4.1)$\times 10^{-4}$ cm^2/W, (2.05-24.63)$\times 10^{-3}$ esu and (0.84-2.62)$\times 10^{-3}$ esu respectively. The slight lower value of NLO coefficients for TZO is due to the relatively poor crystallinity as compared to that of AZO. The $Zn_{1-x}Al_xO$ thin films grown at x=0.05 configuration showed the enhanced values of NLO coefficients and that of for $Zn_{1-x}Ti_xO$ thin films, the maximum values were observed at x=0.020 sample. The thin films showed a good response towards multiphoton absorption induced photoluminescence. The MPA signal was found to be dependent on impurity (Al as well as Ti) content. All the thin film samples showed MPA-PL signal peaking around 349-353

nm. The slopes in the log-log plot of the UV-PL intensity vs pump intensity were found to be in the range of 1.19-1.64 and 1.01-1.46 for AZO and TZO films respectively. The studies indicated that a suitable selection of Al and Ti concentration in $Zn_{1-x}Al_xO$ and $Zn_{1-x}Ti_xO$ thin films respectively can find its applications in nonlinear photonic devices as well as for upconversion.

Bibliography

[1] Robert W. Boyd, "*Nonlinear optics",* Academic Press, 2008.

[2] S. J. Mathews et al., "*Large third-order optical nonlinearity and optical limiting in symmetric and unsymmetrical phthalocyanines studied using Z-scan",* Optics Communications, **280** (2007) 206-212.

[3] Fyad Z. Henari et al., "*Third-order optical nonlinearity and all-optical switching in porous silicon",* Applied Physics Letters, **67** (1995) 323.

[4] MICHAEL J. MORAN et al., "*Interferometric Measurements of the Nonlinear Refractive-Index Coefficient Relative to CS_2, in Laser-System-Related Materials",* IEEE Journal of Quantum Electronics, **QE-11** (1975) 259-263.

[5] Parinda Vasa et al., "*Antiresonant ring interferometry as a sensitive technique for measuring nonlinear optical properties of thin films"* Optics Communications, **233** (2004) 297-304.

[6] ADELBERT OWYOUNG, "*Ellipse Rotation Studies in Laser Host Materials",* IEEE Journal of Quantum Electronics, **QE-9** (1973) 1064-1069.

[7] R. K. Jain and R. C. Lind, "*Degenerate four-wave mixing in semiconductor-doped glasses",* Journal of Optical Society of America B, **73** (1983) 647-653.

[8] Zouhair Sofiani et al., "*Third harmonic generation in undoped and X doped ZnO films (X: Ce, F, Er, Al, Sn) deposited by spray pyrolysis",* Journal of Applied Physics, **101** (2007) 063104.

[9] MANSOOR SHEIK-BAHAE et al., "*Sensitive Measurement of Optical Nonlinearities Using a Single Beam",* IEEE Journal of Quantum Electronics, **26** (1990) 760-769.

[10] M Abd-Lefdil et al., "*Structural, photoinduced optical effects and third-order nonlinear optical studies on Mn doped and Mn–Al codoped ZnO thin films under continuous wave laser irradiation",* Laser Physics, **24** (2014) 035404.

[11] C. S. Suchand Sandeep et al., "*Sol-gel synthesis and nonlinear optical transmission in $Zn_{1-x}Mg_xO(x \le 0.2)$ thin films",* Applied Physics Letters, **89** (2006) 063102.

[12] Vinay Kumari et al., "*Nonlinear optical properties of erbium doped zinc oxide (EZO) thin films",* Optics Communications, **285** (2012) 2182-2188.

[13] C. Torres-Torres et al., "*Optical Kerr phase shift in a nanostructured nickel-doped zinc oxide thin solid film",* Optics Express, **21** (2013) 21357.

[14] J. I. Pankove, "*Optical Processes in Semiconductors",* Dov. Pubublications (2010), **ISBN: 0486602753**.

[15] Eric W. Van Stryland et al., "*Energy band-gap dependence of two-photon absorption",* Optics Letters, **10** (1985) 490-492.

[16] Pingxin Xiong et al., "*Ultraviolet luminescence enhancement of ZnO two-dimensional periodic nanostructures fabricated by the interference of three femtosecond laser beams",* New Journal of Physics, **13** (2011) 023044.

[17] Yun-Pei Chan et al., "*Near-resonant high order nonlinear absorption of ZnO thin films",* Optics Express, **16** (2008) 19900-19908.

[18] X. J. Zhang et al., "*Determination of optical nonlinearities and carrier lifetime in ZnO",* Journal of Optical Society of America B, **14** (1997) 1951-1955.

[19] Dometrios N. Christodoulides et al., "*Nonlinear refraction and absorption: mechanisms and magnitudes",* Advances in Optics and Photonics, **2** (2010) 60.

[20] J. J. Lu et al., "*Conductivity enhancement and semiconductor–metal transition in Ti-doped ZnO films",* Optical Materials, **29** (2007) 1548-1552.

[21] Young Ran Park and Kwang Joo Kim, "*Optical and electrical properties of Ti-doped ZnO films observation of semiconductor–metal transition",* Solid State Communications, **123** (2002) 147–150.

[22] H. Y. Lin et al., "*Giant enhancement of band edge emission based on ZnO/TiO_2 nanocomposites",* Optics Express, **15** (2007) 13832-13837.

[23] K. K. Nagaraja et al., "*Third-order nonlinear optical properties of Mn doped ZnO thin films under cw laser illumination",* Optical Materials, **35** (2013) 431-439.

[24] K. Spoorthi et al., "*Investigations on nonlinear optical properties of electron beam treated Gd:ZnO thin films for photonic device applications",* Laser Physics, **27** (2017) 065403.

[25] G. D. Gilliland, "*Photoluminescence spectroscopy of crystalline semiconductors",* Material Science and Engineering R, **18** (1997) 99-400.

[26] Chennupati Jagadish and Stephen Pearton, "*Zinc Oxide Bulk, Thin Films and Nanostructures",* Elsevier (2006), **ISBN: 9780080447223**.

[27] Gyan Prakash Bharti and Alika Khare, "*Structural and linear and nonlinear optical properties of $Zn_{1-x}Al_xO$ ($0 \le x \le 0.10$) thin films fabricated via pulsed laser deposition technique",* Optical Materials Express, **6** (2016) 2063-2080.

[28] Susanta Kumar Das et al., "*Multiphoton-absorption induced ultraviolet luminescence of ZnO nanorods using low-energy femtosecond pulses",* Journal of Applied Physics, **108** (2010) 043107.

[29] Said Benramache et al., "*Correlation in calculations of electrical conductivity with and without undoped in Al, Co and In doped ZnO thin film",* Optik - International Journal for Light and Electron Optics, **125** (2014) 5776-5779.

[30] Jianhua Hu and Roy G. Gordon, "*Textured aluminum-doped zinc oxide thin films from atmospheric pressure chemical-vapor deposition",* Journal of Applied Physics, **71** (1992) 880-890.

[31] C. F. Zhang et al., "*Multiphoton absorption pumped ultraviolet stimulated emission from ZnO microtubes",* Applied Physics Letters, **91** (2007) 142109.

[32] C. F. Zhang et al., "*Femtosecond pulse excited two-photon photoluminescence and second harmonic generation in ZnO nanowires",* Applied Physics Letters, **89** (2006) 042117.

[33] C. Tolentino Dominguez et al., "*Three-photon excitation of an upconversion random laser in ZnO-on-Si nanostructured films",* Journal of the Optical Society of America B, **31** (2014) 1975.

[34] S. L. Chen et al., "*Efficient upconversion of photoluminescence via two-photon absorption in bulk and nanorod ZnO",* Applied Physics B, **108** (2012) 919-924

Chapter 7

Random lasing action in pulsed laser deposited $Zn_{1-x}Al_xO$ ($0 \le x \le 0.10$) thin films

In the random laser, photons are confined via multiple scattering within the nanoparticles of the gain medium unlike the conventional laser cavity where a repeated back and forth passage of radiation traces its path via reflections from the two mirrors of the cavity **[1, 2]**. Thus, the gain medium for the random laser can be in the form of thin films or pellets. The change in the surface morphology may drastically affect the quality factor of such laser system. If the shape of the particles are of the form of hexagonal or polygon then the reflection from its parallel facets may evolve a Fabry Perot like cavity **[3, 4]**. Additionally, the formation of nano rods in these films will evolve whispering gallery mode (WGM) **[5, 6]**. The schematic of these three possible types of cavity formation in the nanostructured material is shown in Fig. 7.1.

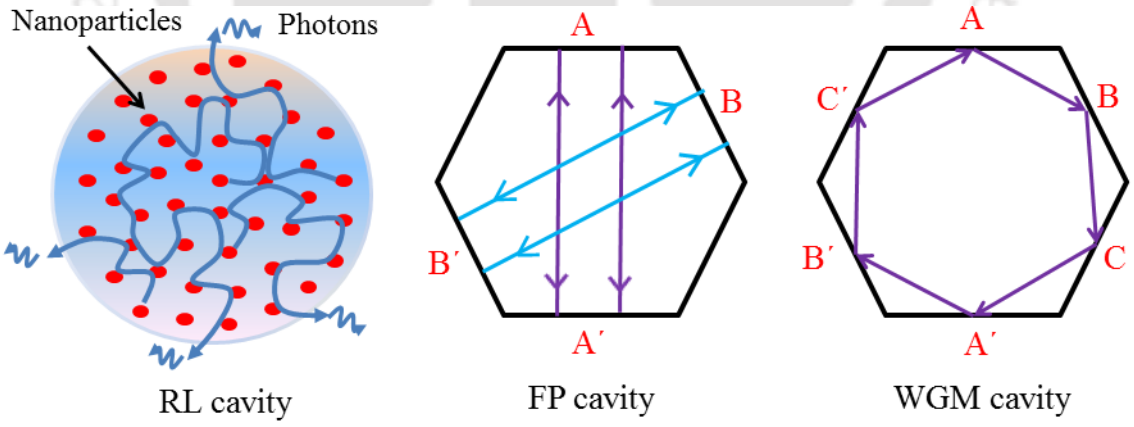

Fig. 7.1 Schematic of different types of mirror less cavity formation.

Among the various hosts for random lasing e.g. Dyes, GaAsN, ZnS, ZnSe, TiO_2 etc. **[7-11]**, ZnO may be a favorable choice due to its emission in ultraviolet spectral range. Its properties can be easily tailored by infusion of impurities along with change in

the surface morphology as well as electronic cloud in the system. It can be grown in the form of nano-micro rods and thus the dwell time of the photon within the medium can be increased and consequently the lasing intensity as well as *Q*-factor of the laser can be enhanced. However, the excessive amount of impurity may cause loss in the signal and reduces the quality factor and needs to be optimized.

In this chapter, the random lasing emission from the pure ZnO pellet and pulsed laser deposited thin films of $Zn_{1-x}Al_xO$ ($0 \leq x \leq 0.10$) pumped by 3rd harmonic of a Q-switched Nd:YAG laser, is presented. The experimental setup is described in section 2.8, Chap. 2. The thin films were subjected to field emission scanning electron microscope measurement to unveil the surface morphology of the thin films so as to get an idea about the possible formation of cavity.

7.1 Field emission scanning electron microscope of ZnO pellet and $Zn_{1-x}Al_xO$ ($0 \leq x \leq 0.10$) PLD thin films

Figure 7.2 (a) displays the field emission scanning electron microscope image of pure ZnO pellet and corresponding particle size distribution in Fig. 7.2 (b).

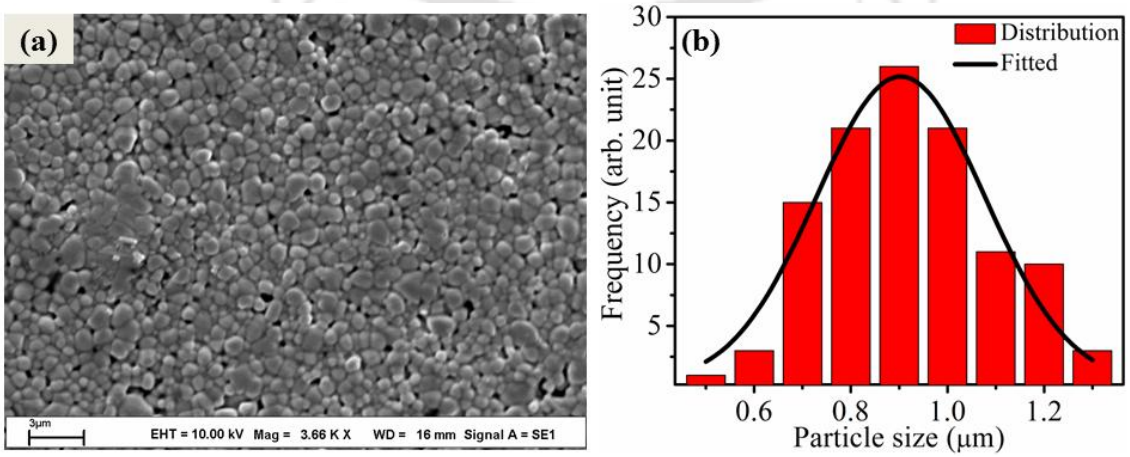

Fig. 7.2 (a) FESEM image of pure ZnO pellet and (b) particle size distribution.

Figure 7.2 (a) clearly depicts the formation of nearly spherical shaped closely packed granular structures on the pellet surface. The average grain size obtained by fitting the Gaussian profile, Fig. 7.2 (b), is found to be ~0.9 μm.

Figure 7.3 shows the FESEM images of $Zn_{1-x}Al_xO$ ($0 \leq x \leq 0.10$) thin films deposited onto fused silica substrate.

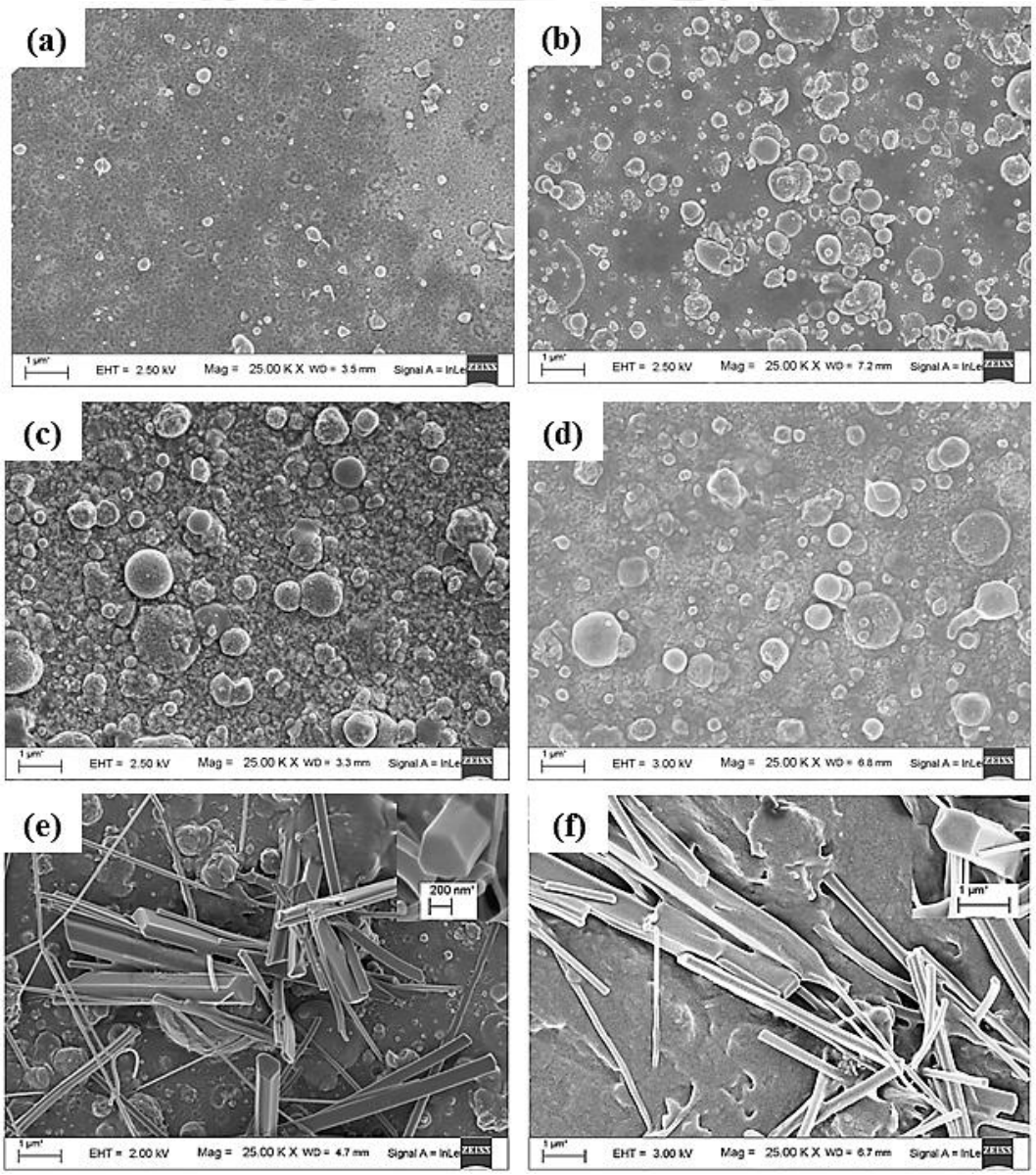

Fig. 7.3 FESEM images of $Zn_{1-x}Al_xO$ thin films (a) x=0.00, (b) x=0.01, (c) x=0.02, (d) x=0.03, (e) x=0.05 and (f) x=0.10.

Pure ZnO thin film, Fig. 7.3 (a), shows smaller and widely spread nearly spherical shaped nanostructures against uniform background. With the increasing Al concentration up-to x=0.03, the particle size as well as their compactness are increasing with x. For x=0.05, there is clear formation of 2D nano rods as well as 1D nano wires within the background of spherical shaped nano clusters. The inset of Fig. 7.3 (e) shows the enlarged view of nearly hexagonal cross section of nano rods. For the film having x=0.10, there is hardly any signature of distribution of spherical particles. The cross section of nano rod for this thin film, shown in inset, Fig. 7.3 (f), similar to that of x=0.05, is of hexagonal shape but there is also an indication of coalescing of the several nano rods. The size distribution of spherical shaped nanostructures for x=0.00 to 0.05 is shown in Fig. 7.4. The average particle size estimated from these is listed in table 7.1.

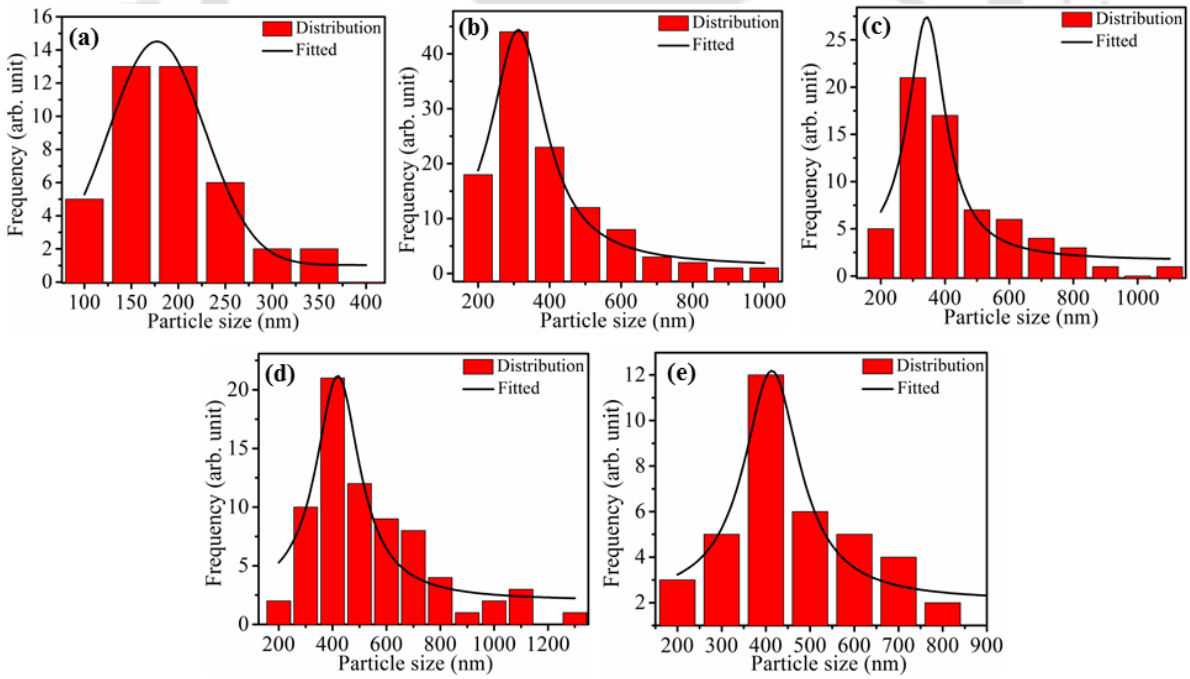

Fig. 7.4 Histogram of particle size distribution in $Zn_{1-x}Al_xO$ thin fims (a) x=0.00, (b) x=0.01, (c) x=0.02, (d) x=0.03, and (e) x=0.05.

The average particle size increases from 177 nm to 419 nm from pure ZnO to Al infused ZnO, up-to x=0.05.This result follows the similar trend as the variation of average crystallite sizes estimated from the XRD measurement **[12].** However, the estimated average particle size is found to be substantially larger as compared to that of the average crystallite size, Table 3.1, Chap. 3. This could be due to the fact that the large numbers of nanocrsytallites agglomerate to form nearly spherical shaped nano particles.

Table 7.1 Average particle size in $Zn_{1-x}Al_xO$ ($0 \leq x \leq 0.05$) thin films.

Sr. No.	Sample (x)	Distribution function	Average particle size (nm)
1.	0.00	Gaussian	177
2.	0.01	Lorentz	312
3.	0.02	Lorentz	343
4.	0.03	Lorentz	414
5.	0.05	Lorentz	419

For the higher Al content ($x \geq 0.05$), the transition from the surface nanostructures from 3-D spherical particulates to low dimensional nanorods and nanowires could be linked to the thermodynamically favored environment created in the presence of higher Al concentration. At very high Al concentration (x=0.10), the surface structure of the film indicates the diffused structures, coalescenced nanorod and nanowires. Furthermore, from fig. 7.3 (e-f), it is observed that the 5wt% Al doped ZnO thin film contains more compact distinct nanorods as compared to that of 10wt% Al doped film. The average length and

diameter of the nanowires and nanorods like structures in $Zn_{1-x}Al_xO$ for x=0.05 and 0.10 thin films, is tabulated in table 7.2.

Table 7.2 Estimation of average length and diameter of 2-dimensional nanostructures in $Zn_{1-x}Al_xO$ ($x \ge 0.05$) thin films.

Sample (x)	Av. length (μm) for nanowire	Av. dia. (nm) for nanowire	Av. length (μm) for nanorod	Av. facet size (nm) for nanorod
0.05	2.9	90	3.1	348
0.10	2.2	127	4.5	448

The average length of nanowires in the 5wt% Al doped ZnO film is found to be ~2.9 μm which is slightly larger (2.2 μm) than that of in 10 wt% Al doped ZnO film. However, the average diameter of the nanowire in 10wt% Al doped ZnO film is quite large as compared to 5wt% Al doped film and same holds for facet size of nano rods, 348 nm and 448 nm for x=0.05 and 0.10 respectively.

7.2 Random lasing in ZnO pellet

The presence of nearly uniformly distributed granular like structure of an average size of ~0.9 μm on the surface of bare ZnO pellet, Fig. 7.2, indicates that it could be a good active medium, for the UV random laser and so it was subjected to lasing set-up of Fig. 2.8, Chap. 2. Figure 7.5 shows the emission due to the random lasing (RL) action in pure ZnO pellet along with the reference signal recorded by blocking the pump laser. The reference signal is quite low and free from any obvious fluctuations. The signal to noise ratio (SNR) is observed to be quite high (~50). Such a large SNR value is favorable for

observing distinct longitudinal modes with clarity in any lasing system. The RL spectrum shown in Fig. 7.5, exhibits nearly equispaced (~3 nm) narrow spikes covering the UV-blue emission range of pure ZnO centered around 381.7 nm. The full width at half maximum (FWHM) of the central mode is estimated to be ~1.38 nm.

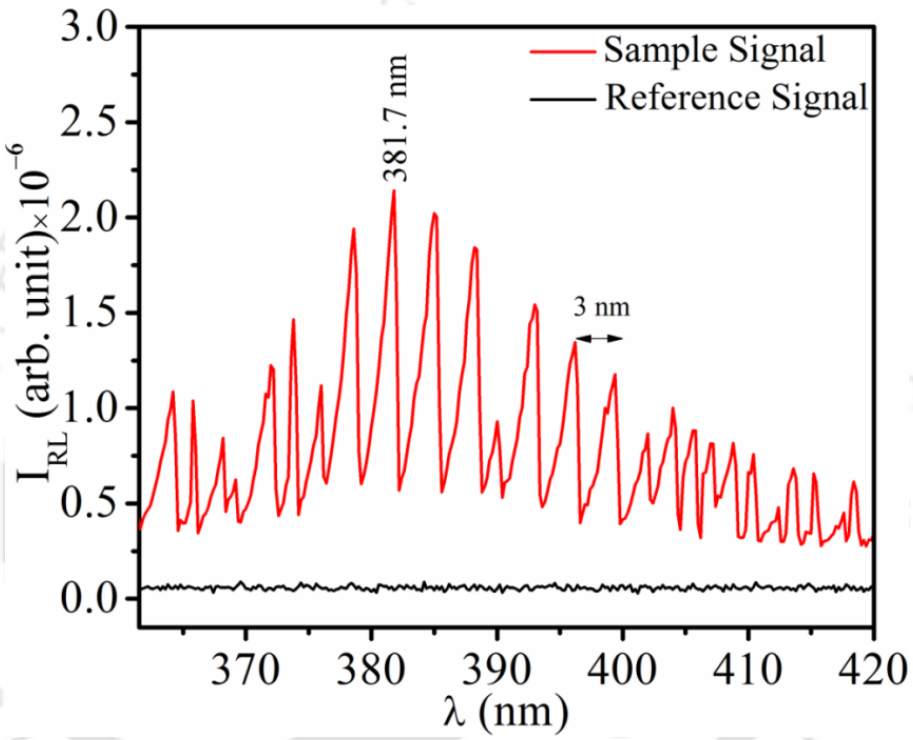

Fig. 7.5 Random lasing spectrum of pure ZnO pellet.

The cavity length (L_C) of the arbitrary cavity formed inside this gain media of ZnO random laser is estimated by using the equation 7.1 **[13]**:

$$L_C = \frac{\lambda_0^{\,2}}{2\Delta\lambda\left(n - \lambda_0 \frac{dn}{d\lambda}\right)} \tag{7.1}$$

where, λ_0 is the wavelength of central mode, $\Delta\lambda$ is the longitudinal mode separation, n is the linear refractive index and $dn/d\lambda$ is the dispersion in the refractive index.

The estimated cavity length in the ZnO pellet from eqn 7.1 is found to be ~10.5 μm. The quality factor (*Q*-factor) for any mode is linked to its wavelength, λ, and its full width at half maxima, FWHM ($\delta\lambda$), according to the following relation **[5]**:

$$Q = \frac{\lambda_0}{\delta\lambda} \tag{7.2}$$

The *Q* value corresponding to the central mode at λ_0 (381.7 nm), for the ZnO pellet, eqn. 7.2, is found to be 277.

There are two types of RL cavities; diffusive cavity and ballistic cavity, formed in a disordered media depending upon the sample length (*L*) under optical excitation and the mean free path (*l*) of the photons inside the gain region **[14].** The diffusive cavity is formed for $L >> l$ and the quasi-ballistic cavity for $L \sim l$. In the present experiment, the sample size (focal spot of the pump laser) is enormously large (L~125μm) as compared to that of mean free path (cavity length, L_C=10.5 μm), indicating the formation of diffusive cavity.

7.3 Effect of Al concentration (x) on Random lasing signal in $Zn_{1-x}Al_xO$ ($0 \le x \le 0.10$) thin films

Figure 7.6 (a) depicts the distinct lasing emission in pure ZnO PLD film. Each mode of RL spectra of thin film consists of closely separated narrow spikes. In this RL, the cavity can be formed via more than one way and therefore, simultaneously the large number of micro cavities are being formed which may have nearly similar length and hence the spacing between the longitudinal modes is nearly same ~3 nm. However, the peak position of each longitudinal mode will be the combination of individual cavity but

will be slightly shifted in wavelength appearing in the form of spikes in the each longitudinal mode. Therefore, in order to access the width of the longitudinal mode, the central mode (λ_0=380.2 nm) is de-convoluted and shown in the Fig. 7.6 (b). The average FWHM corresponding to the most intense mode (Fig. 7.6 (b)) is ~0.56 nm and that of the average separation between the longitudinal modes is ~3.13 nm.

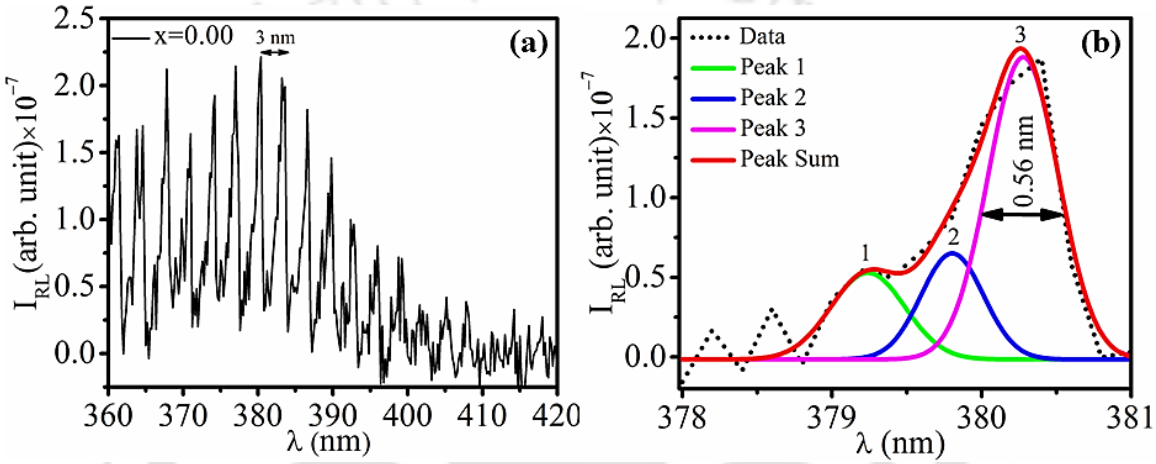

Fig. 7.6 (a) RL emission in ZnO thin film and (b) de-convolution of central mode.

The threshold pump intensity (I_{th}) of pure ZnO thin film was estimated from the plot of RL intensity (I_{RL}) vs. pump intensity. The excitation pump intensity was varied from 2.0-10.9×10^2 MW/cm^2. In order to avoid the damage of the thin film sample, the upper limit of the input pump intensity was limited to a maximum ~10.9×10^2 W/cm^2. A plot of the excitation pump intensity and RL intensity is shown in Fig. 7.7. The sudden change in the RL output beyond the pump intensity of 3.2×10^2 W/cm^2 ascertains it as the threshold pump, I_{th}. Similar values of threshold has also been reported in highly facet ZnO rod **[15].**

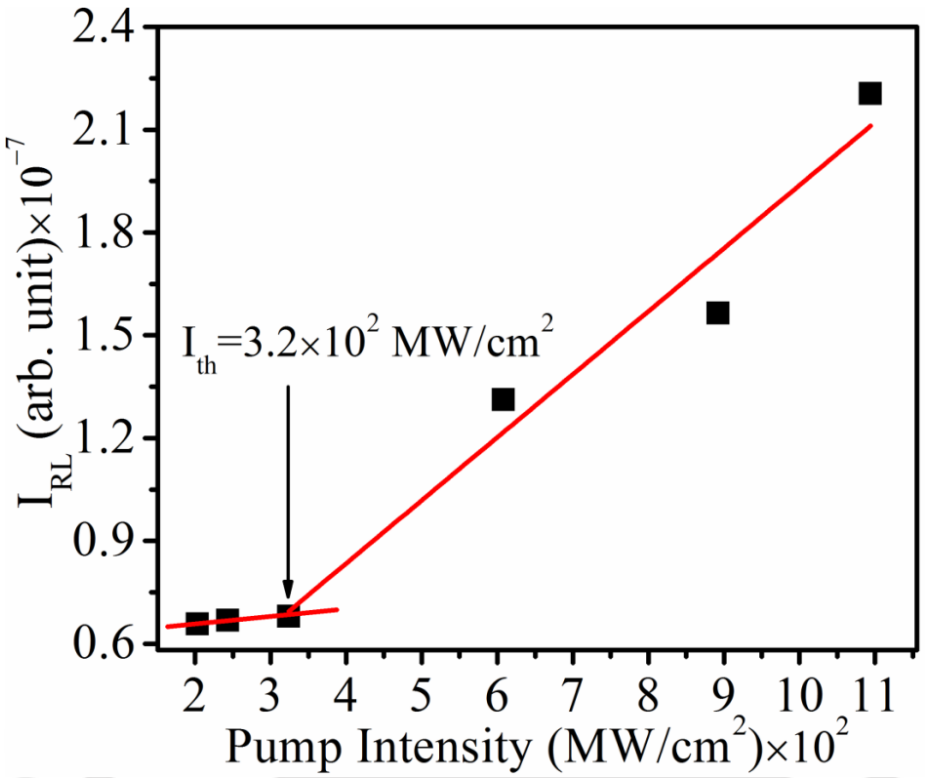

Fig. 7.7 Variation of Random lasing intensity with pump intensity.

Figure 7.8 depicts the RL signal of $Zn_{1-x}Al_xO$ ($0.01 \leq x \leq 0.03$) thin films entirely covered with the nearly spherical shaped particles. All these spectra are recorded at the maximum pump intensity of ~10.9×10^2 MW/cm^2 which is sufficiently above the threshold (Fig. 7.7). All these samples exhibit distinct longitudinal modes similar to that of x=0 thin film sample. The average spacing of the longitudinal modes in these samples are observed to be quite similar, 3.09 nm, 3.12 nm and 3.10 nm for x=0.01, 0.02 and 0.03 thin films respectively. The resonance lasing modes in the films are observed to be close to the near band edge emission of pure ZnO within the spectral range of 375-385 nm. The line width for the longitudinal mode having maximum intensity for samples ($0.01 \leq x \leq 0.03$) was estimated from the de-convoluted spectra, shown in Fig. 7.8 (b, d and f).

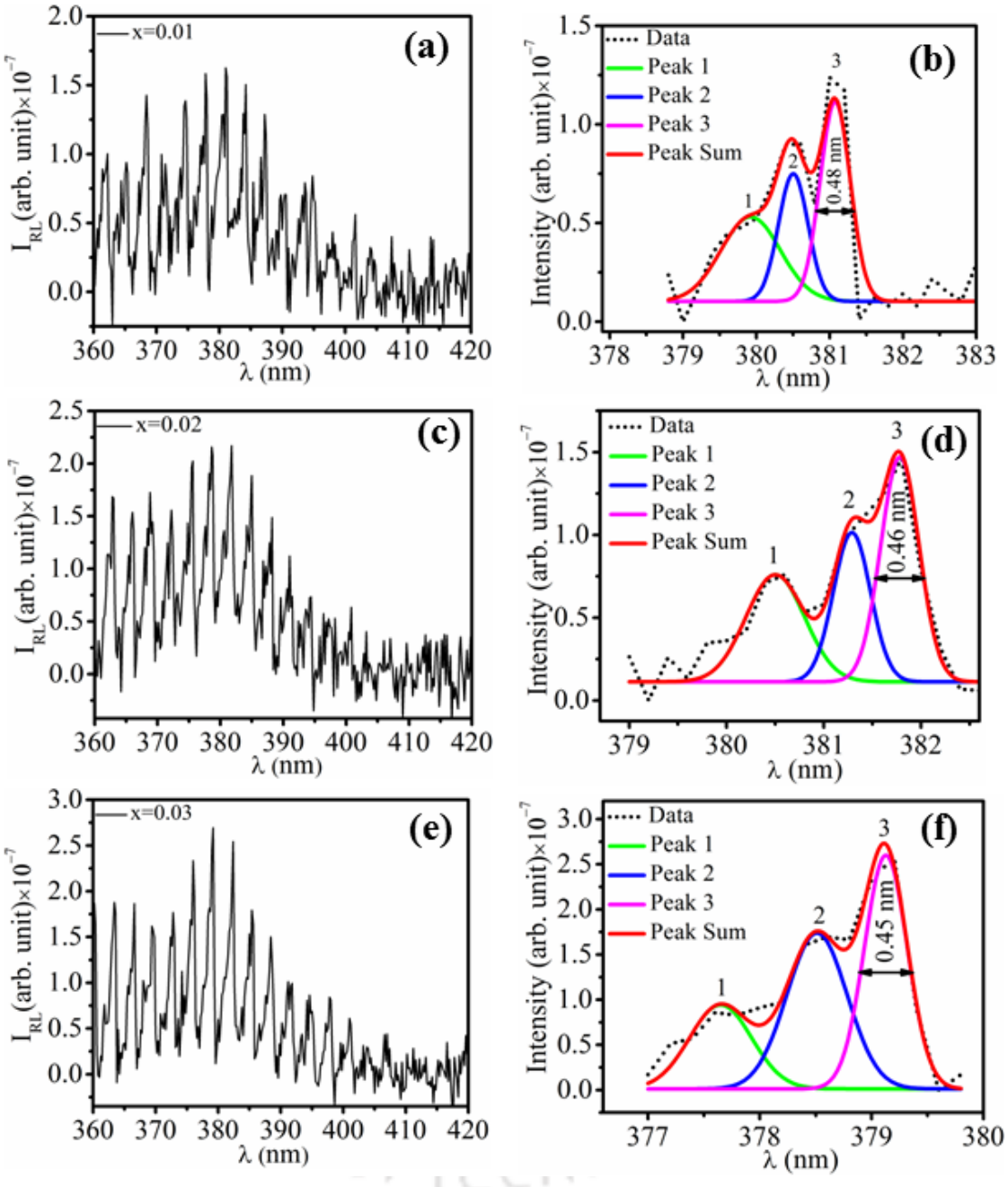

Fig. 7.8 Random lasing spectra of $Zn_{1-x}Al_xO$ ($0.01 \leq x \leq 0.03$) thin film samples and their corresponding de-convoluted spectra of most intense longitudinal mode.

The lasing intensity is observed to be gradually increased with Al content which is due to the increasing average particle size and more compact distribution, favoring the tight coupling of scattered radiation from one particle to the another one. The FWHM of the resonance mode is found to be 0.48 nm, 0.46 and 0.45 respectively.

The plot of lasing spectra of x=0.05 and x=0.10 samples is shown in Fig. 7.9 (a and c) and corresponding de-convoluted spectra for central most intense mode in Fig. 7.9 (b and d) respectively. The line width of most intense mode is marked in de-convoluted spectrum. The values of cavity length and quality factor for all the six films of AZO as a function of x, is listed in table 7.3.

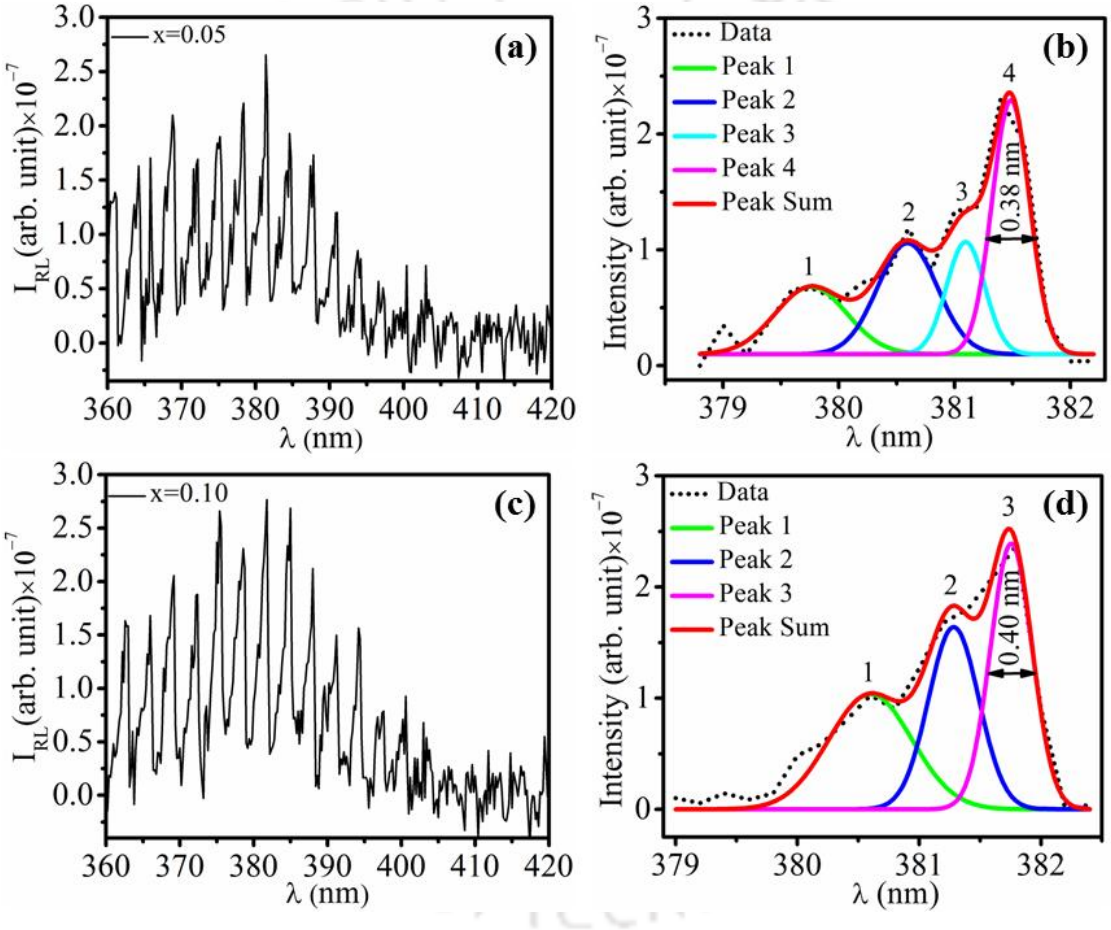

Fig. 7.9 Lasing emission in $Zn_{1-x}Al_xO$ for x=0.05 and x=0.10 thin film samples and their corresponding de-convoluted spectra of the central most intense mode.

The stimulated emission in the nanostructured thin films is linked with three different types of nano-micro cavity formation; the closed loop RL cavity, the FP cavity and the WGM cavity, Fig. 7.1 **[1, 5, 16]**. In the thin film samples, at lower Al content,

$0 \leq x \leq 0.03$, the lasing emission is originated from the spherical shaped nanostructures; hence there is strong possibility of formation of closed loop random lasing cavity only in these samples. The random laser depends only on the density of the scattering elements of the material and does not require any specific geometrical nano-micro structure for onset of laser emission. Cao et al. **[16]** has also demonstrated the lasing action due to the self-formed closed loop RL cavity in polycrystalline ZnO thin film containing nano particles having grain sizes of 50-150 nm. In the thin film samples for x=0.05 and x=0.10, the lasing could be due to the combined formation of FP, WGM as well as random lasing cavity because of the clear emergence of the formation of nanorods and nanowires having facets in hexagonal geometry against the background of spherical particles, Fig. 7.3 (e).

Table 7.3 Estimation of cavity length (L_C) and Q-factor in $Zn_{1-x}Al_xO$ ($0 \leq x \leq 0.10$) thin films.

Sr. No	**Sample (x)**	**Cavity length (L_C) (μm)**	***Q*-factor**
1.	0.00	7.6	691
2.	0.01	7.7	777
3.	0.02	8.1	812
4.	0.03	7.7	842
5.	0.05	7.5	1004
6.	0.10	7.3	954

The length of the optical cavities in these thin film samples are observed to be within a narrow span of 7.3 μm to 8.1μm. The cavity length for pure ZnO thin film,

estimated from the central wavelength (λ_0=380.2 nm) and average mode separation ($\Delta\lambda$=3.13 nm), is found to be 7.6 μm. Moreover, it shows an extension from 7.6 μm to 8.1 μm for x=0.00 to 0.02 samples respectively. The increase in cavity length with the increase in the Al content was attributed to the increase in the particle size as well as reduction in the linear refractive indices of the thin film samples as shown in table, 3.4, Chap. 3. However, for higher Al content, x>0.02, there was a marginal variation in the estimated cavity lengths. The estimated cavity length in all the thin films samples is smaller than the diameter (~125 μm) of the pump area, indicating the nearly uniform illumination of the gain region and thus formation of diffusive cavity.

With the increase in Al concentration, from x=0.01 to x=0.05, the *Q* values are found to increase from 691 to 1004 and then at x=0.10 it decreases slightly to 954. The observed *Q*-values in Table 7.3 can be correlated with the estimated nanostructured sizes (Table 7.2). A plot of nanostructured sizes and *Q*-factors as a function of Al concentration is shown in Fig. 7.10. For the last two samples in the plot, the size of the nano structure is that of the 2D nano rods facets.

For spherical shaped nanostructures, the *Q*-factor is defined in terms of the size of the nano sphere **[17]**.

$$Q = \frac{\lambda^2 D}{2\pi^2 \sigma^2 B} \tag{7.3}$$

where, *D* is the diameter of microsphere, σ is the rms size and *B* is correlation length.

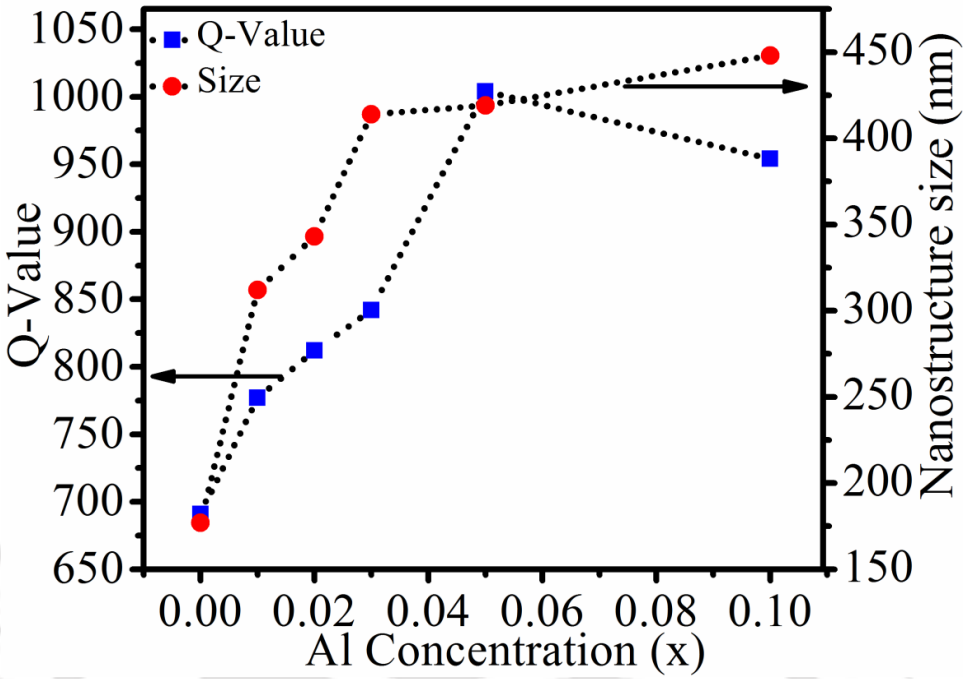

Fig. 7.10 Variation of Q-values and sizes of nanostructures in $Zn_{1-x}Al_xO$ ($0 \le x \le 0.10$) thin films.

For the thin film samples for lower x values, $0.01 \le x \le 0.03$, the particles are of nearly spherical shaped, Fig. 7.3 (b-d), and hence the quality factors in these samples can be correlated with eqn. 7.3 suggesting the linear dependence of *Q*-value over particle size (*D*). Therefore, the *Q*-factor increases with the Al concentration, table 7.3.

For x=0.05 and 0.10, the facets are nearly hexagonal and or polygon, Fig. 7.3 (e and f). Therefore, the *Q*-factor is expressed as **[5, 18]**:

$$Q = \frac{3\sqrt{3}\pi DnR^{3/2}}{2\lambda(1-R^3)} \tag{7.4}$$

In this case, *D* is the diameter of the circle circumscribing the hexagonal structure, *n* is the linear refractive index of the material and *R* is the reflectivity of the side facets.

This equation can hold good for $x \geq 0.05$ thin film samples where hexagonal facets are quite visible. In case of sample x=0.10, due to coalescing of large number of hexagonal facets/rods, the confinement of optical photons inside the structure becomes week and results into reduction in quality factor slightly. Since in both the films, the lasing emission is due to formation of FP and WGM cavity hence, the *Q*-values are observed to be quite large as compared to other samples where the lasing is due to the RL cavity. It is shown that the WGM cavity exhibits maximum *Q*-value compared to those of RL and FP cavity because of the ease of confinement of photons due to total internal reflection **[6]**.

7.4 Conclusion

The lasing action in pure ZnO pellet and PLD $Zn_{1-x}Al_xO$ ($0 \leq x \leq 0.10$) thin films has been demonstrated. The longitudinal lasing modes were observed to be well apart and of nearly equidistant separation of ~3 nm. The average inter-mode separation was observed to be independent of Al concentration in the films. The line widths of the RL spectra in the films were in the range of 0.38-0.56 nm. The lower Al concentration in the films, exhibited nearly spherical shaped nano particles giving rise to formation of random lasing cavity due to strong scattering of optical photons among the particles. The thin films having higher Al content ($x \geq 0.05$) exhibited a mixture of nanorod and nanowire microstructures and exhibited higher laser signal as compared to that of $x \leq 0.03$. In addition, the spikes in each of the longitudinal modes of thin film are observed to be more pronounced as compared to that of bulk sample. The thin film samples for $0 \leq x \leq 0.03$, the lasing emission was observed to be dominated by closed loop random lasing cavity and showed relatively low quality factor as compared to the rest of the thin film samples

having Al content, $x \geq 0.05$, where the lasing was due to the formation of FP and WGM cavity. The lasing threshold in pure ZnO thin film was estimated to be ~3.2×10^2 MW/cm^2 which is reasonably comparable with some of the earlier reports.

Bibliography

[1] DIEDERIK S. WIERSMA, "*The physics and applications of random lasers",* Nature Physics, **4** (2008) 359-367.

[2] WILLIAM T. SILFVAST, "*Laser Fundamentals",* CAMBRIDGE University Press (2004), **ISBN: 978-0-521-13847-5**

[3] Yungting Chen and Yangfang Chen, "*Enhanced random lasing in ZnO nanocombs assisted by Fabry–Perot resonance",* Optics Express, **19** (2011) 8728-8734.

[4] Jitao Li et al., "*Plasmon coupled Fabry-Perot lasing enhancement in graphene/ZnO hybrid microcavity",* Scientific Reports, **5** (2015) 9263.

[5] J. Dai et al., "*Combined whispering gallery mode laser from hexagonal ZnO microcavities",* Applied Physics Letters, **95** (2009) 191117.

[6] Gangyi Zhu et al., "*Lasing Behavior Modulation for ZnO Whispering-Gallery Microcavities",* ACS Applied Materials & Interfaces, **4** (2012) 6195-6201.

[7] J Kitur et al., "*Dependence of the random laser behavior on the concentrations of dye and scatterers",* Journal of Optics, **12** (2010) 024009.

[8] B. Q. Sun et al., "*Epitaxially grown GaAsN random laser",* Journal of Applied Physics, **93** (2003) 5855-5858.

[9] Yue Wang et al., "*Coherent Random lasing from CdSe/CdS/ZnS quantum dots",* JSAP, **18p-D5-9 (**2013**).**

[10] Toru Takahashi et al., "*Blue-light-emitting ZnSe random laser",* Optics Letters, **34** (2009) 3923-3925.

[11] SHU ZHU et al., "*Random lasing at the edge of a TiO_2 nanotube thin film",* Applied Optics, **55** (2016) 5091-5094.

[12] Gyan Prakash Bharti and Alika Khare, "*Structural and linear and nonlinear optical properties of $Zn_{1-x}Al_xO$ ($0 \leq x \leq 0.10$) thin films fabricated via pulsed laser deposition technique",* Optical Materials Express, **6** (2016) 2063-2080.

[13] D. M. Bagnall et al., "*Optically pumped lasing of ZnO at room temperature",* Applied Physics Letters, **70** (1997) 2230-2232.

[14] J. Andreasen et al., "*Modes of random lasers",* Advances in Optics and Photonics, **3** (2011) 88-127.

[15] A. B. Djurisic et al., "*Optical properties of highly faceted ZnO rods",* Journal of Applied Physics, **99** (2006) 033517.

[16] H. Cao et al., "*Ultraviolet lasing in resonators formed by scattering in semiconductor polycrystalline film",* Applied Physics Letters, **73** (1998) 3656-3658.

[17] Alexandro Chiasera et al., "*Spherical whispering-gallery-mode microresonators",* Laser & Photonics Reviews, **4** (2010) 457-482.

[18] Achintya K. Bhowmik, "*Polygonal optical cavities",* Applied Optics, **39** (2000) 3071-3075.

Chapter 8
Conclusions

The work contained in the present thesis is devoted towards the linear and non linear optical characterization of pulsed laser deposited thin films of $Zn_{1-x}Al_xO$ ($0 \leq x \leq 0.10$) and $Zn_{1-x}Ti_xO$ ($0 \leq x \leq 0.050$). The Crystalline features of both types of films, AZO and TZO, were detected by XRD and Raman spectra. The surface quality of these films was obtained by field emission scanning electron microscope (FESEM). The linear refractive index, *n*, absorption coefficient, α, and the band gap of the film was measured via UV-VIS-NIR spectroscopy. In order to study the effect of temperature on the near band edge emission in UV range and the defect level emission in blue- red spectral range, photoluminescence spectra were recorded from room temperature to down to 10K. The non linear refractive index, n_2, non linear absorption coefficient, β, and the third order susceptibility, χ^3 were measured via modified z-scan set-up. The two photon absorption induced photoluminescence in the AZO as well as TZO films were observed by exciting with He: Ne laser at 632.8nm. Finally the $Zn_{1-x}Al_xO$ ($0 \leq x \leq 0.10$) thin films were subjected to Random lasing experiment to study the influence of Al content on the quality factor of the UV laser.

All the thin films of $Zn_{1-x}Al_xO$ ($0 \leq x \leq 0.10$) and $Zn_{1-x}Ti_xO$ ($0 \leq x \leq 0.050$) were fabricated onto fused silica as well as Si substrates via pulsed laser deposition technique at optimum deposition parameters obtained from the literature.

Both sets of the films, AZO and TZO displayed the polycrystalline nature as confirmed by the appearance of (100), (002), (101), (102) and (110) planes in XRD. Moreover, the c-axis oriented (002) diffraction peak was observed to be gradually enhanced with the increase in the impurity content, x, up-to x=0.05 for Al and that of Ti

up-to x=0.02. The higher impurity content (for Al, x>0.05 and Ti, x>0.02) resulted into the lowering of the preferred c-axis orientation. The similar observation was also deduced from the Laser Raman measurements where the dominating E_2(high) mode, corresponding to the wurtzite hexagonal crystal structure, was observed to be significant in AZO as well as TZO film thin films as compared to that of pure ZnO film. The AZO thin films showed tunable optical band gap energy from 3.26 eV to 3.64 eV with the largest band gap obtained for 5wt% Al doped film. Similar trend was observed for TZO film but the maximum band gap was observed for Ti content of 2% by wt. The blue shift in the band gap energy with Al concentration was mainly due to the high carrier density associated Burstein Moss effect. The variation in the estimated linear refractive indices in the AZO thin films was marginal. In case of Ti infused ZnO film, the refractive index was found to increase with the Ti content which is due to the excessive carrier density imparted in the presence of Ti.

The room temperature photoluminescence spectra of AZO and TZO thin films were recorded by exciting the samples with 320 nm line of Xenon lamp. The $Zn_{1-x}Al_xO$ ($0 \leq x \leq 0.10$) thin films showed both near band edge (NBE) band (365-400nm), associated with free exciton (FX) and bound excitons, as well as defect level emission (DLE) bands due to shallow and deep level defects. The AZO films showed an enhancement in the NBE emission and a simultaneously reduction in the DLE emission as compared to that of pure ZnO film. The linear variation of the UV PL peak with the band gap energy was observed in the AZO films. The defect level emission (DLE) spectra of the AZO films (x>0.00) could be deconvoluted into four main peaks in violet-blue region positioned around 410 nm (~3.024 eV), 435 nm (~2.850 eV), 450 nm (~2.755 eV) and 470 nm (~2.63) which were attributed to Zn_i to valence band (VB), Zn_i to V_{Zn}, extended Zn_i to

VB and conduction band (CB) to O_{Zn} transitions respectively. The increase/decrease in the integrated intensity of 410 nm and 435 nm components with Al concentration in the film suggested the increased/decreased concentration of Zn_i/V_{Zn} defects in the films. The Al doped ZnO system resulted into an oxygen rich system therefore; the PL components associated with oxygen deficient defects (V_O, V_{Zn}) were decreased.

Similar to the RT PL spectra in AZO thin films, the TZO films showed both NBE as well as DLE bands. The film grown at x=0.020 Ti composition demonstrated complete quenching of the visible emission which could be due to the improved crystalline quality and weak quantum confinement effect. The higher Ti concentration (x=0.030, 0.050) leads to the enhanced photoluminescence signals in both, NBE as well as DLE. This was due to relatively larger film thickness of these particular samples which was due to excessive electron concentration resulting in lowering the ablation threshold.

The one of the novelty of present thesis was the studies on temperature dependent photoluminescence spectra of the AZO and TZO PLD thin films. The low temperature measurements for PLD thin films of $Zn_{1-x}Al_xO$ (x=0 and x=0.05) and $Zn_{1-x}Ti_xO$ ($0 \leq x \leq 0.050$) were carried out by lowering the sample temperature up-to 10K in the interval of 10K. All the thin film samples exhibited temperature dependent blue shift in NBE band. The pure ZnO thin film showed dominating neutral donor bound exciton (D^0X) line along with longitudinal optical phonon replicas of D^0X (D^0X-1LO and D^0X-2LO) in the low temperature, T<160K, region. There was a faint appearance of free exciton (FX) line at the edge of D^0X line at low temperature but it completely dominated in the temperature range of T=180K to RT. However, the 5wt% Al doped ZnO film exhibited only dominating D^0X line and no clear signature of FX line was observed. A weak signature of an additional line of two electron satellite (TES) transition was also

observed at low temperature in AZO film. The Varshni's thermal coefficients (*a* and *b*) were estimated to be 7.4×10^{-4} eV/K and 390K respectively for pure ZnO thin film. The '*a*' and '*b*' coefficients in the AZO thin films were estimated to be observed to be 4.0×10^{-4} eV/K and 450K respectively. The thermal activation energies (E_a) of the dominating D^0X lines estimated from the Arrhenius equation were found to be 12.69 meV and 11.34 meV for ZnO and AZO thin films respectively. Slightly low value of E_a in AZO thin film as compared to that of ZnO signifies the strong coupling of donor with free exciton at low temperature in the former case. The visible PL in both the films showed a red shift in the peak position with decrease in the sample temperature. In the case of TZO thin films, PL spectra displayed strong coupling of donor bound exciton and phonons as compared to that of pure ZnO thin film at low temperature. As a consequence, the TZO thin film samples exhibited strong D^0X line and absence of FX line as compared to AZO thin film. The activation energies of the neutral donor bound exciton (D^0X) were observed to be within the range of 12.69-5.18 meV with the minimum value (5.18 meV) for x=0.05 thin film sample. This further supported the dominant coupling of donor bound exciton over FX line in Ti doped film as compared to pure ZnO film. The Varshni's coefficients (*a* and *b*) were observed to be increased from 7.4×10^{-4} eV/K to 1.39×10^{-3} and 390K to 822K respectively.

The non linear absorption coefficient, and nonlinear refractive index of all the PLD thin films of AZO and TZO were measured by modified Z-scan. The films were showing reverse saturation behavior suggesting its potential application in optical limiting. In addition, the thin film samples exhibited negative refractive nonlinearity which may find application in optical switching. The nonlinear absorption coefficient (β), was found to be in the range of 3.4-10.0 cm/W in the $Zn_{1-x}Al_xO$ ($0\leq x\leq0.10$) films and the

maximum β (10 cm/W) was achieved in x=0.05 thin film. The nonlinear refractive index coefficients (n_2) of these samples were observed to be in the range of (1.0-5.8)×10^{-4} cm^2/W having the maximum value of 5.8×10^{-4} cm^2/W of n_2 for x=0.05 thin film. The corresponding third order nonlinear optical susceptibilities ($\chi^{(3)}$) in the films were estimated to be (5.47-27.46)×10^{-3} esu and followed the similar variation as β and n_2 with Al content. The increased values of third order nonlinear optical constants (β, n_2 and $\chi^{(3)}$) in the x=0.05 thin film sample were in accordance with the improved crystalinity and increased free carrier concentration of the film with the infusion of Al as an impurity in ZnO. The third order nonlinear optical coefficients β and n_2, of TZO thin films were estimated to be 3.4-6.0 cm/W and (1.0-4.1)×10^{-4} cm^2/W respectively. The estimated ($\chi^{(3)}$) values in the films were found to be (2.2-24.76)×10^{-3} esu. The maximum values of these constants (β =6.0 cm/W, n_2=4.1 cm^2/W and $\chi^{(3)}$=24.76×10^{-3} esu) were corresponding to x=0.020 thin film sample. The estimated third order nonlinear optical coefficients (β and n_2) in both cases, $Zn_{1-x}Al_xO$ ($0 \leq x \leq 0.10$) and $Zn_{1-x}Ti_xO$ ($0 \leq x \leq 0.050$), were observed to be linearly dependent on the linear absorption coefficient (α). Therefore, the observed nonlinear optical constants in the films were of predominating thermal in nature.

The multiphoton absorption induced photoluminescence (MPA-PL) spectra of $Zn_{1-x}Al_xO$ ($0 \leq x \leq 0.10$) and $Zn_{1-x}Ti_xO$ ($0 \leq x \leq 0.050$) thin films, recorded at room temperature by exciting the thin film samples with cw He:Ne laser, was observed to be in the spectral range of 340-370 nm. A slight blue shift in the peak position w.r.t. the corresponding UV-PL spectra under single photon excitation, was due to the generation of hot carriers. The peak positions of MPA-PL spectra in $Zn_{1-x}Al_xO$ ($0 \leq x \leq 0.10$) were shifted towards lower wavelength up-to x=0.05 and thereafter slightly towards higher wavelength for higher x values. The slopes of the linear fit to the logarithmic plot of the

excitation pump intensity and MPA-PL intensity were in the range of 1.30-1.68 conveying the two photon absorption (TPA) process in these films. The maximum value of *m*, was obtained for x=0.05 thin film sample indicating most efficient TPA conversion process. Similar to the AZO thin films, the $Zn_{1-x}Ti_xO$ ($0 \leq x \leq 0.05$) thin films also showed MPA-PL signal. The values of the slopes of $Log(I_{PL})$ vs. $Log(I_{EXC})$ graph in TZO thin films were in the range of 1.01-1.46. The minimum value of *m* (1.01) and maximum value of *m* (1.46) was obtained for x=0.05 and x=0.02 thin film samples respectively. Therefore, it was concluded that the AZO films exhibited better two photon absorption response as compared to that of TZO thin films.

The surface of the film displayed the formation of spherical particles up-to an Al content of x=0.03 and for higher content, it showed the formation of nano wires and nano rods having hexagonal facets and thus indicated that it could be considered as a medium for random lasing. The random lasing emission in PLD AZO thin films was studied by pumping it with 3rd harmonic (355 nm) of Q-switched Nd:YAG laser at room temperature. Narrow and closely spaced longitudinal lasing modes, covering the near band edge emission curve of ZnO, were observed in all the films. The mode separations in the films were of ~3 nm while the spectral widths were estimated to be 0.38 nm to 0.56 nm. There was marginal change in the length of the cavity which is due to the variation in the refractive index with x. The optical cavity length in these samples was in the range of 7.3-8.1 μm. The lasing emission in the films having spherical particulates was due to the pure random lasing where as that of containing the nano rods and nano wire was due to the formation Fabry-Perot (FP) cavity and whispering gallery mode (WGM) cavity. The quality factors (Q-factor) estimated for the RL was in the range of 691-1004. A high quality factor of 1004 was obtained for the thin film grown at x=0.05 composition

containing of nanorods in the background of the spherical particles. The RL threshold for pure ZnO film was estimated to be ~3.2×10^2 MW/cm^2.

Future scope of the work

The multiphoton absorption induced photoluminescence in the AZO as well as TZO films was studied in the present thesis by pumping with a cw laser in which the sub-band gap absorption was accompanied via hot carriers. The study can be further undertaken under short pulsed laser beam for frequency up conversion. The process of multiphoton absorption under pulsed wave pumping is initiated via virtual state which has very short life time (~ns). Therefore, the actual picture about the interaction of optical photon with the material i.e. multiphoton absorption and emission mechanism can be revealed. Furthermore, the presence of donor atoms (Al and Ti) in the form of impurities forming shallow as well as deep donor levels within the gap can modify the lifetime of these states. This may alter the transition probability and consequently the recombination dynamics will be changed.

The random lasing study of AZO thin films showed variable optical cavity and quality factor which was mainly due to the modification in the shape and size of nanostructures in these films. The lasing threshold for the pure ZnO film was observed at ~3.2×10^2 MW/cm^2. The lasing threshold in the presence of external impurity (Al) can be significantly changed which may bring a new insight toward efficient and cost effective way to generate lasing emission. The fabrication of coherent feedback single mode random laser is a challenge. So, it will be of great interest to work towards visualization of single mode random laser.

List of Publications

Journals

1. **Gyan Prakash Bharti** and Alika Khare, "*Quenching of visible photoluminescence and observation of two photon absorption induced photoluminescence in pulsed laser deposited $Zn_{1-x}Ti_xO$ $(0.000 \leq x \leq 0.050)$ thin films*", Journal of Physics D: Applied Physics **52,** 015103 (2018).

2. **Gyan Prakash Bharti**, Partha P Dey and Alika Khare, "*Pulsed laser deposited $Zn_{1-x}Ti_xO$ $(0 \leq x \leq 0.050)$ thin films for tunable refractive index and nonlinear optical applications*", Materials Chemistry and Physics **216**, 206-212 (2018).

3. **Gyan Prakash Bharti** and Alika Khare, "*Single and multiphoton absorption induced photoluminescence in pulsed laser deposited $Zn_{1-x}Al_xO$ $(0 \leq x \leq 0.10)$ thin films*", Journal of Luminescence **197**, 135-141 (2018).

4. **Gyan Prakash Bharti** and Alika Khare, "*Structural and linear and nonlinear optical properties of $Zn_{1-x}Al_xO$ $(0 \leq x \leq 0.10)$ thin films fabricated via pulsed laser deposition technique*", Optical Materials Express **6**, 2063-2080 (2016).

5. **Gyan Prakash Bharti** and Alika Khare, "*Single Photon Assisted Random Lasing Action in ZnO Thin Film Fabricated via Pulsed Laser Deposition Technique*", Journal of Atomic, Molecular, Condensate and Nano Physics (Accepted).

6. **Gyan Prakash Bharti** and Alika Khare, "*Band gap tuning in $Zn_{1-x}Al_xO$ $(0 \leq x \leq 0.10)$ thin films deposited via PLD*", OSA Digital Digest, DOI: 10.1364/PHOTONICS.2014.S5A.76.

7. **Gyan Prakash Bharti** and Alika Khare, "*Effect of Al concentration on optically pumped random lasing in $Zn_{1-x}Al_xO$ $(0 \leq x \leq 0.10)$ thin films fabricated via pulsed laser deposition technique*", (To be submitted).

8. **Gyan Prakash Bharti**, Dushyant Kushvah, B. P. Singh and Alika Khare, "*Mechanism of photoluminescence in pulsed laser deposited AZO thin films in low temperature regime*", (under preparation).

9. **Gyan Prakash Bharti**, Dushyant Kushvah, B. P. Singh and Alika Khare, "*Low temperature photoluminescence in pulsed laser deposited TZO thin films*", (under preparation).

Publications outside thesis

10. Apurba Das, Anil Kumar Chikkala, **Gyan Prakash Bharti**, Rasmi Ranjan Behera, Ravi Sankar Mamilla, Alika Khare, Pamu Dobbidi, "*Effect of thickness on optical and microwave dielectric properties of Hydroxyapatite films deposited by RF magnetron sputtering*", Journal of Alloys and Compounds **739**, 729-736 (2018).

11. Mahesh Peddigari, Vivek Patel, **Gyan Prakash Bharti**, Alika Khare, Pamu Dobbidi, "*Microwave dielectric and nonlinear optical studies on radio frequency sputtered Dy_2O_3- doped KNN thin films*", Journal of American Ceramic Society **100**, 3013-3023 (2017).

12. Mahesh Peddigari, **Gyan Prakash Bharti**, Alika Khare and Pamu Dobbidi, "*Optical and dielectric studies on radio frequency sputtered Gd_2O_3 doped $K_{0.5}Na_{0.5}NbO_3$ thin films for nonlinear photonic and microwave tunable device applications*", Journal of Alloys and Compounds **682**, 634-642 (2016).

13. Mahesh Peddigari, Srinivas Pattipaka, **Gyan Prakash Bharti**, Alika Khare, Pamu Dobbidi, "*Nonlinear optical properties of pulsed laser deposited Gd_2O_3 and Dy_2O_3 doped $K_{0.5}Na_{0.5}NbO_3$ thin films*", Optical Materials **58**, 9-13 (2016).

Conference Presentation in National/International Conferences

1. **Gyan Prakash Bharti** and Alika Khare, "*Multiphoton absorption induced photoluminescence in AZO thin films*", International Conference on light and light based technologies (ICLLT-2016) held at Tezpur University, Tezpur, Assam-India, during November 26-28, 2016.

2. **Gyan Prakash Bharti** and Alika Khare, "*Frequency tripled Nd:YAG laser pumped Random lasing in ZnO and Al doped ZnO thin films fabricated via Pulsed Laser Deposition technique*", National Laser Symposium (NLS-24) held at RRCAT Indore, M. P., India, during December 2-5, 2015.

3. **Gyan Prakash Bharti** and Alika Khare, "*Single Photon Assisted Random Lasing Action in ZnO Thin Film Fabricated via Pulsed Laser Deposition Technique*", 4th

International Conference on Current Development on Atomic, Molecular, Optical & Nano Physics with Applications, CDAMOP-2015, held at Dept. of Physics and Astrophysics, University of Delhi, India, during march 11-14, 2015.

4. **Gyan Prakash Bharti** and Alika Khare, "*Band gap tunning in $Zn_{1-x}Al_xO$ $(0\leq x\leq 0.10)$ thin film deposited via PLD*", 12th International Conference on Optics and Fiber Optics, Photonics-2014, held at Department of Physics, IIT Kharagpur, India, during December13-16, 2014.

5. **Gyan Prakash Bharti** and Alika Khare, "*Third order optical nonlinearity in $Zn_{1-x}Al_xO$ $(0\leq x\leq 0.10)$ thin films deposited via Pulsed Laser Deposition Technique*", National Laser Symposium (NLS-23), Sri Venkateshwara University Tirupati, A. P. (India), December 3-6, 2014.

6. Indrajeet Kumar, **Gyan Prakash Bharti** and Alika Khare, "*Laser power induced disorder in PLD deposited DLC film during Raman measurement*", National Laser Symposium (NLS-23), Sri Venkateshwara University Tirupati, A. P. (India), December 3-6, 2014.

7. **G. P. Bharti,** Satchi Kumari, Archana Kushwaha and Alika Khare,"*Nonlinear Absorption in Pulsed Laser Deposited ZnO thin films*", International Conference on optics and optoelectronics ICOL-2014, held at IRDE Dehradun, India, during April 5-8, 2014.

8. Rahul Kesarwani, **G. P. Bharti**, Partha P Dey, Indrajeet Kumar, A T T Mostako and Alika Khare, "NLO behavior of semitransparent Cu thin film deposited by PLD", International conference on Optics and Optoelectronics ICOL-2014, IRDE Dehradun, India, during March 5-8, 2014.

9. Partha P Dey, **G. P. Bharti** and Alika Khare, "*Third order nonlinear optical properties of PLD deposited Nanostructured SiC Thin Films*", International conference on Optics and Optoelectronics ICOL-2014, IRDE Dehradun, India, during March 5-8, 2014.

10. **G. P. Bharti**, Raja Bonia, Partha P Dey, A. T. T. Mostako, Satchi Kumari and Alika Khare, "*SPR and NLO Behavior of PLD deposited Cu thin films*", National

Symposium on Pulsed Laser Deposition of thin films and Nanostructure PLD-2013, held at IIT Kharagpur, India, during November 14-16, 2013.

11. A. T. T. Mostako, **G. P. Bharti**, Kh. S. Singh, A. K. Sharma and Alika Khare, "*Determination of Electron Density in Laser Induced Molybdenum Plasma*", 27th National Conference on Plasma Science & Technology (Plasma-2012), Pondicherry University, Pondicherry, India, during December 10-13, 2012.

Workshop/School Attended

1. Research Conclave-2017 held at IIT Guwahati, Guwahati, India, during March 16-19, 2017.

2. "One-Day Workshop on Vacuum Technology and its Applications in Optical Science", held at IIT Guwahati, Guwahati on August 19th, 2017.

3. "Light: not a Light Matter' a student symposium", SPIE student chapter, IIT Guwahati held at Dibrugarh University, Dibrugarh, Assam, India on November 12, 2016.

4. Research Conclave-2016 held at IIT Guwahati, Guwahati, India, during March 17-20, 2016.

5. "TEQIP Symposium to Celebrate the 2015 International Year of Light", held at IIT Guwahati, India, on October 31st, 2015.

6. Research Conclave-2016 held at IIT Guwahati, India, during March 23-26, 2015.

7. "IUCr workshop on X-ray diffraction systems and related applications", held at IIT Guwahati, India, during September 11-12, 2014.

8. "Science Fair 2014: National Science Day", held at Cotton College State University, Guwahati, India, during 28th Feb. & 1st March 2014.

9. IEEE Workshop on "*Comprehensive Sensing and Technical Writing*" held at IIT Guwahati, India, during April 6-7, 2013.

10. SERC school on "*Laser Produced Plasmas: Physics and Applications*" held at RRCAT Indore, M.P., India, during July 9-21, 2012.

11. QIP on "*Computational Techniques in Physics*" held at Dept. of Physics, IIT Guwahati, India, during August 1-6, 2011.